

Studies in Physical Biology: Exploring Allosteric
Regulation, Enzymatic Error Correction, and Cytoskeletal
Self-Organization using Theory and Modeling

Thesis by
Vahe Galstyan

In Partial Fulfillment of the Requirements for the
Degree of
Doctor of Philosophy in Biochemistry and Molecular Biophysics

The logo for the California Institute of Technology (Caltech), featuring the word "Caltech" in a bold, orange, sans-serif font.

CALIFORNIA INSTITUTE OF TECHNOLOGY
Pasadena, California

2022
Defended on August 12, 2021

© 2022

Vahe Galstyan

ORCID: 0000-0001-7073-9175

This thesis is distributed under a Creative Commons
Attribution-NonCommercial-ShareAlike License.

ACKNOWLEDGEMENTS

My stay at Caltech has been an intellectually stimulating, transformative, and highly rewarding experience. It all started in the junior year of college when my undergraduate advisor Chris Wiggins gave me his top recommendation to do summer research with Rob Phillips (my PhD advisor). Despite the fact that I lacked any background in biophysics, Rob graciously agreed to bring me along with him to the Marine Biological Laboratory (MBL) where he was the director of the Cell Physiology course. The summer at MBL revealed the wondrous field of biophysics to me. I remember my excitement when Rob's postdoc Brewster, who was a teaching assistant for the course, took the time to perform a gene expression experiment with me, and afterwards I had my own data to analyze and compare with theoretical predictions. Also, Rob himself generously organized a mini-course on statistical mechanics just for me and another visiting undergraduate student, which left a lasting impression on me about Rob's sincere passion for teaching and care for the students.

After that summer, I decided with certainty that I was going to do graduate work in biophysics and with no other person but Rob. During my time at Caltech, Rob has been a friend, a mentor, a coach, and a source of constant inspiration for me. I remember coming into graduate school with a physics background and being too obsessed with complicated formulas and mathematics, unable to appreciate the importance of simplicity and observation. In spite of my stubbornness, over the course of the many years, Rob has put a lot of effort in helping me think clearly, have a feeling for the numbers, and internalize the saying that 'simplicity is the ultimate complexity.' Importantly, Rob gave me the freedom to satisfy my intellectual curiosities and venture into challenging projects where the path to the finish line was not obvious. The guided struggles that I had during my intellectual journeys have helped me immensely in growing as an independent scientist. I am so grateful to Rob for the many things I learned from him about science and life.

I also feel fortunate to be a graduate student at the Biochemistry and Molecular Biophysics program which really gave me the first formal introduction to the field. I would like to thank my course instructors Bil Clemons, Grant Jensen, and Shu-ou Shan, as well as our BMB cohort for creating a friendly and intellectually stimulating community. I would also like to give special thanks to Justin Bois for the very useful data analysis skills that he taught me and for being a caring person to people around

him. I'm thankful also to Nigel Orme for his highly useful and inspiring course on Adobe Illustrator and drawing in general.

My research would have been much less rewarding if it weren't for the wonderful collaborations I've had over the course of many years. I'm deeply grateful to Christina Hueschen, Kabir Husein, Luke Funk, Arvind Murugan, Thu Vu Phuc Nguyen, Jerry Wang, and Dennis Yatunin for sharing intellectual journeys with me, many of which started at summer courses at MBL where, this time around, I was the teaching assistant to Rob. I thank Fangzhou Xiao and Soichi Hirokawa for the great scientific exchanges over the years, and Rachel Banks and Heun Jin Lee for a wonderful multi-year collaboration on an active matter project with regular stimulating meetings. I am thankful to Gabe Salmon for his consistent scientific camaraderie, particularly during the coronavirus pandemic where we had weekly 'feedback' meetings which typically turned into hours-long discussions. Also during the pandemic, I had an amazing collaboration with Pooja Suresh where we would spend hours and hours working together over Zoom doing coding, reading papers jointly, and struggling to understand cell mechanics.

Throughout my PhD, I received valuable suggestions and guidance from my thesis committee members David Van Valen, Matt Thomson, and Erik Winfree. I thank them for encouraging me to be rigorous in my work and to develop a broader perspective on the research questions I studied.

The hardships of graduate school have been alleviated by my excellent roommate Tal Einav whose constant positivity always made me laugh. My officemate Suzy Beeler was also a wonderful friend. I'm grateful to all the other members of our group, namely Stephanie Barnes, Nathan Belliveau, Adam Catching, Griffin Chure, Ana Duarte, Avi Flamholz, Helen Bermudez Foley, Bill Ireland, Zofii Kaczmarek, Gita Mahmoudabadi, Niko McCarty, Muir Morrison, Manuel Razo, Tom Röschinger, Rebecca Rousseau, Scott Saunders, and Franz Weinert for their great company over the years.

I would not have managed to stay sane and focused had it not been for the constant support and encouragement of my family. I am most excited about returning home for an extended period of time after graduation. Last but not least, I would like to thank the circumstances for often playing out favorably against the odds.

ABSTRACT

Physical biology offers powerful tools for quantitatively dissecting the various aspects of cellular life that one cannot attribute to inanimate matter. Signature examples of living matter include adaptation, self-organization, and division. In this thesis, we explore different interconnected facets of these processes using statistical mechanics, nonequilibrium thermodynamics, and biophysical modeling.

One of the key mechanisms underlying physiological and evolutionary adaptation is allosteric regulation. It allows cells to dynamically respond to changes in the state of the environment often expressed through altered levels of different environmental cues. The first thread of our work is dedicated to exploring the combinatorial diversity of responses available to allosteric proteins that are subject to multi-ligand regulation. We demonstrate that proteins characterized through the Monod-Wyman-Changeux model of allostery and operating at thermodynamic equilibrium are capable of eliciting a wide range of response behaviors which include the kinds known from the field of digital circuits (e.g., NAND logic response), as well as more sophisticated computations such as ratiometric sensing.

Despite the fact that biomolecules at thermodynamic equilibrium are able to orchestrate a variety of fascinating behaviors, the cell is ultimately ‘alive’ because it constantly metabolizes nutrients and generates energy to drive functions that cannot be sustained in the absence of energy consumption. One prominent example of such a function is nonequilibrium error correction present in high-fidelity processes such as protein synthesis, DNA replication, or pathogen recognition. We begin the second thread of our work by providing a conceptual understanding of the prevailing mechanism used in explaining this high-fidelity behavior, namely that of kinetic proofreading. Specifically, we develop an allostery-based mechanochemical model of a kinetic proofreader where chemical driving is replaced with a mechanical engine with tunable knobs which allow modulating the amount of dissipation in a transparent way. We demonstrate how varying levels of error correction can be attained at different regimes of dissipation and offer intuitive interpretations for the conditions required for efficient biological proofreading.

We then extend the notion of error correction to equilibrium enzymes not endowed with structural features typically required for proofreading. We show that, under physiological conditions, purely diffusing enzymes can take advantage of the existing

nonequilibrium organization of their substrates in space and enhance the fidelity of catalysis. Our proposed mechanism called spatial proofreading offers a novel perspective on spatial structures and compartmentalization in cells as a route to specificity.

In the last thread of the thesis, we make a transition from molecular-scale studies to the mesoscopic scale, and explore the principles of self-organization in nonequilibrium structures formed in reconstituted microtubule-motor mixtures. In particular, we develop a theoretical framework that predicts the spatial distribution of kinesin motors in radially symmetric microtubule asters formed under various conditions using optogenetic control. The model manages to accurately recapitulate the experimentally measured motor profiles through effective parameters that are specific for each kind of kinesin motor used. Our theoretical work of rigorously assessing the motor distribution therefore offers an avenue for understanding the link between the microscopic motor properties (e.g., processivity or binding affinity) and the large-scale structures they create.

In all, the thesis encompasses a series of case studies with shared themes of allostery and nonequilibrium, highlighting the capacity of living matter to perform remarkable tasks inaccessible to nonliving materials.

PUBLISHED CONTENT AND CONTRIBUTIONS

Galstyan, V., Husain, K., Xiao, F., Murugan, A. & Phillips, R.. Proofreading through spatial gradients. *Elife* **9**:e60415 (2020). DOI: 10.7554/eLife.60415

V. G. initiated the project, performed research, and wrote the manuscript.

Galstyan, V. & Phillips, R.. Allosteric and kinetic proofreading. *J. Phys. Chem. B* **123**, 10990–11002 (2019). DOI: 10.1021/acs.jpcc.9b08380

V. G. initiated the project, performed research, and wrote the manuscript.

Hueschen, C. L., **Galstyan, V.**, Amouzgar, M., Phillips, R. & Dumont, S. Microtubule end-clustering maintains a steady-state spindle shape. *Curr. Biol.* **29**, 700–708 (2019). DOI: 10.1016/j.cub.2019.01.016

V. G. performed data analysis, created figures, and edited and reviewed the manuscript.

Galstyan, V.*, Funk, L.* , Einav, T. & Phillips, R. Combinatorial control through allosteric. *J. Phys. Chem. B* **123**, 2792–2800 (2019). DOI: 10.1021/acs.jpcc.8b12517

V. G. initiated the project, performed research, and wrote the manuscript.

TABLE OF CONTENTS

Acknowledgements	iii
Abstract	v
Published Content and Contributions	vii
Table of Contents	viii
List of Illustrations	xi
List of Tables	xiv
Chapter I: Introduction	1
Chapter II: Combinatorial control through allostery	7
2.1 Abstract	7
2.2 Introduction	7
2.3 Results	10
2.3.1 Logic response of an allosteric protein modulated by two ligands	10
2.3.2 General two-ligand MWC response	13
2.3.3 Modulation by multiple ligands	15
2.4 Discussion	19
References	22
Chapter S2: Supporting information for Chapter 2 Combinatorial control through allostery	26
S2.1 Derivation of conditions for achieving different logic responses	26
S2.1.1 AND gate	27
S2.1.2 OR gate	27
S2.1.3 NAND and NOR gates	28
S2.1.4 XOR and XNOR gates	29
S2.2 The general two-ligand response: Transitioning between OFF and ON states	30
S2.3 Logic switching by tuning the number of ligand binding sites	33
S2.4 Combinatorial control with three regulatory ligands	35
S2.4.1 Functionally unique MWC gates	35
S2.4.2 Logic switching	38
References	40
Chapter III: Allostery and kinetic proofreading	41
3.1 Abstract	41
3.2 Introduction	42
3.3 Model	43
3.4 Results	47
3.4.1 Ratchet and pawl engine enables a tunable control of piston actions	47

3.4.2	Thermodynamic constraints make fidelity enhancement unattainable in the absence of external driving	52
3.4.3	Coupling the engine to the enzyme gives the full description of the piston model	53
3.4.4	Energy–speed–fidelity trade-off in the piston model	56
3.4.5	Up to three proofreading realizations are available to the piston model	61
3.5	Discussion	63
	References	66
Chapter S3: Supporting information for Chapter 3 Allosteric and kinetic proofreading		70
S3.1	Discrimination fidelity in the conceptual scheme of the piston model	70
S3.2	Ratchet and pawl engine	72
S3.2.1	Details of the ratchet and pawl mechanism in the absence of piston coupling	72
S3.2.2	Derivation of $\Delta W_{1/2}$ expressions	74
S3.3	Equilibrium properties of the allosteric enzyme	76
S3.3.1	Constraints on the choice of enzyme’s rate constants	76
S3.3.2	Enzyme fidelity at a fixed ligand concentration	77
S3.4	Full description of the piston model with engine–enzyme coupling .	81
S3.4.1	Equilibrium fidelity of the piston model in the absence of external driving	82
S3.4.2	Obtaining the steady–state occupancy probabilities	84
S3.4.3	Enzyme’s kinetic parameters used for the numerical study in the main section 3.4	86
S3.4.4	Details of the numerical optimization procedure for finding the highest fidelity	87
S3.4.5	Investigation of the $\alpha_{\max} \approx 3$ result for the highest available proofreading index	88
	References	93
Chapter IV: Proofreading through spatial gradients		95
4.1	Abstract	95
4.2	Introduction	95
4.3	Results	98
4.3.1	Slow transport of enzymatic complex enables proofreading .	98
4.3.2	Navigating the speed–fidelity trade-off	100
4.3.3	Energy dissipation and limits of proofreading performance .	103
4.3.4	Proofreading by biochemically plausible intracellular gradients	105
4.4	Discussion	107
	References	110
Chapter S4: Supporting information for Chapter 4 Proofreading through spatial gradients		113
S4.1	Analytical calculations of the complex density profile and fidelity . .	113
S4.1.1	Derivation of the complex density profile $\rho_{\text{ES}}(x)$	113
S4.1.2	Density profile in low and high substrate localization regimes	115

S4.1.3	Fidelity in low and high substrate localization regimes . . .	116
S4.1.4	Fidelity in an intermediate substrate localization regime . . .	118
S4.1.5	Optimal diffusion time scale for maximum fidelity	119
S4.2	Energetics of the scheme	121
S4.2.1	Derivation of the minimum dissipated power	122
S4.2.2	Limits on fidelity enhancement	125
S4.2.3	Energetic cost to set up a concentration gradient	126
S4.3	Studies on the effect of catalysis on the model performance	128
S4.3.1	Derivation of the complex density profile $\rho_{ES}(x)$	128
S4.3.2	Effects on fidelity in low and high substrate localization regimes	130
S4.3.3	Effects on the speed–fidelity trade-off	136
S4.4	Proofreading for substrates with different localization conditions . . .	138
S4.4.1	Limiting cases	139
S4.4.2	Intermediate levels of substrate localization	140
S4.5	Studies on the validity of the uniform free enzyme profile assumption	141
S4.5.1	Effects that relaxing the $\rho_E(x) \approx \text{constant}$ assumption has on the Pareto front	142
S4.5.2	Effects that relaxing the $\rho_E(x) \approx \text{constant}$ assumption has on fidelity in a weak substrate gradient setting	148
S4.6	Proofreading on a kinase/phosphatase-induced gradient	150
S4.6.1	Setup and estimation of fidelity	150
S4.6.2	Energy dissipation	153
	References	154
Chapter V:	Spatial organization of motors in microtubule asters	156
5.1	Introduction	156
5.2	A minimal model accurately captures the observed motor profiles . .	157
5.3	Microtubules in an aster have a broader distribution than motors . . .	161
	References	162
Chapter S5:	Supporting information for Chapter 5 Spatial organization of motors in microtubule asters	164
S5.1	Model formulation	164
S5.2	Extraction of concentration profiles from raw images	168
S5.3	Model fitting	171
S5.4	Accounting for finite MT lengths	173
S5.5	Broader spread of the tubulin profile	175
	References	177

LIST OF ILLUSTRATIONS

<i>Number</i>	<i>Page</i>
1.1 Response behaviors of allosteric proteins under multi-ligand regulation	2
1.2 Elucidating the operational principles of kinetic proofreading through a mechanochemical model	4
1.3 Leveraging space to perform error correction.	5
1.4 Modeling the motor distribution in asters.	6
2.1 Logic gates as molecular responses	8
2.2 States and weights for the allosteric protein	10
2.3 Logic gate realization of an allosteric protein with two ligands	12
2.4 General MWC response with two ligands	14
2.5 Increased number of binding sites can switch the logic of an MWC protein from AND into OR	16
2.6 The third ligand expands the combinatorial diversity of logic responses and enables logic switching	17
2.7 Example logic switches induced by the third ligand	19
S2.1 Additional logic gates as molecular responses	26
S2.2 An XOR gate can be achieved by adding cooperativity	30
S2.3 Balance response behavior approximated by the MWC model	33
S2.4 Three-ligand logic gates that are incompatible with the MWC framework	37
S2.5 Functionally unique 3-ligand MWC gates and possible schemes of logic switching	39
3.1 Conceptual introduction to the piston model	45
3.2 Ratchet and pawl mechanism coupled to the piston	49
3.3 Nonequilibrium features of the engine–piston coupling	51
3.4 Network diagram of enzyme states and transitions between them . . .	53
3.5 Full and thermodynamically consistent treatment of the piston model of proofreading	57
3.6 Parametric studies on the changes in the piston model performance in response to tuning the “knobs” of the engine	60
3.7 Proofreading performance of the piston model under optimized enzyme parameters and external driving conditions	62

S3.1	The two substrate discrimination levels in the conceptual scheme of the piston model	71
S3.2	Working details of the ratchet and pawl mechanism	73
S3.3	The allosteric enzyme in the absence of engine coupling	78
S3.4	Table of possible enzyme states and their statistical weights in the $r \rightarrow 0$ limit where the system is effectively at equilibrium	79
S3.5	The enzyme in the limit of constant activity and in the absence of engine coupling	80
S3.6	Allosteric enzyme's fidelity in the absence of engine coupling (fixed [L]) for different choices of transition rates	81
S3.7	The effective network diagram of the piston model in the absence of driving	83
S3.8	Fidelity of the full piston model in the absence of driving ($\Delta W = 0$) for different choices of model parameters	85
S3.9	Transition rates between the enzyme states	86
S3.10	Fidelity optimization results for each of the 144 parameter initialization options	89
S3.11	Determination of α_{\max} using a trajectory approach	91
S3.12	Three representative 4-filter trajectories paired with ones which have a lower filter number and, necessarily, a higher product formation flux	92
4.1	Error correction schemes that operate by delaying product formation	96
4.2	Dependence of fidelity on the diffusion time scale in the limit of very high substrate localization	100
4.3	Speed–fidelity trade-off and consequences of having weak substrate gradients	101
4.4	Power–fidelity relationship when tuning the effective driving force $\Delta\mu$ for different choices of the diffusion time scale τ_D	104
4.5	Proofreading based on substrate gradients formed by spatially separated kinases and phosphatases	106
S4.1	The effective number of proofreading realizations (n_{eff}) as a function of L/λ_s	120
S4.2	Optimal diffusion time scale for different choices of λ_s	121
S4.3	Discrete–state representation of diffusive transport and substrate binding/unbinding events	123
S4.4	Fidelity enhancement as a function of the effective driving force for varying choices of k_{off}^W	126

S4.5	Dependence of fidelity on the catalysis rate in the case where the substrate profile is uniform	132
S4.6	Fidelity as a function of the catalysis rate in an ideal substrate localization setting	134
S4.7	Pareto front of the speed–fidelity trade-off at different levels of catalytic activity	136
S4.8	Linear trade-off between speed and fidelity when tuning the rate of catalysis	138
S4.9	Fidelity as a function of L/λ_R for different choices of the ratio λ_R/λ_W	141
S4.10	Example profiles of free and substrate–bound enzymes	142
S4.11	Consequences of relaxing the $\rho_E(x) \approx \text{constant}$ assumption on the Pareto front	149
S4.12	Fidelity as a function of diffusion time scale calculated with and without making the $\rho_E(x) \approx \text{constant}$ approximation	150
S4.13	Reduction in the peak effective number of proofreading realizations as a function of p_{bound}	150
S4.14	Energetic performance of the kinase/phosphatase–based mechanism .	155
5.1	Modeling the motor distribution	159
5.2	Relationship between motor and microtubule distributions	161
S5.1	Procedure for extracting protein concentration profiles demonstrated on an example aster	170
S5.2	Demonstration of the model fitting procedure for average as well as separate wedge profiles	171
S5.3	Collection of all fits to motor profiles	172
S5.4	Measured cumulative distribution of microtubule lengths	173
S5.5	Schematic representation of initial motor binding, advection, and stalling at the microtubule end.	174

LIST OF TABLES

<i>Number</i>	<i>Page</i>
S3.1 Values of different transition rates used in the studies of Fig. 3.6. . . .	88
S4.1 Fidelity of the scheme in different regimes of right and wrong complex densities	119
5.1 Motor proteins used and their properties	157
S5.1 Processivities of motors, decay length scales of motor profiles, and corresponding ratios of these two length scales	168

Chapter 1

INTRODUCTION

Living organisms and cells in particular are markedly different from their non-living counterparts. And yet, the physical laws that govern both realms of existence are the same. Then, what sets apart the ‘living’ cells from the ‘dead’ matter? One way to approach this question is to identify the unique *functions* of cells and the *means* by which they implement these functions. Writ large, the goal of my PhD has been to use the toolkit of physical biology to study some of the key functions and mechanisms available to living cells that get implemented from the molecular all the way to the cellular length scales.

One of the main reasons why the life of the cell is so rich is because many of the processes taking place in it are stochastic in their nature. This stochasticity is, in turn, a result of the fact that the energy of thermal motion at the level of atoms and molecules is often comparable to the energies associated with alternative fates of microscopic processes. Examples of such alternative fates are the bound vs. free state of a transcription factor, an open vs. closed conformation of an ion channel, or an active vs. inactive state of a cell surface receptor. One prominent mechanism that harnesses this stochasticity and is essential for cell function is allosteric regulation. Coined ‘the second secret of life’ by the biochemist Jacques Monod, allosteric regulation is the modification of a protein’s affinity and/or catalytic activity for a substrate upon binding of an effector molecule at a site that is different from the protein’s active site. Essentially, the binding of the regulatory ligand alters the dominant conformation of the protein by making it energetically more favorable. This action at a distance mechanism is key in cellular processes such as signal transduction, metabolism, or transcriptional regulation, allowing the cell to adapt to the environment in response to varying concentrations of environmental cues which act as the effector molecule for the allosteric protein. In *Chapter II* of the thesis, we explore the array of behaviors that an allosteric protein can elicit in response to the binding of more than one regulatory ligand (Fig. 1.1A) – a common setting in the kinds of cellular processes mentioned earlier. Specifically, we demonstrate that many of the logic responses known from the world of digital electronics (e.g., AND or NOR logic gates), along with nonconventional ones such as ratiometric sensing, are available to proteins characterized via the Monod-Wyman-Changeux model

of allostery (Fig. 1.1B,C). Further, we found that in cases where the regulation is performed with three different kinds of ligands (as, for instance, in cases of the GIRK channel or the engineered N-WASP signaling protein), modulating the concentration of one of the ligands can cause a switch in the logic response of the other two ligands (Fig. 1.1D). Overall, this work illustrates the combinatorial diversity of control strategies available to living cells via simple mechanisms that operate at thermodynamic equilibrium.

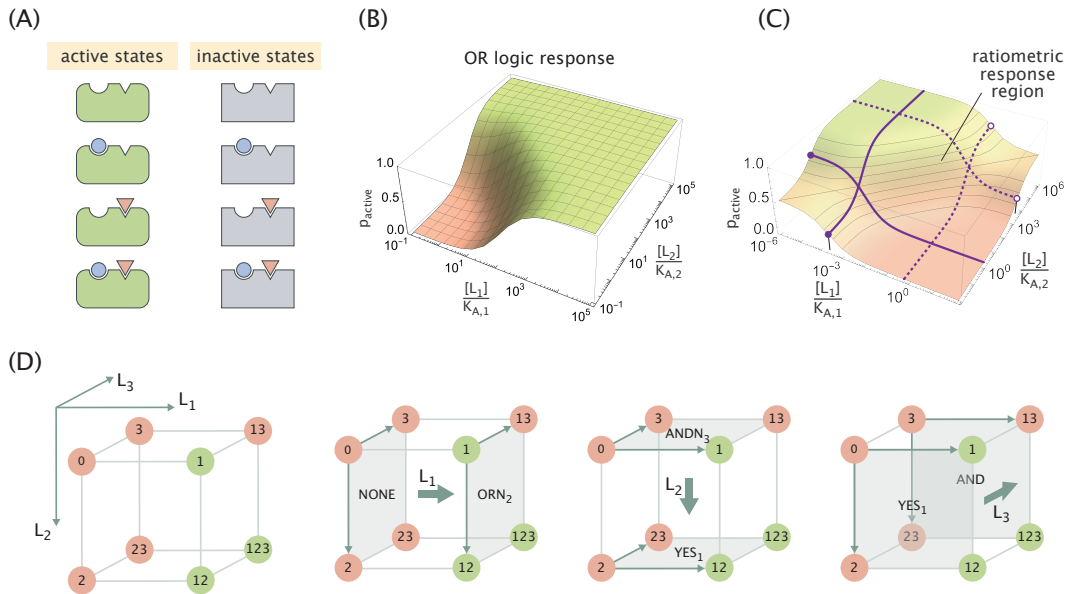


Figure 1.1: Response behaviors of allosteric proteins with multi-ligand regulation. (A) Set of possible states of activity and binding considered in the statistical mechanical characterization of the system. (B,C) Landscapes of protein activity in cases of the OR logic response (B) and the ratiometric response elicited at intermediate ligand concentrations (C). (D) Example activity cube in the 3-ligand regulation setting, along with the set of three different logic switches induced upon the increase in the concentration of one of the three ligands.

Despite the fact that many of the fascinating cellular processes such as allosteric regulation, packing of DNA, or the formation of cellular microcompartments can be explained through the principles of equilibrium thermodynamics, a fundamental and distinguishing feature of the cell as a whole is that it is an open system operating outside of thermodynamic equilibrium. In order to stay ‘alive,’ cells constantly exchange matter and information with their environment and consume energy to fuel processes that by definition assume a well-defined arrow of time. Such processes include cell division, the different steps of the central dogma, or the constant pumping of ions into or out of the cell for the maintenance of its

physiological state. One intriguing aspect of the processes of the central dogma (DNA replication, transcription, translation) as well as many others is the failure of equilibrium thinking to account for the high accuracies at which they operate. The random thermal noise discussed earlier, although important for generating genetic and post-genetic diversity in cells, will often lead to a fatal amount of errors if left unsuppressed. These errors result from the binding and subsequent catalysis of near-cognate substrates that have a lower affinity to the enzyme compared with the correct substrates. In 1970s, scientists John Hopfield (Hopfield, J. J. *Proc. Natl. Acad. Sci. U.S.A.* **71** (1974)) and Jacques Ninio (Ninio, J. *Biochimie* **57** (1975)) independently proposed a generic mechanism called kinetic proofreading now believed to be operating in many of the high-accuracy processes of the cell. This nonequilibrium mechanism suppresses the amount of errors (e.g., incorporations of a wrong amino acid by the ribosome into a growing peptide chain) caused by thermodynamic uncertainties by coupling these processes to the hydrolysis of energy-rich molecules and giving the enzyme catalyzing the reaction a chance to perform error correction. *Chapter III* of my thesis is dedicated to the conceptual understanding of this error-correction scheme. In conventional descriptions of the scheme (Fig. 1.2A), the concept of energy consumption is articulated in the language of chemical potentials and near-irreversible chemical reactions, which are not as intuitive for conveying the idea of dissipation as mechanical descriptions involving lifting or lowering of weights against gravity. With an aim of elucidating the necessity of energy consumption in driving the mechanism of kinetic proofreading, we propose a mechanochemical model of a kinetic proofreader (Fig. 1.2B) that combines ideas from allosteric regulation, nonequilibrium thermodynamics, and mechanics to demonstrate how the amount of energy input can be dynamically tuned through the ‘knobs’ of the engine to achieve variable levels of accuracy (Fig. 1.2C). By drawing parallels between the elements of our proposed scheme and those of traditional proofreading, we offer an intuitive explanation of the conditions that need to be met for efficient error correction from the point of view of the speed-dissipation-accuracy trade-off. We also argue for the importance of the diversity of available biochemical states for proofreading complexes, which, as we show for allosteric enzymes, can enable the system to beat the Hopfield limit of proofreading. Essential as they are for ensuring the accuracy of key biochemical processes, the traditional kinetic proofreading schemes of error correction are quite demanding in terms of their structural requirements on the enzyme, and for that reason, the number of enzymes known to possess this feature is low. In *Chapter IV*, we extend the

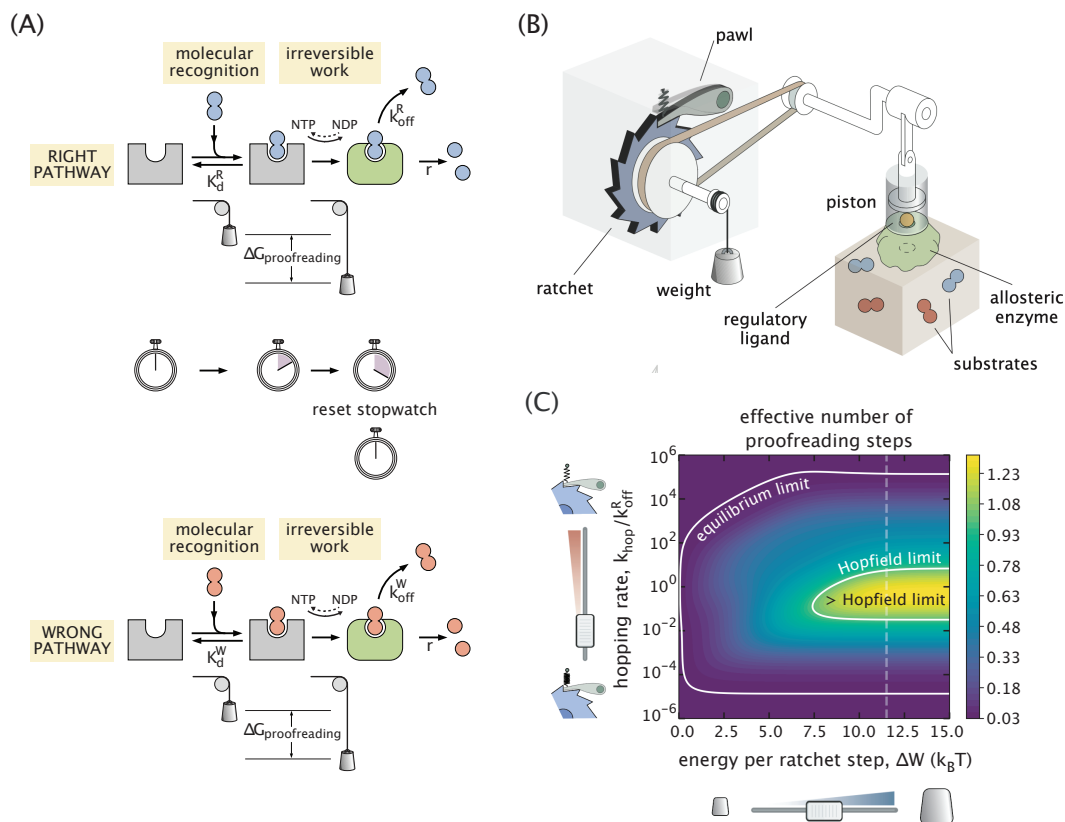


Figure 1.2: Elucidating the operational principles of kinetic proofreading through a mechanochemical model. (A) Illustration of the right and wrong catalysis pathways in Hopfield's proofreading scheme. The first layer of substrate differentiation occurs during the initial substrate binding step, while the second layer happens after the irreversible transition into the active state of the enzyme. (B) Schematic of our proposed mechanochemical model of proofreading. It consists of a ratchet-and-pawl engine driven by a lowering weight, a piston that dictates the activity state of the enzyme by controlling the volume available to the regulatory ligand, and an allosteric enzyme with its catalytic site exposed to a reservoir of right and wrong substrates. (C) Demonstration of the varying levels of proofreading performance in response to tuning the knobs of the mechanical engine (the mass of the weight and the frequency at which the pawl makes a jump over the ratchet teeth).

notion of kinetic proofreading to enzymes that lack those traditional requirements such as the presence of a nucleotide hydrolysis pocket or multiple intermediate conformations needed for delaying product formation and discarding the wrong enzyme-bound substrates. In our proposed mechanism called spatial proofreading, the enzyme instead takes advantage of the localized spatial distribution of its substrates and performs error correction while traveling from the substrate binding site to the substrate delivery/catalysis site (Fig. 1.3A). Importantly, in this scheme,

the dissipation of energy required for proofreading is outsourced to the substrate localization mechanism that is decoupled from the enzyme. We demonstrate that for physiologically relevant substrate gradients, a purely diffusing enzyme with no specialized features of energy consumption can perform efficient error correction, provided that the diffusion time between the substrate binding and catalysis events is sufficiently long (Fig. 1.3B). We also offer an implementation of our proposed scheme using a known mechanism of gradient formation, namely the joint action of membrane-bound kinases and delocalized cytoplasmic phosphatases (Fig. 1.3C), and show that it can achieve proofreading for physiologically relevant values of the system parameters. This work thus offers an avenue for exploring intracellular structures such as spatial gradients or compartmentalization as means of enhanced specificity for enzymes that would otherwise act as equilibrium catalysts in spatially homogeneous environments.

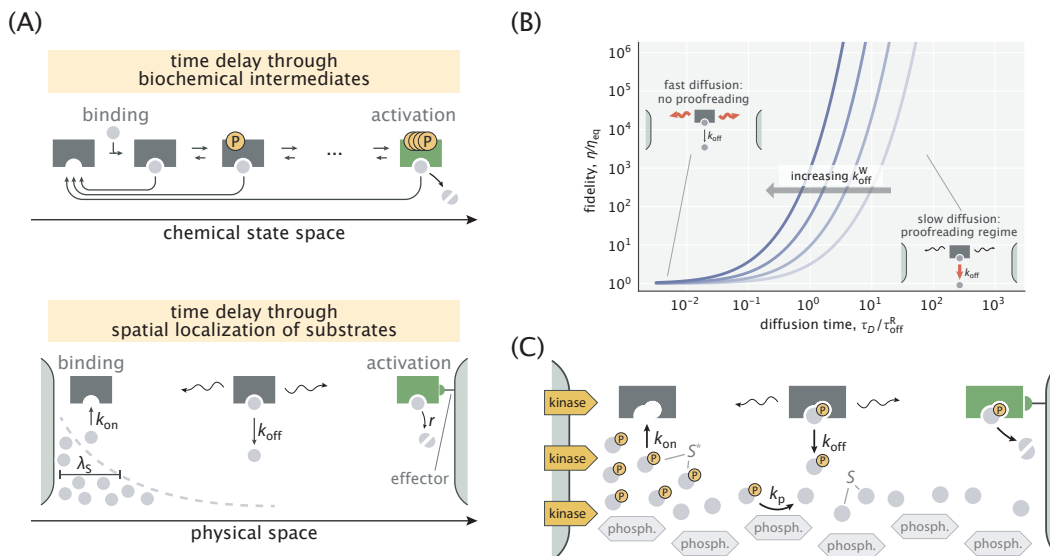


Figure 1.3: Leveraging space to perform error correction. (A) The traditional way of achieving time delays through multiple biochemical intermediates (top) and our proposed alternative of creating a delay through spatially localized substrate binding and diffusive transport (bottom). (B) Enhancement of enzyme fidelity over its equilibrium value ($\eta_{eq} = 10$) as a function of the time required to diffuse between the binding and catalysis sites. (C) Illustration of a kinase/phosphatase-based mechanism of gradient formation and realization of the spatial proofreading scheme.

The nonequilibrium intracellular structures, aside from our hypothesized auxiliary role in the enhancement of enzyme specificity, each have a designated function in the cell, similar to how each organ has its specialized function in humans. The formation

and maintenance of these nonequilibrium structures, such as the Golgi apparatus, the constantly remodeling actomyosin cortex, or the spindle of the dividing cell, are still poorly understood from the perspective of self-organization principles. Using a recently developed optogenetic control tool, our lab studies the organization of an *in vitro* reconstituted cytoskeletal system of microtubules and kinesin motors – two key constituents of the spindle apparatus. Specifically, light is used to induce the dimerization of kinesin motor pairs with spatiotemporal precision, thereby controlling the region of microtubule crosslinking and force generation (Fig. 1.4A). In *Chapter V*, we present our theoretical efforts to characterize the spatial distribution of kinesin motors in radially organized aster structures of microtubules created with our experimental setup under various conditions. We develop a minimal continuum model for the motor distribution (Fig. 1.4B) and demonstrate that it is capable of capturing the experimentally observed motor profiles via effective motor-specific microscopic parameters (Fig. 1.4C, D), indicating a link between individual motor properties and the spatial structures that emerge as a result of their concerted action. Our work of rigorously assessing the motor distribution contributes to ongoing efforts to design and control the structure and dynamics of cytoskeletal active matter systems.

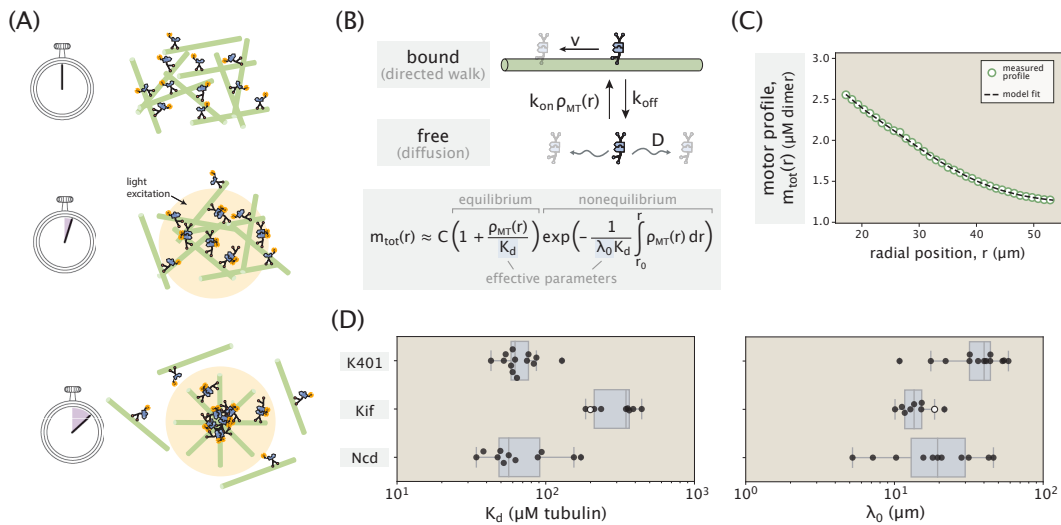
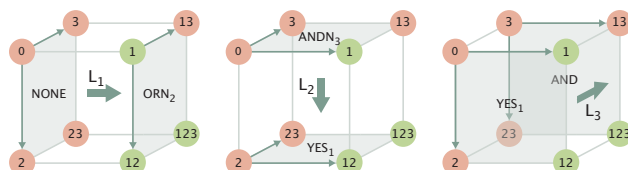


Figure 1.4: Modeling the motor distribution in asters. (A) The optogenetic setup. Motors dimerize in regions of light excitation and reorganize the local microtubule network by exerting forces on it. (B) Our minimal model that predicts the spatial distribution of the motors, the total population of which we separate into ‘bound’ and ‘free’ categories. (C) An example model fit to the measured concentration profile of motors. (D) Collection of fitted values of the effective parameters $K_d = k_{\text{off}}/k_{\text{on}}$ and $\lambda_0 = D/v$ for the three kinds of kinesin motors used in our study.

Chapter 2

COMBINATORIAL CONTROL THROUGH ALLOSTERY



This chapter is based on the journal publication: Galstyan, V., Funk, L., Einav, T. & Phillips, R. Combinatorial control through allostery. *J. Phys. Chem. B* **123**, 2792–2800 (2019). DOI: 10.1021/acs.jpccb.8b12517

2.1 Abstract

Many instances of cellular signaling and transcriptional regulation involve switch-like molecular responses to the presence or absence of input ligands. To understand how these responses come about and how they can be harnessed, we develop a statistical mechanical model to characterize the types of Boolean logic that can arise from allosteric molecules following the Monod-Wyman-Changeux (MWC) model. Building upon previous work, we show how an allosteric molecule regulated by two inputs can elicit AND, OR, NAND, and NOR responses, but is unable to realize XOR or XNOR gates. Next, we demonstrate the ability of an MWC molecule to perform ratiometric sensing – a response behavior where activity depends monotonically on the ratio of ligand concentrations. We then extend our analysis to more general schemes of combinatorial control involving either additional binding sites for the two ligands or an additional third ligand, and show how these additions can cause a switch in the logic behavior of the molecule. Overall, our results demonstrate the wide variety of control schemes that biological systems can implement using simple mechanisms.

2.2 Introduction

A hallmark of cellular signaling and regulation is combinatorial control. Disparate examples ranging from metabolic enzymes to actin polymerization to transcriptional regulation involve multiple inputs that often give rise to a much richer response than what could be achieved through a single-input. For example, the bacterial enzyme phosphofructokinase in the glycolysis pathway is allosterically regulated by both

ADP and PEP [1]. Whereas PEP serves as an allosteric inhibitor, ADP is both an allosteric activator and a competitive inhibitor depending upon its concentration. This modulation by multiple allosteric ligands gives rise to a complex control of the flux through the glycolytic pathway: increasing ADP concentration first increases the activity of phosphofructokinase (via the allosteric modulation), but ultimately decreases it (from competitive inhibition). Another example is offered by the polymerization of actin at the leading edge of motile cells. In particular, the presence of two ligands, Cdc42 and PIP2, is required to activate the protein N-WASP by binding to it in a way that permits it to then activate the Arp2/3 complex and stimulate actin polymerization [2].

In the context of transcriptional regulation, an elegant earlier work explored the conditions under which transcriptional regulatory networks could give rise to the familiar Boolean logic operations, like those shown in Fig. 2.1 [3]. There it was found that the combined effect of two distinct transcription factors on the transcriptional activity of a given promoter depend upon their respective binding strengths as well as the cooperative interactions between each other and the RNA polymerase. Indeed, by tuning the binding strengths and cooperativity parameters, one could generate a panoply of different logic gates such as the familiar AND, OR, NAND (NOT-AND), and NOR (NOT-OR) gates, known from the world of digital electronics [3].

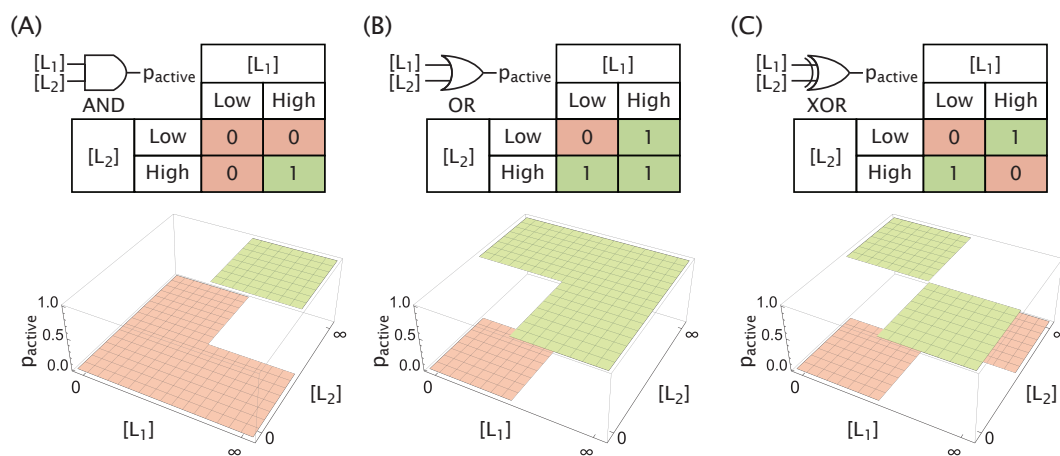


Figure 2.1: Logic gates as molecular responses. The (A) AND, (B) OR, and (C) XOR gates are represented through their corresponding logic tables as well as target activity profiles regulated by two ligands. The behavior of each gate is measured solely by its activity in the absence and at saturating concentrations of each ligand and not by the character of the active/inactive transition.

Here we explore the diversity of combinatorial responses that can be effected by a single allosteric molecule by asking if such molecules can yield multi-input combinatorial control in the same way that transcriptional networks have already been shown to. Specifically, we build on earlier work that shows that an allosteric molecule described by the Monod-Wyman-Changeux (MWC) model can deliver input-output functions similar to the ideal logic gates described in Fig. 2.1 [4–6]. In the MWC model, an allosteric molecule exists in a thermodynamic equilibrium between active and inactive states, with the occupancy of each state being modulated by regulatory ligands [7]. We use statistical mechanics to characterize the input-output response of such a molecule in the limits where each of the two ligands is either absent or at a saturating concentration and determine the necessary conditions to form the various logic gates, with our original contribution on this point focusing on a systematic exploration of the MWC parameter space for each logic gate.

We then analyze the MWC response modulated by two input ligands but outside of traditional Boolean logic functions. In particular, we show how, by tuning the MWC parameters, the response (probability of the allosteric protein being active) in any three of the four concentration limits can be explicitly controlled, along with the ligand concentrations at which transitions between these limit responses occur. Focusing next on the profile of the response near the transition concentrations, we demonstrate how an MWC molecule can exhibit ratiometric sensing which was observed experimentally in the bone morphogenetic protein (BMP) signaling pathway [8] as well as in galactose metabolic (GAL) gene induction in yeast [9].

Additionally, we extend our analysis of logic responses to cases beyond two-ligand control with a single binding site for each ligand. We first discuss the effect of the number of binding sites on the logic response and demonstrate how altering that number, which can occur through evolution or synthetic design, is able to cause a switch in the logic-behavior of an MWC molecule, such as transitioning from AND into OR behavior. Next, we explore the increased diversity of logic responses that can be achieved by three-ligand MWC molecules compared with the two-ligand case and offer an interesting perspective on the role of the third ligand as a regulator that can switch the logic-behavior formed by the other two ligands. We end by a discussion of our theoretical results in the context of a growing body of experimental works on natural and *de novo* designed molecular logic gates. In total, these results hint at simple mechanisms that biological systems can utilize to refine their combinatorial control.









active		inactive	
state	weight	state	weight
	1		$e^{-\beta\Delta\epsilon_{AI}}$
	$\frac{[L_1]}{K_{A,1}}$		$\frac{[L_1]}{K_{I,1}} e^{-\beta\Delta\epsilon_{AI}}$
	$\frac{[L_2]}{K_{A,2}}$		$\frac{[L_2]}{K_{I,2}} e^{-\beta\Delta\epsilon_{AI}}$
	$\left(\frac{[L_1]}{K_{A,1}}\right)\left(\frac{[L_2]}{K_{A,2}}\right)$		$\left(\frac{[L_1]}{K_{I,1}}\right)\left(\frac{[L_2]}{K_{I,2}}\right) e^{-\beta\Delta\epsilon_{AI}}$
$\left(1 + \frac{[L_1]}{K_{A,1}}\right)\left(1 + \frac{[L_2]}{K_{A,2}}\right)$		$\left(1 + \frac{[L_1]}{K_{I,1}}\right)\left(1 + \frac{[L_2]}{K_{I,2}}\right) e^{-\beta\Delta\epsilon_{AI}}$	

Figure 2.2: States and weights for the allosteric protein. The two different ligands (blue circle ($i = 1$) and red triangle ($i = 2$)) are present at concentrations $[L_i]$ and with a dissociation constant $K_{A,i}$ in the active state and $K_{I,i}$ in the inactive state. The energetic difference between the inactive and active states is denoted by $\Delta\epsilon_{AI} = \epsilon_I - \epsilon_A$. Total weights of the active and inactive states are shown below each column and are obtained by summing all the weights in that column.

2.3 Results

2.3.1 Logic response of an allosteric protein modulated by two ligands

Consider an MWC molecule, as shown in Fig. 2.2, that fluctuates between active and inactive states (with $\Delta\epsilon_{AI}$ defined as the free energy difference between the inactive and active states in the absence of ligand). We enumerate the entire set of allowed states of activity and ligand occupancy, along with their corresponding statistical weights. The probability that this protein is active depends on the concentrations of two input molecules, $[L_1]$ and $[L_2]$, and is given by

$$p_{\text{active}}([L_1], [L_2]) = \frac{\left(1 + \frac{[L_1]}{K_{A,1}}\right)\left(1 + \frac{[L_2]}{K_{A,2}}\right)}{\left(1 + \frac{[L_1]}{K_{A,1}}\right)\left(1 + \frac{[L_2]}{K_{A,2}}\right) + e^{-\beta\Delta\epsilon_{AI}}\left(1 + \frac{[L_1]}{K_{I,1}}\right)\left(1 + \frac{[L_2]}{K_{I,2}}\right)}, \quad (2.1)$$

where $K_{A,i}$ and $K_{I,i}$ are the dissociation constants between the i^{th} ligand and the active or inactive protein, respectively. We begin with the two-input case such that $i = 1$ or 2 .

To determine whether this allosteric protein can serve as a molecular logic gate, we first evaluate the probability that it is active when each ligand is either absent ($[L_i] \rightarrow 0$) or at a saturating concentration ($[L_i] \rightarrow \infty$). Fig. 2.3A evaluates these

limits for Eq. 2.1, where we have introduced the parameters $\gamma_1 = \frac{K_{A,1}}{K_{I,1}}$ and $\gamma_2 = \frac{K_{A,2}}{K_{I,2}}$ to simplify the results.

The probabilities in Fig. 2.3A can be compared to the target functions in Fig. 2.1 to determine the conditions on each parameter that would be required to form a given logic gate. For example, the AND, OR, and XOR gates require that in the absence of either ligand ($[L_1] = [L_2] = 0$), there should be as little activity as possible, thereby requiring that the active state has a higher (more unfavored) free energy than the inactive state ($e^{-\beta\Delta\epsilon_{AI}} \gg 1$). We note that in the context of transcriptional regulation, this limit of activity in the absence of ligands is called the leakiness [10], and it is one of the distinguishing features of the MWC model in comparison with other allosteric models such as the Koshland-Némethy-Filmer (KNF) model that exhibits no leakiness.

For the AND and OR gates, the condition that $p_{\text{active}} \approx 1$ when both ligands are saturating ($[L_1], [L_2] \rightarrow \infty$) requires that $\gamma_1\gamma_2e^{-\beta\Delta\epsilon_{AI}} \ll 1$. The two limits where one ligand is absent while the other ligand is saturating lead to the conditions shown in Fig. 2.3B for the AND and OR gates, with representative response profiles shown in Fig. 2.3C using parameter values from the single-ligand allosteric nicotinic acetylcholine receptor [11]. We relegate the derivations to Appendix S2.1, where we also demonstrate that the XOR gate cannot be realized with the form of p_{active} in Eq. 2.1 unless explicit cooperativity is added to the MWC model. In addition, we show that the NAND, NOR, and XNOR gates can be formed if and only if their complementary AND, OR, and XOR gates can be formed, respectively, by replacing $\Delta\epsilon_{AI} \rightarrow -\Delta\epsilon_{AI}$ and $\gamma_i \rightarrow \frac{1}{\gamma_i}$. Finally, Fig. 2.3C demonstrates that the same dissociation constants $K_{A,i}$ and $K_{I,i}$ can give rise to either AND or OR behavior by modulating $\Delta\epsilon_{AI}$, with the transition between these two logic gates occurring at $e^{-\beta\Delta\epsilon_{AI}} \approx \frac{1}{\gamma_1} \approx \frac{1}{\gamma_2}$ (this corresponds to $\Delta\epsilon_{AI} \approx -9 k_B T$ for the values of $K_{A,i}$ and $K_{I,i}$ in Fig. 2.3).

To explore the gating behavior changes across parameter space, we define a quality metric for how closely p_{active} matches its target value at different concentration limits for a given idealized logic gate,

$$Q(\gamma_1, \gamma_2, \Delta\epsilon_{AI}) = \prod_{\lambda_1=0, \infty} \prod_{\lambda_2=0, \infty} (1 - |p_{\lambda_1, \lambda_2}^{\text{ideal}} - p_{\lambda_1, \lambda_2}|), \quad (2.2)$$

where $p_{\lambda_1, \lambda_2} = p_{\text{active}}([L_1] \rightarrow \lambda_1, [L_2] \rightarrow \lambda_2)$. A value of 1 (high quality gate) implies a perfect match between the target function and the behavior of the allosteric

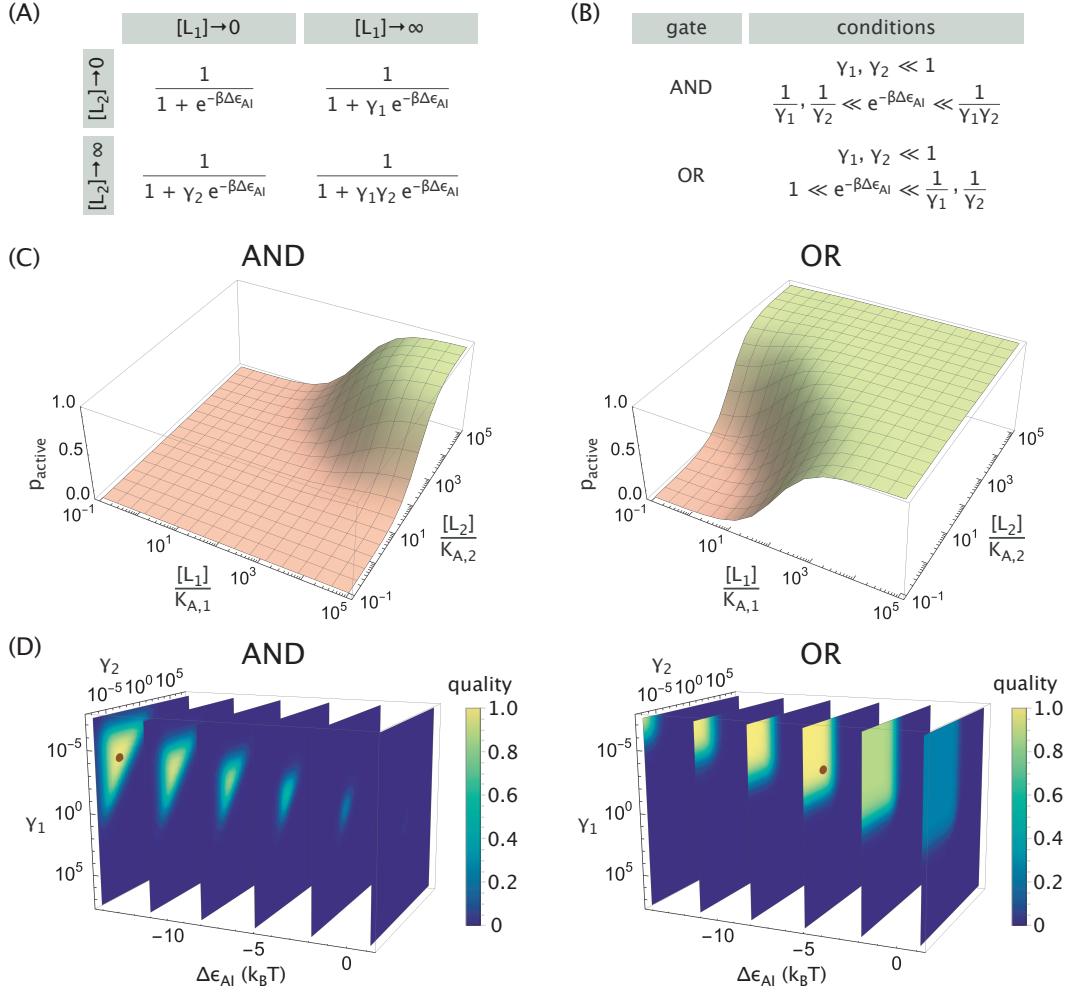


Figure 2.3: Logic gate realization of an allosteric protein with two ligands. (A) Probability that the protein is active (p_{active}) in different limits of ligand concentrations (rows and columns of the matrix). (B) Conditions on the parameters that lead to an AND or OR response. (C) Realizations of the AND and OR logic gates. Parameters used were $K_{A,1} = K_{A,2} = 2.5 \times 10^{-8}$ M, $K_{I,1} = K_{I,2} = 1.5 \times 10^{-4}$ M, and $\Delta\epsilon_{AI} = -14.2 k_B T$ for the AND gate or $\Delta\epsilon_{AI} = -5.0 k_B T$ for the OR gate. (D) Quality of AND (Eq. 2.3) and OR (Eq. 2.4) gates across parameter space. The brown dots indicate the high quality gates in panel C.

molecule while a value near 0 (low quality gate) suggests that the response behavior deviates from the target function in at least one limit.

From Eq. 2.2, the quality for the AND gate becomes

$$Q_{\text{AND}} = (1 - p_{0,0})(1 - p_{\infty,0})(1 - p_{0,\infty})p_{\infty,\infty}, \quad (2.3)$$

while for the OR gate, it takes on the form

$$Q_{\text{OR}} = (1 - p_{0,0}) p_{\infty,0} p_{0,\infty} p_{\infty,\infty}. \quad (2.4)$$

Fig. 2.3D shows the regions in parameter space where the protein exhibits these gating behaviors (the high quality gates from Fig. 2.3C are denoted by brown dots). More specifically, for a fixed $\Delta\epsilon_{\text{AI}}$, the AND behavior is achieved in a finite triangular region in the γ_1 - γ_2 plane which grows larger as $\Delta\epsilon_{\text{AI}}$ decreases. The OR gate, on the other hand, is achieved in an infinite region defined by $\gamma_1, \gamma_2 \lesssim e^{\beta\Delta\epsilon_{\text{AI}}}$. In either case, a high quality gate can be obtained only when the base activity is very low ($\Delta\epsilon_{\text{AI}} \lesssim 0$) and when both ligands are strong activators ($\gamma_1, \gamma_2 \ll 1$), in agreement with the derived conditions (Fig. 2.3B). Lastly, we note that the quality metrics for AND/OR and their complementary NAND/NOR gates obey a simple relation, namely $Q_{\text{AND/OR}}(\gamma_1, \gamma_2, \Delta\epsilon_{\text{AI}}) = Q_{\text{NAND/NOR}}\left(\frac{1}{\gamma_1}, \frac{1}{\gamma_2}, -\Delta\epsilon_{\text{AI}}\right)$, which follows from the functional form of Eq. 2.2 and the symmetry between the two gates (see Appendix S2.1).

2.3.2 General two-ligand MWC response

We next relax the constraint that p_{active} must either approach 0 or 1 in the limits of no ligand or saturating ligand and consider the general behavior that can be achieved by an MWC molecule in the four limits shown in Fig. 2.3A. Manipulating the three parameters (γ_1 , γ_2 and $\Delta\epsilon_{\text{AI}}$) enables us to fix three of the four limits of p_{active} , and these three choices determine the remaining limit. For example, the parameters in Fig. 2.4A were chosen so that $p_{0,0} = 0.5$ ($\Delta\epsilon_{\text{AI}} = 0$), $p_{0,\infty} \approx 0.9$ ($\gamma_2 = 0.1$), and $p_{\infty,0} \approx 0.05$ ($\gamma_1 = 20$), which fixed $p_{\infty,\infty} \approx 0.3$ for the final limit.

In addition to the limits of p_{active} , the locations of the transitions between these limits can be controlled by changing $K_{\text{A},i}$ and $K_{\text{I},i}$ while keeping $\gamma_i = \frac{K_{\text{A},i}}{K_{\text{I},i}}$ constant. In Appendix S2.2, we generalize previous results for the transition of a single-ligand MWC receptor [12] to the present case of two ligands. Interestingly, we find that the midpoint $[L_1^*]_{[L_2] \rightarrow 0}$ of the response in the absence of $[L_2]$ (filled circle in Fig. 2.4A, its value extended along a solid curve) is different from the corresponding midpoint $[L_1^*]_{[L_2] \rightarrow \infty}$ at saturating $[L_2]$ (hollow circle in Fig. 2.4A, its value extended along a dashed curve), with analogous statements holding for the second ligand. More precisely, the two transition points occur at

$$[L_i^*]_{[L_j] \rightarrow 0} = K_{\text{A},i} \frac{1 + e^{-\beta\Delta\epsilon_{\text{AI}}}}{1 + \gamma_i e^{-\beta\Delta\epsilon_{\text{AI}}}}, \quad (2.5)$$

$$[L_i^*]_{[L_j] \rightarrow \infty} = K_{\text{A},i} \frac{1 + \gamma_j e^{-\beta\Delta\epsilon_{\text{AI}}}}{1 + \gamma_1 \gamma_2 e^{-\beta\Delta\epsilon_{\text{AI}}}}. \quad (2.6)$$

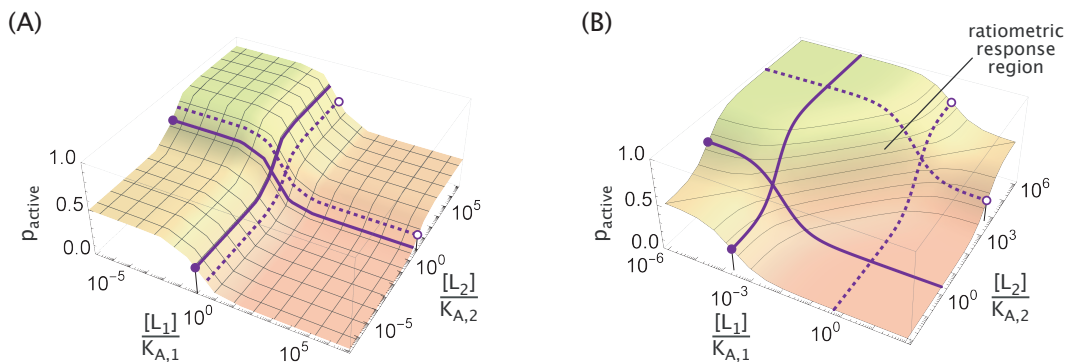


Figure 2.4: General MWC response with two ligands. (A) Three of the four limits of ligand concentrations ($[L_1], [L_2] \rightarrow 0$ or ∞) can be fixed by the parameters $\Delta\epsilon_{AI}$, γ_1 , and γ_2 . Additionally, the midpoint of the $[L_i]$ response when $[L_j] \rightarrow 0$ (filled circles, with the fixed midpoint values extended along solid curves) or $[L_j] \rightarrow \infty$ (hollow circles, with the fixed midpoint values extended along dashed curves) can be adjusted. (B) Within the region determined by the four midpoints, the MWC response becomes ratiometric [8] where the concentration ratio of the two ligands determines the activity of the molecule. This is illustrated by the diagonal contour lines of constant p_{active} in the ratiometric response region.

Notably, the ratio

$$\frac{[L_i^*]_{[L_j] \rightarrow \infty}}{[L_i^*]_{[L_j] \rightarrow 0}} = \frac{(1 + \gamma_1 e^{-\beta\Delta\epsilon_{AI}})(1 + \gamma_2 e^{-\beta\Delta\epsilon_{AI}})}{(1 + e^{-\beta\Delta\epsilon_{AI}})(1 + \gamma_1\gamma_2 e^{-\beta\Delta\epsilon_{AI}})} \quad (2.7)$$

is invariant to ligand swapping ($i \leftrightarrow j$); hence, the transition zones, defined as the concentration intervals between solid and dotted curves, have identical sizes for the two ligands, as can be seen in Fig. 2.4.

The MWC response has its steepest slope when the ligand concentration is within the range set by $[L_i^*]_{[L_j] \rightarrow 0}$ and $[L_i^*]_{[L_j] \rightarrow \infty}$, and interesting response behaviors can arise when both ligand concentrations fall into this regime. For example, Antebi *et al.* recently showed that the BMP pathway exhibits ratiometric response where pathway activity depends monotonically on the ratio of the ligand concentrations [8]. Similar response functions have also been observed in the GAL pathway in yeast, where gene induction is sensitive to the ratio of galactose and glucose [9]. Such behavior can be achieved within the highly sensitive region of the MWC model using one repressor ligand (L_1) and one activator ligand (L_2), as shown in Fig. 2.4B. Parameters chosen for demonstration are $\Delta\epsilon_{AI} = 0$, $K_{A,1} = K_{A,2}$ and $\frac{K_{I,1}}{K_{A,1}} = \frac{K_{A,2}}{K_{I,2}} = 10^{-4}$. In this regime, the probability of the protein being active gets

reduced to

$$p_{\text{active}}([L_1], [L_2]) \approx \frac{\frac{[L_2]}{K_{A,2}}}{\frac{[L_2]}{K_{A,2}} + \frac{[L_1]}{K_{I,1}}}, \quad (2.8)$$

which clearly depends monotonically on the $[L_2]/[L_1]$ ratio (see Appendix S2.2 for details). We note that the region over which the ratiometric behavior is observed can be made arbitrarily large by decreasing the ratios $\frac{K_{I,1}}{K_{A,1}}$ and $\frac{K_{A,2}}{K_{I,2}}$.

2.3.3 Modulation by multiple ligands

A much richer repertoire of signaling responses is available to an MWC protein if we go beyond two ligand inputs with a single binding site for each, as exhibited by phosphofructokinase, for example. Though earlier we mentioned phosphofructokinase in the context of two of its input ligands, in fact, this enzyme has even more inputs than that, and thus provides a rich example of multi-ligand combinatorial control [1]. To start exploring the diversity of these responses, we generalize Eq. 2.1 to consider cases with N input ligands, where the i^{th} ligand has n_i binding sites, concentration $[L_i]$, and dissociation constants $K_{A,i}$ and $K_{I,i}$ with the molecule's active and inactive states, respectively. In general, it is impractical to write the states and weights as we have done in Fig. 2.2, since the total number of possible states, given by $2^{1+\sum_{i=1}^N n_i}$, grows exponentially with the number of binding sites. However, by analogy with the earlier simple case, the general formula for the probability that the protein is active can be written as

$$p_{\text{active}}([L_1], [L_2], \dots, [L_N]) = \frac{\prod_{i=1}^N \left(1 + \frac{[L_i]}{K_{A,i}}\right)^{n_i}}{\prod_{i=1}^N \left(1 + \frac{[L_i]}{K_{A,i}}\right)^{n_i} + e^{-\beta\Delta\epsilon_{AI}} \prod_{i=1}^N \left(1 + \frac{[L_i]}{K_{I,i}}\right)^{n_i}}. \quad (2.9)$$

We first consider an MWC molecule with $N = 2$ input ligands as in the previous section but with n_i ligand binding sites for ligand i . As derived in Appendix S2.3, the criteria for the AND and OR gates are identical to those for a protein with $n_i = 1$ binding site per ligand, except that we make the $\gamma_i \rightarrow \gamma_i^{n_i}$ substitution in the conditions shown in Fig. 2.3B. The protein thus exhibits OR behavior if $e^{-\beta\Delta\epsilon_{AI}} \ll \min\left(\frac{1}{\gamma_1^{n_1}}, \frac{1}{\gamma_2^{n_2}}\right)$ or AND behavior if $e^{-\beta\Delta\epsilon_{AI}} \gg \max\left(\frac{1}{\gamma_1^{n_1}}, \frac{1}{\gamma_2^{n_2}}\right)$.

Over evolutionary time or through synthetic approaches, the number of binding sites displayed by a single molecule can be tuned, enabling such systems to test a variety of responses with a limited repertoire of regulatory molecules. Since $\gamma_1, \gamma_2 \ll 1$, increasing the number of binding sites while keeping all other parameters the same

can shift a response from AND→OR as shown in Fig. 2.5. The opposite logic switching (OR→AND) is similarly possible by decreasing the number of binding sites, and analogous results can be derived for the complementary NAND and NOR gates (see Appendix S2.3). In the limit where the number of binding sites becomes large ($n_1, n_2 \gg 1$), an allosteric molecule’s behavior will necessarily collapse into OR logic provided $\gamma_1, \gamma_2 < 1$, since the presence of either ligand occupying the numerous binding sites has sufficient free energy to overcome the active-inactive free energy difference $\Delta\epsilon_{AI}$. In addition, having a large number of binding sites makes the p_{active} response sharper (Fig. 2.5B), as was seen in the context of chromatin remodeling where ~ 150 bp of DNA “buried” within a nucleosome can be made available for transcription by the binding of multiple transcription factors [13].

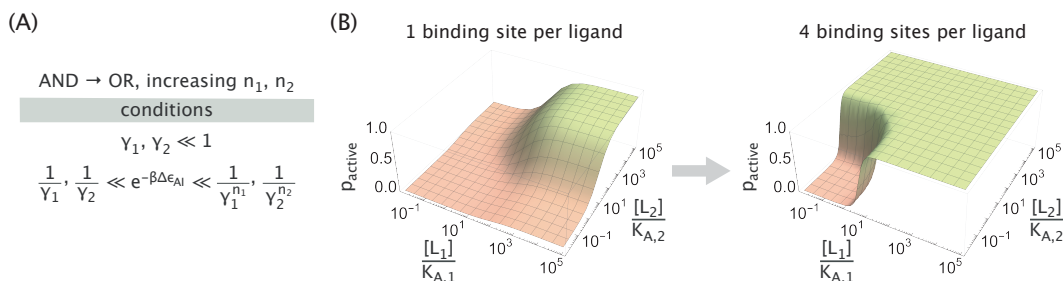


Figure 2.5: Increased number of binding sites can switch the logic of an MWC protein from AND into OR. (A) Parameter conditions required for AND \rightarrow OR switching upon an increase in the number of binding sites. (B) Representative activity plots showing the AND \rightarrow OR switching. Parameters used were $K_{A,i} = 2.5 \times 10^{-8}$ M, $K_{I,i} = 2.5 \times 10^{-6}$ M and $\Delta\epsilon_{AI} = -7 k_B T$.

Next, we examine an alternative possibility of generalizing the MWC response, namely considering a molecule with $N = 3$ distinct ligands, each having a single binding site ($n_i = 1$). The logic response is now described by a $2 \times 2 \times 2$ cube corresponding to the activity at low and saturating concentrations of each of the three ligands (an example realization is shown in Fig. 2.6A). Since each of the 8 cube elements can be either OFF or ON (red and green circles, respectively), the total number of possible responses becomes $2^8 = 256$. This number, however, includes functionally redundant responses, as well as ones that are not admissible in the MWC framework. We therefore eliminate these cases in order to accurately quantify the functional diversity of 3-input MWC proteins.

We consider two responses to be functionally identical if one can be obtained from another by relabeling the ligands, e.g., $(1, 2, 3) \rightarrow (3, 1, 2)$. Eliminating all redundant responses leaves 80 unique cases out of the 256 possibilities (see

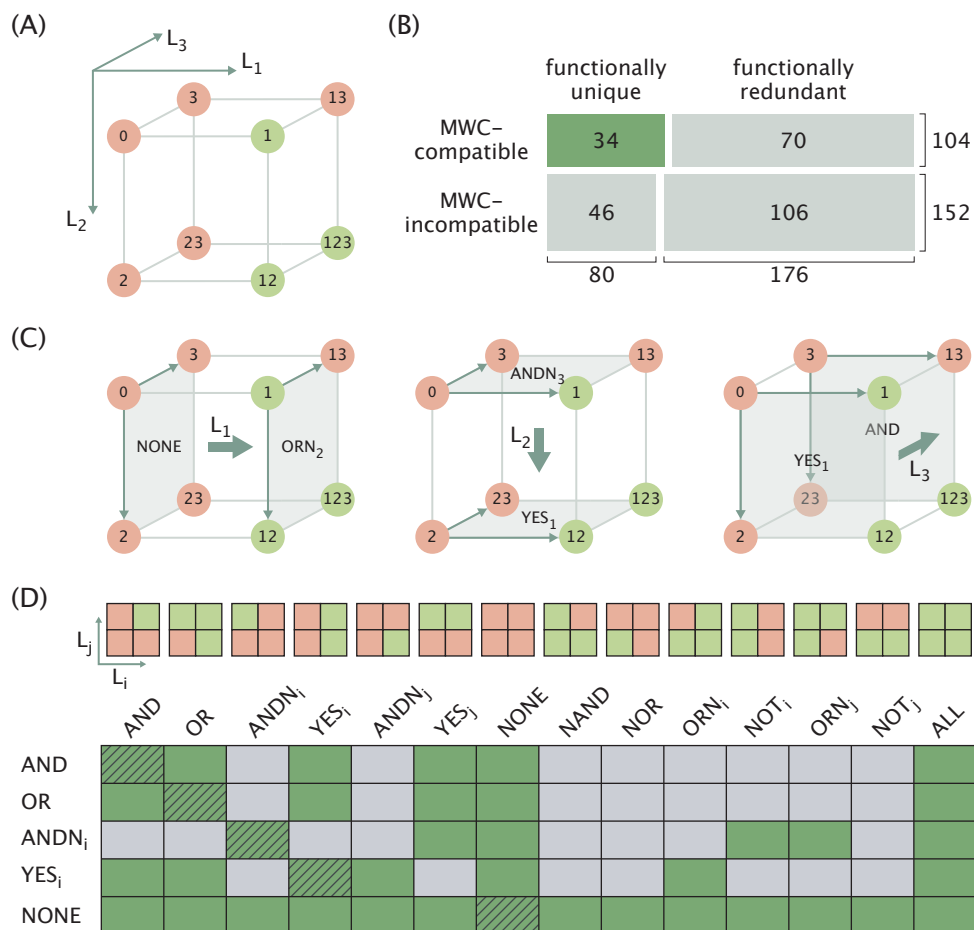


Figure 2.6: The third ligand expands the combinatorial diversity of logic responses and enables logic switching. (A) Cubic diagram of a representative molecular logic response. The label “0” stands for the limit when all ligands are at low concentrations. Each digit in the labels of other limits indicates the high concentration of the corresponding ligand (for example, in the “12” limits the ligands 1 and 2 are at high concentrations). Red and green colors indicate the OFF and ON states of the molecule, respectively. (B) Diagram representing the numbers of 3-ligand logic gates categorized by their MWC compatibility and functional uniqueness. The area of each cell is proportional to the number of gates in the corresponding category. (C) Demonstration of different logic transitions induced by a third ligand (thick arrows) on the example of the 3-input gate in panel A. (D) Table of all possible logic transitions (row \rightarrow column, green cells) inducible by a third ligand in the MWC framework. Schematics of the 14 MWC-compatible 2-ligand gates corresponding to each column entry are displayed on top (i and j represent different ligands). Results for the transitions between logical complements (NOT row \rightarrow NOT column) are identical to the results for row \rightarrow column transitions and are not shown. Trivial transitions between identical gates where the third ligand has no effect are marked with hatching lines.

Appendix S2.4). In addition, since the molecule's activity in the eight ligand concentration limits is determined by only four MWC parameters, namely $\{\Delta\epsilon_{AI}, \gamma_1, \gamma_2, \gamma_3\}$, we expect the space of possible 3-input gates to be constrained (analogous to XOR/XNOR gates being inaccessible to 2-input MWC proteins). Imposing the constraints leaves 34 functionally unique logic responses that are compatible with the MWC framework (see Figure 2.6B for the summary statistics and Appendix S2.4 for the detailed discussion of how the constraints were imposed).

In addition to expanding the scope of combinatorial control relative to the two-input case, we can think of the role of the third ligand as a regulator whose presence switches the logic performed by the other two ligands. We illustrate this role in Fig. 2.6C by first focusing on the leftmost cubic diagram. The gating behavior on the left face of the cube (in the absence of L_1) exhibits NONE logic while the behavior on the right face of the cube (in the presence of saturating L_1) is the ORN₂ logic (see the schematics at the top of Fig. 2.6D for the definition of all possible gates). In this way, adding L_1 switches the logic of the remaining two ligands from NONE \rightarrow ORN₂. In a similar vein, adding L_2 changes the logic from ANDN₃ \rightarrow YES₁, while adding L_3 causes a YES₁ \rightarrow AND switch.

We repeat the same procedure for all functionally unique 3-ligand MWC gates (see Appendix S2.4) and obtain a table of all possible logic switches that can be induced by a third ligand (green cells in Figure 2.6D that indicate row \rightarrow column logic switches). As we can see, a large set of logic switches are feasible, the majority of which (the left half of the table) do not involve a change in the base activity (i.e., activity in the absence of the two ligands). Comparatively fewer transitions that involve flipping of the base activity from OFF to ON are possible (the right half of the table).

As a demonstration of the regulatory function of the third ligand, we show two examples of logic switching induced by increasing $[L_3]$, namely AND \rightarrow OR (Fig. 2.7A,B) and AND \rightarrow YES₁ (Fig. 2.7C,D), along with the parameter conditions that need to be satisfied to enable such transitions (see Appendix S2.4 for derivations). An interesting perspective is to view the L_3 ligand as a modulator of the free energy difference $\Delta\epsilon_{AI}$. For example, when $[L_3] = 0$, the protein behaves identically to the $N = 2$ case given by Eq. 2.1; at a saturating concentration of L_3 , however, the protein behaves as if it had $N = 2$ ligands with a modified free energy difference $\Delta\epsilon'_{AI}$ given by

$$\Delta\epsilon'_{AI} = \Delta\epsilon_{AI} - k_B T \log \gamma_3. \quad (2.10)$$

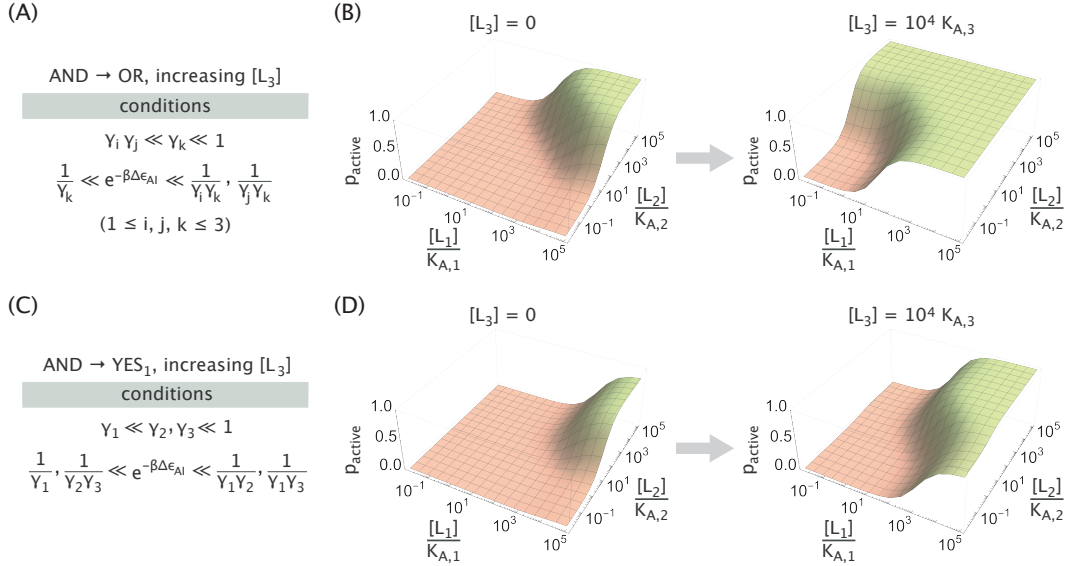


Figure 2.7: Example logic switches induced by the third ligand. Parameter conditions and representative activity plots of an allosteric molecule exhibiting AND logic in the absence of the third ligand, while exhibiting OR logic (A,B) or YES₁ logic (C,D) when L_3 is present at a saturating concentration. Parameters used were $K_{A,i} = 2.5 \times 10^{-8}$ M and $K_{I,i} = 2.5 \times 10^{-4}$ M in panel B, $K_{A,i} = 2.5 \times 10^{-8}$ M, $K_{I,1} = 2.5 \times 10^{-4}$ M and $K_{I,2/3} = 2.5 \times 10^{-6}$ M in panel D, along with $\Delta \epsilon_{AI} = -12 k_B T$ in both panels.

From this perspective, the third ligand increases the effective free energy difference in the examples shown in Fig. 2.7, since in both cases the $\gamma_3 \ll 1$ condition is satisfied. For the AND \rightarrow OR transition, the increase in $\Delta \epsilon_{AI}$ is sufficient to let either of the two ligands activate the molecule (hence, the OR gate). In the AND \rightarrow YES₁ transition, the change in $\Delta \epsilon_{AI}$ utilizes the asymmetry between the binding strengths of the two ligands ($\gamma_1 \ll \gamma_2$) to effectively “silence” the activity of the ligand L_2 . We note in passing that such behavior for the $N = 3$ allosteric molecule is reminiscent of a transistor which can switch an input signal in electronics.

2.4 Discussion

Combinatorial control is a ubiquitous strategy employed by cells. Networks of cellular systems of different kinds, such as transcriptional [14, 15], signaling [16], or metabolic [1], integrate information from multiple inputs in order to produce a single output. The statistical mechanical MWC model we employ allows us to systematically explore the combinatorial diversity of output responses available to such networks and determine the conditions that the MWC parameters need to satisfy to realize a particular response.

In this paper, we built on earlier work to show that the response of an allosteric MWC molecule can mimic Boolean logic. Specifically, we demonstrated that a protein that binds to two ligands can exhibit an AND, OR, NAND, or NOR response (also shown by others [4–6]), where the former two cases require the protein to be inherently inactive and that both ligands preferentially bind to the active conformation, whereas the latter two cases require the converse conditions. We derived the MWC parameter ranges within which an allosteric protein would exhibit an AND or OR response (Fig. 2.3B), and showed that the corresponding parameter ranges for NAND or NOR responses could be achieved by simply substituting $\gamma_i \rightarrow \frac{1}{\gamma_i}$ and $\Delta\epsilon_{AI} \rightarrow -\Delta\epsilon_{AI}$ in the parameter condition equations (Appendix S2.1.3). Since the NAND and NOR gates are known in digital electronics as universal logic gates, all other logic functions can be reproduced by hierarchically layering these gates. In the context of this work, such layering could be implemented if the MWC protein is an enzyme that only catalyzes in the active state so that its output (the amount of product) could serve as an input for the next enzyme, thereby producing more complex logic functions via allostery, though at the cost of noise amplification and response delays.

As in earlier work [4, 5], we showed that the XOR and XNOR responses cannot be achieved within the original MWC framework (Eq. 2.1), but are possible when cooperativity between the two ligands is introduced (Appendix S2.1.4). Biological XOR and XNOR behaviors are uncommon in non-transcriptional systems and have also been challenging for synthetic design and optimization [17]. One of the few examples of such systems is a synthetic metallochromic chromophore whose transmittance output level is modulated by Ca^{2+} and H^+ ions in a XOR-like manner [18, 19].

In addition to traditional Boolean logic, we recognized further manifestations of combinatorial control by two-ligand MWC proteins. In particular, we showed that the protein activity in three of the four ligand concentration limits can be set independently by tuning the MWC parameters γ_1 , γ_2 , and $\Delta\epsilon_{AI}$, and that the ligand concentrations at which transitions between limit responses take place can be separately controlled by proportionally changing $K_{A,i}$ and $K_{I,i}$, while keeping $\gamma_i = \frac{K_{A,i}}{K_{I,i}}$ constant (Eqs. 2.5 and 2.6). We also showed that when the ranges of ligand concentrations are close to those transition values, then ratiometric sensing observed in the BMP [8] and GAL pathways [9], can be recapitulated through the MWC model (Fig. 2.4B), with larger regions of sensitivity achievable by an appropriate tuning of the parameters. We note that parameter “tuning” can be realized either through

evolutionary processes over long time scales or synthetically, using mutagenesis or other approaches [20].

Apart from altering the thermodynamic parameters such as the ligand binding affinity or the free energy of active and inactive protein conformations, the number of ligand binding sites of an allosteric molecule can also be changed. This can occur evolutionarily through recombination events, synthetically by engineering combinations of protein domains [21], or through binding of competitive effectors that reduce the effective number of ligand binding sites. We found that these alterations in the number of ligand binding sites are capable of switching the logic behavior between AND \leftrightarrow OR or NAND \leftrightarrow NOR gates (Fig. 2.5B). Since the MWC model has been applied in unusual situations such as the regulation of promoter accessibility in nucleosomal DNA that can unwrap upon the binding of multiple transcription factors [13, 22], these results on combinatorial control can also be relevant for eukaryotic transcription, where the number of transcription factor binding sites can be tuned using synthetic approaches [23–26]. In developing *Drosophila* embryos, for instance, different patterns of gene expression were obtained using synthetically designed enhancers with different numbers of repressor and activator binding sites [24]. Knowing the spatial distribution of transcription factor concentrations across the embryo, the authors obtained gene activity profiles and observed effectively a switch from ANDN1 logic into YES2 logic upon increasing the number of activator binding sites [24], which is a switching behavior accessible to an MWC molecule as well (Appendix S2.3).

Lastly, we generalized the analysis of logic responses for a molecule whose activity is modulated by three ligands, and identified 34 functionally unique and MWC-compatible gates out of 256 total possibilities. We offered a perspective on the function of any of the three ligands as a “regulator” that can cause a switch in the type of logic performed by the other two ligands and derived the full list of such switches (Fig. 2.6D). Within the MWC model, the role of this regulatory ligand can be viewed as effectively changing the free energy difference $\Delta\epsilon_{AI}$ between the protein’s active and inactive states (Appendix S2.4.2), which, in turn, is akin to the role of methylation [27, 28] or phosphorylation [28] in adaptation, but without the covalent linkage. Our in-depth analysis of the logic repertoire available to 3-input MWC molecules can serve as a theoretical framework for designing new allosteric proteins and also for understanding the measured responses of existing systems. Examples of such systems that both act as 3-input AND gates include the GIRK

channel, the state of which (open or closed) is regulated by the G protein $G_{\beta\gamma}$, the lipid PIP_2 and Na^+ ions [29], or the engineered N-WASP signaling protein which is activated by SH3, Cdc42 and PDZ ligands [30]. We note that these 3-input AND gates exhibit a NONE \rightarrow AND logic switch upon the increase of any of the three inputs. More sophisticated logic switches can, in principle, be achieved by engineering a similar three-ligand N-WASP protein, but this time having one of the ligands act as a repressor and the other two as activators [2]. Our treatment of multi-ligand gating can also serve as a theoretical framework for dissecting the combinatorial control of the BMP signaling protein by more than 20 ligands, different pairs of which have been shown to exhibit different response behaviors (e.g., the action of BMP4 and BMP9 ligands results in an OR gate, while the action of BMP4 and GDF5 ligands results in a YES1 gate) [8].

The exquisite control that arises from the web of interactions underlying biological systems is difficult to understand and replicate. A first step to overcoming this hurdle is to carefully quantify the types of behaviors that can arise from multi-component systems. As our ability to harness and potentially design *de novo* allosteric systems grows [21, 29–33], we can augment our current level of combinatorial control in biological contexts, such as transcriptional regulation [3, 14, 15, 34, 35], to create even richer dynamics.

Acknowledgements

It is a great pleasure to acknowledge the contributions of Bill Eaton to our understanding of allostery. We thank Chandana Gopalakrishnappa, Parijat Sil, and Armando Reimer for their input on this work, and Michael Elowitz for his insights and valuable feedback on the manuscript. This research was supported by the La Fondation Pierre-Gilles de Gennes, the Rosen Center at Caltech, the Department of Defense through the National Defense Science & Engineering Graduate Fellowship (NDSEG) Program (LF), and the National Institutes of Health DP1 OD000217 (Director's Pioneer Award), R01 GM085286, and 1R35 GM118043-01 (MIRA). We are grateful to the Burroughs-Wellcome Fund for its support of the Physical Biology of the Cell Course at the Marine Biological Laboratory, where part of this work was completed.

References

1. Blangy, D., Buc, H. & Monod, J. Kinetics of the allosteric interactions of phosphofructokinase from *Escherichia coli*. *J. Mol. Biol.* **31**, 13–35 (1968).

2. Dueber, J. E., Yeh, B. J., Chak, K. & Lim, W. A. Reprogramming control of an allosteric signaling switch through modular recombination. *Science* **301**, 1904–1908 (2003).
3. Buchler, N. E., Gerland, U. & Hwa, T. On schemes of combinatorial transcription logic. *Proc. Natl. Acad. Sci. U. S. A.* **100**, 5136–5141 (2003).
4. Graham, I. & Duke, T. The logical repertoire of ligand-binding proteins. *Phys. Biol.* **2**, 159–165 (2005).
5. De Ronde, W., ten Wolde, P. R. & Mugler, A. Protein logic: A statistical mechanical study of signal integration at the single-molecule level. *Biophys. J.* **103**, 1097–1107 (2012).
6. Agliari, E., Altavilla, M., Barra, A., Schiavo, L. D. & Katz, E. Notes on stochastic (bio)-logic gates: computing with allosteric cooperativity. *Sci. Rep.* **5**, 9415 (2015).
7. Martins, B. M. & Swain, P. S. Trade-offs and constraints in allosteric sensing. *PLoS Comput. Biol.* **7**, e1002261 (2011).
8. Antebi, Y. E., Linton, J. M., Klumpe, H., Bintu, B., Gong, M., Su, C., McCardell, R. & Elowitz, M. B. Combinatorial signal perception in the BMP pathway. *Cell* **170**, 1184–1196 (2017).
9. Escalante-Chong, R., Savir, Y., Carroll, S. M., Ingraham, J. B., Wang, J., Marx, C. J. & Springer, M. Galactose metabolic genes in yeast respond to a ratio of galactose and glucose. *Proc. Natl. Acad. Sci. U. S. A.* **112**, 1636–1641 (2015).
10. Razo-Mejia, M., Barnes, S. L., Belliveau, N. M., Chure, G., Einav, T., Lewis, M. & Phillips, R. Tuning transcriptional regulation through signaling: A predictive theory of allosteric induction. *Cell Syst.* **6**, 456–469 (2018).
11. Auerbach, A. Thinking in cycles: MWC is a good model for acetylcholine receptor-channels. *J. Physiol.* **590**, 93–98 (2012).
12. Marzen, S., Garcia, H. G. & Phillips, R. Statistical mechanics of Monod-Wyman-Changeux (MWC) models. *J. Mol. Biol.* **425**, 1433–1460 (2013).
13. Mirny, L. A. Nucleosome-mediated cooperativity between transcription factors. *Proc. Natl. Acad. Sci. U. S. A.* **107**, 22534–22539 (2010).
14. Scholes, C., DePace, A. H. & Sánchez, Á. Combinatorial gene regulation through kinetic control of the transcription cycle. *Cell Syst.* **4**, 97–108 (2017).
15. Kinkhabwala, A. & Guet, C. C. Uncovering *cis* regulatory codes using synthetic promoter shuffling. *PLoS One* **3**, e2030 (2008).
16. Dueber, J. E., Yeh, B. J., Bhattacharyya, R. P. & Lim, W. A. Rewiring cell signaling: the logic and plasticity of eukaryotic protein circuitry. *Curr. Opin. Struct. Biol.* **14**, 690–699 (2004).

17. Privman, V., Zhou, J., Halánek, J. & Katz, E. Realization and properties of biochemical-computing biocatalytic XOR gate based on signal change. *J. Phys. Chem. B* **114**, 13601–13608 (2010).
18. De Silva, A. P. & McClenaghan, N. D. Simultaneously multiply-configurable or superposed molecular logic systems composed of ICT (internal charge transfer) chromophores and fluorophores integrated with one- or two-ion receptors. *Chem. - Eur. J.* **8**, 4935–4945 (2002).
19. De Silva, A. P. & Uchiyama, S. Molecular logic and computing. *Nat. Nanotechnol.* **2**, 399 (2007).
20. Bloom, J. D., Meyer, M. M., Meinhold, P., Otey, C. R., MacMillan, D. & Arnold, F. H. Evolving strategies for enzyme engineering. *Curr. Opin. Struct. Biol.* **15**, 447–452 (2005).
21. Guntas, G. & Ostermeier, M. Creation of an allosteric enzyme by domain insertion. *J. Mol. Biol.* **336**, 263–273 (2004).
22. Narula, J. & Igoshin, O. A. Thermodynamic models of combinatorial gene regulation by distant enhancers. *IET Syst. Biol.*, **4**, 393–408 (2010).
23. Löhr, U., Chung, H.-R., Beller, M. & Jäckle, H. Antagonistic action of Bicoid and the repressor Capicua determines the spatial limits of *Drosophila* head gene expression domains. *Proc. Natl. Acad. Sci. U. S. A.* **106**, 21695–21700 (2009).
24. Fakhouri, W. D., Ay, A., Sayal, R., Dresch, J., Dayringer, E. & Arnosti, D. N. Deciphering a transcriptional regulatory code: modeling short-range repression in the *Drosophila* embryo. *Mol. Syst. Biol.* **6**, 341 (2010).
25. Chen, H., Xu, Z., Mei, C., Yu, D. & Small, S. A system of repressor gradients spatially organizes the boundaries of Bicoid-dependent target genes. *Cell* **149**, 618–629 (2012).
26. Crocker, J., Tsai, A. & Stern, D. L. A fully synthetic transcriptional platform for a multicellular eukaryote. *Cell Rep.* **18**, 287–296 (2017).
27. Hansen, C. H., Endres, R. G. & Wingreen, N. S. Chemotaxis in *Escherichia coli*: A molecular model for robust precise adaptation. *PLoS Comput. Biol.* **4**, e1 (2008).
28. Lan, G., Sartori, P., Neumann, S., Sourjik, V. & Tu, Y. The energy–speed–accuracy trade-off in sensory adaptation. *Nat. Phys.* **8**, 422 (2012).
29. Wang, W., Touhara, K. K., Weir, K., Bean, B. P. & MacKinnon, R. Cooperative regulation by G proteins and Na(+) of neuronal GIRK2 K(+) channels. *eLife* **5**, e157519 (2016).
30. Dueber, J. E., Mirsky, E. A. & Lim, W. A. Engineering synthetic signaling proteins with ultrasensitive input/output control. *Nat. Biotechnol.* **25**, 660–662 (2007).

31. Raman, A. S., White, K. I. & Ranganathan, R. Origins of allostery and evolvability in proteins: A case study. *Cell* **166**, 468–480 (2016).
32. Huang, P. S., Boyken, S. E. & Baker, D. The coming of age of *de novo* protein design. *Nature* **537**, 320 (2016).
33. Guntas, G., Mansell, T. J., Kim, J. R. & Ostermeier, M. Directed evolution of protein switches and their application to the creation of ligand-binding proteins. *Proc. Natl. Acad. Sci. U. S. A.* **102**, 11224–11229 (2005).
34. Wei, H., Hu, B., Tang, S., Zhao, G. & Guan, Y. Repressor logic modules assembled by rolling circle amplification platform to construct a set of logic gates. *Sci. Rep.* **6**, 37477 (2016).
35. Macía, J., Posas, F. & Solé, R. Distributed computation: the new wave of synthetic biology devices. *Trends Biotechnol.* **30**, 342–349 (2012).

SUPPORTING INFORMATION FOR CHAPTER 2 | COMBINATORIAL CONTROL THROUGH ALLOSTERY

Supplementary *Mathematica* notebook from which all protein activity response plots and gate quality metric plots can be reproduced and supplementary Jupyter Notebooks where the set of functionally unique gates and constraints conditions are derived are available on the publication webpage (DOI: 10.1021/acs.jpcc.8b12517).

S2.1 Derivation of conditions for achieving different logic responses

In this section, we derive the conditions necessary for an MWC molecule modulated by two ligands (with one binding site for each ligand) to exhibit the behavior of various logic gates shown in Fig. 2.1. In addition to the three logic gates shown in Fig. 2.1, we will also discuss the three complimentary gates NAND, NOR, and XNOR depicted in Fig. S2.1.

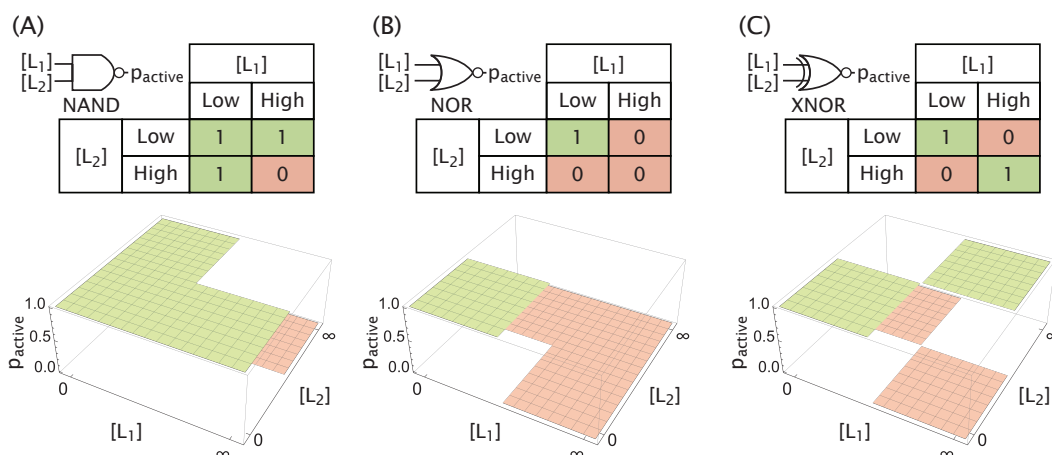


Figure S2.1: Additional logic gates as molecular responses. The (A) NAND, (B) NOR, and (C) XNOR gates are the compliments of the AND, OR, and XOR gates, respectively, shown in Fig. 2.1.

To simplify our notation, we define the value of p_{active} from Eq. 2.1 in the following limits,

$$p_{0,0} = p_{\text{active}}([L_1] \rightarrow 0, [L_2] \rightarrow 0) = \frac{1}{1 + e^{-\beta\Delta\epsilon_{\text{AI}}}}, \quad (\text{S2.1})$$

$$p_{\infty,0} = p_{\text{active}}([L_1] \rightarrow \infty, [L_2] \rightarrow 0) = \frac{1}{1 + \gamma_1 e^{-\beta\Delta\epsilon_{\text{AI}}}}, \quad (\text{S2.2})$$

$$p_{0,\infty} = p_{\text{active}}([L_1] \rightarrow 0, [L_2] \rightarrow \infty) = \frac{1}{1 + \gamma_2 e^{-\beta\Delta\epsilon_{\text{AI}}}}, \quad (\text{S2.3})$$

$$p_{\infty,\infty} = p_{\text{active}}([L_1] \rightarrow \infty, [L_2] \rightarrow \infty) = \frac{1}{1 + \gamma_1 \gamma_2 e^{-\beta\Delta\epsilon_{\text{AI}}}}, \quad (\text{S2.4})$$

where $\gamma_i = \frac{K_{\text{A},i}}{K_{\text{I},i}}$ is the ratio of the dissociation constants between the i th ligand and the protein in the active and inactive states. From the ideal logic gate behaviors visualized in Fig. 2.1 and Fig. S2.1, we can then deduce the desired constraints that model parameters need to meet for an effective realization of each gate.

S2.1.1 AND gate

Starting from the AND gate, we require $p_{0,0} \approx 0$, $p_{0,\infty} \approx 0$, $p_{\infty,0} \approx 0$ and $p_{\infty,\infty} \approx 1$, which yields the following conditions:

$$e^{-\beta\Delta\epsilon_{\text{AI}}} \gg 1, \quad (\text{S2.5})$$

$$\gamma_1 e^{-\beta\Delta\epsilon_{\text{AI}}} \gg 1, \quad (\text{S2.6})$$

$$\gamma_2 e^{-\beta\Delta\epsilon_{\text{AI}}} \gg 1, \quad (\text{S2.7})$$

$$\gamma_1 \gamma_2 e^{-\beta\Delta\epsilon_{\text{AI}}} \ll 1. \quad (\text{S2.8})$$

Combining Eqs. S2.6-S2.8, we obtain the condition for an AND gate, namely

$$\frac{1}{\gamma_1}, \frac{1}{\gamma_2} \ll e^{-\beta\Delta\epsilon_{\text{AI}}} \ll \frac{1}{\gamma_1 \gamma_2}. \quad (\text{S2.9})$$

Note that the outer inequalities imply

$$\gamma_1, \gamma_2 \ll 1, \quad (\text{S2.10})$$

meaning that both ligands bind more tightly to the protein in the active than the inactive state.

S2.1.2 OR gate

For p_{active} to represent an OR gate across ligand concentration space, it must satisfy $p_{0,0} \approx 0$, $p_{0,\infty} \approx 1$, $p_{\infty,0} \approx 1$ and $p_{\infty,\infty} \approx 1$. This requires that the parameters obey

$$e^{-\beta\Delta\epsilon_{\text{AI}}} \gg 1, \quad (\text{S2.11})$$

$$\gamma_1 e^{-\beta\Delta\epsilon_{\text{AI}}} \ll 1, \quad (\text{S2.12})$$

$$\gamma_2 e^{-\beta\Delta\epsilon_{\text{AI}}} \ll 1, \quad (\text{S2.13})$$

$$\gamma_1 \gamma_2 e^{-\beta\Delta\epsilon_{\text{AI}}} \ll 1. \quad (\text{S2.14})$$

Combining Eqs. S2.11-S2.13, we obtain a constraint on the free energy difference,

$$1 \ll e^{-\beta\Delta\epsilon_{AI}} \ll \frac{1}{\gamma_1}, \frac{1}{\gamma_2}. \quad (\text{S2.15})$$

As with the AND gate, the outer inequalities imply that the ligands prefer binding to the protein in the active state,

$$\gamma_1, \gamma_2 \ll 1. \quad (\text{S2.16})$$

S2.1.3 NAND and NOR gates

Because the NAND and NOR gates are the logical complements of AND and OR gates, respectively, the parameter constraints under which they are realized are the opposites of those for AND and OR gates. Hence, the conditions for a NAND gate are given by

$$\frac{1}{\gamma_1\gamma_2} \ll e^{-\beta\Delta\epsilon_{AI}} \ll \frac{1}{\gamma_1}, \frac{1}{\gamma_2}, \quad (\text{S2.17})$$

while the conditions for NOR gates are

$$\frac{1}{\gamma_1}, \frac{1}{\gamma_2} \ll e^{-\beta\Delta\epsilon_{AI}} \ll 1. \quad (\text{S2.18})$$

We note that in both cases, the outer inequalities imply that both ligands bind more tightly to the protein in the inactive state than in the active state, $\gamma_1, \gamma_2 \gg 1$.

The symmetry between AND/OR and NAND/NOR gates also implies a simple relation between their quality metrics, namely

$$Q_{\text{AND/OR}}(\gamma_1, \gamma_2, \Delta\epsilon_{AI}) = Q_{\text{NAND/NOR}}\left(\frac{1}{\gamma_1}, \frac{1}{\gamma_2}, -\Delta\epsilon_{AI}\right). \quad (\text{S2.19})$$

Here we provide a proof for the AND gate and invite the reader to do the same for the OR gate. From Eq. 2.2, the quality metrics for the AND and NAND gates can be written as

$$\begin{aligned} Q_{\text{AND}}(\gamma_1, \gamma_2, \omega) &= (1 - p_{0,0})(1 - p_{\infty,0})(1 - p_{0,\infty})p_{\infty,\infty} \\ &= \left(1 - \frac{1}{1 + \omega}\right) \left(1 - \frac{1}{1 + \gamma_1\omega}\right) \left(1 - \frac{1}{1 + \gamma_2\omega}\right) \left(\frac{1}{1 + \gamma_1\gamma_2\omega}\right) \\ &= \frac{\gamma_1\gamma_2\omega^3}{(1 + \omega)(1 + \gamma_1\omega)(1 + \gamma_2\omega)(1 + \gamma_1\gamma_2\omega)}, \end{aligned} \quad (\text{S2.20})$$

$$\begin{aligned} Q_{\text{NAND}}(\gamma_1, \gamma_2, \omega) &= p_{0,0}p_{\infty,0}p_{0,\infty}(1 - p_{\infty,\infty}) \\ &= \left(\frac{1}{1 + \omega}\right) \left(\frac{1}{1 + \gamma_1\omega}\right) \left(\frac{1}{1 + \gamma_2\omega}\right) \left(1 - \frac{1}{1 + \gamma_1\gamma_2\omega}\right) \end{aligned}$$

$$= \frac{\gamma_1 \gamma_2 \omega}{(1 + \omega)(1 + \gamma_1 \omega)(1 + \gamma_2 \omega)(1 + \gamma_1 \gamma_2 \omega)}, \quad (\text{S2.21})$$

where we introduced $\omega = e^{-\beta \Delta \epsilon_{\text{AI}}}$. Substituting $\gamma_1 \rightarrow \gamma_1^{-1}, \gamma_2 \rightarrow \gamma_2^{-1}, \omega \rightarrow \omega^{-1}$ (equivalent to $\Delta \epsilon_{\text{AI}} \rightarrow -\Delta \epsilon_{\text{AI}}$) in Eq. S2.21, we obtain

$$\begin{aligned} Q_{\text{NAND}}(\gamma_1^{-1}, \gamma_2^{-1}, \omega^{-1}) &= \frac{\gamma_1^{-1} \gamma_2^{-1} \omega^{-1}}{(1 + \omega^{-1})(1 + \gamma_1^{-1} \omega^{-1})(1 + \gamma_2^{-1} \omega^{-1})(1 + \gamma_1^{-1} \gamma_2^{-1} \omega^{-1})} \times \frac{\gamma_1^2 \gamma_2^2 \omega^4}{\gamma_1^2 \gamma_2^2 \omega^4} \\ &= \frac{\gamma_1 \gamma_2 \omega^3}{(1 + \omega)(1 + \gamma_1 \omega)(1 + \gamma_2 \omega)(1 + \gamma_1 \gamma_2 \omega)} \\ &\equiv Q_{\text{AND}}(\gamma_1, \gamma_2, \omega). \end{aligned} \quad (\text{S2.22})$$

S2.1.4 XOR and XNOR gates

Here, we show that the XOR gate (and by symmetry the XNOR gate) are not achievable with the form of p_{active} given in Eq. 2.1. An XOR gate satisfies $p_{0,0} \approx 0$, $p_{0,\infty} \approx 1$, $p_{\infty,0} \approx 1$ and $p_{\infty,\infty} \approx 0$ which necessitates the parameter conditions

$$e^{-\beta \Delta \epsilon_{\text{AI}}} \gg 1, \quad (\text{S2.23})$$

$$\gamma_1 e^{-\beta \Delta \epsilon_{\text{AI}}} \ll 1, \quad (\text{S2.24})$$

$$\gamma_2 e^{-\beta \Delta \epsilon_{\text{AI}}} \ll 1, \quad (\text{S2.25})$$

$$\gamma_1 \gamma_2 e^{-\beta \Delta \epsilon_{\text{AI}}} \gg 1. \quad (\text{S2.26})$$

However, these conditions cannot all be satisfied, as the left-hand side of Eq. S2.26 can be written in terms of the left-hand sides of Eqs. S2.23-S2.25,

$$\gamma_1 \gamma_2 e^{-\beta \Delta \epsilon_{\text{AI}}} = \frac{(\gamma_1 e^{-\beta \Delta \epsilon_{\text{AI}}}) (\gamma_2 e^{-\beta \Delta \epsilon_{\text{AI}}})}{e^{-\beta \Delta \epsilon_{\text{AI}}}} \ll 1, \quad (\text{S2.27})$$

contradicting Eq. S2.26.

The XOR gate could be realized if an explicit cooperativity energy $\epsilon_{\text{A,coop}}$ is added when both ligands are bound in the active state and $\epsilon_{\text{I,coop}}$ when both are bound in the inactive state. These cooperative interactions modify Eq. 2.1 to the form

$$p_{\text{active}}([L_1], [L_2]) = \frac{1 + \frac{[L_1]}{K_{\text{A},1}} + \frac{[L_2]}{K_{\text{A},2}} + \frac{[L_1][L_2]}{K_{\text{A},1}K_{\text{A},2}} e^{-\beta \epsilon_{\text{A,coop}}}}{1 + \frac{[L_1]}{K_{\text{A},1}} + \frac{[L_2]}{K_{\text{A},2}} + \frac{[L_1][L_2]}{K_{\text{A},1}K_{\text{A},2}} e^{-\beta \epsilon_{\text{A,coop}}} + e^{-\beta \Delta \epsilon_{\text{AI}}} \left(1 + \frac{[L_1]}{K_{\text{I},1}} + \frac{[L_2]}{K_{\text{I},2}} + \frac{[L_1][L_2]}{K_{\text{I},1}K_{\text{I},2}} e^{-\beta \epsilon_{\text{I,coop}}} \right)}. \quad (\text{S2.28})$$

Fig. S2.2 demonstrates that the same parameter values from Fig. 2.3B together with the (unfavorable) cooperativity energy $\epsilon_{\text{A,coop}} = 15 k_{\text{B}}T$ and $\epsilon_{\text{I,coop}} = 0$ can create an XOR gate.

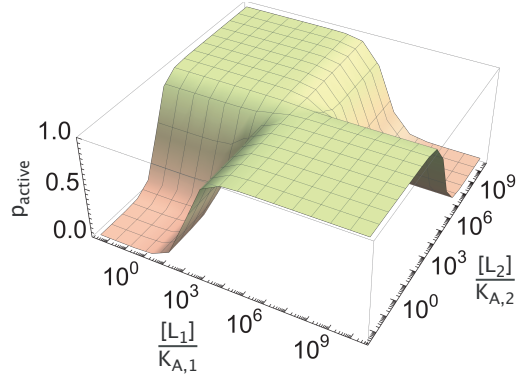


Figure S2.2: An XOR gate can be achieved by adding cooperativity. The activity profile defined in Eq. S2.28 for the parameter values from Fig. 2.3B, along with the cooperativity energies $\epsilon_{A,\text{coop}} = 15 k_B T$ and $\epsilon_{1,\text{coop}} = 0$, give rise to an XOR response.

S2.2 The general two-ligand response: Transitioning between OFF and ON states

In the preceding section, we have been solely concerned with the behavior of the MWC molecule in the limits of ligand concentration ($[L_i] = 0$ and $[L_i] \rightarrow \infty$), and have ignored the details about the transition from ON to OFF (e.g., its shape and steepness) and also the possibility of $p_{\text{active}} \neq 0$ or 1. In this section, we examine and derive in greater detail some of the additional response behaviors that are possible for an MWC molecule regulated with $N = 2$ ligands when the locations of transitions between limit responses are taken into account.

To examine the transitions between p_{active} levels, we derive expressions for the concentrations at which transitions are at their midpoint. Since p_{active} is a function of two different ligand concentrations, $[L_1]$ and $[L_2]$, we define two different midpoint concentrations of ligand L_i : one in the absence of ligand L_j , $[L_i^*]_{[L_j] \rightarrow 0}$, and another when L_j is saturating, $[L_i^*]_{[L_j] \rightarrow \infty}$. In particular, $[L_i^*]_{[L_j] \rightarrow 0}$ is defined such that

$$p_{\text{active}} \left([L_i^*]_{[L_j] \rightarrow 0}, [L_j] = 0 \right) = \frac{p_{\text{active}} ([L_i] = 0, [L_j] = 0) + p_{\text{active}} ([L_i] \rightarrow \infty, [L_j] = 0)}{2}, \quad (\text{S2.29})$$

i.e., the concentration of ligand i where p_{active} is equal to the mean of the two p_{active} limit values being transitioned between. If we evaluate the left hand side of Eq. S2.29 with $i = 1$ and $j = 2$ using Eq. 2.1, and the right hand side using the limits

from Fig. 2.3A, we obtain

$$\frac{\left(1 + \frac{[L_1^*]_{[L_2] \rightarrow 0}}{K_{A,1}}\right)}{\left(1 + \frac{[L_1^*]_{[L_2] \rightarrow 0}}{K_{A,1}}\right) + e^{-\beta\Delta\epsilon_{AI}} \left(1 + \frac{[L_1^*]_{[L_2] \rightarrow 0}}{K_{I,1}}\right)} = \frac{1}{2} \left(\frac{1}{1 + e^{-\beta\Delta\epsilon_{AI}}} + \frac{1}{1 + \gamma_1 e^{-\beta\Delta\epsilon_{AI}}} \right). \quad (\text{S2.30})$$

Introducing $\gamma_1 = K_{A,1}/K_{I,1}$, we can solve for $[L_1^*]_{[L_2] \rightarrow 0}$ to find

$$\frac{[L_1^*]_{[L_2] \rightarrow 0}}{K_{A,1}} = \frac{1 + e^{-\beta\Delta\epsilon_{AI}}}{1 + \gamma_1 e^{-\beta\Delta\epsilon_{AI}}}. \quad (\text{S2.31})$$

Eq S2.31 can be rewritten for $[L_2^*]_{[L_1] \rightarrow 0}$ by merely interchanging all ligand and parameter indices, i.e., $1 \leftrightarrow 2$.

The midpoint concentration when one ligand is saturating can be derived similarly. Specifically, to find an expression for $[L_i^*]_{[L_j] \rightarrow \infty}$, we can re-write S2.29 using Eq. 2.1 in the case that $[L_j] \rightarrow \infty$ with $i = 1$ and $j = 2$, resulting in

$$\frac{\left(1 + \frac{[L_1^*]_{[L_2] \rightarrow \infty}}{K_{A,1}}\right)}{\left(1 + \frac{[L_1^*]_{[L_2] \rightarrow \infty}}{K_{A,1}}\right) + \gamma_2 e^{-\beta\Delta\epsilon_{AI}} \left(1 + \frac{[L_1^*]_{[L_2] \rightarrow \infty}}{K_{I,1}}\right)} = \frac{1}{2} \left(\frac{1}{1 + \gamma_2 e^{-\beta\Delta\epsilon_{AI}}} + \frac{1}{1 + \gamma_1 \gamma_2 e^{-\beta\Delta\epsilon_{AI}}} \right). \quad (\text{S2.32})$$

Eq S2.32 can be solved for $[L_1^*]_{[L_2] \rightarrow \infty}$ to produce,

$$\frac{[L_1^*]_{[L_2] \rightarrow \infty}}{K_{A,1}} = \frac{1 + \gamma_2 e^{-\beta\Delta\epsilon_{AI}}}{1 + \gamma_1 \gamma_2 e^{-\beta\Delta\epsilon_{AI}}}. \quad (\text{S2.33})$$

Again, the symmetric expression for $[L_2^*]_{[L_1] \rightarrow \infty}$ is found by swapping ligand and parameter indices, $1 \leftrightarrow 2$.

This approach to define concentration transition zones can be used to produce additional MWC behaviors, including the ratiometric response in the BMP pathway recently analyzed by Antebi *et al.* [1], which was briefly discussed earlier. Specifically, this response can be approximated by choosing parameter values that satisfy two desired limits, $p_{\infty,0} \approx 0$ ($\gamma_1 e^{-\beta\Delta\epsilon_{AI}} \gg 1$) and $p_{0,\infty} \approx 1$ ($\gamma_2 e^{-\beta\Delta\epsilon_{AI}} \ll 1$), as well as produce a large transition region sensitive to both ligands, i.e., the ratio in Eq. 2.7, $\frac{[L_i^*]_{[L_j] \rightarrow \infty}}{[L_i^*]_{[L_j] \rightarrow 0}}$ is far from 1. One way to satisfy these conditions is to set $K_{I,2} \gg K_{A,1} = K_{A,2} \gg K_{I,1}$ and $\Delta\epsilon_{AI} = 0$ in Eq. 2.1. Notice that with these parameter choices and, provided the ligand concentrations satisfy

$$\frac{[L_1]}{K_{A,1}}, \frac{[L_2]}{K_{I,2}} \ll 1,$$

$$\frac{[L_1]}{K_{I,1}}, \frac{[L_2]}{K_{A,2}} \gg 1, \quad (\text{S2.34})$$

the probability that the protein is active reduces to

$$p_{\text{active}}([L_1], [L_2]) \approx \frac{\frac{[L_2]}{K_{A,2}}}{\frac{[L_2]}{K_{A,2}} + \frac{[L_1]}{K_{I,1}}}. \quad (\text{S2.35})$$

Hence, only the ratio of $[L_1]$ and $[L_2]$ matters, as shown in Fig. 2.4B where Eq. S2.34 is satisfied, provided that $10^{-4} \lesssim \frac{[L_1]}{K_{A,1}} \lesssim 10^0 \lesssim \frac{[L_2]}{K_{A,2}} \lesssim 10^4$.

Additionally, we consider the remaining three types of input-output computations shown by Antebi *et al.* to exist in the BMP pathway which they called the additive, imbalance, and balance responses [1]. The additive response (which responds more to larger input concentrations) is an OR gate which we showed is possible in Fig. 2.3B. The imbalance response (which responds maximally to extreme ratios of the two input ligands) is similar to an XOR behavior which, as discussed in Appendix S2.1.4, is only achievable with an explicit cooperativity energy.

The balance response is defined as

$$p_{\text{active}}^{\text{balance}} = \begin{cases} 1 & [L_1] \approx [L_2] \\ 0 & [L_1] \neq [L_2] \end{cases} \quad (\text{S2.36})$$

so that the protein is only ON when both ligands are present in the same amount as shown in Fig. S2.3A. Such behavior is not possible within the MWC model because starting from any point $\overline{[L_1]} = \overline{[L_2]}$, p_{active} in Eq. 2.1 must either monotonically increase or monotonically decrease with $[L_1]$ (depending on γ_1), whereas Eq. S2.36 requires that p_{active} must decrease for both $[L_1] > \overline{[L_1]}$ and $[L_1] < \overline{[L_1]}$ (with similar contradictory statements for $[L_2]$). The closest behavior achievable by the MWC model is to zoom into the transition region of an XNOR gate as shown in Fig. S2.3B. As we zoom out of the concentration ranges shown, the four square regions of the plot will continue to expand as squares and the behavior will no longer approximate the ideal balance response.

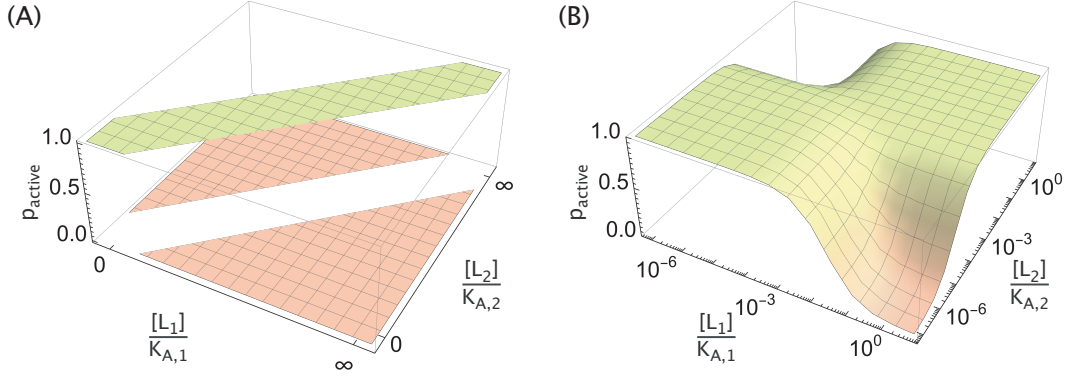


Figure S2.3: Balance response behavior approximated by the MWC model. (A) The ideal balance response from the BMP pathway and (B) the closest behavior that an MWC molecule can exhibit using the complementary parameters from Fig. S2.2 ($K_{A,i} = 1.5 \times 10^{-4}$ M, $K_{I,i} = 2.5 \times 10^{-8}$ M, $\Delta\epsilon_{AI} = 5 k_B T$, $\epsilon_{A,\text{coop}} = -15 k_B T$ and $\epsilon_{I,\text{coop}} = 0$).

S2.3 Logic switching by tuning the number of ligand binding sites

In this section, we show how an MWC molecule whose activity is given by Eq. 2.9 can switch between exhibiting AND \leftrightarrow OR, NAND \leftrightarrow NOR or ANDN $_1 \leftrightarrow$ YES $_2$ behaviors by tuning the number of binding sites. To begin, we define the probability p_{active} that the molecule is active in the case when the i th ligand has n_i binding sites, namely

$$p_{0,0} = p_{\text{active}}([L_1] \rightarrow 0, [L_2] \rightarrow 0) = \frac{1}{1 + e^{-\beta\Delta\epsilon_{AI}}}, \quad (\text{S2.37})$$

$$p_{\infty,0} = p_{\text{active}}([L_1] \rightarrow \infty, [L_2] \rightarrow 0) = \frac{1}{1 + \gamma_1^{n_1} e^{-\beta\Delta\epsilon_{AI}}}, \quad (\text{S2.38})$$

$$p_{0,\infty} = p_{\text{active}}([L_1] \rightarrow 0, [L_2] \rightarrow \infty) = \frac{1}{1 + \gamma_2^{n_2} e^{-\beta\Delta\epsilon_{AI}}}, \quad (\text{S2.39})$$

$$p_{\infty,\infty} = p_{\text{active}}([L_1] \rightarrow \infty, [L_2] \rightarrow \infty) = \frac{1}{1 + \gamma_1^{n_1} \gamma_2^{n_2} e^{-\beta\Delta\epsilon_{AI}}}. \quad (\text{S2.40})$$

Note that the only effect of having an arbitrary number of ligand binding sites (as opposed to $n_i = 1$ as in Appendix S2.1) is that the ratio of dissociation constants always appears raised to the power equal to the number of binding sites, $\gamma_i^{n_i}$. Hence, the parameter conditions derived for AND and OR behaviors for $n_i = 1$ can be used in the case of general n_i by substituting $\gamma_i \rightarrow \gamma_i^{n_i}$.

Now, suppose a molecule with $N = 2$ ligands and with n'_1 and n'_2 binding sites for ligands 1 and 2 represents an AND gate, while this same molecule with n_1 and n_2 binding sites serves as an OR gate, as in Fig. 2.5B with $n'_1 = n'_2 = 1$ and $n_1 = n_2 = 4$.

From Fig. 2.3B, the conditions in the former case (AND gate) are

$$\frac{1}{\gamma_1^{n'_1}}, \frac{1}{\gamma_2^{n'_2}} \ll e^{-\beta\Delta\epsilon_{AI}} \ll \frac{1}{\gamma_1^{n'_1}\gamma_2^{n'_2}}, \quad (\text{S2.41})$$

while the conditions in the latter case (OR gate) are

$$1 \ll e^{-\beta\Delta\epsilon_{AI}} \ll \frac{1}{\gamma_1^{n'_1}}, \frac{1}{\gamma_2^{n'_2}}. \quad (\text{S2.42})$$

Combining these conditions, we find that the requirements for the AND \leftrightarrow OR switching are given by

$$\frac{1}{\gamma_1^{n'_1}}, \frac{1}{\gamma_2^{n'_2}} \ll e^{-\beta\Delta\epsilon_{AI}} \ll \frac{1}{\gamma_1^{n'_1}}, \frac{1}{\gamma_2^{n'_2}}, \frac{1}{\gamma_1^{n'_1}\gamma_2^{n'_2}}, \quad (\text{S2.43})$$

where we have used the fact that the outer inequalities imply $\gamma_1^{n'_1}, \gamma_2^{n'_2} \ll 1$ (so that $1 \ll \frac{1}{\gamma_1^{n'_1}}, \frac{1}{\gamma_2^{n'_2}}$). In the limit $n'_1 = n'_2 = 1$, Eq. S2.43 reduces to the condition shown in Fig. 2.5A. We note that since NAND is the complement of AND while NOR is the complement of OR, the class switching requirements in S2.43 become the requirements for NAND \leftrightarrow NOR switching when $\gamma_i \rightarrow \frac{1}{\gamma_i}$ and $\Delta\epsilon_{AI} \rightarrow -\Delta\epsilon_{AI}$.

Lastly, we show that the switching behavior ANDN $_1 \rightarrow$ YES $_2$, observed upon increasing the number of activator binding sites in a *Drosophila* enhancer [2], is also available to an MWC molecule. Let us assume that L_1 is a repressor with a fixed number of binding sites (n_1), and L_2 is an activator whose number of binding sites is increased from n_2 to n'_2 .

The requirements on the limiting p_{active} values for an ANDN $_1$ gate are

$$p_{0,0}, p_{\infty,0}, p_{\infty,\infty} \ll 1, \quad (\text{S2.44})$$

$$p_{0,\infty} \gg 1, \quad (\text{S2.45})$$

which translate into conditions on the model parameters given by

$$1, \frac{1}{\gamma_1^{n_1}}, \frac{1}{\gamma_1^{n_1}\gamma_2^{n_2}} \ll e^{-\beta\Delta\epsilon_{AI}} \ll \frac{1}{\gamma_2^{n_2}}. \quad (\text{S2.46})$$

Note that the outer inequalities suggest that $\gamma_2^{n_2} \ll 1$ and $\gamma_1^{n_1} \gg 1$, confirming that L_2 is an activator and L_1 is a repressor. With these conditions, Eq. S2.46 simplifies into

$$1, \frac{1}{\gamma_1^{n_1}\gamma_2^{n_2}} \ll e^{-\beta\Delta\epsilon_{AI}} \ll \frac{1}{\gamma_2^{n_2}}. \quad (\text{S2.47})$$

We now repeat the same procedure for the YES₂ gate, this time assigning $n'_2 > n_2$ binding sites to the activator L_2 . The requirements on the limiting p_{active} values read

$$p_{0,0}, p_{\infty,0} \ll 1, \quad (\text{S2.48})$$

$$p_{0,\infty}, p_{\infty,\infty} \gg 1, \quad (\text{S2.49})$$

which result in conditions on the model parameters given by

$$1, \frac{1}{\gamma_1^{n_1}} \ll e^{-\beta\Delta\epsilon_{AI}} \ll \frac{1}{\gamma_2^{n'_2}}, \frac{1}{\gamma_1^{n_1}\gamma_2^{n'_2}}. \quad (\text{S2.50})$$

Using the fact that $\gamma_1^{n_1} \gg 1$, we simplify Eq. S2.50 into

$$1, \frac{1}{\gamma_1^{n_1}} \ll e^{-\beta\Delta\epsilon_{AI}} \ll \frac{1}{\gamma_1^{n_1}\gamma_2^{n'_2}}. \quad (\text{S2.51})$$

As a last step, we combine Eqs. S2.47 and S2.51 to obtain the required conditions for ANDN₁ → YES₂ switching, namely

$$1, \frac{1}{\gamma_1^{n_1}\gamma_2^{n_2}} \ll e^{-\beta\Delta\epsilon_{AI}} \ll \frac{1}{\gamma_2^{n'_2}}, \frac{1}{\gamma_1^{n_1}\gamma_2^{n'_2}}. \quad (\text{S2.52})$$

An example set of parameters that satisfies these conditions is $n_1 = n_2 = 1$, $n'_2 = 2$, $\gamma_1 = \frac{1}{\gamma_2} = 10^3$ and $e^{-\beta\Delta\epsilon_{AI}} = 10^2$.

S2.4 Combinatorial control with three regulatory ligands

In this section, we first present the methodology used to identify the functionally unique and MWC-compatible 3-ligand logic gates. We then use the full list of admissible gates to find all possible logic switches that can be induced by increasing the concentration of a third ligand. We finish by deriving the conditions required for achieving the logic switches AND → OR and AND → YES₁ shown in Fig. 2.7D.

S2.4.1 Functionally unique MWC gates

To identify the set of functionally unique MWC gates, we first iterate over the 256 possible responses and eliminate those redundant ones that can be obtained by shuffling the ligand labels of already selected gates. The Python implementation of this procedure that leaves 80 functionally unique gates can be found in the supplementary Jupyter Notebook 1.

Having singled out the functionally unique responses, we proceed to identify those that are admissible in the MWC framework. To that end, we first write the analytic

forms for the probability of the protein being active (p_{active}) at eight different ligand concentration limits (Figure S2.4A). Since the functional form in all cases is $p_{\text{active}} = (1 + w_{I/A})^{-1}$, where $w_{I/A}$ is the total weight of the inactive states divided by the total weight of the active states in the appropriate limit (as seen in Fig. 2.3A), a Boolean response ($p_{\text{active}} \approx 0$ or 1) can only be achieved when $w_{I/A} \gg 1$ or $w_{I/A} \ll 1$, respectively. Hence, the values of $w_{I/A}$ at the eight different limits of ligand concentration will determine the full logic response of the protein.

Note that since cooperative interactions between ligands are absent in the MWC framework, the eight different $w_{I/A}$ expressions depend on only four independent MWC parameters, namely $\{\Delta\epsilon_{AI}, \gamma_1, \gamma_2, \gamma_3\}$. Therefore, only four of the eight limiting $w_{I/A}$ values can be independently tuned, and any $w_{I/A}$ limit can be expressed as a function of four different and independent $w_{I/A}$ limits, resulting in a constraint condition. Since each $w_{I/A}$ is a product of some γ_i 's and $e^{-\beta\Delta\epsilon_{AI}}$ (Fig. S2.4A), we look for constraint conditions that have a multiplicative form, namely

$$w_{s^*} = \prod_{i=1}^4 w_{s_n}^{\alpha_n}, \quad (\text{S2.53})$$

where w_{s^*} is the target limit, $s_n \neq s^*$ ($1 \leq n \leq 4$) are the labels of four different limits and, α_n are real coefficients. Searching over all conditions of such a form (see the supplementary Jupyter Notebook 2 for details), we identify a total of eight functionally unique constraints,

$$w_{ij} \times w_0 = w_i \times w_j, \quad (\text{S2.54})$$

$$w_{123} \times w_j = w_{ij} \times w_{jk}, \quad (\text{S2.55})$$

$$w_{ij} \times w_k = w_{ik} \times w_j, \quad (\text{S2.56})$$

$$w_{123} \times w_0 = w_{ij} \times w_k, \quad (\text{S2.57})$$

$$w_{ij} \times w_k^2 = w_0 \times w_{ik} \times w_{jk}, \quad (\text{S2.58})$$

$$w_{123} \times w_0^2 = w_1 \times w_2 \times w_3, \quad (\text{S2.59})$$

$$w_{123}^2 \times w_0 = w_{12} \times w_{13} \times w_{23}, \quad (\text{S2.60})$$

$$w_{123} \times w_i \times w_j = w_{ij}^2 \times w_k, \quad (\text{S2.61})$$

where $1 \leq i, j, k \leq 3$.

Further searching for a minimum set of constraints that can account for all gates incompatible with the MWC framework, we identify the constraints in Eqs. S2.54-S2.57 as the necessary and sufficient ones (see the supplementary Jupyter Notebook

2). Graphical representations of these four constraints on a cubic diagram are shown in Fig. S2.4B. Note that these conditions are all of the form

$$w_{s_1} w_{s_2} = w_{s_3} w_{s_4}, \quad (\text{S2.62})$$

where s_i are labels corresponding to different ligand concentration limits. Logic responses where $w_{s_1}, w_{s_2} \ll 1$ ($\gg 1$) while $w_{s_3}, w_{s_4} \gg 1$ ($\ll 1$) cannot be achieved, since they contradict the constraint condition. Conditions 1 and 2 in Figure S2.4B, for example, demonstrate that XOR and XNOR gates cannot be realized by any two ligands in the absence (condition 1) or presence (condition 2) of a third ligand – a result expected from the 2-ligand analysis done earlier. On the other hand, conditions 3 and 4 are specific to the 3-ligand response.

Checking the 80 functionally unique gates against the four constraints in Fig. S2.4B, we obtain a set of 34 functionally unique and MWC-compatible gates, 17 of which are shown in Fig. S2.5A while the other half are their logical complements (i.e. ON \leftrightarrow OFF swapping is performed for each of the cube elements).

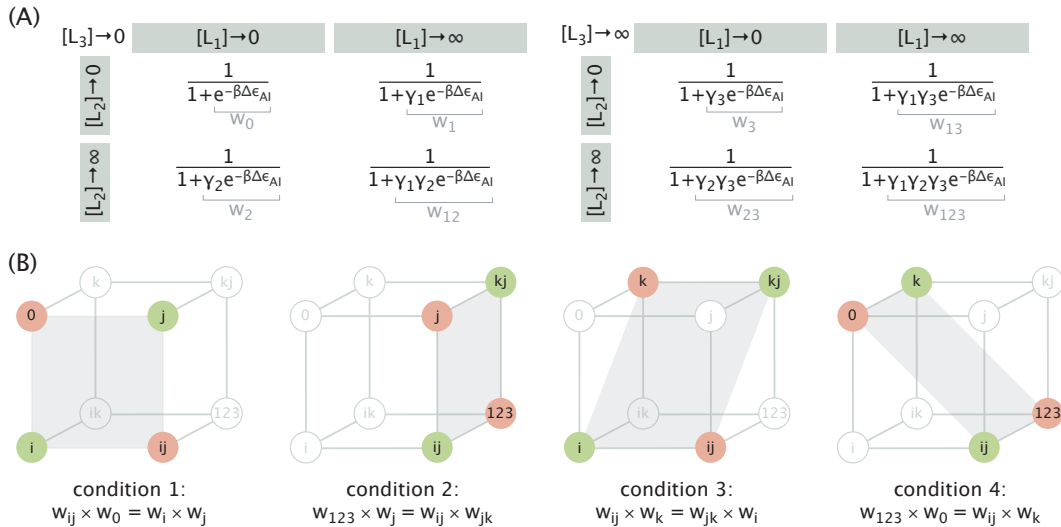


Figure S2.4: Three-ligand logic gates that are incompatible with the MWC framework. (A) Probability that the protein is active in the 8 different ligand concentration limits. The total weight of the inactive states relative to the active states is indicated in gray for all limits. (B) Cubic diagrams of logic responses that are incompatible with the MWC framework, along with the constraint equations used to obtain them. The limits relevant to the constraint conditions are shown in color, and a transparent gray plane containing these relevant limits is added for clarity. In all four diagrams, $1 \leq i, j, k \leq 3$.

S2.4.2 Logic switching

Here we describe how the table of all possible logic switches inducible by a third ligand (Fig. 2.6D) can be obtained from the list of MWC-compatible 3-ligand gates (Fig. S2.5), and also derive the parameter conditions for AND \rightarrow OR and AND \rightarrow YES₁ logic switches.

As illustrated in Fig. 2.6C, logic switching can be achieved by increasing the concentration of any of the three ligands. Following the same procedure, we iterate over the list of gates shown in Fig. S2.5A and for each of them identify the set of possible logic switches. The set of all logic switches present in Fig. S2.5A together constitute the entries of the table in Fig. 2.6D. Note that if a gate is compatible with the MWC framework, then its logical complement is also compatible, and therefore, the possibility of switching between two gates, Gate 1 \rightarrow Gate 2, implies the possibility of switching between their logical complements, NOT (Gate 1) \rightarrow NOT (Gate 2).

Now we show how an MWC protein can exhibit the switching behaviors in Fig. 2.7B,D (AND \rightarrow OR and AND \rightarrow YES₁) by saturating the concentration of the third ligand. We first consider the behavior of the protein in the absence of the third ligand ($[L_3] = 0$, with p_{active} limits given in Figure S2.4A, left), and then consider how the protein acts at the saturating concentration of the third ligand ($[L_3] \rightarrow \infty$, with p_{active} limits given in Fig. S2.4A, right). With $[L_3] = 0$, the protein ignores the third ligand and behaves identically to a protein with $N = 2$ ligands. In the limit $[L_3] \rightarrow \infty$, however, the protein behaves as if it only has two ligands with an altered free energy difference $\Delta\epsilon'_{\text{AI}}$ between the active and inactive states given by

$$\Delta\epsilon'_{\text{AI}} = \Delta\epsilon_{\text{AI}} - k_{\text{B}}T \log \gamma_3. \quad (\text{S2.63})$$

Suppose that a protein acts as an AND gate when $[L_3] = 0$ and transitions into an OR gate when $[L_3] \rightarrow \infty$, as in Fig. 2.7B. From Figure 2.3B, the MWC parameters must satisfy

$$\frac{1}{\gamma_1}, \frac{1}{\gamma_2} \ll e^{-\beta\Delta\epsilon_{\text{AI}}} \ll \frac{1}{\gamma_1\gamma_2} \quad (\text{S2.64})$$

in the absence of L_3 (AND behavior) and

$$1 \ll e^{-\beta\Delta\epsilon'_{\text{AI}}} \ll \frac{1}{\gamma_1}, \frac{1}{\gamma_2} \quad (\text{S2.65})$$

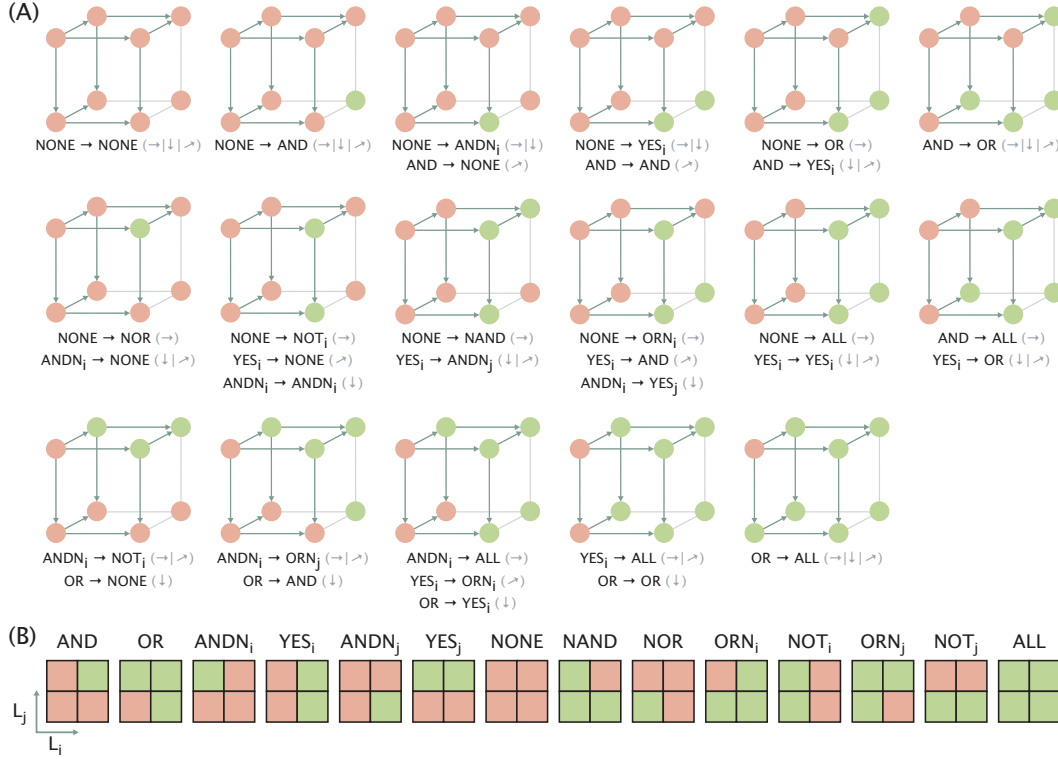


Figure S2.5: Functionally unique 3-ligand MWC gates and possible schemes of logic switching. (A) List of functionally unique 3-ligand MWC gates that have an inactive base state (in the absence of ligands). The set of logic switches that can be achieved by increasing the concentration of one of the ligands is listed on the bottom of each gate, with the gray arrows indicating the corresponding directions of increasing ligand concentration. Transitions with swapped labels ($i \leftrightarrow j$) are also possible and are not listed. Arrows corresponding to the ligand axes on different faces of the cube are included to assist the derivation of possible logic switches. (B) Schematics of 2-ligand gates adapted from Fig. 2.6D for convenience.

when $[L_3]$ is saturating (OR behavior). Using Eq. S2.63, we can rewrite the condition S2.65 as

$$\frac{1}{\gamma_3} \ll e^{-\beta\Delta\epsilon_{AI}} \ll \frac{1}{\gamma_1\gamma_3}, \frac{1}{\gamma_2\gamma_3}. \quad (\text{S2.66})$$

Combining Eq. S2.64 and Eq. S2.66, we find the second condition reported in Fig. 2.7A, namely

$$\frac{1}{\gamma_1}, \frac{1}{\gamma_2}, \frac{1}{\gamma_3} \ll e^{-\beta\Delta\epsilon_{AI}} \ll \frac{1}{\gamma_1\gamma_2}, \frac{1}{\gamma_1\gamma_3}, \frac{1}{\gamma_2\gamma_3}. \quad (\text{S2.67})$$

The first condition in Fig. 2.7A is then obtained by using the outer inequalities, that is,

$$\frac{1}{\gamma_k} \ll \frac{1}{\gamma_i\gamma_j} \Rightarrow \gamma_i\gamma_j \ll \gamma_k \quad \text{and} \quad (\text{S2.68})$$

$$\frac{1}{\gamma_i} \ll \frac{1}{\gamma_i \gamma_k} \Rightarrow \gamma_k \ll 1. \quad (\text{S2.69})$$

Lastly, we derive the parameter conditions needed to achieve an AND \rightarrow YES₁ switching by saturating the third ligand. Conditions for the AND behavior in the absence of the third ligand are already known (Eq. S2.64). To achieve a YES₁ gate, p_{active} at $[L_3] \rightarrow \infty$ needs to meet the following limits:

$$p_{0,0,\infty} = \frac{1}{1 + \gamma_3 e^{-\beta \Delta \epsilon_{\text{AI}}}} \approx 0, \quad (\text{S2.70})$$

$$p_{0,\infty,\infty} = \frac{1}{1 + \gamma_2 \gamma_3 e^{-\beta \Delta \epsilon_{\text{AI}}}} \approx 0, \quad (\text{S2.71})$$

$$p_{\infty,0,\infty} = \frac{1}{1 + \gamma_1 \gamma_3 e^{-\beta \Delta \epsilon_{\text{AI}}}} \approx 1, \quad (\text{S2.72})$$

$$p_{\infty,\infty,\infty} = \frac{1}{1 + \gamma_1 \gamma_2 \gamma_3 e^{-\beta \Delta \epsilon_{\text{AI}}}} \approx 1. \quad (\text{S2.73})$$

These limits suggest constraints on $\Delta \epsilon_{\text{AI}}$, which, combined with Eq. S2.64, result in

$$\frac{1}{\gamma_1}, \frac{1}{\gamma_2}, \frac{1}{\gamma_3}, \frac{1}{\gamma_2 \gamma_3} \ll e^{-\beta \Delta \epsilon_{\text{AI}}} \ll \frac{1}{\gamma_1 \gamma_2}, \frac{1}{\gamma_1 \gamma_3}, \frac{1}{\gamma_2 \gamma_3}, \frac{1}{\gamma_1 \gamma_2 \gamma_3}. \quad (\text{S2.74})$$

The outer inequalities, in turn, suggest conditions for the γ parameters, namely

$$\frac{1}{\gamma_i} \ll \frac{1}{\gamma_i \gamma_k} \Rightarrow \gamma_k \ll 1, \quad (\text{S2.75})$$

$$\frac{1}{\gamma_2 \gamma_3} \ll \frac{1}{\gamma_1 \gamma_2} \Rightarrow \gamma_1 \ll \gamma_2, \quad (\text{S2.76})$$

$$\frac{1}{\gamma_2 \gamma_3} \ll \frac{1}{\gamma_1 \gamma_3} \Rightarrow \gamma_1 \ll \gamma_3. \quad (\text{S2.77})$$

Accounting for these additional constraints, Eq. S2.74 simplifies into

$$\frac{1}{\gamma_1}, \frac{1}{\gamma_2 \gamma_3} \ll e^{-\beta \Delta \epsilon_{\text{AI}}} \ll \frac{1}{\gamma_1 \gamma_2}, \frac{1}{\gamma_1 \gamma_3}, \quad (\text{S2.78})$$

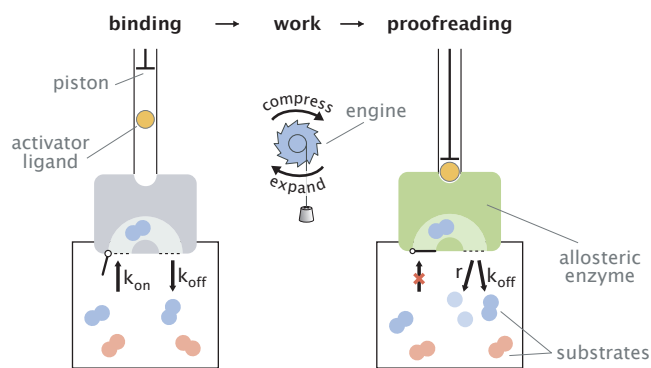
as shown in Fig. 2.7C.

References

1. Antebi, Y. E., Linton, J. M., Klumpe, H., Bintu, B., Gong, M., Su, C., McCardell, R. & Elowitz, M. B. Combinatorial signal perception in the BMP pathway. *Cell* **170**, 1184–1196 (2017).
2. Fakhouri, W. D., Ay, A., Sayal, R., Dresch, J., Dayringer, E. & Arnosti, D. N. Deciphering a transcriptional regulatory code: modeling short-range repression in the *Drosophila* embryo. *Mol. Syst. Biol.* **6**, 341 (2010).

Chapter 3

ALLOSTERY AND KINETIC PROOFREADING



This chapter is based on the journal publication: Galstyan, V. & Phillips, R. Allostery and kinetic proofreading. *J. Phys. Chem. B* **123**, 10990–11002 (2019). DOI: 10.1021/acs.jpcc.9b08380

3.1 Abstract

Kinetic proofreading is an error correction mechanism present in the processes of the central dogma and beyond, and typically requires the free energy of nucleotide hydrolysis for its operation. Though the molecular players of many biological proofreading schemes are known, our understanding of how energy consumption is managed to promote fidelity remains incomplete. In our work, we introduce an alternative conceptual scheme called “the piston model of proofreading” where enzyme activation through hydrolysis is replaced with allosteric activation achieved through mechanical work performed by a piston on regulatory ligands. Inspired by Feynman’s ratchet and pawl mechanism, we consider a mechanical engine designed to drive the piston actions powered by a lowering weight, whose function is analogous to that of ATP synthase in cells. Thanks to its mechanical design, the piston model allows us to tune the “knobs” of the driving engine and probe the graded changes and trade-offs between speed, fidelity, and energy dissipation. It provides an intuitive explanation of the conditions necessary for optimal proofreading and reveals the unexpected capability of allosteric molecules to beat the Hopfield limit of fidelity by leveraging the diversity of states available to them. The framework that we built for the piston model can also serve as a basis for additional studies of driven biochemical systems.

3.2 Introduction

Many enzymatic processes in biology need to operate with very high fidelities in order to ensure the physiological well-being of the cell. Examples include the synthesis of molecules making up Crick's so-called "two great polymer languages" (i.e., replication [1], transcription [2], and translation [3]), as well as processes that go beyond those of the central dogma, such as protein ubiquitylation mediated by the anaphase-promoting complex [4], signal transduction through MAP kinases [5], pathogen recognition by T-cells [6, 7], or protein degradation by the 26S proteasome [8]. In all of these cases, the designated enzyme needs to accurately select its correct substrate from a pool of incorrect substrates. Importantly, the fidelity of these processes that one would predict solely based on the free energy difference between correct and incorrect substrate binding is far lower than what is experimentally measured, raising a challenge of explaining the high fidelities that this naive equilibrium thermodynamic thinking fails to account for.

The conceptual answer to this challenge was provided more than 40 years ago in the work of John Hopfield [9] and Jacques Ninio [10] and was coined "kinetic proofreading" in Hopfield's elegant paper entitled "Kinetic proofreading: A new mechanism for reducing errors in biosynthetic processes requiring high specificity" [9]. The key idea behind kinetic proofreading is to introduce a delay between substrate binding and turnover steps, effectively giving the enzyme more than one chance to release the incorrect substrate (hence, the term "proofreading"). The sequential application of substrate filters on the way to product formation gives directionality to the flow of time and is necessarily accompanied by the expenditure of free energy, making kinetic proofreading an intrinsically nonequilibrium phenomenon. In a cell, this free energy is typically supplied to proofreading pathways through the hydrolysis of energy-rich nucleotides, whose chemical potential is maintained at large out-of-equilibrium values through the constant operation of the cell's metabolic machinery (e.g., the ATP synthase).

Since its original formulation by Hopfield and Ninio, the concept of kinetic proofreading has been generalized and employed in explaining many of the high-fidelity processes in the cell [8, 11–17]. However, despite the fact that the molecular players and mechanisms of these processes have been largely identified, we find that an intuitive picture of how energy transduction promotes biological fidelity is still incomplete. To complement our understanding of how energy is managed to beat the equilibrium limit of fidelity, we propose a conceptual model called "the piston model

of kinetic proofreading” where chemical hydrolysis is replaced with mechanical work performed by a piston on an allosteric enzyme. Our choice of allostery is motivated by the fact that in proofreading schemes, hydrolysis typically triggers a conformational change in the enzyme–substrate complex and activates it for product formation [16, 18, 19] – an effect that our model achieves through the binding of a regulatory ligand to the enzyme. By temporally controlling the concentration of regulatory ligands which determine the catalytic state of the enzyme, the piston sequentially changes the enzyme’s state from inactive to active, creating a delay in product formation necessary for increasing the fidelity of substrate discrimination. The piston actions are, in turn, driven by a Brownian ratchet and pawl engine powered by a lowering weight, whose function is akin to that of ATP synthase. The mechanical design of the piston model allows us to transparently control the energy input into the system by tuning the “knobs” of the engine and examine the graded changes in the model’s performance metrics, intuitively demonstrating the driving conditions required for optimal proofreading.

We begin the presentation of our results by first introducing in section 3.3 the high–level concept behind the piston model of proofreading, while at the same time drawing parallels between its features and those of Hopfield’s original scheme. Then in sections 3.4.1 and 3.4.2, we provide a comprehensive description of the two key constituents of the piston model, namely the Brownian ratchet and pawl engine that drives the piston actions, and the allosteric enzyme whose catalytic state is regulated by an activator ligand. This is followed by building the full thermodynamically consistent framework of the piston model in section 3.4.3 where we couple the external driving mechanism to the enzyme and introduce the expressions for key performance metrics of the model. In the remaining sections 3.4.4 and 3.4.5, we explore how tuning the “knobs” of the engine leads to graded changes and trade-offs between speed, fidelity and energy dissipation, and probe the performance limits of the piston model as a function of a select set of key enzyme parameters.

3.3 Model

The piston model of kinetic proofreading is designed in analogy with Hopfield’s scheme. The main idea there was to give the enzyme a second chance to discard the wrong substrate by introducing an additional kinetic intermediate for the enzyme–substrate complex (Fig. 3.1A). The difference between substrate binding energies in Hopfield’s original formulation was based solely on their unbinding rates (i.e., $k_{\text{off}}^{\text{W}} > k_{\text{off}}^{\text{R}}$ and $k_{\text{on}}^{\text{W}} = k_{\text{on}}^{\text{R}} = k_{\text{on}}$) – a convention we adopt throughout our analysis.

The first layer of substrate discrimination in Hopfield's scheme is achieved during the initial binding event where the ratio of right and wrong substrate-bound enzymes approaches $k_{\text{off}}^{\text{W}}/k_{\text{off}}^{\text{R}}$. The complex then moves into its catalytically active high-energy state accompanied by the hydrolysis of an NTP molecule, after which the second discrimination layer is realized. Specifically, right and wrong substrates are turned into products with an additional bias given by the ratio of their Michaelis constants, namely $(k_{\text{off}}^{\text{W}} + r)/(k_{\text{off}}^{\text{R}} + r)$. Importantly, for this second layer to be efficiently realized, the rates of binding directly to the second kinetic intermediate need to be vanishingly small in order to prevent the incorporation of unfiltered substrates [9].

With this information in mind, consider now the conceptual illustration of the piston model shown in Fig. 3.1B, where we have made several pedagogical simplifications to help verbally convey the model's intuition, reserving the full thermodynamically consistent treatment to the following sections. The central constituent of the model is an allosteric enzyme, the catalytic activity of which is regulated by activator ligands (the orange circle). The enzyme is inactive when it is not bound to a ligand, and, conversely, it is active when bound to a ligand. The volume occupied by ligands and hence, their concentration is, in turn, controlled by a piston. The ligand concentration is very low when the piston is expanded, and very high when the piston is compressed in order to guarantee that in those piston states the ligand is free and bound to the enzyme, respectively.

The active site of the enzyme is exposed to a container filled with right and wrong substrates of concentrations $[R]$ and $[W]$, respectively, which we take to be equal for the rest of our analysis ($[R] = [W]$). And unlike in Hopfield's scheme where the substrates exist in energy-rich and energy-depleted states (e.g., tRNAs first arrive in the EF-Tu-GTP-tRNA ternary complex and then release EF-Tu and GDP after hydrolysis), in the piston model substrates exist in a single state and do not carry an energy source. In the expanded piston state (Fig. 3.1B, left), substrates can bind and unbind to the inactive enzyme, but do not get turned into products. The highest level of discrimination achievable in this state therefore becomes

$$\eta_1 = \frac{k_{\text{off}}^{\text{W}}}{k_{\text{off}}^{\text{R}}}, \quad (3.1)$$

in analogy to that achieved during the initial binding step of Hopfield's scheme.

After the first layer of substrate discrimination is established in the expanded state of the piston, mechanical work is performed to compress it. This increases the ligand

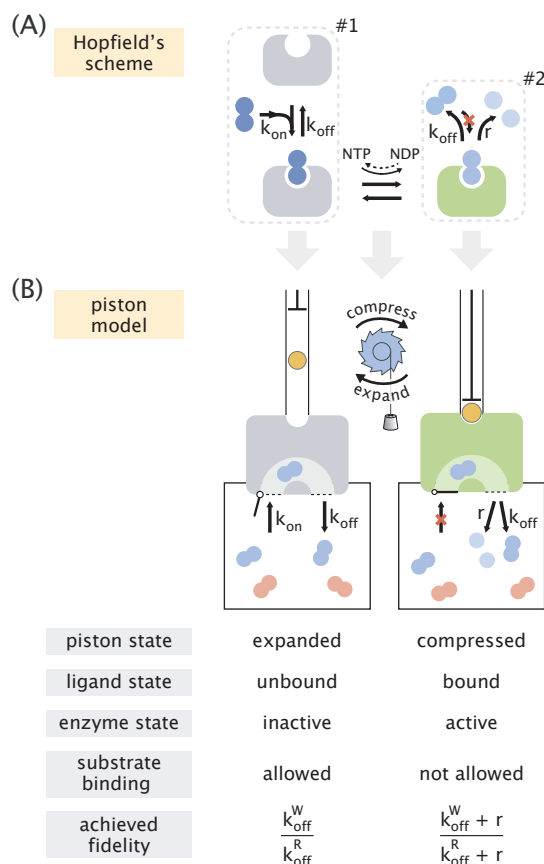


Figure 3.1: Conceptual introduction to the piston model. (A) Hopfield's scheme of kinetic proofreading where two layers of substrate discrimination take place on the driven pathway – the first one during the initial binding of energy-rich substrates (#1 in the diagram) and the second one upon the release of the energy-depleted substrates (#2 in the diagram). Energy consumption takes place during the hydrolysis reaction $\text{NTP} \rightleftharpoons \text{NDP}$ accompanying the transition between the two intermediates. (B) Pedagogically simplified conceptual scheme of the piston model. The orange circle represents the activator ligand. Blue and red colors stand for the right and wrong substrates, respectively. The closed “entrance door” along with the red cross on the binding arrow in the active state of the enzyme suggests the vanishingly small rate of substrate binding when in this state. The ratchet with a hanging weight stands for the mechanical engine that drives the piston actions. Various features of the system in the two piston states, along with the expressions for achieved fidelities are listed below the diagram. Transparent arrows between panels A and B indicate the analogous parts in Hopfield's scheme and the piston model.

concentration, which, in turn, leads to the activation of the enzyme where catalytic action is now possible. To prevent the incorporation of unfiltered substrates, we assume that in the active enzyme state, the rate of substrate binding is vanishingly small, similar to Hopfield's treatment (Fig. 3.1B, right). If the piston is kept

compressed long enough, a filtered substrate that got bound earlier when the piston was expanded will experience one of these two outcomes: it will either turn into a product with a rate r (which is taken to be the same for the two kinds of substrates) or it will fall off with a rate k_{off} . The product formation reaction will take place with probability $r/(k_{\text{off}} + r)$. Thus, due to the difference in the falloff rate constants between the right and the wrong substrates, the extra fidelity achieved after piston compression equals

$$\eta_2 = \frac{k_{\text{off}}^{\text{W}} + r}{k_{\text{off}}^{\text{R}} + r}. \quad (3.2)$$

Once this extra fidelity is established, the piston is expanded back, repeating the cycle (the detailed derivation of the results for η_1 and η_2 is provided in Appendix S3.1). Notably, the total fidelity achieved during the piston expansion and compression cycle, namely

$$\eta = \eta_1 \eta_2 = \left(\frac{k_{\text{off}}^{\text{W}}}{k_{\text{off}}^{\text{R}}} \right) \left(\frac{k_{\text{off}}^{\text{W}} + r}{k_{\text{off}}^{\text{R}} + r} \right), \quad (3.3)$$

exceeds the Michaelis–Menten fidelity (η_2) by a factor of $\eta_1 = k_{\text{off}}^{\text{W}}/k_{\text{off}}^{\text{R}}$, demonstrating the attainment of efficient proofreading.

The cyclic compressions and expansions of the piston in our model also stand in direct analogy to the hydrolysis–involving transitions between the two enzyme–substrate intermediates in Hopfield’s scheme. In particular, they need to be externally driven for the mechanism to do proofreading. We perform this driving using a mechanical ratchet and pawl engine powered by a lowering weight. In our pedagogical description of the model’s operation, we implicitly assumed that this weight was very large in order to enable the mechanism to proofread, similar to how the hydrolysis energy needs to be large for Hopfield’s scheme to operate effectively [9]. In the full treatment of the model in section 3.4, however, we will demonstrate how the tuning of the weight can give us graded levels of fidelity enhancement, and will also show that in the absence of this weight the equilibrium fluctuations of the piston alone cannot lead to proofreading.

In our model introduction, we have also made several simplifying assumption for clarity of presentation which do not conform with the principle of microscopic reversibility, and it is important that we relax them in the full treatment of the model to make it thermodynamically consistent. In particular, we assumed that the ligand is necessarily unbound and that the enzyme is necessarily inactive when the piston

is expanded, with the reverse assumptions made when the piston is compressed. We also assumed that substrate binding was prohibited in the active state of the enzyme. These assumptions allowed us to claim that no premature product formation takes place in the expanded piston state and that no unfiltered substrates bind to the activated enzyme in the compressed piston state, which, in turn, justified the use of long waiting times between the piston actions necessary to establish high levels of fidelity in each piston state. In the detailed analysis of our model presented in section 3.4, we relax these assumptions and consider the full diversity of enzyme states at each piston position with reversible transitions between them. This, as we will demonstrate, will not only ensure the thermodynamic consistency of our treatment but will also reveal the possibility of doing proofreading more than once by leveraging the presence of multiple inactive intermediates in between enzyme's substrate-unbound and production states which were not accounted for in our conceptual introduction of the model.

3.4 Results

3.4.1 Ratchet and pawl engine enables a tunable control of piston actions

To drive the cyclic compressions and expansions of the piston necessary for achieving proofreading, we use a ratchet and pawl engine whose design is inspired by Feynman's original work [20]. In his celebrated lectures, Feynman presented two implementations of the ratchet and pawl engine – one operating on the temperature difference between two thermal baths, and another driven by a weight that goes down due to gravity. In the piston model, we adopt the second scheme as it involves fewer parameters and illustrates the process of energy transduction more transparently.

The ratchet and pawl engine coupled to the piston is shown in Fig. 3.2A. The engine is powered by a weight of mass m which is hanging from an axle connected to the ratchet. The free rotational motion of the ratchet is rectified by a pawl; when the pawl sits on a ratchet tooth, it prevents the ratchet from rotating in the clockwise (backwards) direction. The mechanical coupling between the engine and the piston is achieved through a crankshaft mechanism which translates each discrete ratchet step into a full compression (up \rightarrow down) or a full expansion (down \rightarrow up) of the piston. We assume that the volume regulated by the piston contains a single ligand – a choice motivated by Szilard's thermodynamic interpretation of information, where a piston compressing a single gas molecule was considered [21].

The clockwise (backward) and counterclockwise (forward) steps of the microscopic ratchet are enabled through environmental fluctuations. Specifically, a backward step is taken whenever the pawl acquires sufficient energy from the environment to lift itself over the ratchet tooth that it is sitting on, allowing the tooth to slip under it (hence, the name “backward”). Following Feynman’s treatment [20], we write the rate of such steps as

$$k_b = \tau^{-1} e^{-\beta E_0}, \quad (3.4)$$

where τ^{-1} is the attempt frequency, E_0 is the amount of energy needed to lift the pawl over a ratchet tooth, and $\beta = 1/k_B T$ is the inverse of the thermal energy scale (see Appendix S3.2.1 for a detailed discussion of the ratchet and pawl mechanism). Every backward step of the ratchet is accompanied by either a full compression or a full expansion of the piston, as well as the lowering of the weight by an amount of Δz , which reduces its potential energy by $\Delta W = mg\Delta z$.

Unlike in backward stepping, for a forward step to take place, the rotational energy acquired by the ratchet through fluctuations should be sufficient to not only overcome the resistance of the spring pressing the pawl onto the ratchet, but also to lift the weight and to alter the state of the piston. This is a pure consequence of the geometric design of the ratchet and the positioning of the pawl. We assume that piston actions take place isothermally and in a quasistatic way, and therefore, write the changes in ligand free energy upon compression ($u \rightarrow d$) and expansion ($d \rightarrow u$) as

$$\Delta F_{u \rightarrow d} = \beta^{-1} \ln f, \quad \text{and} \quad (3.5)$$

$$\Delta F_{d \rightarrow u} = -\beta^{-1} \ln f, \quad (3.6)$$

respectively, where $f = V_u/V_d \geq 1$ is the fraction by which the volume occupied by the ligand decreases upon compression. The signs of free energy differences suggest that piston compressions slow down the forward steps, while expansions speed them up. These features are reflected in the two kinds of forward stepping rates that are given by

$$k_f^{u \rightarrow d} = \tau^{-1} e^{-\beta(E_0 + \Delta W + \Delta F)} = f^{-1} k_b e^{-\beta \Delta W}, \quad (3.7)$$

$$k_f^{d \rightarrow u} = \tau^{-1} e^{-\beta(E_0 + \Delta W - \Delta F)} = f k_b e^{-\beta \Delta W}, \quad (3.8)$$

where $\Delta F = \beta^{-1} \ln f$ and was used with a “+” and “-” sign in the place of $\Delta F_{u \rightarrow d}$ and $\Delta F_{d \rightarrow u}$, respectively. The rates of all four kinds of transitions, namely forward or backward ratchet steps, accompanied by either a compression or an expansion of the piston are summarized in Fig. 3.2B.

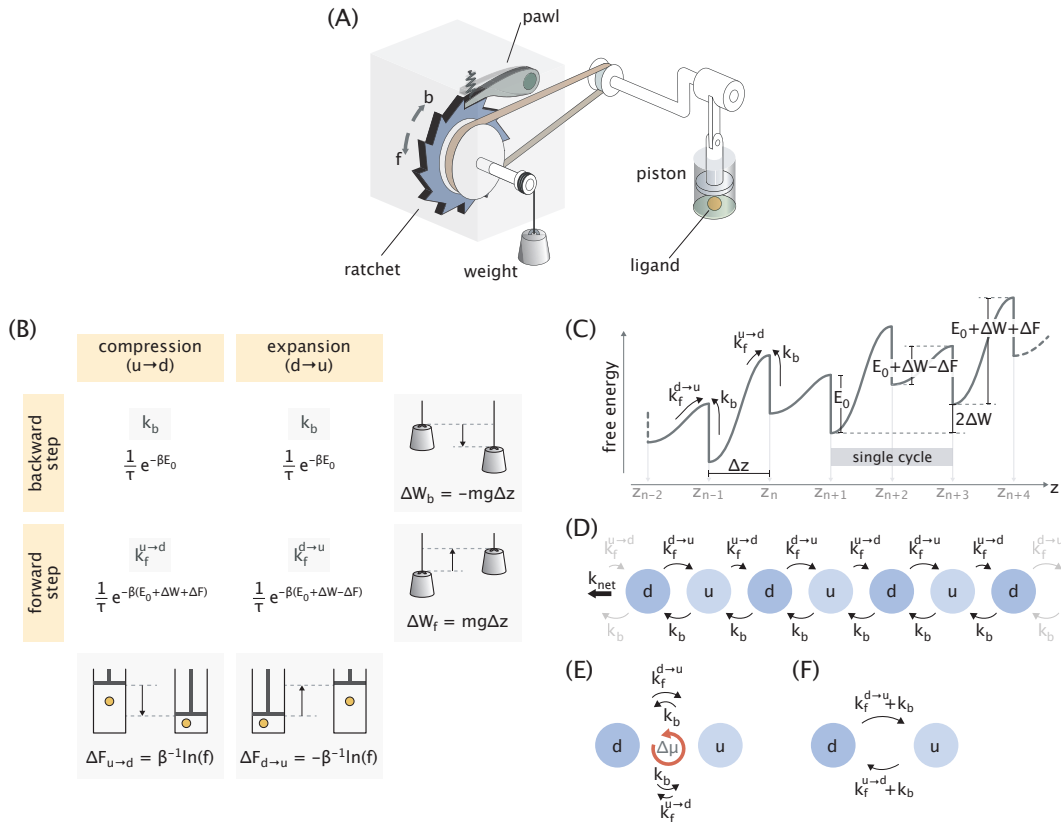


Figure 3.2: Ratchet and pawl mechanism coupled to the piston. (A) Schematic representation of the mechanism. The different radii of the ratchet wheel and the axle of the crankshaft ensure that a single ratchet step translates into a full compression or a full expansion of the piston (i.e., a 180° rotation of the crankshaft). Arrows with symbols “b” and “f” indicate the directions of backward and forward ratchet rotation, respectively. (B) Rates of the four kinds of transitions (symbols in shaded boxes with explicit expressions below), along with the accompanying changes in the potential energy of the weight and the free energy of the ligand. (C) Free energy landscape corresponding to the non-equilibrium dynamics of the system in the presence of a non-zero weight. Discrete positions of the weight (z_n) corresponding to energy minima of the landscape are marked on the reaction coordinate. (D) Infinite chain representation of the dynamics of discrete system states. k_{net} stands for the net rate at which the weight goes down. (E) Equivalent two-state representation of the engine dynamics where the driving force $\Delta\mu = 2\Delta W$ breaks the detailed balance in the diagram. (F) Collapsed representation of the diagram in panel E shown with the net transition rates from the two pathways.

In the presence of a nonzero weight ($\Delta W > 0$), the ratchet will on average rotate backwards – a feature reflected in the tilted free energy landscape shown in Fig. 3.2C. As can be seen, the average dissipation per step is ΔW , and it is independent of ΔF . In addition, the work performed on the ligand upon compression is fully returned

upon expansion, which, as we will demonstrate in section 3.4.4, will generally not be the case when we introduce the enzyme coupling. To further study the nonequilibrium dynamics of the driving mechanism, we map the local minima of the energy landscape corresponding to discrete vertical positions of the weight (equivalently, discrete ratchet angles) into an infinite chain of transitions shown in Fig. 3.2D. There “d” and “u” stand for the compressed and expanded states of the piston, respectively. The net stepping rate k_{net} at which the weight goes down can be written as

$$k_{\text{net}} = \left(k_b - k_f^{\text{d} \rightarrow \text{u}}\right) \pi_{\text{d}} + \left(k_b - k_f^{\text{u} \rightarrow \text{d}}\right) \pi_{\text{u}}, \quad (3.9)$$

where π_{d} and π_{u} are the steady state probabilities of the compressed and expanded piston states, respectively. These probabilities can be obtained by considering the equivalent two-state diagram in Fig. 3.2E where the vertical position of the weight has been eliminated, and the nonequilibrium nature of the dynamics is instead captured via the cycle through two alternative pathways connecting the piston states. The driving force $\Delta\mu$ in this cycle is given by [22]

$$\Delta\mu = \beta^{-1} \ln \left(\frac{k_b^2}{k_f^{\text{d} \rightarrow \text{u}} k_f^{\text{u} \rightarrow \text{d}}} \right) = 2\Delta W, \quad (3.10)$$

demonstrating the broken detailed balance in the presence of a nonzero weight, and confirming the dissipation of $2\Delta W$ per cycle observed in the energy landscape (Fig. 3.2C). We note that this procedure of mapping a linear network onto a cyclic one has also been used for modeling the processivity of molecular motors, where the linear coordinate corresponds to the position of the motor while the alternating states correspond to different motor conformations [23, 24].

At steady state, the net incoming and outgoing fluxes at each piston state in Fig. 3.2E should cancel each other (seen more vividly in the collapsed diagram in Fig. 3.2F), namely

$$\left(k_f^{\text{d} \rightarrow \text{u}} + k_b\right) \pi_{\text{d}} = \left(k_f^{\text{u} \rightarrow \text{d}} + k_b\right) \pi_{\text{u}}. \quad (3.11)$$

Substituting the expressions for forward stepping rates (Eq. 3.7 and Eq. 3.8) into Eq. 3.11 and additionally imposing the probability normalization constraint ($\pi_{\text{d}} + \pi_{\text{u}} = 1$), we can solve for π_{d} and π_{u} to obtain

$$\pi_{\text{d}} = \frac{1 + e^{-\beta(\Delta W + \Delta F)}}{2(1 + \cosh(\beta\Delta F) e^{-\beta\Delta W})}, \quad (3.12)$$

$$\pi_u = \frac{1 + e^{-\beta(\Delta W - \Delta F)}}{2(1 + \cosh(\beta\Delta F) e^{-\beta\Delta W})}. \quad (3.13)$$

Notably, in the absence of external drive ($\Delta W = 0$), piston state occupancies follow the Boltzmann distribution, that is, $(\pi_d/\pi_u)_{\text{eq}} = e^{-\beta\Delta F} = f^{-1}$, suggesting that at equilibrium the piston will predominantly dwell in the expanded state. Conversely, as can be seen in Fig. 3.3A, when the work per step exceeds ΔF by several $k_B T$, the occupancies of the two piston states become equal to each other. This happens because at large ΔW values, forward ratchet stepping becomes very unlikely and the dynamics proceeds only through backward steps with a rate k_b which is identical for both compressive and expansive steps. As will be shown in section 3.4.4, suppressing this equilibrium bias set by ΔF is essential for achieving efficient proofreading, analogous to the need for driving the transitions between the two enzyme–substrate intermediates in Hopfield’s scheme (Fig. 3.1A) [9].

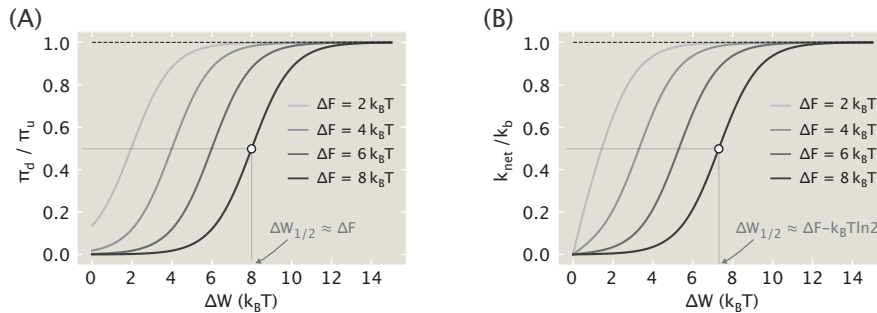


Figure 3.3: Nonequilibrium features of the engine–piston coupling. (A) Steady state probability ratio of compressed (“d”) and expanded (“u”) piston states and (B) normalized net rate of backward stepping (k_{net}/k_b) as a function of the work per step (ΔW) for different choices of the ligand compression energy (ΔF). The $\Delta W_{1/2}$ expressions stand for the values of ΔW where the corresponding value on the y-axis is 0.5 (Appendix S3.2.2). Negative ΔW values are not considered as they further increase the undesired bias in piston state occupancies.

With the steady state probabilities known, we can now substitute them into Eq. 3.9 to find the net rate at which the weight goes down, obtaining

$$k_{\text{net}} = \frac{(1 - e^{-2\beta\Delta W}) k_b}{1 + \cosh(\Delta F) e^{-\beta\Delta W}}. \quad (3.14)$$

As expected, k_{net} vanishes at equilibrium ($\Delta W = 0$), and asymptotes to k_b at large ΔW values, as shown in Fig. 3.3B. The knowledge of k_{net} allows us to calculate the power (P) dissipated for the maintenance of the nonequilibrium steady state.

Specifically, since k_{net} is the rate at which the weight goes down and ΔW is the dissipation per step, the power P becomes their product, namely

$$P = k_{\text{net}}\Delta W. \quad (3.15)$$

The formalism developed in this section for characterizing the steady state behavior of the system will be used as a basis for defining the different performance metrics of the model in section 3.4.3.

3.4.2 Thermodynamic constraints make fidelity enhancement unattainable in the absence of external driving

In order to implement a thermodynamically consistent coupling between the engine and the allosteric enzyme, we need to consider the full diversity of possible enzyme states [25], and not just the dominant ones depicted in Fig. 3.1B. Therefore, in this section, we provide a comprehensive discussion of the enzyme in an equilibrium setting before introducing its coupling to the engine.

The network diagram of all possible enzyme states is depicted in Fig. 3.4. As can be seen, each of the twelve states are defined by enzyme's catalytic activity and whether or not a ligand and a right/wrong substrate are bound to the enzyme. Following the principle of microscopic reversibility [26], we assign non-zero rate constants to the transitions between enzyme states. Only the product formation (with rate r) is taken to be an irreversible reaction under the assumption that the system is open where the formed products are taken out and an influx of new substrates is maintained. Since in our model neither the enzyme nor the substrates carry an energy source, the choice of the different rate constants cannot be arbitrary. Specifically, the cycle condition needs to be satisfied for each closed loop of the diagram, requiring the product of rate constants in the clockwise direction to equal the product in the counterclockwise direction (Appendix S3.3.1) [22].

With these equilibrium restrictions imposed on the rate constants, we can show that when the ligand concentration is held fixed ($[L](t) = \text{const}$), the fidelity of the enzyme cannot exceed that defined by the ratio of the off-rates, namely $k_{\text{off}}^{\text{W}}/k_{\text{off}}^{\text{R}}$ (see Appendix S3.3.2). What allows the enzyme to beat this equilibrium limit of fidelity without direct coupling to hydrolysis is the cyclic alteration of the ligand concentration between low and high values (thus, $[L](t) \neq \text{const}$). In our model, we achieve this cyclic alteration through the ratchet and pawl engine driving the piston actions – a choice motivated by our objective to provide an explicit

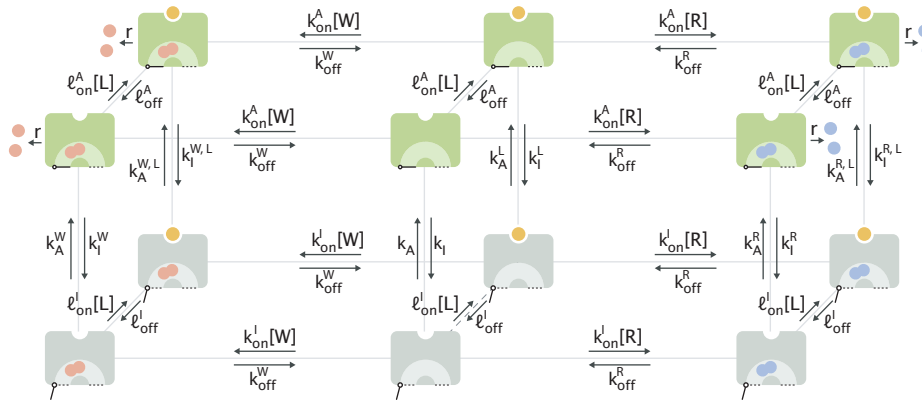


Figure 3.4: Network diagram of enzyme states and transitions between them. Right (“R”) and wrong (“W”) substrates are depicted in blue and red, respectively. The orange circle represents the ligand (“L”). Active (“A”) and inactive (“I”) enzymes are shown in green and gray, respectively.

treatment of energy management. We note, however, that fidelity enhancement can be achieved irrespective of the driving agency as long as the cyclic alteration of ligand concentration is maintained at a certain “resonance” frequency, the presence of which we demonstrate in section 3.4.4.

3.4.3 Coupling the engine to the enzyme gives the full description of the piston model

Having separately introduced the driving mechanism in section 3.4.1 and the allosteric enzyme with the full diversity of its states in section 3.4.2, we now couple the two together to obtain the full driven version of the piston model, shown in Fig. 3.5A. The coupling is achieved by exposing the ligand binding site of the enzyme to the piston compartment where the activator ligand is present. The enzyme can therefore “sense” the state of the piston (and, thereby, the effects of driving) through the induced periodic changes in the ligand concentration.

In the absence of enzyme coupling, the network diagram capturing the nonequilibrium dynamics of the system was an infinite one-dimensional chain (Fig. 3.2D), where each discrete state was defined by the vertical position of the weight (z_n) and the state of the piston (“u” or “d”). In the layout where the engine and the enzyme are coupled, the full specification of the system state now requires three items: the position of the weight (z_n), the piston state (“u” or “d”), and the state of the enzyme (one of the 12 possibilities). By converting the three-dimensional view of the enzyme state network (Fig. 3.4) into its planar equivalent, we represent the

nonequilibrium dynamics of this coupled layout again through an infinite chain, but this time each slice at a fixed weight position (z_n) corresponding to the planar view of the enzyme state network (Fig. 3.5B). The slices alternate between the compressed and expanded piston states (dark and light blue circles, respectively), with high and low ligand concentrations used in the transition network inside each slice.

Arrows between the slices (not all of them shown for clarity) represent the forward and backward steps of the ratchet. Crucially, as a consequence of coupling, the rates of forward stepping now depend on the state of the enzyme. In particular, when the ligand is bound to the enzyme, it no longer exerts pressure on the piston and therefore, in those cases, the forward stepping rates become simply

$$k_f^{u \rightarrow d, L} = k_f^{d \rightarrow u, L} = k_b e^{-\beta \Delta W}, \quad (3.16)$$

where the superscript ‘‘L’’ indicates that the ligand is bound (orange circles in Fig. 3.5B). We note that in the general case with N ligands, the pressure would drop down to that of $(N - 1)$ ligands upon ligand binding, correspondingly altering the rates of forward stepping (see Appendix S3.4.1 for details). This adjustment of forward rates is essential for the thermodynamic consistency of coupling the engine to the enzyme. Specifically, it ensures that any cycle of transitions that brings the enzyme and the weight back into their original states is not accompanied by dissipation, consistent with the fact that in the piston model energy is spent only when there is a net lowering of the weight. As a demonstration of this feature, consider the cycle in Fig. 3.5C which is extracted from the larger network. Using the expression of forward stepping rates in Eqs. 3.7 and 3.16, we can write the cycle condition for this sub-network as

$$\frac{k_f^{u \rightarrow d, L} \times \ell_{\text{off}}^A \times k_b \times \ell_{\text{on}}^A [\text{L}]_u}{k_b \times \ell_{\text{off}}^A \times k_f^{u \rightarrow d} \times \ell_{\text{on}}^A [\text{L}]_d} = \frac{[\text{L}]_u f}{[\text{L}]_d} = 1, \quad (3.17)$$

where the equality $f = V_u/V_d = [\text{L}]_d/[\text{L}]_u$ was used. The fact that the products of rate constants in clockwise and counterclockwise directions are identical shows that no dissipation occurs when traversing the cycle.

Now, to study how driving affects the proofreading performance of the piston model, we need to obtain the steady state probabilities of the different enzyme states. To that end, we convert the full network diagram into an equivalent form shown in Fig. 3.5D, where we have eliminated the position of the weight (z_n), akin to the earlier treatment of the uncoupled engine in Fig. 3.2E. Note that the transitions between the two slices again represent piston compression and expansion events

driven by a force $\Delta\mu = 2\Delta W$, as in Eq. 3.10. The steady state probabilities π_i of the 24 different states in Fig. 3.5D (12 enzyme states \times 2 piston states) can be obtained from the set of all rate constants, the details of which we discuss in Appendix S3.4.2. With these probabilities known, we calculate the rate of energy dissipation (P), speed of forming right products (v_R), and fidelity (η) as

$$P = \underbrace{\sum_{i=1}^{24} (k_b - k_f^{(i)}) \pi_i}_{k_{\text{net}}} \times \Delta W, \quad (3.18)$$

$$v_R = \sum_{i \in S_R^A} \pi_i \times r, \quad (3.19)$$

$$\eta = \frac{v_R}{v_W} = \frac{\sum_{i \in S_R^A} \pi_i}{\sum_{i \in S_W^A} \pi_i}, \quad (3.20)$$

where $k_f^{(i)}$ is the rate constant of making a forward step from the i^{th} state ($1 \leq i \leq 24$), while S_R^A and S_W^A are the sets of catalytically active enzyme states with a right and wrong substrate bound, respectively.

One significant downside of using these “raw” metrics in the numerical evaluation of the model performance is their high sensitivity to the particular choices of parameter values. We therefore introduce their scaled alternatives which we will use for the numerical studies in sections 3.4.4 and 3.4.5. Specifically, as a measure of energetic efficiency, we use the dissipation per right product formed, defined as

$$\varepsilon = \frac{P}{v_R}. \quad (3.21)$$

This way, the metric of energetics has units of $k_B T$ and is independent of the choice of absolute timescale. Then, as a dimensionless metric of speed, we introduce the normalized quantity

$$v = \frac{v_R}{v_R^{\text{MM}}}, \quad (3.22)$$

which represents the fraction by which the rate of forming right products in the proofreading setting (v_R) is slower than that in the simple Michaelis–Menten scheme (v_R^{MM}) where the allosteric effects are absent. This normalizing Michaelis–Menten speed is given in terms of the model parameters via

$$v_R^{\text{MM}} = \frac{\frac{k_{\text{on}}^{\text{I}}[\text{R}]}{k_{\text{off}}^{\text{R}}+r}}{1 + \frac{k_{\text{on}}^{\text{I}}[\text{R}]}{k_{\text{off}}^{\text{R}}+r} + \frac{k_{\text{on}}^{\text{I}}[\text{W}]}{k_{\text{off}}^{\text{W}}+r}} \times r. \quad (3.23)$$

Next, we define the proofreading index α as a fidelity metric which represents the degree to which the fidelity is amplified in multiples of $k_{\text{off}}^{\text{W}}/k_{\text{off}}^{\text{R}}$ over its Michaelis–Menten value (η_{MM}), that is,

$$\eta = \underbrace{\left(\frac{k_{\text{off}}^{\text{W}} + r}{k_{\text{off}}^{\text{R}} + r} \right)}_{\eta_{\text{MM}}} \left(\frac{k_{\text{off}}^{\text{W}}}{k_{\text{off}}^{\text{R}}} \right)^{\alpha}, \quad (3.24)$$

$$\alpha = \frac{\ln \eta - \ln \eta_{\text{MM}}}{\ln \left(\frac{k_{\text{off}}^{\text{W}}}{k_{\text{off}}^{\text{R}}} \right)}. \quad (3.25)$$

Note that the proofreading index of Hopfield’s scheme is $\alpha_{\text{Hopfield}} = 1$, as it involves a single proofreading realization. Also, since in the absence of external driving the highest fidelity is $\eta_{\text{eq}}^{\text{max}} = k_{\text{off}}^{\text{W}}/k_{\text{off}}^{\text{R}}$, the corresponding upper limit in the proofreading index becomes $\alpha_{\text{eq}} = 1 - \ln \eta_{\text{MM}}/\ln \eta_{\text{eq}}^{\text{max}}$.

As a final descriptor of piston model’s nonequilibrium behavior, we introduce the fraction of returned work (κ) defined as the ratio of the rate at which the ligand performs work on the piston upon expansion to the rate at which the piston performs work on the ligand upon compression. We calculate κ via

$$\kappa = - \frac{\sum_{i \in S_{\text{d}}} \left(k_{\text{b}} + k_{\text{f}}^{(i)} \right) \pi_i \Delta F_{\text{d} \rightarrow \text{u}}^{(i)}}{\sum_{i \in S_{\text{u}}} \left(k_{\text{b}} + k_{\text{f}}^{(i)} \right) \pi_i \Delta F_{\text{u} \rightarrow \text{d}}^{(i)}}, \quad (3.26)$$

where S_{d} and S_{u} are the sets of states where the piston is compressed and expanded, respectively. The negative sign is introduced to account for the fact that the ligand free energy decreases upon piston expansion (i.e., the system gets the work back). In the absence of enzyme coupling (section 3.4.1), this ratio was 1 because the ligand constantly exerted pressure on the piston. With enzyme coupling, however, the work performed on the ligand upon compression may not be fully returned since with some probability the ligand will be bound to the enzyme and exert no pressure on the piston during expansion. We therefore expect κ to be generally less than 1, indicating a net rate of performing work on the ligand in the nonequilibrium setting.

Having defined analytical expressions for the key model performance metrics, we now proceed to studying their graded changes and the trade-offs between them numerically.

3.4.4 Energy–speed–fidelity trade-off in the piston model

Because of its mechanical construction, the piston model of proofreading has a distinguishing feature – in it the external driving mechanism is physically separated

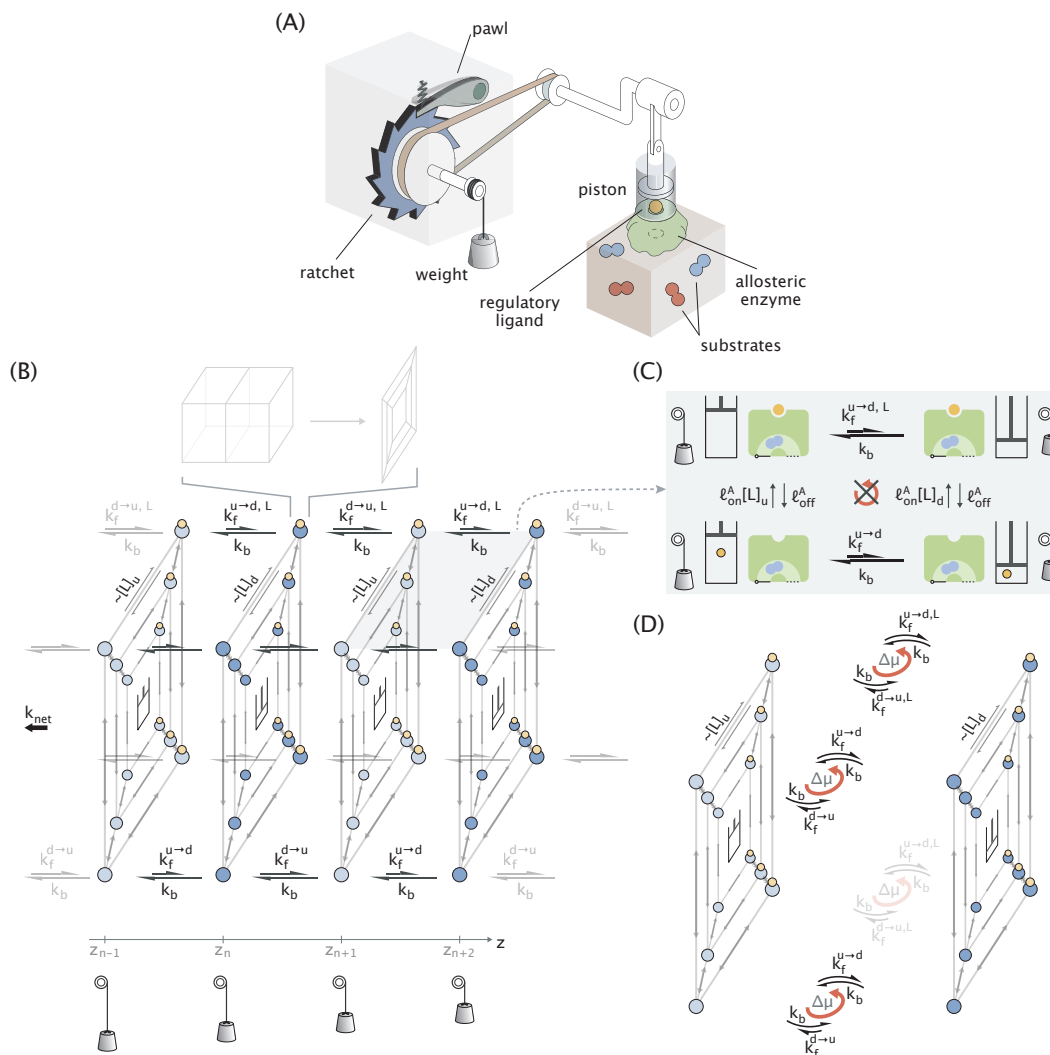


Figure 3.5: Full and thermodynamically consistent treatment of the piston model of proofreading. (A) Schematic representation of the full model, with the ratchet and pawl engine coupled to the enzyme. (B) Network diagram of the full model. Each slice of the diagram represents the planar view of the enzyme state network, with the alternating colors corresponding to the compressed (dark blue) and expanded (light blue) states of the piston. Ligand-bound enzyme states are marked with an orange circle. The horizontal arrows connecting the slices stand for forward and backward ratchet steps. Only those at the outer edges are shown for clarity; however, transitions are present between all horizontally neighboring enzyme states. Also for clarity, the stepping rate constants are shown only at two of the outer edges where the ligand is either unbound (bottom edge) or bound to the enzyme (top edge). The hanging weight at different vertical positions is displayed below the diagram to symbolize energy expenditure as it gets lowered with a net rate k_{net} . (C) Sub-network of the full diagram in panel B where the state of the system is unchanged after doing a cyclic traversal. The red arrow with a cross on top indicates that the cycle condition holds in the sub-network. (D) The finite-state equivalent of the full network in panel B with the weight position (z_n) eliminated. Red arrows indicate the driving with a force $\Delta\mu = 2\Delta W$.

from the allosteric enzyme. This feature allows us to independently examine how tuning the “knobs” of the engine and varying the kinetic parameters of the enzyme alter the performance of the model.

We begin our numerical analysis by first exploring the effects of external driving, where the tuning “knobs” include the rate of backward stepping (k_b), the work per step (ΔW), the ligand concentration in the compressed piston state ($[L]_d$) and the compression factor ($f = [L]_d/[L]_u$). Choosing a set of enzyme’s kinetic parameters which make proofreading possible (see Appendix S3.4.3 for the full list of parameters), we keep them fixed for the rest of the analysis. We conduct the first parametric study by tuning k_b and ΔW and evaluating the proofreading index (Figures 3.6A). As anticipated, the proofreading index does not exceed its equilibrium limit in the absence of driving ($\Delta W = 0$). This expected feature can be paralleled by Brownian motors where purely equilibrium fluctuations of the motor’s energy landscape are unable to generate directed motion [27]. In addition, the proofreading index achieves its highest value if ΔW is comparable to or larger than the ligand compression energy ΔF , and if the backward hopping rate k_b is at its “resonance” value. The presence of a “resonance” hopping rate is intuitive since if piston actions take place very slowly, then the fidelity will be reduced due to the small but nonzero rate of forming unfiltered products (i.e., “leakiness”) in the quasi-equilibrated enzyme states. And, conversely, if piston actions take place too rapidly, then the activator ligand will almost always be bound to the enzyme, preventing the realization of multiple substrate discrimination layers through sequential enzyme activation and inactivation. We note that analogous resonance responses were also identified for Brownian particles which attain their highest nonequilibrium drift velocity in a ratchet-like potential landscape when the temperature [28] or the landscape profile [29] are temporally modulated at specific resonance frequencies. A similar feature is present in Hopfield’s model as well; namely, optimal proofreading is attained only when the rate of hydrolysis is neither too low, nor too high [12]. Interestingly, when the driving is hard enough ($\Delta W \gtrsim \Delta F$) and the backward hopping rate is close to its resonance value, the fidelity of the piston model beats the Hopfield limit ($\alpha = 1$) and raises the question of the largest attainable fidelity, which we discuss in the next section.

Trends similar to those for the proofreading index are observed for the speed of forming right products as well (Fig. 3.6B). Specifically, product formation is very slow in the absence of driving and increases monotonically with ΔW , until plateauing

when $\Delta W \gtrsim \Delta F$. Also, the highest speed is achieved at a resonance k_b value which is different from that of the proofreading index. The existence of such a resonance frequency is again intuitive, since at fast rates of piston actions the enzyme is predominantly active and unable to bind new substrates, while at slow rates the enzyme activation for catalysis via piston compression happens very rarely. Notably, since the enzyme parameters were chosen in a way so as to yield high fidelities, the largest speed value is substantially lower than the corresponding speed for a single-step Michaelis–Menten enzyme ($v_{\max} \approx 10^{-2}$).

In the last parametric study, we explore how the choice of the high and low ligand concentrations affects the performance of the model. To that end, we tune the high ligand concentration ($[L]_d$) and the compression factor ($f = [L]_d/[L]_u$), and evaluate the highest proofreading index at the resonant k_b value with $\Delta W > \Delta F$. As we can see, large fidelity enhancements are achieved when $[L]_d$ is comparable to or larger than the ligand dissociation constant in the inactive enzyme state (R_d^I), which is necessary to activate the enzyme upon piston compression. In addition, the compression factor needs to be large enough (or, equivalently, the ligand concentration in the expanded piston state should be low enough) so as to inactivate the enzyme when piston enters its expanded state. This requirement of having a large free energy difference between the compressed and expanded piston states ($\beta\Delta F = \ln(f) \gg 1$) can be paralleled with a similar condition in Hopfield’s model where for optimal proofreading the energy of the activated enzyme–substrate complex needs to be much larger than that of the inactive complex.

Knowing separately how tuning the engine “knobs” affects the fidelity and speed, we now explore the trade-offs between the model’s performance metrics as we vary the driving parameters k_b and ΔW , while holding the high and low ligand concentrations at fixed values (the red dot in Fig. 3.6C). We start with the trade-off between fidelity and speed, depicted in Fig. 3.6D, where we continuously tune the hopping rate k_b for different choices of the driving force ΔW . As expected from the results of the individual parametric studies in Fig. 3.6A and Fig. 3.6B, both fidelity and speed increase monotonically with ΔW . Also, since the values of the hopping rate k_b that maximize fidelity and speed are not identical, these two performance metrics are negatively correlated in the range of k_b values defined by the two different resonance rates (region between the dotted lines in Fig. 3.6D), but are positively correlated otherwise. Variations in the metrics in the region of their negative correlation, however, are moderate, suggesting that for an allosteric enzyme

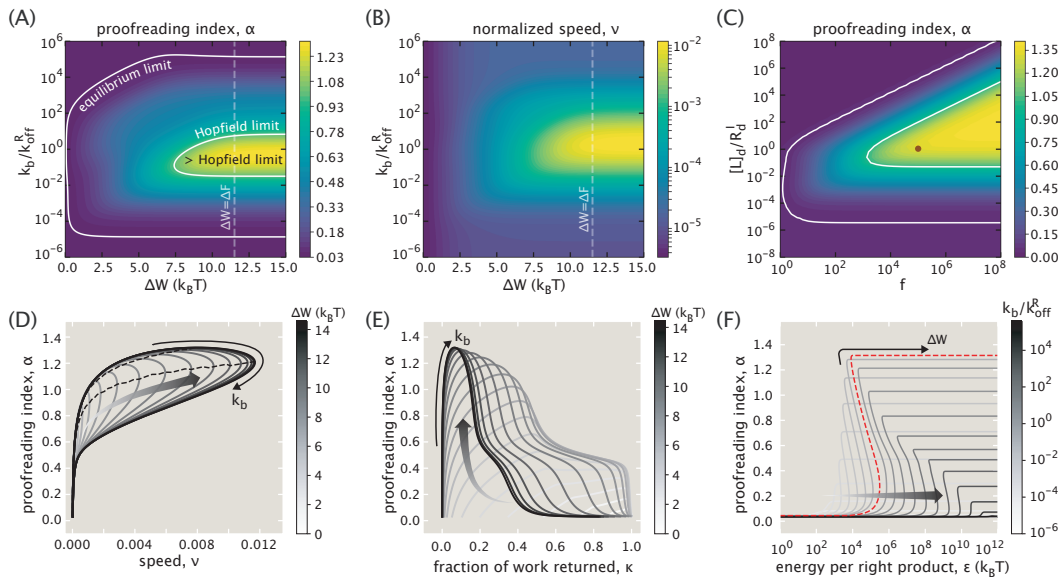


Figure 3.6: Parametric studies on the changes in the piston model performance in response to tuning the “knobs” of the engine. (A,B) Variations in the proofreading index (A) and speed (B) as the rate of backward stepping (k_b) and the work per step (ΔW) are tuned. The dotted line corresponds to the value of ΔW equal to the ligand free energy change upon compression (ΔF). (C) Variations in the proofreading index when the high ligand concentration ($[L]_d$) and the compression factor (f) are tuned. R_d^I represents the ligand dissociation constant in the inactive enzyme state. The red dot indicates the pair of $[L]_d$ and f values used in the studies of the other panels. (D) Fidelity–speed trade-off as k_b is continuously varied for different choices of ΔW (gradient arrow shows the direction of increase). The dotted black lines connect the highest fidelity and speed values as ΔW is tuned. Between these dotted lines fidelity and speed are negatively correlated. (E) Relation between fidelity and fraction of returned work for discrete choices of ΔW and continuously tuned k_b values (the gradient arrow indicates increasing ΔW). (F) Fidelity–dissipation trade-off obtained by continuously tuning ΔW for discrete choices of the hopping rate (k_b). The gradient arrow indicates the direction of increasing k_b . The red dotted curve corresponds to the case with resonance k_b .

that has been optimized for doing proofreading, the largest speed and fidelity could be achieved at similar external driving conditions.

Next, we consider the relation between fidelity and fraction of work returned, shown in Fig. 3.6E. As can be seen, no fidelity enhancement is achieved when κ is close to 1 which happens either in the absence of driving (lighter curves) or in the presence of driving, provided that the hopping rate is very fast. On the other hand, κ is much less than 1 at the peak fidelity which is achieved when the hopping rate is at its resonance value and when driving is large ($\Delta W \gtrsim \Delta F$). Overall, this trade-off study

demonstrates that irreversible work performed on the ligand is a required feature for the attainment of fidelity enhancement in the piston model.

Lastly, we look at how fidelity varies with energy dissipation, with the latter characterized through the energy expended per right product (ε). The results of the trade-off study are shown in Fig. 3.6F. There, the driving force is continuously tuned for different choices of the hopping rate. As can be seen, there is a minimum dissipation per product required to attain the given level of performance. This minimum dissipation (the first intercept at a given y-level) is achieved when the hopping rates are less than the corresponding resonant values (the lighter curves on the left side of the dotted red curve). Additionally, for a given hopping rate, increasing the driving force (ΔW) could lead to an increased proofreading performance and a decreased dissipation per product up a critical point where the performance metric reaches its saturating value (horizontal region), demonstrating how increasing the driving force could in fact improve the energetic efficiency of proofreading. We note here that the minimum ε values needed for significant proofreading are $\sim 10^3 - 10^4 k_B T$ in Fig. 3.6F which is ~ 2 orders of magnitude higher than what is calculated for translation by the ribosome [12]. This low energetic efficiency can be a consequence of our particular parameter choice for the study as well as the performance limitations of our engine design, the investigation of which we leave to future work.

3.4.5 Up to three proofreading realizations are available to the piston model

In the previous section, we chose a set of kinetic rate constants for the enzyme and, keeping them fixed, explored the effects of tuning the external driving conditions on the performance of the model. In this section, we explore the parameter space from a different angle, namely we study how tuning the enzyme's kinetic parameters changes the model performance under optimal driving conditions. Since there are more than a dozen rates defining the kinetic behavior of the enzyme, it is impractical to probe their individual effects. Instead, we choose to vary two representative parameters about the effects of which we have a prejudice. These include the rate of substrate binding to the active enzyme (k_{on}^A) and the unbinding rate of wrong substrates (k_{off}^W). We know already from Hopfield's analysis that, for efficient proofreading, direct substrate binding to the active enzyme should be very slow. Therefore, we expect the proofreading performance to improve as k_{on}^A is reduced. We also expect the minimum requirement for k_{on}^A to be lower for larger k_{off}^W values to ensure that wrong substrates do not enter through the unfiltered pathway [9].

With these expectations in mind, we performed a parametric study to find the highest fidelity, the results of which are summarized in Fig. 3.7A. There we varied k_{on}^{A} for several choices of $k_{\text{off}}^{\text{W}}$, and for each pair numerically optimized over the enzyme's remaining kinetic rates and external driving conditions to get maximum fidelity (see Appendix S3.4.4 for implementation details). As expected, the highest attainable fidelity decreases monotonically with increasing “leakiness” ($k_{\text{on}}^{\text{A}}/k_{\text{on}}^{\text{I}}$), and the minimum requirement on k_{on}^{A} decreases with increasing $k_{\text{off}}^{\text{W}}$.

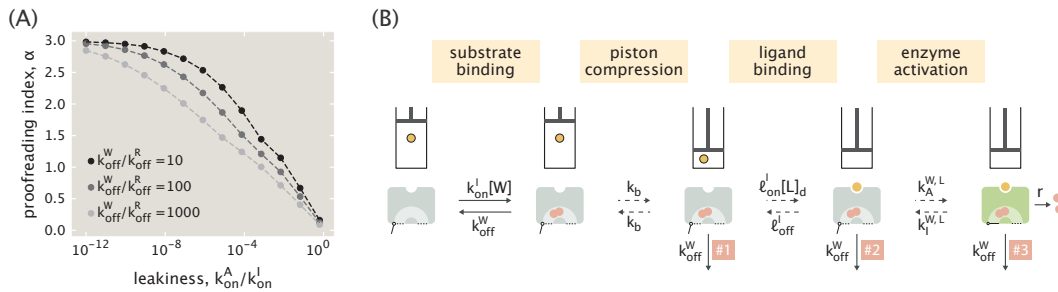


Figure 3.7: Proofreading performance of the piston model under optimized enzyme parameters and external driving conditions. (A) The highest proofreading index (α) available to the piston model as a function of leakiness ($k_{\text{on}}^{\text{A}}/k_{\text{on}}^{\text{I}}$) for different choices of $k_{\text{off}}^{\text{W}}$. (B) The dominant trajectory that the system takes to form a wrong product in the case where $k_{\text{on}}^{\text{A}}/k_{\text{on}}^{\text{I}} = 10^{-12}$. Numbers 1, 2, 3 stand for the different proofreading filters along the trajectory. The dotted arrows indicate that the respective rates are much slower than the substrate unbinding rate $k_{\text{off}}^{\text{W}}$ (see Appendix S3.4.5 for their numerical values for the $k_{\text{off}}^{\text{W}}/k_{\text{off}}^{\text{R}} = 100$ case).

Interestingly, we also see that for small enough leakiness, the piston model manages to perform proofreading (i.e., enhance the fidelity by a factor of $k_{\text{off}}^{\text{W}}/k_{\text{off}}^{\text{R}}$) up to three times, as $\alpha_{\text{max}} \approx 3$ (Fig. 3.7A). To understand this unexpected feature, we identified the dominant trajectory that the system would take to form a wrong product for the case where $k_{\text{on}}^{\text{A}}/k_{\text{on}}^{\text{I}} = 10^{-12}$ (Fig. 3.7B, see Appendix S3.4.5 for details). As we can see, after initial binding the wrong substrate indeed passes through three different proofreading filters, and these are realized efficiently because the transitions between intermediate states are much slower than the rate of substrate unbinding. The first filter occurs right after piston compression, while the enzyme is waiting for the activator ligand to bind (#1). We note that this particular filter is made possible due to the presence of alternative piston states (equivalently, alternative environments that the enzyme could “sense”). The remaining two filters (#2 and #3) take place while the ligand-bound enzyme is waiting to get activated and while the active enzyme is waiting to turn the wrong substrate into a product, respectively. The

presence of these two filters is purely a consequence of allostery. Importantly, the $\alpha_{\max} \approx 3$ result in Fig. 3.7 represents the theoretical upper limit of the model's proofreading index – a feature that we justify analytically in Appendix S3.4.5.

In light of this analysis, we can now explain why the pedagogically simplified version of the model introduced in section 3.3 achieved only a single proofreading realization. There we made the implicit assumption that ligand binding after piston compression and enzyme activation after ligand binding took place instantly. Because of this, proofreading filters #1 and #2 were not realized, leaving filter #3 as the only available one which we showed in Fig. 3.1B.

3.5 Discussion

A distinctive feature of kinetic proofreading is that it is a nonequilibrium mechanism, by virtue of which its operation needs to involve energy expenditure [9, 10]. Mechanical work, being an intuitive representation of energy expenditure, has been used in the past to elucidate important physical concepts such as information-to-energy conversion in the thought experiment by Szilard [21], or the mechanical equivalence of heat in Joule's apparatus [30]. Yet, a similar demonstration of how mechanical work could be harnessed in a graded fashion to beat the equilibrium limit in substrate discrimination fidelity has been lacking. Our aim in this work was to offer such a demonstration through the mechanically designed piston model of proofreading.

We started off by providing the conceptual picture of the piston model, with its constituents having direct parallels with Hopfield's original proofreading scheme (Fig. 3.1). The key idea of the model was to replace the nucleotide hydrolysis step present in Hopfield's scheme with piston compression which served an identical role of activating the enzyme, but in our case achieved through allostery and mechanical work. Just like in the case of biological proofreading, where hydrolysis itself cannot lead to fidelity enhancement unless the nucleotide triphosphates are held at fixed out-of-equilibrium chemical potentials, in the case of piston model too, the compressive and expansive actions of the piston cannot result in proofreading unless they are driven by an energy-consuming engine. Motivated by Feynman's ratchet and pawl mechanism [20], we then proposed a dissipative mechanical engine to drive the cyclic piston actions, which maintained the nonequilibrium distribution of enzyme states necessary for achieving proofreading. The function of this engine can be paralleled to that of the ATP synthase in the cell whose constant operation

maintains a finite chemical potential of ATP, which different biochemical pathways can then take advantage of.

To study how the cyclic variations in ligand concentration generated by the engine alter the occupancies of enzyme states, we performed a thermodynamically consistent coupling between the engine and the enzyme (Fig. 3.5). There we considered the full diversity of states that the enzyme could take and, importantly, the feedback mechanism for the engine to “sense” the state of the enzyme. The accounting of this latter feature, which makes the piston model an example of a bi-partite system [31, 32], was motivated by our aim of proposing a framework where we could consistently calculate the total dissipation as opposed to only the minimum dissipation needed for maintaining the nonequilibrium steady state of the enzyme (without considering the driving engine) [12, 33, 34]. Although the dissection of different contributions to dissipation and their interconnectedness was not among the objectives of our work, the framework that we proposed in our model can serve as a basis for additional studies of periodically driven molecular systems (e.g., Brownian clocks or artificial molecular motors) where the driving protocol and thermodynamics are of importance [35–37]. As noted earlier, however, in the presence of a periodically changing ligand concentration, the allosteric enzyme could perform proofreading irrespective of the driving agency, which suggests a possible biochemical mechanism of fidelity enhancement without the direct coupling of the enzyme state transitions to hydrolysis.

Having explicit control over the “knobs” of the mechanical engine, we then probed the performance of the model under different driving conditions. We found that both speed and fidelity increased as we tuned up the mass of the hanging weight, until plateauing at a point where the free energy bias of the expanded piston state was fully overcome ($\Delta W \gtrsim \Delta F$), beyond which increasing the weight only increased the dissipation without improving the model performance (Fig. 3.6A,B). This result can be paralleled with the presence of a minimum threshold for the strength of driving in Hopfield’s model, past which the highest fidelity becomes attainable [9]. In addition, we found that in the piston model there is a “resonance” rate of piston actions which maximizes fidelity, analogous to the similar feature of Hopfield’s scheme where both very fast and very slow rates of hydrolysis reduce the quality of proofreading [12].

The tunable control over the driving parameters also allowed us to study the trade-off between fidelity, speed, and energy spent per right product. These studies revealed

that the correlation between speed and fidelity could be both positive and negative when varying the rate of driving. Notably, theoretical investigations of translation by the *Escherichia coli* ribosome under Hopfield's scheme identified a similar behavior for the fidelity–speed correlation in response to tuning the GTP hydrolysis rate, with the experimentally measured values being in the negative correlation (i.e., trade-off) region [17]. In contrast to the ribosome study, however, where the two metrics vary by several orders of magnitude in the trade-off region, in the piston model the variations in fidelity and speed in the negative correlation region are moderate (Fig. 3.6D), calling for additional investigations of the underlying reasons behind this difference and search for the realization of the latter advantageous behavior in biological proofreading systems. Furthermore, our studies showed that the minimum dissipation required to reach the given level of fidelity was achieved for hopping rates necessarily lower than their resonance values, and that increasing the work performed per step (analogously, the chemical potential of ATP) could actually improve the energetic efficiency of the model – features that again motivate the identification of their realization in biochemical systems.

In the end, we explored the limits in the proofreading performance of the piston model for various choices of the allosteric enzyme's "leakiness" ($k_{\text{on}}^{\text{A}}/k_{\text{on}}^{\text{I}}$) and the ratio of the wrong and right substrate off-rates ($k_{\text{off}}^{\text{W}}/k_{\text{off}}^{\text{R}}$). We found that the trends for the highest available fidelity matched analogously with the features of Hopfield's original scheme, suggesting their possible ubiquity for general proofreading networks. More importantly, our analysis revealed that the piston model could do proofreading not just once but up to three times in the limit of very low leakiness, despite the fact that energy consumption takes place during a single piston compression. This is in contrast to the typical involvement of several energy consumption instances in multistep proofreading schemes which manage to beat the Hopfield limit of fidelity, as, for example, in the cases of the T-cell or MAPK activation pathways which require multiple phosphorylation reactions [5, 6, 33]. Our finding therefore suggests the possibility of achieving several proofreading realizations with a single energy consuming step by leveraging the presence of multiple inactive intermediates intrinsically available to allosteric molecules. We would like to mention here that the presence of a similar feature was also experimentally demonstrated recently for the ribosome which was shown to use the free energy of a single GTP hydrolysis to perform proofreading twice after the initial tRNA selection – first, at the EF-Tu-GDP-bound inactive state and second, at the EF-Tu-free active state [38].

In the presentation of the piston model, we focused on the thermodynamic consistency of the framework for managing the energy dissipation and did not consider strategies for improving the performance of the mechanism. One such possibility that can be considered in future work is to use a more elaborate design for the ratchet and pawl engine with alternating activation barriers for pawl hopping which would allow to have different rates of piston compression and expansion, analogous to how hydrolysis and condensation reactions generally occur with different rates in biological proofreading [17, 39]. Another avenue is to consider alternative ways of allocating the mechanical energy dissipation across the different ratchet transition steps, similar to how optimization schemes of allocating the free energy of ATP hydrolysis were studied for molecular machine cycles [40]. Incorporating these additional features would allow us to probe the performance limits of the piston model and compare them with the fundamental limits set by thermodynamics [41].

Acknowledgements

We thank Tal Einav, Erwin Frey, Christina Hueschen, Sarah Marzen, Arvind Murugan, Manuel Razo-Mejia, Matt Thomson, Yuhai Tu, Jin Wang, Jerry Wang, Ned Wingreen, and Fangzhou Xiao for fruitful discussions. We also thank Haojie Li and Dennis Yatunin for their input on this work, Alexander Grosberg, David Sivak, and Pablo Sartori for providing valuable feedback, and Nigel Orme for his assistance in making the illustrations. This work was supported by the National Institutes of Health through the grant 1R35 GM118043-01 (MIRA), and the John Templeton Foundation as part of the Boundaries of Life Initiative grants 51250 and 60973.

References

1. Kunkel, T. A. DNA replication fidelity. *J. Biol. Chem.* **279**, 16895–16898 (2004).
2. Sydow, J. F. & Cramer, P. RNA polymerase fidelity and transcriptional proofreading. *Curr. Opin. Struc. Biol.* **19**, 732–739 (2009).
3. Rodnina, M. V. & Wintermeyer, W. Fidelity of aminoacyl-tRNA selection on the ribosome: Kinetic and structural mechanisms. *Annu. Rev. Biochem.* **70**, 415–435 (2001).
4. Lu, Y., Wang, W. & Kirschner, M. W. Specificity of the anaphase-promoting complex: A single-molecule study. *Science* **348**, 1248737 (2015).
5. Swain, P. & Siggia, E. The role of proofreading in signal transduction specificity. *Biophys. J.* **82**, 2928–2933 (2002).

6. Mckeithan, T. W. Kinetic proofreading in T-cell receptor signal transduction. *Proc. Natl. Acad. Sci. U.S.A.* **92**, 5042–5046 (1995).
7. Goldstein, B., Faeder, J. R. & Hlavacek, W. S. Mathematical and computational models of immune-receptor signalling. *Nat. Rev. Immunol.* **4**, 445 (2004).
8. Bard, J. A., Bashore, C., Dong, K. C. & Martin, A. The 26S proteasome utilizes a kinetic gateway to prioritize substrate degradation. *Cell* **92**, 5042–5046 (2019).
9. Hopfield, J. J. Kinetic proofreading: A new mechanism for reducing errors in biosynthetic processes requiring high specificity. *Proc. Natl. Acad. Sci. U.S.A.* **71**, 4135–4139 (1974).
10. Ninio, J. Kinetic amplification of enzyme discrimination. *Biochimie* **57**, 587–595 (1975).
11. Murugan, A., Huse, D. A. & Leibler, S. Speed, dissipation, and error in kinetic proofreading. *Proc. Natl. Acad. Sci. U.S.A.* **109**, 12034–12039 (2012).
12. Wong, F., Amir, A. & Gunawardena, J. Energy-speed-accuracy relation in complex networks for biological discrimination. *Phys. Rev. E.* **98**, 012420 (2018).
13. Sartori, P. & Pigolotti, S. Kinetic versus energetic discrimination in biological copying. *Phys. Rev. Lett.* **110**, 188101 (2013).
14. Depken, M., Parrondo, J. M. & Grill, S. W. Intermittent transcription dynamics for the rapid production of long transcripts of high fidelity. *Cell Rep.* **5**, 521–530 (2013).
15. Qian, H. Phosphorylation energy hypothesis: Open chemical systems and their biological functions. *Annu. Rev. Phys. Chem.* **58**, 113–142 (2007).
16. Semlow, D. R. & Staley, J. P. Staying on message: ensuring fidelity in pre-mRNA splicing. *Trends Biochem. Sci.* **37**, 263–273 (2012).
17. Banerjee, K., Kolomeisky, A. B. & Igoshin, O. A. Elucidating interplay of speed and accuracy in biological error correction. *Proc. Natl. Acad. Sci. U.S.A.* **114**, 5183–5188 (2017).
18. Blanchard, S. C., Gonzalez Jr, R. L., Kim, H. D., Chu, S. & Puglisi, J. D. tRNA selection and kinetic proofreading in translation. *Nat. Struct. Mol. Biol.* **11**, 1008 (2004).
19. Yan, J., Magnasco, M. O. & Marko, J. F. Kinetic proofreading can explain the suppression of supercoiling of circular DNA molecules by type-II topoisomerases. *Phys. Rev. E* **63**, 031909 (2001).
20. Feynman, R. P., Leighton, R. B. & Sands, M. *The Feynman Lectures on Physics* (Addison-Wesley, Reading, MA, 1963).

21. Szilard, L. Über die entropieverminderung in einem thermodynamischen system bei eingriffen intelligenter wesen. *Z. Phys.* **53**. [Szilard, L. On the decrease of entropy in a thermodynamic system by the intervention of intelligent beings. *Behav. Sci.* 1964, 9, 301-310], 840–856 (1929).
22. Hill, T. L. *Free Energy Transduction in Biology* (Academic Press, New York, NY, 1977).
23. Qian, H. A simple theory of motor protein kinetics and energetics. *Biophys. Chem.* **67**, 263–267 (1997).
24. Wagoner, J. A. & Dill, K. A. Molecular motors: Power strokes outperform Brownian ratchets. *J. Phys. Chem. B* **120**, 6327–6336 (2016).
25. Einav, T., Mazutis, L. & Phillips, R. Statistical mechanics of allosteric enzymes. *J. Phys. Chem. B* **120**, 6021–6037 (2016).
26. Tolman, R. C. *The Principles of Statistical Mechanics* (Dover, New York, 1979).
27. Astumian, R. D. & Hänggi, P. Brownian motors. *Phys. Today* **55**, 33–39 (2002).
28. Reimann, P., Bartussek, R., Häussler, R. & Hänggi, P. Brownian motors driven by temperature oscillations. *Phys. Lett. A* **215**, 26–31 (1996).
29. Faucheux, L. P., Bourdieu, L. S., Kaplan, P. D. & Libchaber, A. J. Optical thermal ratchet. *Phys. Rev. Lett.* **74**, 1504 (1995).
30. Joule, J. P. On the mechanical equivalent of heat. *Phil. Trans. R. Soc. Lond.* **140**, 61–82 (1850).
31. Horowitz, J. M. & Esposito, M. Thermodynamics with continuous information flow. *Phys. Rev. X* **4**, 031015 (2014).
32. Barato, A. C., Hartich, D. & Seifert, U. Efficiency of cellular information processing. *New J. Phys.* **16**, 103024 (2014).
33. Cui, W. & Mehta, P. Identifying feasible operating regimes for early T-cell recognition: The speed, energy, accuracy trade-off in kinetic proofreading and adaptive sorting. *PloS One* **13**, e0202331 (2018).
34. Horowitz, J. M., Zhou, K. & England, J. L. Minimum energetic cost to maintain a target nonequilibrium state. *Phys. Rev. E* **95**, 042102 (2017).
35. Barato, A. C. & Seifert, U. Thermodynamic cost of external control. *New J. Phys.* **19**, 073021 (2017).
36. Barato, A. C. & Seifert, U. Cost and precision of Brownian clocks. *Phys. Rev. X* **6**, 041053 (2016).
37. Leigh, D. A., K., W. J., Dehez, F. & Zerbetto, F. Unidirectional rotation in a mechanically interlocked molecular rotor. *Nature* **424**, 174–179 (2003).

38. Jeong, K. W., Uzun, Ü., Selmer, M. & Ehrenberg, M. Two proofreading steps amplify the accuracy of genetic code translation. *Proc. Natl. Acad. Sci. U.S.A.* **113**, 13744–13749 (2016).
39. Chen, K. Y., Zuckerman, D. M. & Nelson, P. C. Stochastic simulation to visualize gene expression and error correction in living cells. *ArXiv* **1809.05619v1** (2018).
40. Brown, A. I. & Sivak, D. A. Allocating dissipation across a molecular machine cycle to maximize flux. *Proc. Natl. Acad. Sci. U.S.A.* **114**, 11057–11062 (2017).
41. Qian, H. Reducing intrinsic biochemical noise in cells and its thermodynamic limit. *J. Mol. Biol.* **362**, 387–392 (2006).

Chapter S3

SUPPORTING INFORMATION FOR CHAPTER 3 |
ALLOSTERY AND KINETIC PROOFREADING

Python scripts and Jupyter notebooks used for generating the results of the different numerical studies are available as supplementary files on the publication webpage (DOI: 10.1021/acs.jpcc.9b08380).

S3.1 Discrimination fidelity in the conceptual scheme of the piston model

In this section, we derive the expressions for the fidelities achieved at the two piston steps introduced in section 3.3 of the main text, namely $\eta_1 = k_{\text{off}}^{\text{W}}/k_{\text{off}}^{\text{R}}$ when the piston is expanded, and $\eta_2 = (k_{\text{off}}^{\text{W}} + r)/(k_{\text{off}}^{\text{R}} + r)$ when the piston is compressed. In our discussion, we retain the simplifying assumptions made during the presentation of the model concept.

As discussed in section 3.3, the first level of substrate discrimination occurs in the expanded piston state. If the waiting time for compression is long enough for the substrates to equilibrate with the inactive enzyme, we can impose the detailed balance condition at the two pairs of edges in Fig. S3.1A to obtain

$$p_{\text{I}}^{\text{R}} k_{\text{off}}^{\text{R}} = p_{\text{I}} k_{\text{on}}[\text{R}], \quad (\text{S3.1})$$

$$p_{\text{I}}^{\text{W}} k_{\text{off}}^{\text{W}} = p_{\text{I}} k_{\text{on}}[\text{W}]. \quad (\text{S3.2})$$

Here p_{I} , p_{I}^{R} , and p_{I}^{W} stand for the probabilities of the empty, right substrate-bound, and wrong substrate-bound inactive states of the enzyme, respectively. Taking the substrate concentrations to be identical ($[\text{R}] = [\text{W}]$), we can equate the left sides of Eqs. S3.1 and S3.2 to find

$$\frac{p_{\text{I}}^{\text{R}}}{p_{\text{I}}^{\text{W}}} = \frac{k_{\text{off}}^{\text{W}}}{k_{\text{off}}^{\text{R}}}. \quad (\text{S3.3})$$

The above ratio of probabilities represents the proportion in which right and wrong substrate-bound inactive enzymes enter the active state, and therefore, becomes equivalent to the fidelity η_1 achieved in the first discrimination step.

The second level of substrate differentiation takes place when the piston gets compressed, leading to the activation of the enzyme. We assume that in its active

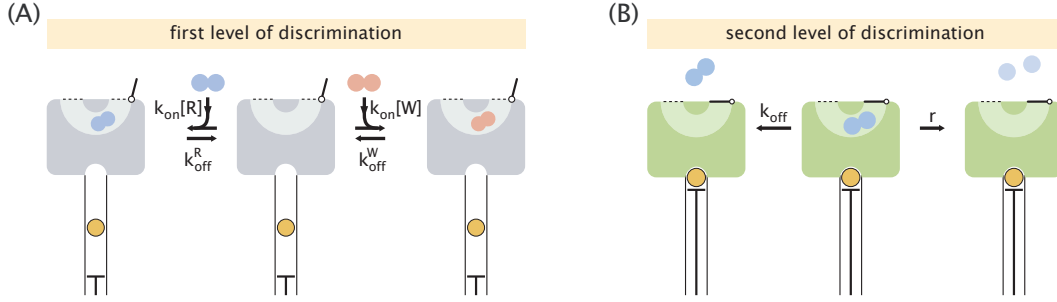


Figure S3.1: The two substrate discrimination levels in the conceptual scheme of the piston model. (A) The first level is achieved when the piston is expanded and a roughly equilibrium distribution of substrate–bound and free enzyme states is established. (B) The second level is achieved in the compressed state of the piston where the enzyme is active and can either release the bound substrate or turn it into a product.

state, the enzyme can no longer bind new substrates. If we wait long enough, a substrate that was already bound before piston compression will either unbind with a rate k_{off} or get turned into a product with a rate r . The probability that a product is formed can be written as

$$p_{\text{prod}} = \int_0^{\infty} dt' p_{\text{bound}}(t') \times r, \quad (\text{S3.4})$$

where $p_{\text{bound}}(t')$ is the probability that the substrate is still bound by time t' . Using the fact that the waiting time distribution of substrate release (either through unbinding or product formation) is $P_{\text{release}}(t) = (k_{\text{off}} + r)e^{-(k_{\text{off}}+r)t}$, the probability $p_{\text{bound}}(t)$ can be found as

$$p_{\text{bound}}(t) = \int_t^{\infty} dt' P_{\text{release}}(t') = e^{-(k_{\text{off}}+r)t}. \quad (\text{S3.5})$$

Substituting this result into Eq. S3.4 and performing the integration, we obtain

$$p_{\text{prod}} = \frac{r}{k_{\text{off}} + r}. \quad (\text{S3.6})$$

Due to the difference in the off-rates of the right and wrong substrates, their respective probabilities of production will also be different, resulting in the second level of fidelity given by the ratio of these probabilities, namely

$$\eta_2 = \frac{p_{\text{prod}}^{\text{R}}}{p_{\text{prod}}^{\text{W}}} = \frac{k_{\text{off}}^{\text{W}} + r}{k_{\text{off}}^{\text{R}} + r}. \quad (\text{S3.7})$$

S3.2 Ratchet and pawl engine

In this section, we first provide a detailed discussion of the ratchet and pawl mechanism in the absence of piston coupling. Then, for the case of piston coupling, we derive the expressions for the work per step ($\Delta W_{1/2}$) shown in Fig. 3.3 that take the ratio of piston state probabilities (π_d/π_u) and the net rate of backward stepping (k_{net}) to 50% of their respective saturation values.

S3.2.1 Details of the ratchet and pawl mechanism in the absence of piston coupling

The ratchet and pawl mechanism was originally proposed by Richard Feynman with an aim of demonstrating the validity of the second law of thermodynamics [1]. In his description, the mechanism had an additional element, namely vanes that were connected to the ratchet through a massless axle (Fig. S3.2A). The purpose of the vanes was to induce forward ratchet steps through thermal fluctuations. When the temperature in the vane compartment was maintained at a higher value than that in the ratchet compartment ($T_2 > T_1$), the mechanism could utilize this difference to operate as a heat engine and lift a weight hanging from the axle.

In the piston model, instead of running the ratchet and pawl mechanism as a heat engine, we drive it at a constant temperature through the expenditure of the gravitational potential energy of the hanging weight. We have therefore removed the vane compartment from our description of the engine and ascribed forward stepping to random rotational fluctuations of the ratchet instead (Fig. S3.2B).

As mentioned in section 3.4.1, backward stepping takes place whenever the pawl borrows sufficient energy from the environment to overcome the potential energy barrier E_0 of the spring and lift itself over the ratchet tooth that it is sitting on, allowing the tooth to slip under it (Fig. S3.2C). Once the pawl gets over the ratchet tooth (step 2 in Fig. S3.2C), the hanging weight and the recovering pawl start applying torque on the ratchet, causing it to rotate in the clockwise direction (step 3 in Fig. S3.2C). Following Feynman's treatment, we assume that when the pawl hits the bottom of the next tooth (step 4 in Fig. S3.2C), the total kinetic energy of the system, which is the sum of the energy borrowed by the pawl and the change in the potential energy of the weight per step ($\Delta W = mg\Delta z$), gets dissipated due to the perfectly inelastic collision of the pawl with the ratchet. Therefore, as a result of a single backward step, the net heat dissipated into the environment becomes ΔW , as reflected in the free energy landscape in Fig. S3.2E.

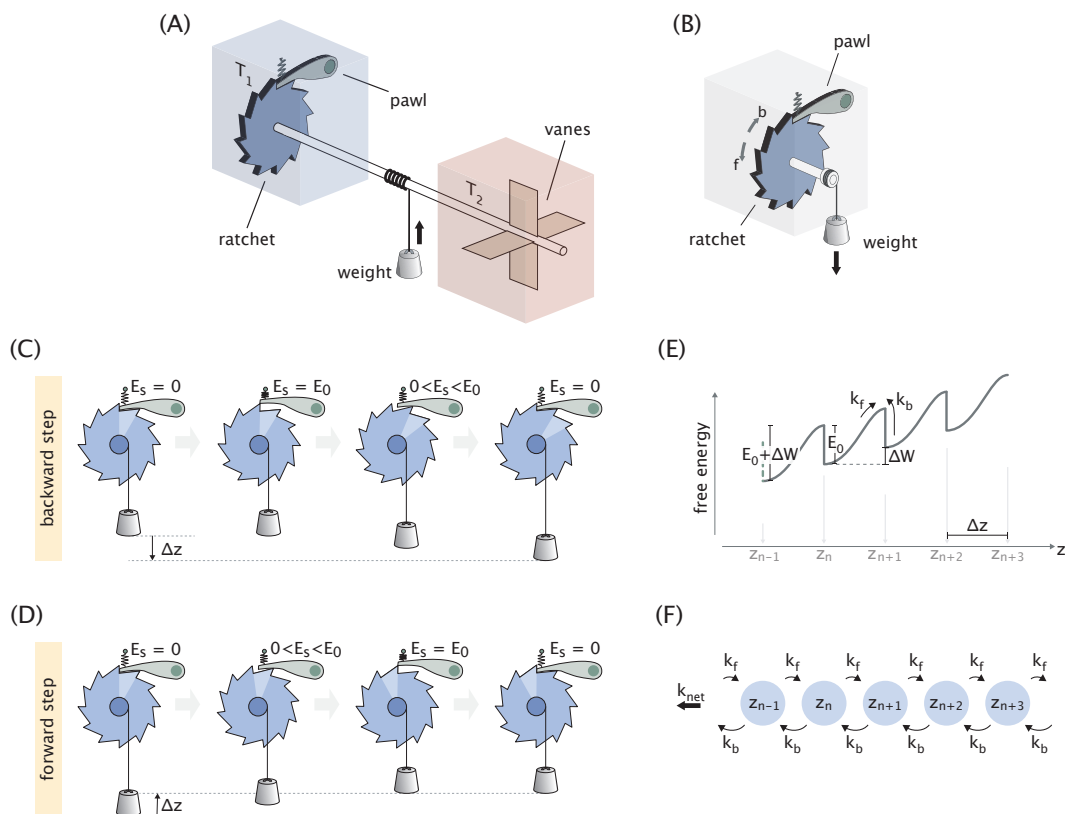


Figure S3.2: Working details of the ratchet and pawl mechanism. (A) Feynman's original ratchet and pawl mechanism operating as a heat engine [1]. (B) Ratchet and pawl engine driven by a hanging weight that is used in the piston model. Arrows with symbols "b" and "f" indicate the directions of backward and forward ratchet rotation, respectively. (C)-(D) Breakdown of backward (C) and forward (D) steps of the ratchet, accompanied by the lowering or the lifting of the weight, respectively. E_s stands for the potential energy of the spring. (E) Free energy landscape corresponding to the directionally biased rotations of the ratchet due to a net lowering of the weight. Discrete positions of the weight (z_n) corresponding to the energy minima of the landscape are marked on the reaction coordinate. (F) Infinite chain representation of the discrete state dynamics. When a non-zero weight is hung from the axle, the ratchet makes backward steps with a net rate k_{net} .

A similar set of arguments for forward stepping would imply that initially the mechanism needs to borrow enough energy from the environment to overcome the spring barrier and to lift the weight by an amount of Δz (step 3 in Fig. S3.2D). We again assume, that once the pawl passes over the next tooth and inelastically hits the ratchet, it dissipates all its accumulated potential energy. Therefore, in the end of a single forward step, the total energy extracted from the environment is equal to the increase in the potential energy of the weight per forward step (Fig. S3.2E).

Implicit in our treatment of ratchet stepping has been the assumption that we could discretize the possible configurations of the mechanism into states where the pawl fully rests on ratchet teeth. Within this formalism, we took E_0 to be the activation energy of backward stepping and $(E_0 + \Delta W)$ to be the activation energy of forward stepping, resulting in rate constants given by

$$k_b = \tau^{-1} e^{-\beta E_0}, \quad (\text{S3.8})$$

$$k_f = \tau^{-1} e^{-\beta(E_0 + \Delta W)}, \quad (\text{S3.9})$$

where τ^{-1} is the attempt frequency. The choice of identical attempt frequencies for forward and backward steps is, in a way, a requirement in the discretization formalism to ensure that in the absence of driving ($\Delta W = 0$) no net rotation of the ratchet is generated, since $k_{\text{net}} = k_b - k_f$ (Fig. S3.2F). We note that a more rigorous treatment of ratchet stepping kinetics would need to account for the precise shape of the energy landscape, defined both by the position of the weight (equivalently, the ratchet angle) and the angular position of the fluctuating pawl, similar to the analysis done by Magnasco and Stolovitzky [2].

S3.2.2 Derivation of $\Delta W_{1/2}$ expressions

We begin by deriving the $\Delta W_{1/2}$ expression at which the ratio π_d/π_u is 1/2. From Eqs. 3.12 and 3.13, this ratio, evaluated at $\Delta W_{1/2}$, can be written as

$$\left. \frac{\pi_d}{\pi_u} \right|_{\Delta W_{1/2}} = \frac{1 + e^{-\beta(\Delta W_{1/2} + \Delta F)}}{1 + e^{-\beta(\Delta W_{1/2} - \Delta F)}} = \frac{1}{2}. \quad (\text{S3.10})$$

Solving for $\Delta W_{1/2}$, we obtain

$$\begin{aligned} \Delta W_{1/2} &= \Delta F + \ln \left(1 + e^{-2\beta\Delta F} \right) \\ &= \Delta F + \ln \left(1 + f^{-2} \right), \end{aligned} \quad (\text{S3.11})$$

where in the last step, we used the expression for the ligand free energy change written in terms of the compression factor, that is, $\Delta F = \beta^{-1} \ln f$. Since for efficient proofreading the compression factor needs to be large ($f \gg 1$), the $\Delta W_{1/2}$ expression reduces into

$$\Delta W_{1/2} \approx \Delta F. \quad (\text{S3.12})$$

To estimate how much the work per step needs to exceed ΔF in order for the ratio π_d/π_u to reach its saturation value of 1, we calculate the derivative of the ratio at

$\Delta W_{1/2} \approx \Delta F$, namely

$$\begin{aligned} \left. \frac{\partial}{\partial \Delta W} \left(\frac{\pi_d}{\pi_u} \right) \right|_{\Delta W_{1/2}} &= \frac{-\beta e^{-\beta(\Delta W_{1/2} + \Delta F)} (1 + e^{-\beta(\Delta W_{1/2} - \Delta F)}) + (1 + e^{-\beta(\Delta W_{1/2} + \Delta F)}) \beta e^{-\beta(\Delta W_{1/2} - \Delta F)}}{(1 + e^{-\beta(\Delta W_{1/2} - \Delta F)})^2} \\ &= \frac{\beta(1 - e^{-2\beta\Delta F})}{4} \\ &\approx \frac{1}{4k_B T}, \end{aligned} \quad (\text{S3.13})$$

where we again employed the $e^{-2\beta\Delta F} \ll 1$ approximation. These results indicate that in order to overcome the equilibrium bias in piston state probabilities caused by the higher ligand entropy in the expanded state, the work per step needs to exceed the ligand free energy change upon compression (ΔF) by several $k_B T$ values.

Now, we perform a similar set of calculations for the net rate of backward stepping (k_{net}). Using its expression in Eq. 3.14, we obtain

$$k_{\text{net}}|_{\Delta W_{1/2}} = \frac{(1 - e^{-2\beta\Delta W_{1/2}}) k_b}{1 + \cosh(\beta\Delta F) e^{-\beta\Delta W_{1/2}}} = \frac{k_b}{2}. \quad (\text{S3.14})$$

Rearranging the terms, we obtain a quadratic equation for $e^{\beta\Delta W_{1/2}}$, namely

$$e^{2\beta\Delta W_{1/2}} - \cosh(\beta\Delta F) e^{\beta\Delta W_{1/2}} - 2 = 0. \quad (\text{S3.15})$$

Since $e^{\beta\Delta W_{1/2}} > 0$, we take the positive solution and obtain

$$e^{\beta\Delta W_{1/2}} = \frac{\cosh(\beta\Delta F) + \sqrt{\cosh^2(\beta\Delta F) + 8}}{2}. \quad (\text{S3.16})$$

For large degrees of compression ($e^{\beta\Delta F} \gg 1$), we can make the approximation $\cosh(\beta\Delta F) \approx e^{\beta\Delta F}/2$ and ignore the constant term in the square root, which yields

$$e^{\beta\Delta W_{1/2}} \approx \frac{e^{\beta\Delta F}}{2}, \quad (\text{S3.17})$$

$$\Delta W_{1/2} \approx \Delta F - \beta^{-1} \ln 2. \quad (\text{S3.18})$$

Like in the treatment of the ratio π_d/π_u , we now estimate how much the work per step needs to exceed $\Delta W_{1/2}$ in order for the backward stepping rate (k_{net}) to reach its saturating value k_b . To that end, we calculate the derivative of k_{net}/k_b at $\Delta W_{1/2}$, namely

$$\begin{aligned} \left. \frac{\partial}{\partial \Delta W} \left(\frac{k_{\text{net}}}{k_b} \right) \right|_{\Delta W_{1/2}} &= \frac{2\beta e^{-2\beta\Delta W_{1/2}} (1 + \cosh(\beta\Delta F) e^{-\beta\Delta W_{1/2}}) + (1 - e^{-2\beta\Delta W_{1/2}}) \cosh(\Delta F) \beta e^{-\beta\Delta W_{1/2}}}{(1 + \cosh(\beta\Delta F) e^{-\beta\Delta W_{1/2}})^2} \\ &\approx \frac{2\beta e^{-2\beta\Delta W_{1/2}} (1 + \frac{1}{2} e^{\beta\Delta F} e^{-\beta\Delta W_{1/2}}) + (1 - e^{-2\beta\Delta W_{1/2}}) \frac{1}{2} e^{\beta\Delta F} \beta e^{-\beta\Delta W_{1/2}}}{(1 + \frac{1}{2} e^{\beta\Delta F} e^{-\beta\Delta W_{1/2}})^2} \end{aligned}$$

$$\begin{aligned}
&= \frac{4\beta e^{-2\beta\Delta W_{1/2}} + \beta(1 - e^{-2\beta\Delta W_{1/2}})}{4} \\
&\approx \frac{1}{4k_{\text{B}}T}.
\end{aligned} \tag{S3.19}$$

Here we made the approximation $\cosh(\Delta F) \approx e^{\beta\Delta F}/2$ in the first step, used the result from Eq. S3.17 to write $\frac{1}{2}e^{\beta\Delta F}e^{-\beta\Delta W_{1/2}} = 1$ in the second step, and in the last step ignored the $e^{-2\beta\Delta W_{1/2}}$ terms since from Eq. S3.17, we have $e^{-2\beta\Delta W_{1/2}} = 4e^{-2\beta\Delta F} \ll 1$ for large degrees of compression.

As we can see, when the work per step exceeds ΔF by several $k_{\text{B}}T$ values, the chances of forward stepping become vanishingly small compared with backward stepping, resulting in a net backward stepping rate $k_{\text{net}} \approx k_{\text{b}}$.

S3.3 Equilibrium properties of the allosteric enzyme

In this section, we introduce the constraints on the choices of rate constants for the enzyme stemming from the cycle condition (based on the fact that it does not consume energy), and also, discuss the fidelity available to it when the ligand concentration is held at a fixed value.

S3.3.1 Constraints on the choice of enzyme's rate constants

Consider the network of enzyme states and transitions in the absence of engine coupling redrawn in Fig. S3.3A for convenience. Because the transitions between the states of the enzyme are not coupled to external energy consuming processes, the choice of the rate constants is constrained by the cycle condition which states that the products of rate constants in the clockwise and counterclockwise directions should be equal to each other in all the loops of the network diagram [3]. Imposing the cycle condition results in the constraint equations for the different loops shown in Fig. S3.3B. In our analysis, we choose substrate unbinding to be the only process whose rate is different between right and wrong substrates ($k_{\text{off}}^{\text{W}} > k_{\text{off}}^{\text{R}}$). Therefore, the rate constants of all other identical processes are chosen to be the same between the substrates, i.e.,

$$k_{\text{A}}^{\text{R}} = k_{\text{A}}^{\text{W}} \equiv k_{\text{A}}^{\text{S}}, \tag{S3.20}$$

$$k_{\text{I}}^{\text{R}} = k_{\text{I}}^{\text{W}} \equiv k_{\text{I}}^{\text{S}}, \tag{S3.21}$$

$$k_{\text{A}}^{\text{R,L}} = k_{\text{A}}^{\text{W,L}} \equiv k_{\text{A}}^{\text{S,L}}, \tag{S3.22}$$

$$k_{\text{I}}^{\text{R,L}} = k_{\text{I}}^{\text{W,L}} \equiv k_{\text{I}}^{\text{S,L}}, \tag{S3.23}$$

where the superscript ‘‘S’’ stands for both right (‘‘R’’) and wrong (‘‘W’’) substrates. Using this general notation, we write the full set of constraint conditions on the rate

constants obtained from the different loops (mid, front, and back) as

$$\text{mid: } \frac{k_I^L}{k_A^L} = \frac{\ell_{\text{off}}^A / \ell_{\text{on}}^A}{\ell_{\text{on}}^I / \ell_{\text{off}}^I} \frac{k_I}{k_A}, \quad (\text{S3.24})$$

$$\text{front: } \frac{k_I^S}{k_A^S} = \frac{k_{\text{on}}^I}{k_{\text{on}}^A} \frac{k_I}{k_A}, \quad (\text{S3.25})$$

$$\text{back: } \frac{k_I^{S,L}}{k_A^{S,L}} = \frac{k_{\text{on}}^I}{k_{\text{on}}^A} \frac{k_I^L}{k_A^L}. \quad (\text{S3.26})$$

Note that the conditions imposed on the side loops follow directly from those of the other three loops via

$$\text{side} = \frac{\text{mid} \times \text{back}}{\text{front}}, \quad (\text{S3.27})$$

which is why the side loops do not contribute a unique condition.

When writing the cycle conditions, we did not include the product formation rate constant r , despite the fact that production takes the enzyme into its substrate-free state, just like what unbinding through k_{off} reactions does. The reason for this is that r is an effective rate constant for the process $\text{E:S} \xrightarrow{r} \text{E} + \text{P}$ representing the coarse-grained version of the full biochemical pathway of enzymatic production, namely $\text{E:S} \rightleftharpoons \text{E:P} \rightleftharpoons \text{E} + \text{P}$, which is distinct from the k_{off} pathway of emptying the enzyme. In our treatment, we assume that product formation is practically irreversible which will be true if the product concentration is kept low and, optionally, if the reverse reaction $\text{P} \longrightarrow \text{S}$ is energetically highly unfavorable (e.g., requires a spontaneous formation of a covalent bond).

If the product formation rate is nonzero ($r > 0$), the enzyme will be out of equilibrium despite the fact that its individual transitions are not coupled to an energy source. This is due to the implicit assumption of having the right and wrong substrate concentrations fixed, which makes the system open (i.e., new substrates enter and products exit the system). We discuss the implications of this open system feature on the fidelity of the enzyme in the absence of driving in the next section.

S3.3.2 Enzyme fidelity at a fixed ligand concentration

As mentioned in the previous section, the presence of a nonzero production rate ($r > 0$) makes the system open and thereby takes the enzyme out of equilibrium even at a fixed ligand concentration where the engine-enzyme coupling is absent. For Hopfield's scheme, it can be shown that in an analogous situation where driving

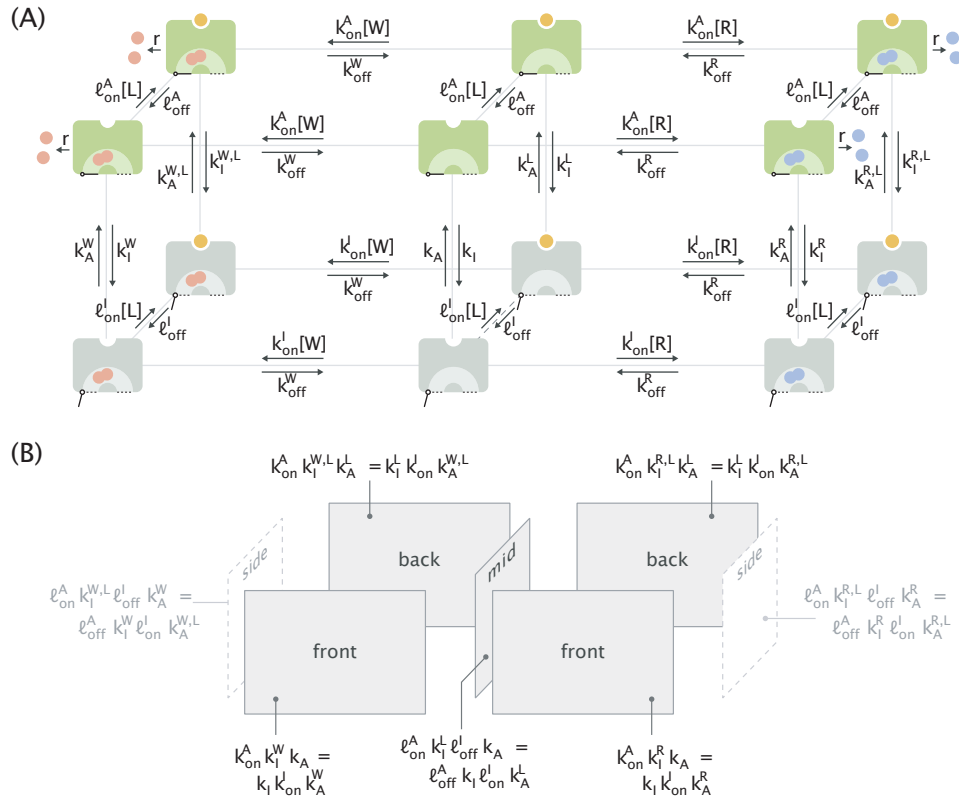


Figure S3.3: The allosteric enzyme in the absence of engine coupling. (A) Network diagram of enzyme states and transitions between them at a fixed ligand concentration. The diagram is redrawn identically from Fig. 3.4 for convenience. (B) Cycle condition on rate constants applied for the different loops of the diagram. The lighter color of the side loop conditions indicates that they are redundant and follow from the conditions on the other three loops.

is absent but the system is open, the “equilibrium” (un-driven) fidelity is confined in a range defined by the ratio of the Michaelis and dissociation constants, which, for equal on-rates ($k_{on}^R = k_{on}^W$), becomes

$$\eta_{eq} \in \left[\frac{k_{off}^W + r}{k_{off}^R + r}, \frac{k_{off}^W}{k_{off}^R} \right]. \quad (S3.28)$$

We hypothesize that the same holds true for the allosteric enzyme as well despite the much wider diversity of states available to it. To demonstrate that, we first consider the limiting $r \rightarrow 0$ case where the product formation is so slow that the system effectively exists in a thermodynamic equilibrium. All possible enzyme states along with their statistical weights in this equilibrium setting are shown in Fig. S3.4. Fidelity can be found by adding the statistical weights of the right and

wrong substrate-bound active states and dividing them, yielding

$$\eta_{\text{eq}}(r \rightarrow 0) = \frac{[\text{R}]}{[\text{W}]} \frac{K_D^{\text{W,A}}}{K_D^{\text{R,A}}} = \frac{k_{\text{off}}^{\text{W}}}{k_{\text{off}}^{\text{R}}}, \quad (\text{S3.29})$$

where we used $[\text{R}] = [\text{W}]$ and the equal on-rate assumption to go from dissociation constants to unbinding rates. This corresponds to the upper limit in Eq. S3.28.













state	weight	state	weight	state	weight
	$\frac{[\text{W}]}{K_D^{\text{W,A}}} e^{-\epsilon_A}$		$e^{-\epsilon_A}$		$\frac{[\text{R}]}{K_D^{\text{R,A}}} e^{-\epsilon_A}$
	$\frac{[\text{W}]}{K_D^{\text{W,I}}} e^{-\epsilon_I}$		$e^{-\epsilon_I}$		$\frac{[\text{R}]}{K_D^{\text{R,I}}} e^{-\epsilon_I}$
	$\frac{[\text{L}]}{R_D^{\text{A}}} \frac{[\text{W}]}{K_D^{\text{W,A}}} e^{-\epsilon_A}$		$\frac{[\text{L}]}{R_D^{\text{A}}} e^{-\epsilon_A}$		$\frac{[\text{L}]}{R_D^{\text{A}}} \frac{[\text{R}]}{K_D^{\text{R,A}}} e^{-\epsilon_A}$
	$\frac{[\text{L}]}{R_D^{\text{I}}} \frac{[\text{W}]}{K_D^{\text{W,I}}} e^{-\epsilon_I}$		$\frac{[\text{L}]}{R_D^{\text{I}}} e^{-\epsilon_I}$		$\frac{[\text{L}]}{R_D^{\text{I}}} \frac{[\text{R}]}{K_D^{\text{R,I}}} e^{-\epsilon_I}$
$\left(1 + \frac{[\text{L}]}{R_D^{\text{A}}}\right) \frac{[\text{W}]}{K_D^{\text{W,A}}} e^{-\epsilon_A}$				$\left(1 + \frac{[\text{L}]}{R_D^{\text{A}}}\right) \frac{[\text{R}]}{K_D^{\text{R,A}}} e^{-\epsilon_A}$	

Figure S3.4: Table of possible enzyme states and their statistical weights in the $r \rightarrow 0$ limit where the system is effectively at equilibrium. Here ϵ_A and ϵ_I stand for the energies of the enzyme in its active and inactive states, respectively. The dissociation constants of the ligand and the substrates are denoted by R_D and K_D , respectively.

Intuitively, the presence of a nonzero production rate ($r > 0$) should reduce the fidelity since the enzyme would have less time to perform substrate filtering in its active state before product formation takes place. To study how large this reduction can be, let us first consider a limiting case where the enzyme is exclusively in its active state – a setting where we expect the reduction effect to be manifested the most. The active “slice” of the full network diagram corresponding to this limiting case is depicted in Fig. S3.5A. Since product formation is just another path to substrate unbinding, we can derive a corresponding reduced network diagram by adding the production rate to the off-rates, as shown in Fig. S3.5B.

A peculiar feature of this network is that the cycle condition holds in its two loops, despite the fact that the system is open ($r > 0$). This means that at steady state, the detailed balance condition will hold on all edges of the network (cf. Schnakenberg

[4], section X), allowing us to assign effective statistical mechanical weights to the different states (Fig. S3.5C).

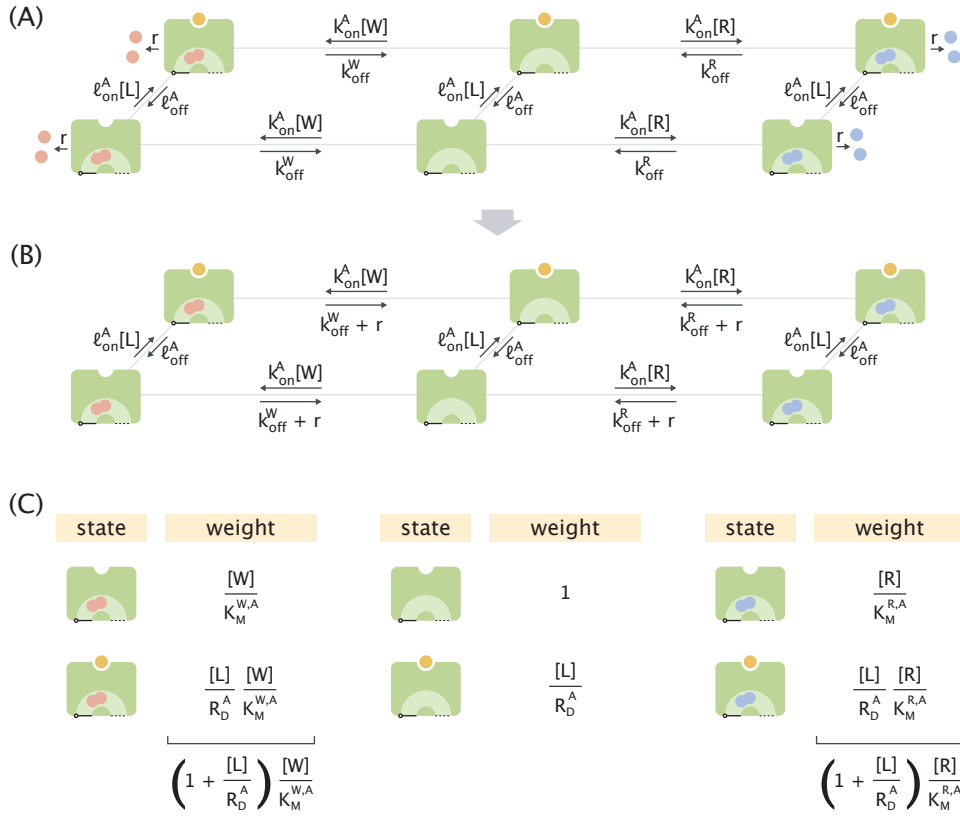


Figure S3.5: The enzyme in the limit of constant activity and in the absence of engine coupling. (A) The active “slice” of the enzyme’s full network diagram depicted in Fig. S3.3A. (B) The reduced diagram corresponding to the network in panel A with the production and off-rates combined under the same reaction arrow. (C) Table of the different enzyme states and their effective statistical weights. K_M stands for the Michaelis constant. Total weights of the wrong and right substrate–bound states are shown below the left and right columns, respectively.

Dividing the total weights of the right and wrong substrate–bound states, we obtain the fidelity in this special limit where the enzyme is exclusively in its active state, namely

$$\eta_{\text{eq}}^{\text{active}}(r > 0) = \frac{[R]}{[W]} \frac{K_M^{W,A}}{K_M^{R,A}} = \frac{k_{\text{off}}^W + r}{k_{\text{off}}^R + r}. \quad (\text{S3.30})$$

Here we again used $[R] = [W]$ and the equal on-rate assumption. Note that this corresponds to the lower fidelity limit in the un-driven Hopfield model (Eq. S3.28).

We now hypothesize that the enzyme’s fidelity falls between these two limits in the general case where the system is open ($r > 0$) and when the states are not constrained to be in the active “slice” of the full network diagram. Since obtaining the exact expression of fidelity in the general case is highly complicated due to the presence of a large number of states and loops in the network diagram, and since a paper-and-pencil approach where the symmetries existing between the left and right “wings” of the network could potentially be taken advantage of to provide an analytical proof is also not straightforward, we use a numerical method instead to justify our hypothesis.

To that end, we fixed the ratio of the wrong and right substrate off-rates to be $k_{\text{off}}^{\text{W}}/k_{\text{off}}^{\text{R}} = 100$, sampled values for enzyme’s remaining transition rate constants from the $[10^{-4}k_{\text{off}}^{\text{R}}, 10^4k_{\text{off}}^{\text{R}}]$ range (generating 20,971,520 independent sets in total), and evaluated the fidelity for each parameter set. The results of the numerical study are summarized in Fig. S3.6. As can be seen, despite the wider diversity of allosteric enzyme’s states, its fidelity in the absence of engine coupling still falls between the “equilibrium” limits of Hopfield’s model (Eq. S3.28).

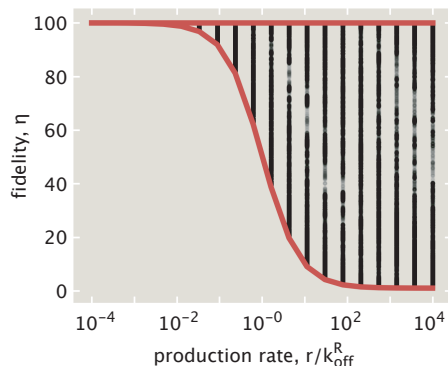


Figure S3.6: Allosteric enzyme’s fidelity in the absence of engine coupling (fixed [L]) for different choices of transition rates. The upper and lower red curves correspond to the ratios of the dissociation (Eq. S3.29) and Michaelis constants (Eq. S3.30), respectively. Only the data points with fidelity values different up to the third significant digit were used in the plot.

S3.4 Full description of the piston model with engine–enzyme coupling

In this section, we provide details on the analytical and numerical explorations of the full model. In section S3.4.1, we discuss the thermodynamics of coupling the engine to the allosteric enzyme. Then, in section S3.4.2, we present the methodology for obtaining the steady state probabilities of system states under external drive. In

sections S3.4.3 and S3.4.4, we provide the parameters used in the numerical study of main section 3.3 and describe the fidelity optimization strategy used in study of the main section 3.4, respectively. Lastly, in section S3.4.5, we investigate in detail the $\alpha_{\max} \approx 3$ result for the highest fidelity of the model.

S3.4.1 Equilibrium fidelity of the piston model in the absence of external driving

In Appendix S3.3.2, we showed that at a fixed ligand concentration the fidelity of the allosteric enzyme was constrained within the range given in Eq. S3.28. Here we demonstrate that the same result holds also for the full model in the absence of external driving when a thermodynamically consistent coupling is made between the engine and the enzyme.

In the absence of driving, the finite–state equivalent of the full network (Fig. 3.5D) can be reduced into the one shown in Fig. S3.7 where we have combined the ratchet transitions through forward and backward pathways under a single arrow – a procedure allowed when the transitions are not driven [5]. Because of the equilibrium constraints imposed on the enzyme’s transition rates discussed in Appendix section S3.3.1, the cycle condition will hold for the loops in the left and right “layers” of the diagram in Fig. S3.7. The loops where the cycle condition could possibly be violated are the ones that involve transitions between the two layers, i.e., piston compressions and expansions.

The first class of such loops does not involve ligand binding and unbinding events (e.g., the shaded vertical rectangle in Fig. S3.7), and therefore, the cycle condition is automatically satisfied in such loops since for each clockwise transition there is a corresponding counterclockwise transition with an identical rate. The second class of loops that connect the two layers involves ligand binding and unbinding events which affect the rate of switching between the layers (e.g., the shaded horizontal rectangle in Fig. S3.7). The driving force in these loops is given by

$$\Delta\mu = \beta^{-1} \ln \frac{(k_f^{u \rightarrow d} + k_b)(k_f^{d \rightarrow u, L} + k_b)[L]_d}{(k_f^{d \rightarrow u} + k_b)(k_f^{u \rightarrow d, L} + k_b)[L]_u}, \quad (\text{S3.31})$$

where we used the fact that the ligand binding rates are proportional to ligand concentrations. Now, in the general case where there are N ligands under the piston (one of which can be bound to the enzyme), the different forward stepping rates become

$$k_f^{u \rightarrow d} = k_b e^{-\beta(\Delta W_{\text{eq}} + \beta^{-1} N \ln f)} = k_b f^{-N}, \quad (\text{S3.32})$$

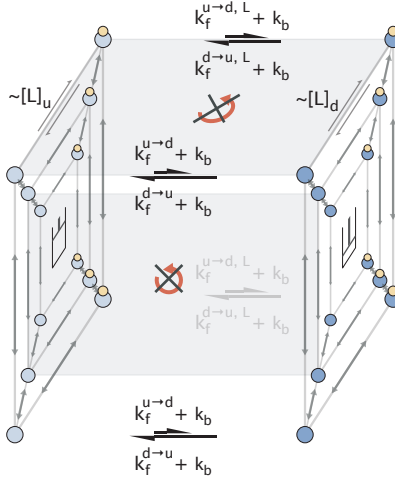


Figure S3.7: The effective network diagram of the piston model in the absence of driving. The forward and backward pathways connecting the two layers of the diagram are combined to yield effective rates. The two kinds of cycles where ligand binding events are present or absent are shown as horizontal and vertical shaded rectangles, respectively. The crossed cycling arrows indicate the absence of driving forces in the shaded loops.

$$k_f^{u \rightarrow d, L} = k_b e^{-\beta(\Delta W_{\text{eq}} + \beta^{-1}(N-1) \ln f)} = k_b f^{-(N-1)}, \quad (\text{S3.33})$$

$$k_f^{d \rightarrow u} = k_b e^{-\beta(\Delta W_{\text{eq}} - \beta^{-1} N \ln f)} = k_b f^N, \quad (\text{S3.34})$$

$$k_f^{d \rightarrow u, L} = k_b e^{-\beta(\Delta W_{\text{eq}} - \beta^{-1}(N-1) \ln f)} = k_b f^{N-1}. \quad (\text{S3.35})$$

Here we set $\Delta W_{\text{eq}} = 0$ to account for the absence of driving and used the fact that the free energy change of N ligands upon isothermal compression is $\beta^{-1} N \ln f$ (with a negative sign upon expansion) and that N should be replaced with $N - 1$ when one of the ligands is bound to the enzyme.

Substituting these expressions into Eq. S3.31 and using the identity $[L]_d = f[L]_u$, we find

$$\begin{aligned} \Delta\mu &= \beta^{-1} \ln \frac{(f^{-N} + 1)(f^{N-1} + 1)f}{(f^N + 1)(f^{1-N} + 1)} \\ &= \beta^{-1} \ln \left(\frac{f^{-N}(1 + f^N)}{f^N + 1} \times \frac{f^{N-1}(1 + f^{1-N})}{f^{1-N} + 1} \times f \right) \\ &= \beta^{-1} \ln (f^{-N} \times f^{N-1} \times f) = \beta^{-1} \ln 1 = 0. \end{aligned} \quad (\text{S3.36})$$

This shows that in the absence of external driving ($\Delta W = 0$) the cycle condition holds for all loops of the network, demonstrating the thermodynamic consistency of the coupling between the engine and the enzyme.

As in our separate treatment of the allosteric enzyme in Appendix S3.3.2, here too in the $r \rightarrow 0$ limit, the system will approach a thermodynamic equilibrium. Since we already know that in the equilibrium limit the fidelity of the enzyme at a fixed ligand concentration is given by the ratio of the wrong and right off-rates, we can apply this result to the left and right layers of the diagram in Fig. S3.7 and obtain a relation between the net statistical weights of the right and wrong substrate-bound active states, namely

$$\frac{w_u^R}{w_u^W} = \frac{w_d^R}{w_d^W} = \frac{k_{\text{off}}^W}{k_{\text{off}}^R}. \quad (\text{S3.37})$$

Here “u” and “d” stand for the expanded (left layer) and compressed (right layer) states of the piston. We can then write the fidelity of the full network in terms of these weights as

$$\eta_{\text{eq}}(r \rightarrow 0) = \frac{w_u^R + w_d^R}{w_u^W + w_d^W} = \frac{w_u^W \left(\frac{k_{\text{off}}^W}{k_{\text{off}}^R} \right) + w_d^W \left(\frac{k_{\text{off}}^W}{k_{\text{off}}^R} \right)}{w_u^W + w_d^W} = \frac{k_{\text{off}}^W}{k_{\text{off}}^R}, \quad (\text{S3.38})$$

which corresponds to the upper limit of the equilibrium fidelity range in Eq. S3.28.

To demonstrate that in the absence of driving the coupled system meets also the lower fidelity limit given by $(k_{\text{off}}^W + r)/(k_{\text{off}}^R + r)$, we again use a numerical approach and sample the parameter space, evaluating the fidelity at each of the 10,628,820 sampled sets of parameters. As in the study of Fig. S3.7, here too we set the ratio of off-rates to be $k_{\text{off}}^W/k_{\text{off}}^R = 100$. The results are summarized in Fig. S3.8, where it can be seen that all points lie between the limits of Eq. S3.28. Overall, this study shows that in the absence of driving, the coupling of the engine to the enzyme alone cannot lead to fidelity enhancement.

S3.4.2 Obtaining the steady-state occupancy probabilities

The kinetics of the full piston model is characterized by a 24×24 transition rate matrix \mathbf{Q} , which has the block form

$$\mathbf{Q} = \begin{pmatrix} \mathbf{Q}_u^{\text{enzyme}} & \mathbf{Q}_{d \rightarrow u} \\ \mathbf{Q}_{u \rightarrow d} & \mathbf{Q}_d^{\text{enzyme}} \end{pmatrix}. \quad (\text{S3.39})$$

Here the non-diagonal elements of the 12×12 matrices $\mathbf{Q}_u^{\text{enzyme}}$ and $\mathbf{Q}_d^{\text{enzyme}}$ represent the transition rates between the different enzyme states when the ligand concentration is $[L] = [L]_u$ and $[L] = [L]_d$, respectively. These non-diagonal terms at a given ligand concentration $[L]$ are depicted in Fig. S3.9.

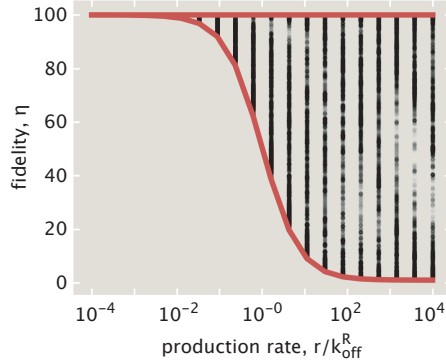


Figure S3.8: Fidelity of the full piston model in the absence of driving ($\Delta W = 0$) for different choices of model parameters. The upper and lower red curves correspond to the ratios of the dissociation (Eq. S3.29) and Michaelis constants (Eq. S3.30), respectively. Only the data points with fidelity values different up to the third significant digit were used in the plot.

The other two matrices, namely, $\mathbf{Q}_{d \rightarrow u}$ and $\mathbf{Q}_{u \rightarrow d}$, are diagonal whose elements stand for the net piston compression ($d \rightarrow u$) and expansion ($u \rightarrow d$) rates that alter the piston state but leave the state of the enzyme unchanged. They are given by

$$\mathbf{Q}_{d \rightarrow u} = \text{diag} \left(\underbrace{(k_b + k_f^{d \rightarrow u}), \dots, (k_b + k_f^{d \rightarrow u})}_{6 \text{ terms}}, \underbrace{(k_b + k_f^{d \rightarrow u, L}), \dots, (k_b + k_f^{d \rightarrow u, L})}_{6 \text{ terms}} \right), \quad (\text{S3.40})$$

$$\mathbf{Q}_{u \rightarrow d} = \text{diag} \left(\underbrace{(k_b + k_f^{u \rightarrow d}), \dots, (k_b + k_f^{u \rightarrow d})}_{6 \text{ terms}}, \underbrace{(k_b + k_f^{u \rightarrow d, L}), \dots, (k_b + k_f^{u \rightarrow d, L})}_{6 \text{ terms}} \right). \quad (\text{S3.41})$$

Note that since the forward stepping rates depend on whether the ligand is bound or not, they appear without a superscript “L” in the first 6 terms (where the ligand is unbound), and with a superscript “L” in the last 6 terms (where the ligand is bound). Lastly, the diagonal elements of \mathbf{Q} are assigned such that $Q_{jj} = -\sum_{i \neq j} Q_{ij}$, ensuring that the columns sum to zero.

The dynamics of the coupled engine–enzyme system is described via

$$\frac{d\vec{p}}{dt} = \mathbf{Q}\vec{p}, \quad (\text{S3.42})$$

where \vec{p} is a column vector whose 24 elements stand for the probabilities of the different system states (12 enzyme states \times 2 piston states). We are interested in the steady state behavior of the piston model, where $d\vec{p}/dt = \vec{0}$. Since the

k_A	$k_{\text{off}}^R + r$	0	$k_{\text{off}}^W + r$	0	e_{off}^A	0	0	0	0	0	0
k_i		0	k_{off}^R	0	k_{off}^W	0	e_{off}^l	0	0	0	0
$k_{\text{on}}^A[\text{R}]$	0		k_A^R	0	0	0	0	e_{off}^A	0	0	0
0	$k_{\text{on}}^l[\text{R}]$	k_i^R		0	0	0	0	0	e_{off}^l	0	0
$k_{\text{on}}^A[\text{W}]$	0	0	0		k_A^W	0	0	0	0	e_{off}^A	0
0	$k_{\text{on}}^l[\text{W}]$	0	0	k_i^W		0	0	0	0	0	e_{off}^l
$e_{\text{on}}^A[\text{L}]$	0	0	0	0	0		k_A^L	$k_{\text{off}}^R + r$	0	$k_{\text{off}}^W + r$	0
0	$e_{\text{on}}^l[\text{L}]$	0	0	0	0	k_i^L		0	k_{off}^R	0	k_{off}^W
0	0	$e_{\text{on}}^A[\text{L}]$	0	0	0	$k_{\text{on}}^A[\text{R}]$	0		$k_A^{R,L}$	0	0
0	0	0	$e_{\text{on}}^l[\text{L}]$	0	0	0	$k_{\text{on}}^l[\text{R}]$	$k_i^{R,L}$		0	0
0	0	0	0	$e_{\text{on}}^A[\text{L}]$	0	$k_{\text{on}}^A[\text{W}]$	0	0	0		$k_A^{W,L}$
0	0	0	0	0	$e_{\text{on}}^l[\text{L}]$	0	$k_{\text{on}}^l[\text{W}]$	0	0	$k_i^{W,L}$	

Figure S3.9: Transition rates between the enzyme states. The element $Q_{i,j}^{\text{enzyme}}$ stands for the rate of transitioning from the j^{th} into the i^{th} state of the enzyme ($i \neq j$) at a fixed ligand concentration $[L]$. Red- and blue-colored cells show transitions involving the binding or release of incorrect and correct substrates, respectively. Green- and gray-colored cells show inactivating and activating enzyme transitions, respectively. The diagonals are shaded to indicate that they are not used when constructing \mathbf{Q} .

exact analytical expression for the steady state probability vector $\vec{p}_{\text{ss}} \equiv \vec{\pi}$ is highly convoluted, in our parametric studies we use numerical methods to find $\vec{\pi}$ from $\mathbf{Q}\vec{\pi} = \vec{0}$ and $\sum_i \pi_i = 1$, where the latter equation guarantees that the probabilities sum to 1.

S3.4.3 Enzyme's kinetic parameters used for the numerical study in the main section 3.4

Here we provide the list of enzyme's transition rates used for numerically studying the effects of tuning the engine “knobs” in section 3.4. Since none of the performance

metrics used in the study depend on the absolute timescale of the model's dynamics, we set the unbinding rate of the right substrate to be unity ($k_{\text{off}}^{\text{R}} = 1$), and defined all other rates relative to it. Specifically, we chose $k_{\text{off}}^{\text{W}} = 100$ so that the fidelity after a single proofreading realization roughly matched that of the ribosome ($\eta_{\text{translation}} \sim 10^4$) [6]. Also, we chose the catalysis rate to be much slower compared with the off-rates ($r = 0.2$) – a condition for high fidelity suggested in Hopfield's original paper.

The remaining rate constants were assigned values that meet the intuitive expectations from the conceptual introduction of the model in section 2. Specifically, the rate of substrate binding to the active enzyme was chosen to be much less than the rate of binding to the inactive enzyme in order to yield low leakiness ($k_{\text{on}}^{\text{A}}/k_{\text{on}}^{\text{I}} = 10^{-5} \ll 1$). Next, the enzyme was chosen to be predominantly inactive in its native state to allow for new substrate binding events ($k_{\text{I}}/k_{\text{A}} = 50 \gg 1$). Lastly, the rates of ligand binding and unbinding were assigned values that ensure that the ligand acts as a strong activator ($\frac{\ell_{\text{off}}^{\text{I}}/\ell_{\text{on}}^{\text{I}}}{\ell_{\text{off}}^{\text{A}}/\ell_{\text{on}}^{\text{A}}} = 10^6 \gg 1$).

The values of the independent parameters k_{A}^{L} and k_{A}^{S} were assigned after manually inspecting the effect of different numerical choices on the model performance. Finally, the values of the remaining four parameters (lower section in Table S3.1) were calculated from the cycle conditions in Eqs. S3.24-S3.26 under the assumption that ligand binding does not alter the ratio of inactivation or activation rates in the substrate-bound and substrate-unbound states (i.e., $k_{\text{I}}^{\text{S,L}}/k_{\text{I}}^{\text{L}} = k_{\text{I}}^{\text{S}}/k_{\text{I}}$ and $k_{\text{A}}^{\text{S,L}}/k_{\text{A}}^{\text{L}} = k_{\text{A}}^{\text{S}}/k_{\text{A}}$).

S3.4.4 Details of the numerical optimization procedure for finding the highest fidelity

In our optimization scheme, we first chose the values of rates which were kept fixed for the rest of the study. These include the unbinding rate of right substrates ($k_{\text{off}}^{\text{R}} = 1$), the catalysis rate ($r = 0.2$), and the effective first-order rate of substrate binding to the inactive enzyme state ($k_{\text{on}}^{\text{I}}[\text{S}] = 1$). Also, since no limits were imposed on the amount of energy expenditure, we chose large values for the compression factor ($f = 10^{100}$) and the work per step ($\Delta W = 1000 k_{\text{B}}T$) to maximize the quality of proofreading.

Then, we considered a set of 144 different initialization options for the remaining parameters to be used in our numerical optimization procedure. To avoid the completely independent tuning of related enzyme activation and inactivation rates,

Transition rate	Value
$k_{\text{off}}^{\text{R}}, k_{\text{off}}^{\text{W}}$	1, 100
r	0.2
$k_{\text{on}}^{\text{A}}[\text{S}]$	10^{-5}
$k_{\text{on}}^{\text{I}}[\text{S}]$	1
k_{A}	20
k_{I}	1000
$\ell_{\text{on}}^{\text{A}}$	0.1
$\ell_{\text{off}}^{\text{A}}$	5
$\ell_{\text{on}}^{\text{I}}$	0.01
$\ell_{\text{off}}^{\text{I}}$	500000
k_{A}^{L}	2000
k_{A}^{S}	0.01
k_{I}^{L}	0.1
k_{I}^{S}	50000
$k_{\text{A}}^{\text{S,L}}$	1
$k_{\text{I}}^{\text{S,L}}$	5

Table S3.1: Values of different transition rates used in the studies of Fig. 3.6.

we considered three possible options that met the cycle condition. Namely, 1) $k_{\text{A}}^{\text{S}} = k_{\text{A}}$ and $k_{\text{I}}^{\text{S}} = k_{\text{I}}/\gamma$, 2) $k_{\text{A}}^{\text{S}} = \sqrt{\gamma}k_{\text{A}}$ and $k_{\text{I}}^{\text{S}} = k_{\text{I}}/\sqrt{\gamma}$, 3) $k_{\text{A}}^{\text{S}} = \gamma k_{\text{A}}$ and $k_{\text{I}}^{\text{S}} = k_{\text{I}}$, where $\gamma = k_{\text{on}}^{\text{A}}/k_{\text{on}}^{\text{I}}$. All of these three options satisfy the cycle constraint $k_{\text{on}}^{\text{A}}k_{\text{I}}^{\text{S}}k_{\text{A}} = k_{\text{on}}^{\text{I}}k_{\text{A}}^{\text{S}}k_{\text{I}}$ (Fig. S3.3B). Options for the transition rates between ligand-bound enzyme states (i.e., $k_{\text{A}}^{\text{S,L}}$ and $k_{\text{I}}^{\text{S,L}}$) were chosen analogously.

In our custom-written maximization algorithm, we iteratively perturbed all the parameters for multiple rounds with decreasing amplitudes until the convergence criterion was met or until the number of iterations exceeded the specified threshold (at most 20 iterations for each of the 6 decreasing amplitudes). The results from each of these local maximization procedures are summarized in Fig. S3.10. We chose the largest among the different local maxima to represent the highest fidelity available for the given $(k_{\text{on}}^{\text{A}}, k_{\text{off}}^{\text{W}})$ pair.

S3.4.5 Investigation of the $\alpha_{\text{max}} \approx 3$ result for the highest available proof-reading index

Our numerical scheme for optimizing the fidelity (Appendix S3.4.4) revealed that the piston model could perform proofreading up to three times ($\alpha_{\text{max}} \approx 3$). To gain intuition on how this is possible, let us consider the wrong ‘‘wing’’ of the full reaction network (Fig. S3.11A). Each system state is characterized by the piston

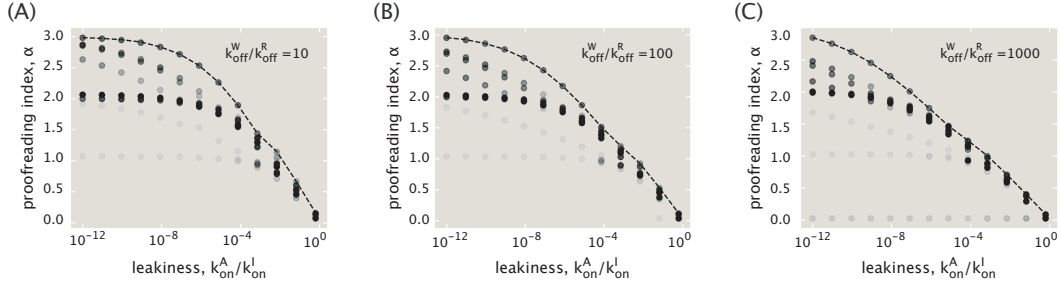


Figure S3.10: Fidelity optimization results for each of the 144 parameter initialization options. (A) $k_{\text{off}}^{\text{W}}/k_{\text{off}}^{\text{R}} = 10$. (B) $k_{\text{off}}^{\text{W}}/k_{\text{off}}^{\text{R}} = 100$. (C) $k_{\text{off}}^{\text{W}}/k_{\text{off}}^{\text{R}} = 1000$. The dotted lines in each panel represent the trends for the globally optimal fidelities.

position (up or down) and the state of the enzyme (one of 8 possibilities). To turn a wrong substrate into a product, the system needs to traverse a trajectory that starts at a substrate–unbound state on the right side of the diagram and reaches one of the substrate–bound active states on the left side, at which point catalysis can take place. Using the terminology introduced in Murugan *et al.*[7], we can say that a proofreading filter can be realized every time the system makes a transition parallel to the “discriminatory fence” of the network (Fig. S3.11A). Rates which are on either side of the fence do not discriminate between the two kinds of substrates; only those that cross the fence do, which in our case are the off-rates ($k_{\text{off}}^{\text{W}} > k_{\text{off}}^{\text{R}}$). Thus, the number of such parallel transitions that the system makes before reaching the catalytically active state represents the largest number of proofreading filters available to the given trajectory.

Fig. S3.11B shows the full list of unique trajectories that start on the right side of the network, cross the discriminatory fence, and eventually reach an active enzyme state after traversing through a series of inactive states. The trajectories are grouped by the number of these inactive states visited on the left side of the wing prior to reaching the active state. For example, entries of the first group represent trajectories where the substrate binds directly to the active enzyme and hence, undergoes zero proofreading filtrations. The discriminatory capacity of the piston model will therefore depend on which of the trajectories dominates in product formation.

To compare the contributions from different trajectories, we assign each of them a probability flux, which approximates the average rate of product formation through the trajectory. We define this flux via

$$J_{\vec{s}} = \pi_{s_0} k_{s_0 \rightarrow s_1} \left(\prod_{i=1}^{N-2} p_{s_i \rightarrow s_{i+1}} \right) P_{s_{N-1}}^{\text{cat}}, \quad (\text{S3.43})$$

where \vec{s} is the set of N states in the trajectory, $\pi_{s_0} k_{s_0 \rightarrow s_1}$ is the substrate binding flux that crosses the fence at the start of the trajectory, $p_{s_i, s_{i+1}}$ are the probabilities of staying on the trajectory during traversal, and, lastly, $p_{s_{N-1}}^{\text{cat}}$ is the probability of catalysis once the system has reached the active enzyme state s_{N-1} . Note that the flux expression does not account for backtracking events whose contribution we expect to be insignificant for efficient proofreading trajectories, since for them, $p_{s_i \rightarrow s_{i+1}} \ll 1$.

Having defined a flux metric for each trajectory, we then calculated its value for all trajectories listed in Fig. S3.11B in the case where $k_{\text{off}}^{\text{W}}/k_{\text{off}}^{\text{R}} = 100$ and $k_{\text{on}}^{\text{A}}/k_{\text{on}}^{\text{I}} = 10^{-12}$ (low leakiness). Fig. S3.11C shows the fluxes normalized by the highest one and grouped by the number of proofreading filters. As we can see, the dominant trajectory indeed contains three filters. This dominant trajectory is highlighted in red in Fig. S3.11B and also corresponds to the one shown in Fig. 3.7B of the main text.

We would like to note here that the model parameters inferred from the unconstrained fidelity optimization were degenerate, and there was an alternative set with $\alpha \approx 3$ proofreading index whose corresponding dominant trajectory was different from the one highlighted in Fig. S3.11B. Some of the parameters of this set, however, contradicted our model criteria (e.g., the binding rate in the expanded piston state was very high), which is why we did not use this alternative set for our main discussion. Parameters that did satisfy our model criteria are shown for the $k_{\text{off}}^{\text{W}}/k_{\text{off}}^{\text{R}} = 100$ case in Fig. S3.11D. The transition rates between intermediates are much slower compared with the off-rate, as expected for an efficient proofreading performance.

Lastly, as can be seen in Fig. S3.11B, the highest number of filters that a unique trajectory could, in principle, realize is 4 and not 3. This raises the question of why a trajectory with 4 potential filters cannot be a dominant one, as our numerical results in Fig. S3.11C have suggested. We answer this question for three representative cases and invite the reader to work through the remaining examples. Our approach will be to show that the flux through a given 4-filter trajectory is necessarily less than that of some other trajectory with fewer filters, which would suggest that it cannot be a dominant one.

Fig. S3.12 shows three different 4-filter trajectories next to corresponding trajectories with fewer filters, flux through which, as we will show, will necessarily be greater. Throughout our analysis, we will be making use of the fact that the rates of piston expansion and compression are identical (and equal to k_b) in the large driving limit

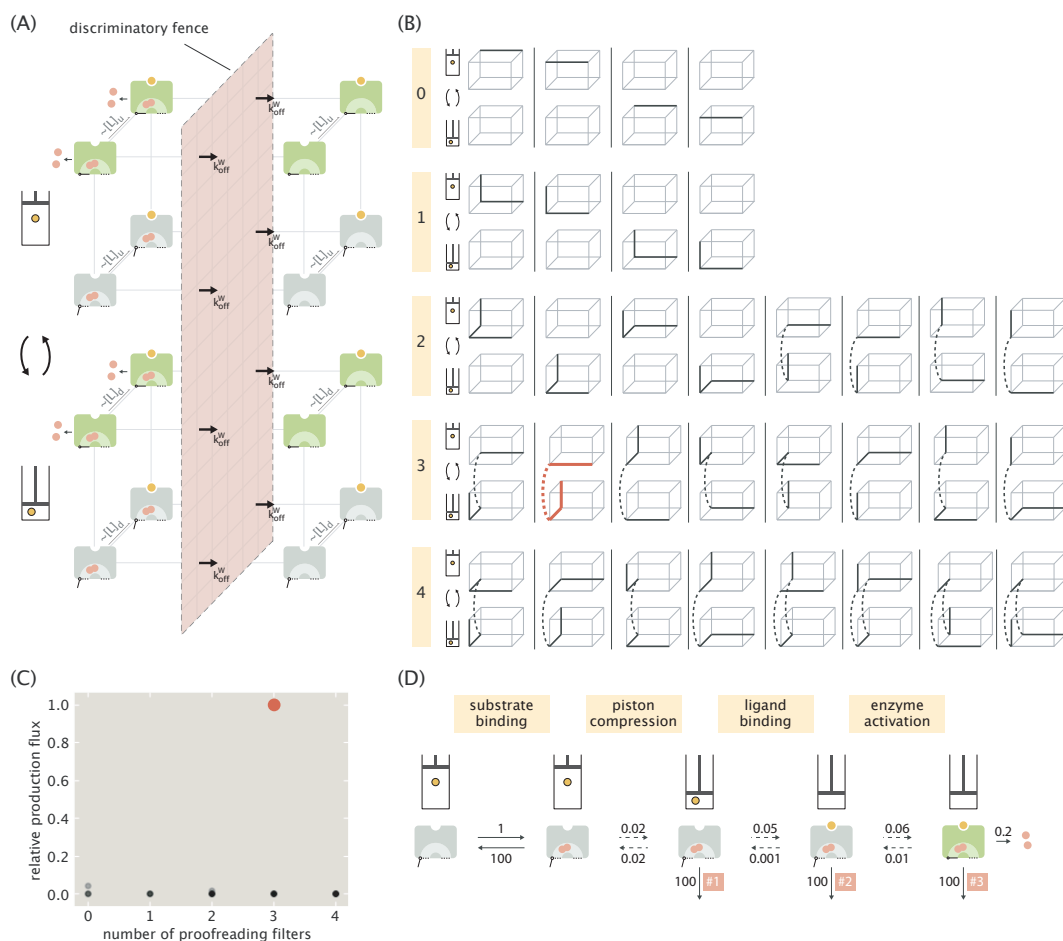


Figure S3.11: Determination of α_{\max} using a trajectory approach. (A) The wrong “wing” of the full reaction network along with the discriminatory fence. Ligand concentrations that enter the ligand binding rates are shown to indicate the difference between the upper and lower halves of the diagram. (B) The full set of unique trajectories that start on the right side of the network and end up at an active enzyme state on the left side. Numbers of proofreading filters available to trajectories are shown on the side. Piston state transitions are marked with dotted lines for clarity. The dominant trajectory in panel C is highlighted in red. (C) The relative product formation fluxes of all possible trajectories calculated for the case where $k_{\text{off}}^W/k_{\text{off}}^R = 100$ and $k_{\text{on}}^A/k_{\text{on}}^I = 10^{-12}$, and grouped by the number of filters. The red dot indicates the dominant one. (D) Schematic illustration of the dominant trajectory in panel C along with the numerical values of the rates. The dotted arrows suggest that the intermediate transitions are much slower than the off-rate.

considered here. Let us start from the first example. Using Eq. S3.43, we can write the fluxes through 4-filter ($J_{(4)}$) and 3-filter ($J_{(3)}$) trajectories, respectively, as

$$J_{(4)} = \pi_0 k_{0 \rightarrow 1} \times p_{1 \rightarrow 2} p_{2 \rightarrow 3} p_{3 \rightarrow 4} p_{4 \rightarrow 5} \times p_5^{\text{cat}}, \quad (\text{S3.44})$$

$$J_{(3)} = \pi_0 k_{0 \rightarrow 1} \times p_{1 \rightarrow 2} p_{2 \rightarrow 3} p_{3 \rightarrow 6} \times p_6^{\text{cat}}. \quad (\text{S3.45})$$

Since the states (3) and (4) correspond to the same enzyme state and have identical outgoing rates, we have $p_{4 \rightarrow 5} = p_{3 \rightarrow 6}$. From the same argument for states (5) and (6), we find $p_5^{\text{cat}} = p_6^{\text{cat}}$. With these identities at hand, we can write the ratio of the two fluxes as

$$\frac{J_{(4)}}{J_{(3)}} = p_{3 \rightarrow 4} < 1. \quad (\text{S3.46})$$

Therefore, the 4-filter trajectory is necessarily slower than the 3-filter one and cannot dominate the dynamics of wrong product formation.

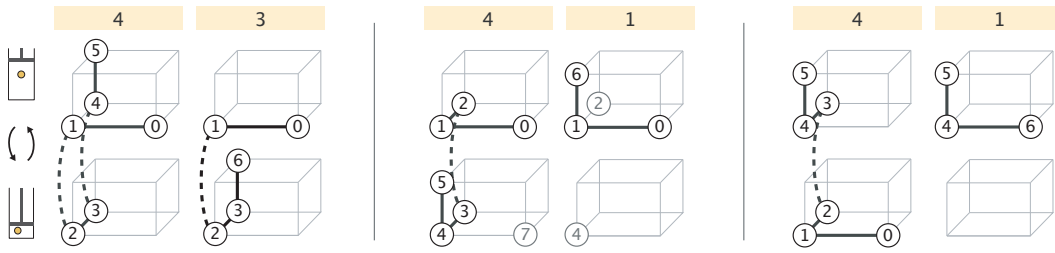


Figure S3.12: Three representative 4-filter trajectories paired with ones which have a lower filter number and, necessarily, a higher product formation flux. The state indices are added to facilitate the comparison between the corresponding trajectories.

Now let us look at the slightly more complicated second example. There the fluxes of the 4-filter and 1-filter trajectories are

$$J_{(4)} = \pi_0 k_{0 \rightarrow 1} \times p_{1 \rightarrow 2} p_{2 \rightarrow 3} p_{3 \rightarrow 4} p_{4 \rightarrow 5} \times p_5^{\text{cat}}, \quad (\text{S3.47})$$

$$J_{(1)} = \pi_0 k_{0 \rightarrow 1} \times p_{1 \rightarrow 6} \times p_6^{\text{cat}}, \quad (\text{S3.48})$$

respectively. The full expression of the transition probability $p_{4 \rightarrow 5}$ is

$$p_{4 \rightarrow 5} = \frac{k_{4 \rightarrow 5}}{k_{4 \rightarrow 5} + k_{4 \rightarrow 3} + k_{4 \rightarrow 1} + k_{4 \rightarrow 7}}. \quad (\text{S3.49})$$

Similarly, the expression for $p_{1 \rightarrow 6}$ is

$$p_{1 \rightarrow 6} = \frac{k_{1 \rightarrow 6}}{k_{1 \rightarrow 6} + k_{1 \rightarrow 2} + k_{1 \rightarrow 4} + k_{1 \rightarrow 0}}. \quad (\text{S3.50})$$

All corresponding rates in the above probability expressions are equal to each other (i.e., $k_{4 \rightarrow 5} = k_{1 \rightarrow 6} = k_A^S$, $k_{4 \rightarrow 1} = k_{1 \rightarrow 4} = k_b$, $k_{4 \rightarrow 7} = k_{1 \rightarrow 0} = k_{\text{off}}^W$), with the exception of $k_{4 \rightarrow 3} = \ell_{\text{on}}^l[\text{L}]_d$ and $k_{1 \rightarrow 2} = \ell_{\text{on}}^l[\text{L}]_u$. Now, since $[\text{L}]_d > [\text{L}]_u$, we

obtain $p_{4 \rightarrow 5} < p_{1 \rightarrow 6}$. With an identical reasoning, we can also find that $p_5^{\text{cat}} < p_6^{\text{cat}}$. Therefore, the ratio of the 4-filter and 1-filter trajectory fluxes becomes

$$\frac{J_{(4)}}{J_{(1)}} = p_{1 \rightarrow 2} p_{2 \rightarrow 3} p_{3 \rightarrow 4} \underbrace{\left(\frac{p_{4 \rightarrow 5}}{p_{1 \rightarrow 6}} \right)}_{<1} \underbrace{\left(\frac{p_5^{\text{cat}}}{p_6^{\text{cat}}} \right)}_{<1} < 1, \quad (\text{S3.51})$$

proving our claim.

Lastly, we consider the third example in Fig. S3.12. We again start off by writing the trajectory fluxes, namely

$$J_{(4)} = \pi_0 k_{0 \rightarrow 1} \times p_{1 \rightarrow 2} p_{2 \rightarrow 3} p_{3 \rightarrow 4} p_{4 \rightarrow 5} \times p_5^{\text{cat}}, \quad (\text{S3.52})$$

$$J_{(1)} = \pi_6 k_{6 \rightarrow 4} \times p_{4 \rightarrow 5} \times p_5^{\text{cat}}. \quad (\text{S3.53})$$

The two rates appearing in the flux expression represent the substrate binding rate and are equal to each other, that is, $k_{0 \rightarrow 1} = k_{6 \rightarrow 4} = k_{\text{on}}^{\text{I}}[\text{S}]$. Now, note that π_6 is the steady state probability of the inactive ligand–unbound enzyme state at a low ligand concentration, whereas π_0 is the probability of the same enzyme state at a high ligand concentration. Since these are ligand–unbound states, the one in the presence of a lower ligand concentration will have a higher probability, i.e., $\pi_6 > \pi_0$. Thus, taking the ratio of the two fluxes, we obtain

$$\frac{J_{(4)}}{J_{(1)}} = \underbrace{\left(\frac{\pi_0}{\pi_6} \right)}_{<1} p_{1 \rightarrow 2} p_{2 \rightarrow 3} p_{3 \rightarrow 4} < 1, \quad (\text{S3.54})$$

suggesting that the 4-filter trajectory in the third example also cannot be the dominant one.

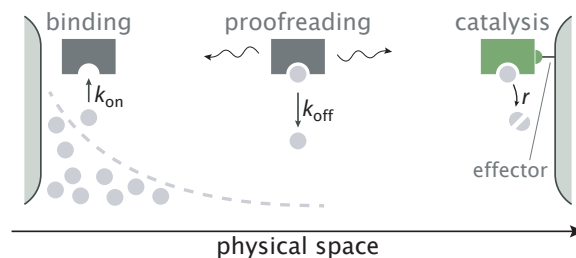
References

1. Feynman, R. P., Leighton, R. B. & Sands, M. *The Feynman Lectures on Physics* (Addison-Wesley, Reading, MA, 1963).
2. Magnasco, M. O. & Stolovitzky, G. Feynman’s ratchet and pawl. *J. Stat. Phys.* **93**, 615–632 (1998).
3. Hill, T. L. *Free Energy Transduction in Biology* (Academic Press, New York, NY, 1977).
4. Schnakenberg, J. Network theory of microscopic and macroscopic behavior of master equation systems. *Rev. Mod. Phys.* **48**, 571 (1976).

5. Horowitz, J. M., Zhou, K. & England, J. L. Minimum energetic cost to maintain a target nonequilibrium state. *Phys. Rev. E* **95**, 042102 (2017).
6. Hopfield, J. J. Kinetic proofreading: A new mechanism for reducing errors in biosynthetic processes requiring high specificity. *Proc. Natl. Acad. Sci. U.S.A.* **71**, 4135–4139 (1974).
7. Murugan, A., Huse, D. A. & Leibler, S. Discriminatory proofreading regimes in nonequilibrium systems. *Phys. Rev. X* **4**, 021016 (2014).

Chapter 4

PROOFREADING THROUGH SPATIAL GRADIENTS



This chapter is based on the journal publication Galstyan, V., Husain, K., Xiao, F., Murugan, A. & Phillips, R. Proofreading through spatial gradients. *eLife* 9:e60415 (2020). DOI: 10.7554/eLife.60415

4.1 Abstract

Key enzymatic processes use the nonequilibrium error correction mechanism called kinetic proofreading to enhance their specificity. The applicability of traditional proofreading schemes, however, is limited since they typically require dedicated structural features in the enzyme, such as a nucleotide hydrolysis site or multiple intermediate conformations. Here, we explore an alternative conceptual mechanism that achieves error correction by having substrate binding and subsequent product formation occur at distinct physical locations. The time taken by the enzyme-substrate complex to diffuse from one location to another is leveraged to discard wrong substrates. This mechanism does not have the typical structural requirements, making it easier to overlook in experiments. We discuss how the length scales of molecular gradients dictate proofreading performance, and quantify the limitations imposed by realistic diffusion and reaction rates. Our work broadens the applicability of kinetic proofreading and sets the stage for studying spatial gradients as a possible route to specificity.

4.2 Introduction

The nonequilibrium mechanism called kinetic proofreading [1, 2] is used for reducing the error rates of many biochemical processes important for cell function (e.g., DNA replication [3], transcription [4], translation [5, 6], signal transduction [7], or pathogen recognition [8–10]). Proofreading mechanisms operate by inducing

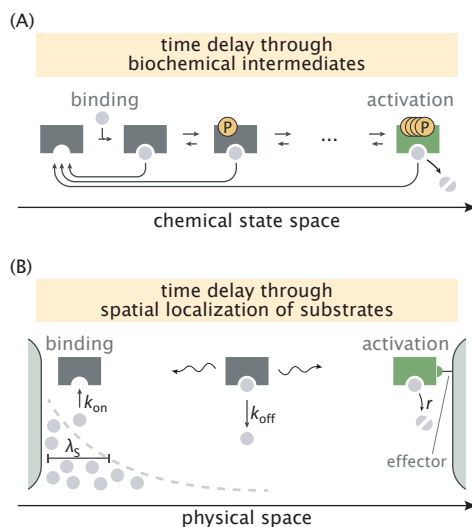


Figure 4.1: Error correction schemes that operate by delaying product formation. (A) The traditional proofreading scheme with multiple biochemically distinct intermediates, transitions between which are typically accompanied by energy-consuming reactions. The T-cell activation mechanism with successive phosphorylation events is used for demonstration [8, 10]. (B) The spatial proofreading scheme where the delay between binding and catalysis is created by constraining these events to distinct physical locations. The wavy arrows stand for the diffusive motion of the complex. Binding events primarily take place on the length scale λ_s of substrate localization.

a delay between substrate binding and product formation via intermediate states for the enzyme–substrate complex. Such a delay gives the enzyme multiple chances to release the wrong substrate after initial binding, allowing far lower error rates than what one would expect solely from the binding energy difference between right and wrong substrates.

Traditional proofreading schemes require dedicated molecular features such as an exonuclease pocket in DNA polymerases [3] or multiple phosphorylation sites on T-cell receptors [8, 9]; such features create intermediate states that delay product formation (Fig. 4.1A) and thus allow proofreading. Additionally, since proofreading is an active nonequilibrium process often involving near-irreversible reactions, the enzyme typically needs to have an ATP or GTP hydrolysis site to enable the use of energy supplies of the cell [5, 11]. Due to such stringent structural requirements, the number of confirmed proofreading enzymes is relatively small. Furthermore, generic enzymes without such dedicated features are assumed to not have active error correction available to them.

In this work, we propose an alternative scheme where the delay between initial substrate binding and product formation steps is achieved by separating these events in space. If substrates are spatially localized and product formation is favorable only in a region of low substrate concentration where an activating effector is present, then the time taken by the enzyme–substrate complex to travel from one location to the other can be used to discard the wrong substrates, which are assumed to unbind from the enzyme more readily than the right substrates (Fig. 4.1B). When this delay is longer than substrate unbinding time scales, very low error rates of product formation can be achieved, allowing this spatial proofreading scheme to outperform biochemical mechanisms with a finite number of proofreading steps.

In contrast to traditional proofreading, the nonequilibrium mechanism here does not require any direct energy consumption by the enzyme or substrate itself (e.g., through ATP hydrolysis). This liberates the enzyme from any proofreading–specific molecular features; indeed, any ‘equilibrium’ enzyme with a localized effector can proofread using our scheme if appropriate concentration gradients of the substrates or enzymes are set up. In this way, the energetic and structural requirements of proofreading can be outsourced from the enzyme and substrate to the gradient maintaining mechanism. It also means that spatial proofreading is easy to overlook in experiments, and that the fidelity of reconstituted reactions *in vitro* could be lower than the fidelity *in vivo*.

The lack of reliance on structure makes spatial proofreading more adaptable. We study how tuning the length scale of concentration gradients can trade off error rate against speed and energy consumption on the fly. In contrast, traditional proofreading schemes rely on nucleotide chemical potentials, e.g., the out of equilibrium [ATP]/[ADP] ratio in the cell, and cannot modulate their operation without broader physiological disruptions.

Our proposed scheme can be leveraged for specificity if appropriate concentration gradients are set. Such gradients arise in multiple cellular contexts (e.g., near the nucleus, the plasma membrane, the Golgi apparatus, the endoplasmic reticulum (ER), kinetochores, microtubules [12–14]), and several gradient–forming mechanisms have been discussed in the literature [14–16]. We conclude our analysis of spatial proofreading by quantifying its limitations as set by realistic reaction rates and gradient formation mechanisms, and discuss examples from the literature, including the localization of mRNAs in polarised cells, and the non-vesicular transport of lipids in eukaryotic cells, in which this mechanism might be in play. Our work

motivates a detailed investigation of spatial structures and compartmentalization in living cells as possible delay mechanisms for proofreading enzymatic reactions.

4.3 Results

4.3.1 Slow transport of enzymatic complex enables proofreading

Our proposed scheme is based on spatially separating substrate binding and product formation events for the enzyme (Fig. 1B). Such a setting arises naturally if substrates are spatially localized by having concentration gradients in a cellular compartment. Similarly, an effector needed for product formation (e.g., through allosteric activation) may have a spatial concentration gradient localized elsewhere in that compartment. To keep our model simple, we assume that the right (R) and wrong (W) substrates have identical concentration gradients of length scale λ_s but that the effector is entirely localized to one end of the compartment, e.g., via membrane tethering.

We model our system using coupled reaction–diffusion equations for the substrate–bound (“ES” with $S = R, W$) and free (“E”) enzyme densities, namely

$$\frac{\partial \rho_{ER}}{\partial t} = D \frac{\partial^2 \rho_{ER}}{\partial x^2} - k_{\text{off}}^R \rho_{ER} + k_{\text{on}} \rho_R \rho_E, \quad (4.1)$$

$$\frac{\partial \rho_{EW}}{\partial t} = D \frac{\partial^2 \rho_{EW}}{\partial x^2} - k_{\text{off}}^W \rho_{EW} + k_{\text{on}} \rho_W \rho_E, \quad (4.2)$$

$$\frac{\partial \rho_E}{\partial t} = D \frac{\partial^2 \rho_E}{\partial x^2} + \sum_{S=R,W} k_{\text{off}}^S \rho_{ES} - \sum_{S=R,W} k_{\text{on}} \rho_S \rho_E. \quad (4.3)$$

Here, D is the enzyme diffusion constant, k_{on} and k_{off}^S (with $k_{\text{off}}^W > k_{\text{off}}^R$) are the substrate binding and unbinding rates, respectively, and $\rho_S(x) \sim e^{-x/\lambda_s}$ is the spatially localized substrate concentration profile which we take to be exponentially decaying, which is often the case for profiles created by cellular gradient formation mechanisms [17, 18]. We limit our discussion to this one-dimensional setting of the system, though our treatment can be generalized to two and three dimensions in a straightforward way.

The above model does not explicitly account for several effects relevant to living cells, such as depletion of substrates or distinct diffusion rates for the free and substrate–bound enzymes. More importantly, it does not account for the mechanism of substrate gradient formation. We analyze a biochemically detailed model with this latter feature and experimentally constrained parameters later in the paper. Here, we proceed with the minimal model above for explanatory purposes. To identify the

key determinants of the model's performance, we assume throughout our analysis that the amount of substrates is sufficiently low that the enzymes are mostly free with a roughly uniform profile (i.e., $\rho_E \approx \text{constant}$). This assumption makes Eqs. (4.1)-(4.3) linear and allows us to solve them analytically at steady state. We demonstrate in Appendix S4.5 that proofreading is, in fact, most effective under this assumption and discuss the consequences of having high substrate amounts on the performance of the scheme.

In our simplified picture, enzyme activation and catalysis take place upon reaching the right boundary at a rate r that is identical for both substrates. Therefore, the density of substrate-bound enzymes at the right boundary can be taken as a proxy for the rate of product formation v_S , since

$$v_S = r\rho_{ES}(L), \quad (4.4)$$

where L is the size of the compartment. In order to keep the analytical results concise and intuitive, we perform our main analyses under the assumption that catalysis is slow, mirroring the study of traditional proofreading schemes [1]. In Appendix S4.3, we derive the precise conditions under which this treatment is valid, and generalize our analysis to arbitrary catalysis rates.

To demonstrate the proofreading capacity of the model, we first analyze the limiting case where substrates are localized to the left end of the compartment ($\lambda_s \rightarrow 0$). In this limit, the fidelity η , defined as the number of right products formed per single wrong product, becomes

$$\eta = \frac{v_R}{v_W} = \sqrt{\eta_{\text{eq}}} \frac{\sinh\left(\sqrt{\tau_D k_{\text{off}}^W}\right)}{\sinh\left(\sqrt{\tau_D k_{\text{off}}^R}\right)}, \quad (4.5)$$

where $\eta_{\text{eq}} = k_{\text{off}}^W/k_{\text{off}}^R$ is the equilibrium fidelity, and $\tau_D = L^2/D$ is the characteristic time scale of diffusion across the compartment (see Appendix S4.1 for the derivation).

Eq. 4.5 is plotted in Fig. 4.2 for a family of different parameter values. As can be seen, when diffusion is fast (small τ_D), fidelity converges to its equilibrium value and proofreading is lost ($\eta \approx \sqrt{\eta_{\text{eq}}} \times \sqrt{\tau_D k_{\text{off}}^W/\tau_D k_{\text{off}}^R} = \eta_{\text{eq}}$). Conversely, when diffusion is slow (large τ_D), the enzyme undergoes multiple rounds of binding a substrate at the left end and unbinding midway until it manages to diffuse across the whole compartment as a complex and form a product. These rounds serve as 'futile cycles'

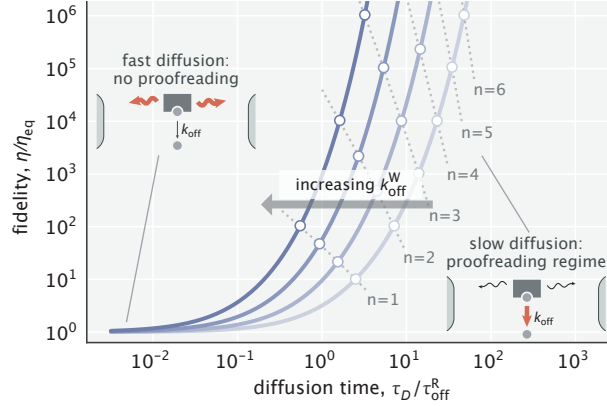


Figure 4.2: Dependence of fidelity on the diffusion time scale in the limit of very high substrate localization. Individual curves were made for different choices of $k_{\text{off}}^{\text{W}}$ (varied in the $[10 - 100] k_{\text{off}}^{\text{R}}$ range). $\tau_{\text{off}}^{\text{R}} = 1/k_{\text{off}}^{\text{R}}$ is the unbinding time scale of right substrates, kept fixed in the study. Fidelity values corresponding to integer degrees of proofreading in a traditional sense ($\eta/\eta_{\text{eq}} = \eta_{\text{eq}}^n$, $n = 1, 2, 3, \dots$) are marked as circles. Dominant processes in the two limiting regimes are highlighted in red in the schematics shown as insets.

that endow the system with proofreading. In this regime, fidelity scales as

$$\eta \sim e^{\left(\sqrt{k_{\text{off}}^{\text{W}}} - \sqrt{k_{\text{off}}^{\text{R}}}\right)\sqrt{\tau_D}}. \quad (4.6)$$

To get further insights, we introduce an effective number of extra biochemical intermediates (n) that a traditional proofreading scheme would need to have in order to yield the same fidelity, i.e., $\eta/\eta_{\text{eq}} = \eta_{\text{eq}}^n$. We calculate this number as (see Appendix S4.1)

$$n \approx \frac{\sqrt{\tau_D k_{\text{off}}^{\text{W}}}}{\ln \eta_{\text{eq}}}. \quad (4.7)$$

Notably, since $\tau_D \sim L^2$, the result above suggests a linear relationship between the effective number of proofreading realizations and the compartment size ($n \sim L$). In addition, because the right-hand side of Eq. 4.7 is an increasing function of $k_{\text{off}}^{\text{W}}$, the proofreading efficiency of the scheme rises with larger differences in substrate off-rates (Fig. 4.2) – a feature that ‘hard-wired’ traditional proofreading schemes with a fixed number of proofreading steps lack.

4.3.2 Navigating the speed–fidelity trade-off

As is inherent to all proofreading schemes, the fidelity enhancement described earlier comes at a cost of reduced product formation speed. This reduction, in our

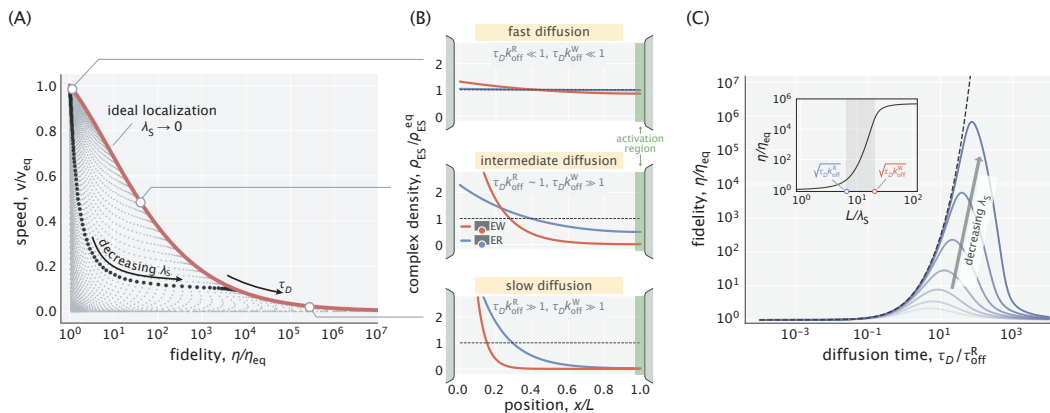


Figure 4.3: Speed–fidelity trade-off and consequences of having weak substrate gradients. (A) Speed and fidelity evaluated for sampled values of the diffusion time scale (τ_D) and substrate localization length scale (λ_s). Here, $v_{eq} \sim 1/k_{off}^R$ is the speed in the equilibrium limit of a uniform substrate profile ($\lambda_s \rightarrow \infty$). The red line corresponds to the Pareto–optimal front, and is reached in the high substrate localization limit. The example speed–fidelity trade-off illustrated through the black dotted curve is obtained for $\tau_D \approx 20 \tau_{off}^R$. (B) Density profiles of wrong (EW) and right (ER) complexes in three qualitatively different performance regimes. The normalization factor ρ_{ES}^{eq} corresponds to the equilibrium complex densities. (C) Fidelity as a function of diffusion time scale for different choices of λ_s (varied in the $[0.04, 0.4] L$ range). The dashed line corresponds to the ideal substrate localization limit ($\lambda_s \rightarrow 0$). Inset: Fidelity as a function of L/λ_s for a fixed τ_D . Shaded area indicates the range where the bulk of fidelity enhancement takes place. Equilibrium fidelity $\eta_{eq} = 10$ was used in generating all the panels.

case, happens because of increased delays in diffusive transport. Here, we explore the resulting speed–fidelity trade-off and its different regimes by varying two of the model parameters: diffusion time scale τ_D and the substrate localization length scale λ_s .

Speed and fidelity for different sampled values of τ_D and λ_s are depicted in Fig. 4.3A. As can be seen, for a fixed τ_D , the reduction of λ_s can trade off fidelity against speed. This trade-off is intuitive; with tighter substrate localization, the complexes are formed closer to the left boundary. Hence, a smaller fraction of complexes reach the activation region, reducing reaction speed. The Pareto–optimal front of the trade-off over the whole parameter space, shown as a red curve on the plot, is reached in the limit of ideal substrate localization ($\lambda_s \rightarrow 0$). Varying the diffusion time scale allows one to navigate this optimal trade-off curve and access different performance regimes.

Specifically, if the diffusion time scale is fast compared with the time scales of substrate unbinding (i.e., $\tau_D \ll 1/k_{\text{off}}^R, 1/k_{\text{off}}^W$), then both right and wrong complexes that form near the left boundary arrive at the activation region with high probability, resulting in high speeds, though at the expense of error-prone product formation (Fig. 4.3B, top). In the opposite limit of slow diffusion, both types of complexes have exponentially low densities at the activation region, but due to the difference in substrate off-rates, production is highly accurate (Fig. 4.3B, bottom). There also exists an intermediate regime where a significant fraction of right complexes reach the activation region while the vast majority of wrong complexes do not (Fig. 4.3B, middle). As a result, an advantageous trade-off is achieved where a moderate decrease in the production rate yields high fidelity enhancement – a feature that was also identified in multi-step traditional proofreading models [19].

In Appendix S4.3, we also study this trade-off caused by varying the catalysis rate r . Briefly, we find that when all other parameters are fixed, increasing r trades off fidelity against speed in a linear fashion, with the ratio of highest and lowest fidelity values falling in the $[\sqrt{\eta_{\text{eq}}}, \eta_{\text{eq}}]$ range. The Pareto-optimal front of the trade-off, however, monotonically shifts toward the higher speed region, suggesting that faster catalysis is, in fact, more favorable if the diffusion time scale τ_D can be adjusted accordingly (see Appendix S4.3 for details).

We saw in Fig. 4.3A that in the case of ideal substrate localization, the slowdown of diffusive transport necessarily reduced the production rate and increased the fidelity. The latter part of this statement, however, breaks down when substrate gradients are weak. Indeed, fidelity exhibits a non-monotonic response to tuning τ_D when the substrate gradient length scale λ_s is non-zero (Fig. 4.3C). The reason for the eventual decay in fidelity is the fact that with slower diffusion (larger τ_D), substrate binding and unbinding events take place more locally and therefore, the right and wrong complex profiles start to resemble the substrate profile itself, which does not discriminate between the two substrate kinds. We show in Appendix S4.1 that the optimal diffusion time scale can be roughly approximated as $\tau_D^*/\tau_{\text{off}}^R \approx \eta_{\text{eq}}^{-1}(L/\lambda_s)^2$, which increases monotonically with L/λ_s , consistent with the shifting peaks in Fig. 4.3C.

Not surprisingly, the error-correcting capacity of the scheme improves with better substrate localization (lower λ_s). For a fixed τ_D , the bulk of this improvement takes place when L/λ_s is tuned in a range set by the two key dimensionless numbers of the model, namely, $\sqrt{\tau_D k_{\text{off}}^R}$ and $\sqrt{\tau_D k_{\text{off}}^W}$ (Fig. 4.3C, inset). In Appendix S4.1, we

provide an analytical justification for this result. Taken together, these parametric studies uncover the operational principles of the spatial proofreading scheme and demonstrate how the speed–fidelity trade-off could be dynamically navigated as needed by tuning the key time and length scales of the model.

4.3.3 Energy dissipation and limits of proofreading performance

A hallmark signature of proofreading is that it is a nonequilibrium mechanism with an associated free energy cost. In our scheme, the enzyme itself is not directly involved in any energy-consuming reactions, such as hydrolysis. Instead, the free energy cost comes from maintaining the spatial gradient of substrates, which the enzymatic reaction tends to homogenize by releasing bound substrates in regions of low substrate concentration. As the activating effectors are assumed to be tethered at $x = L$, they do not require dissipation to remain localized.

While mechanisms of substrate gradient maintenance may differ in their energetic efficiency, there exists a thermodynamically dictated minimum energy that any such mechanism must dissipate per unit time. We calculate this minimum power P as

$$P = \sum_{S \in \{R,W\}} \int_0^L j_S(x) \mu(x) dx. \quad (4.8)$$

Here $j_S(x) = k_{\text{on}} \rho_S(x) \rho_E - k_{\text{off}}^S \rho_{ES}(x)$ is the net local binding flux of substrate “S”, and $\mu(x)$ is the local chemical potential (see Appendix S4.2.1 for details). For substrates with an exponentially decaying profile considered here, the chemical potential is given by

$$\mu(x) = \mu(0) + k_B T \ln \frac{\rho_S(x)}{\rho_S(0)} = \mu(0) - k_B T \frac{x}{\lambda_S}, \quad (4.9)$$

where $k_B T$ is the thermal energy scale. Notably, the chemical potential difference across the compartment, which serves as an effective driving force for the scheme, is set by the inverse of the nondimensionalized substrate localization length scale, namely

$$\beta \Delta \mu = \frac{L}{\lambda_S}, \quad (4.10)$$

where $\beta^{-1} = k_B T$. This driving force is zero for a uniform substrate profile ($\lambda_S \rightarrow \infty$) and increases with tighter localization (lower λ_S), as intuitively expected.

We used Eq. 4.8 to study the relationship between dissipation and fidelity enhancement as we tuned $\Delta \mu$ for different choices of the diffusion time scale τ_D . As can be seen

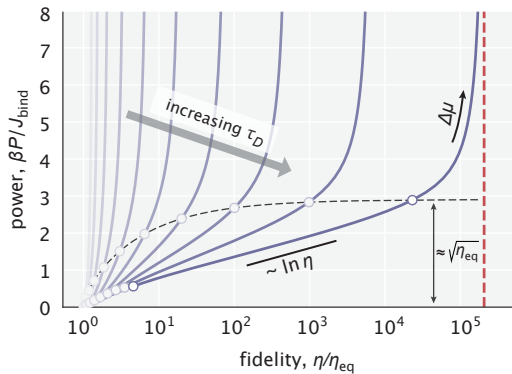


Figure 4.4: Power–fidelity relationship when tuning the effective driving force $\Delta\mu$ for different choices of the diffusion time scale τ_D . $J_{\text{bind}} = k_{\text{on}}\rho_E \int \rho_S(x) dx$ is the integrated rate of substrate binding. The red line indicates the large dissipation limit of fidelity given by Eq. 4.5. The circles indicate the $\Delta\mu$ range specified in Eq. 4.11 for different τ_D choices. For sufficiently large τ_D values, the cost per binding event approaches $\beta\sqrt{\eta_{\text{eq}}}$ at the end of this range (see Appendix S4.2.1 for details). In making this plot, $\eta_{\text{eq}} = 10$ was used.

in Fig. 4.4, power rises with increasing fidelity, diverging when fidelity reaches its asymptotic maximum given by Eq. 4.5 in the large $\Delta\mu$ limit. For the bulk of each curve, power scales as the logarithm of fidelity, suggesting that a linear increase in dissipation can yield an exponential reduction in error. Notably, such a scaling relationship has also been calculated in the context of *E. coli* chemoreceptor adaptation [20]. In particular, it was shown that the adaptation error decreases exponentially with energy dissipated through multiple methylation–demethylation cycles which are used to stabilize the activity state of the receptor. Analogies in the cost–performance trade-off across these functionally distinct mechanisms contribute to the search for overarching thermodynamic themes underlying cellular information processing [20–23].

The logarithmic scaling is achieved in our model when the driving force is in a range where most of the fidelity enhancement takes place, namely

$$\beta\Delta\mu \in \left[\sqrt{\tau_D k_{\text{off}}^{\text{R}}}, \sqrt{\tau_D k_{\text{off}}^{\text{W}}} \right]. \quad (4.11)$$

At the end of this range, the cost per substrate binding event approaches $\sqrt{\eta_{\text{eq}}}$ in $k_{\text{B}}T$ units (see Appendix S4.2.1 for details). Beyond the range, additional error correction is attained at an increasingly higher cost.

Note that the power computed here does not include the baseline cost of creating the substrate gradient, which, for instance, would depend on the substrate diffusion

constant. We only account for the additional cost to be paid due to the operation of the proofreading scheme which works to homogenize this substrate gradient. The baseline cost in our case is analogous to the work that ATP synthase needs to perform in order to maintain a nonequilibrium [ATP]/[ADP] ratio in the cell, whereas our calculated power is analogous to the rate of ATP hydrolysis by a traditional proofreading enzyme. We discuss the comparison between these two classes of dissipation in greater detail in Appendix S4.2.3.

Just as the cellular chemical potential of ATP or GTP imposes a thermodynamic upper bound on the fidelity enhancement by any proofreading mechanism [24], the effective driving force $\Delta\mu$ imposes a similar constraint for the spatial proofreading model. This thermodynamic limit depends only on the available chemical potential and is equal to $e^{\beta\Delta\mu}$. This limit can be approached very closely by our model, which for $\Delta\mu \gtrsim 1$ achieves the exponential enhancement with an additional linear prefactor, namely $(\eta/\eta_{\text{eq}})^{\text{max}} \approx e^{\beta\Delta\mu}/\beta\Delta\mu$ (see Appendix S4.2.2). Such scaling behavior was theoretically accessible only to infinite-state traditional proofreading schemes [24, 25]. This offers a view of spatial proofreading as a procession of the enzyme through an infinite series of spatial filters and suggests that, from the perspective of peak error reduction capacity, our model outperforms the finite-state schemes.

4.3.4 Proofreading by biochemically plausible intracellular gradients

Our discussion of the minimal model thus far was not aimed at a particular biochemical system and thus did not involve the use of realistic reaction rates and diffusion constants typically seen in living cells. Furthermore, we did not account for the possibility of substrate diffusion, as well as for the homogenization of substrate concentration gradients due to enzymatic reactions, and have thereby abstracted away the gradient maintaining mechanism. The quantitative inspection of such mechanisms is important for understanding the constraints on spatial proofreading in realistic settings.

Here, we investigate proofreading based on a widely applicable mechanism for creating gradients by the spatial separation of two opposing enzymes [12, 18, 26]. Consider a protein S that in its free state is phosphorylated by a membrane-bound kinase and dephosphorylated by a delocalized cytoplasmic phosphatase, as shown in Fig. 4.5A. This setup will naturally create a gradient of the active form of protein (S^*), with the gradient length scale controlled by the rate of phosphatase activity

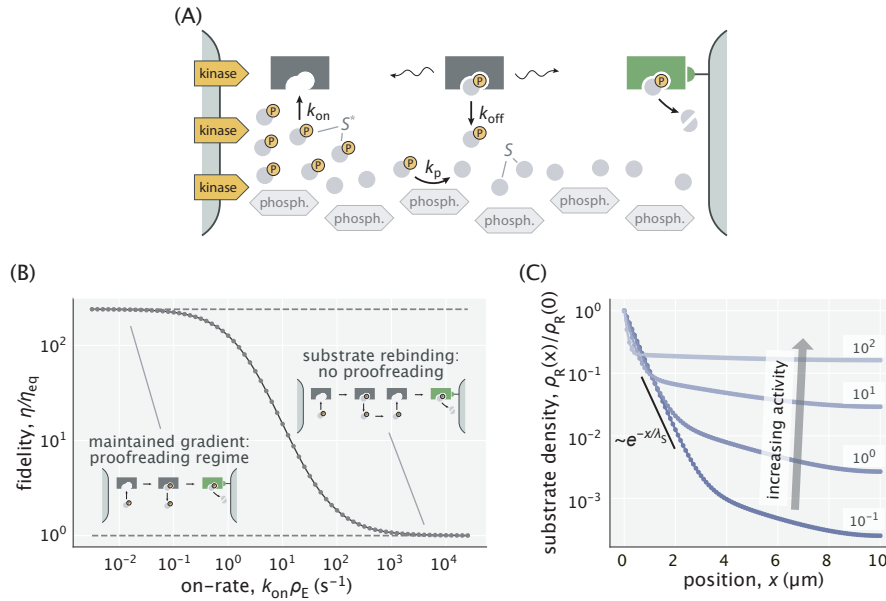


Figure 4.5: Proofreading based on substrate gradients formed by spatially separated kinases and phosphatases. (A) The active form S^* of many proteins exhibits gradients because kinases that phosphorylate S are anchored to a membrane while phosphatases can diffuse in the cytoplasm [14]. An enzyme can exploit the resulting spatial gradient for proofreading. (B) At low enzyme activity (i.e., low $k_{\text{on}}\rho_E$), the gradient of S^* is successfully maintained, allowing for proofreading. The upper dashed line corresponds to the peak fidelity when the substrate profile is exponential. At high enzyme activity (large $k_{\text{on}}\rho_E$), the dephosphorylation with rate $k_p = 5 \text{ s}^{-1}$ is no longer sufficient to maintain the gradient and proofreading is lost. (C) Profiles of right substrates for different choices of enzyme activity. Numbers indicate $k_{\text{on}}\rho_E$ in s^{-1} units. The black line shows an exponential substrate profile with a length scale $\lambda_S = \sqrt{D/k_p} \sim 0.5 \mu\text{m}$.

$k_p (S^* \xrightarrow{k_p} S)$. Such mechanisms are known to create gradients of the active forms of MEK and ERK [14], of GTPases such as Ran (with GEF and GAP [27] playing the role of kinase and phosphatase, respectively), of cAMP [14], and of stathmin oncoprotein 18 (Op18) [28, 29] near the plasma membrane, the Golgi apparatus, the ER, kinetochores, and other places.

We test the proofreading power of such gradients, assuming experimentally constrained biophysical parameters for the gradient forming mechanism. Specifically, we consider an enzyme E that acts on active forms of cognate (R^*) and non-cognate (W^*) substrates which have off-rates 0.1 s^{-1} and 1 s^{-1} , respectively (hence, $\eta_{\text{eq}} = 10$). These off-rates are consistent with typical values for substrates proofread by cellular signalling systems [10, 30]. The kinases and phosphatases in our setup act identically

on right and wrong substrates. We consider a dephosphorylation rate constant $k_p = 5 \text{ s}^{-1}$ that falls in the range $0.1 - 100 \text{ s}^{-1}$ reported for different phosphatases [18, 31, 32], and a cytosolic diffusion constant $D = 1 \mu\text{m}^2/\text{s}$ for all proteins in this model. With this setup, exponential gradients of length scale $\sim 0.5 \mu\text{m}$ are formed for R^* and W^* . We evaluate the proofreading and energetic performance of the model in a compartment of size $L = 10 \mu\text{m}$ – a typical length scale in eukaryotic cells (see Appendix S4.4 for details).

Though not cost-efficient, this setup achieves proofreading in a wide range of regimes. Specifically, it is most effective when the enzyme–substrate binding is slow, in which case the exponential substrate profile is maintained and the system attains the fidelity predicted by our earlier explanatory model (Fig. 4.5B). The system’s proofreading capacity is retained if the first-order on-rate is raised up to $k_{\text{on}}\rho_E \sim 10 \text{ s}^{-1}$, where around 10-fold increase in fidelity is still possible. If the binding rate constant (k_{on}) or the enzyme’s expression level (ρ_E) is any higher, then enzymatic reactions overwhelm the ability of the kinase/phosphatase system to keep the active forms of substrates sufficiently localized (Fig. 4.5C) and proofreading is lost. Overall, this model suggests that enzymes can work at reasonable binding rates and still proofread, when accounting for an experimentally characterized gradient maintaining mechanism.

4.4 Discussion

We have outlined a way for enzymatic reactions to proofread and improve specificity by exploiting spatial concentration gradients of substrates. Like the classic model, our proposed spatial proofreading scheme is based on a time delay; but unlike the classic model, here the delay is due to spatial transport rather than transitions through biochemical intermediates. Consequently, the enzyme is liberated from the stringent structural requirements imposed by traditional proofreading, such as multiple intermediate conformations and hydrolysis sites for energy coupling. Instead, our scheme exploits the free energy supplied by active mechanisms that maintain spatial structures.

The decoupling of the two crucial features of proofreading – time delay and free energy dissipation – allows the cell to tune proofreading on the fly. For instance, all proofreading schemes offer fidelity at the expense of reaction speed and energy. For traditional schemes, navigating this trade-off is not always feasible, as it needs to involve structural changes via mutations or modulation of the $[\text{ATP}]/[\text{ADP}]$ ratio

which can cause collateral effects on the rest of the cell. In contrast, the spatial proofreading scheme is more adaptable to the changing conditions and needs of the cell. The scheme can prioritize speed in one context, and fidelity in another, simply by tuning the length scale of intracellular gradients (e.g., through the regulation of the phosphatase or free enzyme concentration in the scheme discussed earlier).

On the other hand, this modular decoupling can complicate the experimental identification of proofreading enzymes and the interpretation of their fidelity. Here, the enzymes need not be endowed with the structural and biochemical properties typically sought for in a proofreading enzyme. At the same time, any attempt to reconstitute enzymatic activity in a well-mixed, *in vitro* assay, will show poor fidelity compared to *in vivo* measurements, even when all necessary molecular players are present *in vitro*. Therefore, more care is required in studies of cellular information processing mechanisms that hijack a distant source of free energy compared to the case where the relevant energy consumption is local and easier to link causally to function.

While we focused on spatially localized substrates and delocalized enzymes, our framework would apply equally well to other scenarios, e.g., a spatially localized enzyme (or its active form [27, 33]) and effector with delocalized substrates, an example of which would be an alternative version of the scheme in Fig. 4.5A where the target of the kinase/phosphatase activity is changed from substrates to enzymes. Our framework can also be extended to signaling cascades, where slightly different phosphatase activities can result in magnified concentration ratios of two competing signaling molecules at the spatial location of the next cascade step [14, 34, 35].

The spatial gradients needed for the operation of our model can be created and maintained through multiple mechanisms in the cell, ranging from the kinase/phosphatase system modeled here, to the passive diffusion of substrates/ligands combined with active degradation (e.g., Bicoid and other developmental morphogens), to active transport processes combined with diffusion. A particularly simple implementation of our scheme is via compartmentalization – substrates and effectors are localized in two spatially separated compartments with the enzyme–substrate complex having to travel from one to another to complete the reaction.

Many molecular localization pathways involving the naturally compartmentalized parts of the cell require high substrate selectivity and are therefore potential candidates for the implementation of spatial proofreading. For example, in polarized, asymmetric cells (e.g., budding yeast or neuronal cells), gene expression often needs to be

spatially regulated [36, 37]. Such regulation is achieved with designated ribonucleo-proteins that bind specific mRNAs near the cell nucleus, perform a biased random walk to the mRNA localization site, and deliver them for translation. During transport, mRNAs are protected from ribosome binding and when they unbind, they are subject to degradation which would prevent rebinding events at intermediate locations. Another example process is the non-vesicular transport of lipids between the membrane-bound domains of the cells (e.g., the ER, mitochondria, the Golgi apparatus, or the plasma membrane). This transport mechanism is mediated by lipid-transfer proteins that bind lipids on the donor membrane, diffuse to the acceptor membrane and upon interacting with it, undergo a conformational change, delivering the ‘cargo’ [38]. Though the higher proximity of the two membranes is thought to enhance the transport efficiency, it would be interesting to study the optimality of the inter-membrane distance in the context of fidelity-transport efficiency trade-off, given the fact that some of the lipid-transfer proteins are known to exhibit specificity for their cognate substrates.

Our scheme may also be applicable as a quality control mechanism in protein secretion pathways [39, 40], in high-fidelity targeting of membrane proteins mediated by signal recognition particles [41, 42], as well as in selective glycosylation reactions in the Golgi apparatus [43]. Lastly, considering the recent advances in generating synthetic morphogen patterns in multicellular organisms [44, 45], spatial proofreading could also be employed in pathways acting on engineered protein gradients. Experimental investigations of these processes in light of our work will reveal the extent to which spatial transport promotes specificity.

In conclusion, we have analyzed the role played by spatial structures in endowing enzymatic reactions with kinetic proofreading. Simply by spatially segregating substrate binding from catalysis, enzymes can enhance their specificity. This suggests that enzymatic reactions may acquire *de-novo* proofreading capabilities by coupling to pre-existing spatial gradients in the cell.

Acknowledgments

We thank Anatoly Kolomeisky, Shu-ou Shan, and Erik Winfree for insightful discussions, and to Soichi Hirokawa and Avi Flamholz for providing useful feedback on the manuscript. We also thank Alexander Grosberg whose idea of a compartmentalized ‘rotary demon’ motivated the development of our model. This work was supported by the NIH Grant 1R35 GM118043-01, the John Templeton Foundation

Grants 51250 and 60973 (to R.P.), a James S. McDonnell Foundation postdoctoral fellowship (to K.H.), and the Simons Foundation (A.M.).

References

1. Hopfield, J. J. Kinetic proofreading: A new mechanism for reducing errors in biosynthetic processes requiring high specificity. *Proc. Natl. Acad. Sci. U.S.A.* **71**, 4135–4139 (1974).
2. Ninio, J. Kinetic amplification of enzyme discrimination. *Biochimie* **57**, 587–595 (1975).
3. Kunkel, T. A. DNA replication fidelity. *J. Biol. Chem.* **279**, 16895–16898 (2004).
4. Sydow, J. F. & Cramer, P. RNA polymerase fidelity and transcriptional proofreading. *Curr. Opin. Struct. Biol.* **19**, 732–739 (2009).
5. Rodnina, M. V. & Wintermeyer, W. Fidelity of aminoacyl-tRNA selection on the ribosome: Kinetic and structural mechanisms. *Annu. Rev. Biochem.* **70**, 415–435 (2001).
6. Jeong, K. W., Uzun, Ü., Selmer, M. & Ehrenberg, M. Two proofreading steps amplify the accuracy of genetic code translation. *Proc. Natl. Acad. Sci. U.S.A.* **113**, 13744–13749 (2016).
7. Swain, P. & Siggia, E. The role of proofreading in signal transduction specificity. *Biophys. J.* **82**, 2928–2933 (2002).
8. Mckeithan, T. W. Kinetic proofreading in T-cell receptor signal transduction. *Proc. Natl. Acad. Sci. U.S.A.* **92**, 5042–5046 (1995).
9. Goldstein, B., Faeder, J. R. & Hlavacek, W. S. Mathematical and computational models of immune-receptor signalling. *Nat. Rev. Immunol.* **4**, 445 (2004).
10. Cui, W. & Mehta, P. Identifying feasible operating regimes for early T-cell recognition: The speed, energy, accuracy trade-off in kinetic proofreading and adaptive sorting. *PloS one* **13**, e0202331 (2018).
11. Yamane, T. & Hopfield, J. J. Experimental evidence for kinetic proofreading in the aminoacylation of tRNA by synthetase. *Proc. Natl. Acad. Sci. U.S.A.* **13**, 2246–2250 (1977).
12. Bivona, T. G., Pérez De Castro, I., Ahearn, I. M., Grana, T. M., Chiu, V. K., Lockyer, P. J., Cullen, P. J., Pellicer, A., Cox, A. D. & Philips, M. R. Phospholipase C γ activates Ras on the Golgi apparatus by means of RasGRP1. *Nature* **424**, 694–698 (2003).
13. Caudron, M., Bunt, G., Bastiaens, P. & Karsenti, E. Spatial coordination of spindle assembly by chromosome-mediated signaling gradients. *Science* **309**, 1373–1376 (2005).

14. Kholodenko, B. N. Cell-signalling dynamics in time and space. *Nat. Rev. Mol. Cell Biol.* **7**, 165–176 (2006).
15. Wu, Y., Han, B., Li, Y., Munro, E., Odde, D. J. & Griffin, E. E. Rapid diffusion-state switching underlies stable cytoplasmic gradients in the *Caenorhabditis elegans* zygote. *Proc. Natl. Acad. Sci. U.S.A.* **115**, E8440–E8449 (2018).
16. Kholodenko, B. N. Four-dimensional organization of protein kinase signaling cascades: the roles of diffusion, endocytosis and molecular motors. *J. Exp. Biol.* **206**, 2073–2082 (2003).
17. Driever, W. & Nüsslein-Volhard. A gradient of *bicoid* protein in *Drosophila* embryos. *Cell* **54**, 83–93 (1988).
18. Brown, G. C. & Kholodenko, B. N. Spatial gradients of cellular phosphoproteins. *FEBS Lett.* **457**, 452–454 (1999).
19. Murugan, A., Huse, D. A. & Leibler, S. Speed, dissipation, and error in kinetic proofreading. *Proc. Natl. Acad. Sci. U.S.A.* **109**, 12034–12039 (2012).
20. Lan, G., Sartori, P., Neumann, S., Sourjik, V. & Tu, Y. The energy–speed–accuracy trade-off in sensory adaptation. *Nat. Phys.* **8**, 422 (2012).
21. Lan, G. & Tu, Y. The cost of sensitive response and accurate adaptation in networks with an incoherent type-1 feed-forward loop. *J. R. Soc. Interface* **10**, 20130489 (2013).
22. Horowitz, J. M., Zhou, K. & England, J. L. Minimum energetic cost to maintain a target nonequilibrium state. *Phys. Rev. E* **95**, 042102 (2017).
23. Sartori, P. & Pigolotti, S. Thermodynamics of error correction. *Phys. Rev. X* **5**, 041039 (2015).
24. Qian, H. Reducing intrinsic biochemical noise in cells and its thermodynamic limit. *J. Mol. Biol.* **362**, 387–392 (2006).
25. Ehrenberg, M. & Blomberg, C. Thermodynamic constraints on kinetic proofreading in biosynthetic pathways. *Biophys. J.* **31**, 333–358 (1980).
26. Stelling, J. & Kholodenko, B. N. Signaling cascades as cellular devices for spatial computations. *J. Math. Biol.* **58**, 35–55 (2009).
27. Kalab, P., Weis, K. & Heald, R. Visualization of a Ran-GTP gradient in interphase and mitotic *Xenopus* egg extracts. *Science* **295**, 2452–2456 (2002).
28. Bastiaens, P., Caudron, M., Niethammer, P. & Karsenti, E. Gradients in the self-organization of the mitotic spindle. *Trends Cell Biol.* **16**, 125–134 (2006).
29. Niethammer, P., Bastiaens, P. & Karsenti, E. Stathmin-tubulin interaction gradients in motile and mitotic cells. *Science* **303**, 1862–1866 (2004).
30. Gascoigne, N. R., Zal, T. & Alam, S. M. T-cell receptor binding kinetics in T-cell development and activation. *Expert Rev. Mol. Med.* **3**, 1–17 (2001).

31. Kholodenko, B. N., Brown, G. C. & Hoek, J. B. Diffusion control of protein phosphorylation in signal transduction pathways. *Biochem. J.* **350**, 901–907 (2000).
32. Todd, J. L., Tanner, K. G. & Denu, J. M. Extracellular regulated kinases (ERK) 1 and ERK2 are authentic substrates for the dual-specificity protein-tyrosine phosphatase VHR: A novel role in down-regulating the ERK pathway. *J. Biol. Chem.* **274**, 13271–13280 (1999).
33. Nalbant, P., Hodgson, L., Kraynov, V., Touthkine, A. & Hahn, K. M. Activation of endogenous Cdc42 visualized in living cells. *Science* **305**, 1615–1619 (2004).
34. Roy, J. & Cyert, M. S. Cracking the phosphatase code: Docking interactions determine substrate specificity. *Sci. Signal.* **2**, re9 (2009).
35. Bauman, A. L. & Scott, J. D. Kinase- and phosphatase-anchoring proteins: harnessing the dynamic duo. *Nat. Cell Biol.* **4**, E203–206 (2002).
36. Parton, R. M., Davidson, A., Davis, I. & Weil, T. T. Subcellular mRNA localisation at a glance. *J. Cell Sci.* **127**, 2127–2133 (2014).
37. Martin, K. C. & Ephrussi, A. mRNA localization: Gene expression in the spatial dimension. *Cell* **136**, 719–730 (2009).
38. Lev, S. Non-vesicular lipid transport by lipid-transfer proteins and beyond. *Nat. Rev. Mol. Cell Biol.* **11**, 739–750 (2010).
39. Ellgaard, L. & Helenius, A. Quality control in the endoplasmic reticulum. *Nat. Rev. Mol. Cell Biol.* **4**, 181–191 (2003).
40. Arvan, P., Zhao, X., Ramos-Castaneda, J. & Chang, A. Secretory pathway quality control operating in Golgi, plasmalemmal, and endosomal systems. *Traffic* **3**, 771–780 (2002).
41. Rao, M., Okreglak, V., Chio, U. S., Cho, H., Walter, P. & Shan, S. O. Multiple selection filters ensure accurate tail-anchored membrane protein targeting. *Elife* **5**, e21301 (2016).
42. Chio, U. S., Cho, H. & Shan, S. O. Mechanisms of tail-anchored membrane protein targeting and insertion. *Annu. Rev. Cell Dev. Biol.* **33**, 417–438 (2017).
43. Jaiman, A. & Thattai, M. Golgi compartments enable controlled biomolecular assembly using promiscuous enzymes. *Elife* **9**, e49573 (2020).
44. Toda, S., McKeithan, W. L., Hakkinen, T. J., Lopez, P., Klein, O. D. & Lim, W. A. Engineering synthetic morphogen systems that can program multicellular patterning. *Science* **370**, 327–331 (2020).
45. Stapornwongkul, K. S., de Gennes, M., Cocconi, L., Salbreux, G. & Vincent, J. P. Patterning and growth control in vivo by an engineered GFP gradient. *Science* **370**, 321–327 (2020).

SUPPORTING INFORMATION FOR CHAPTER 4 | PROOFREADING THROUGH SPATIAL GRADIENTS

The code files used for performing the different numerical studies are available as supplementary files on the publication webpage (DOI: 10.7554/eLife.60415).

S4.1 Analytical calculations of the complex density profile and fidelity

We begin this section by deriving an analytical expression for the density profile of substrate-bound enzymes ($\rho_{\text{ES}}(x)$) in the case where the $\rho(x) \approx \text{constant}$ assumption holds. Based on this result, we then obtain expressions for fidelity in low, high, and intermediate substrate localization regimes. We reserve the studies of speed and fidelity in the general case of a nonuniform free enzyme profile to Appendix S4.5.

S4.1.1 Derivation of the complex density profile $\rho_{\text{ES}}(x)$

The ordinary differential equation (ODE) that defines the steady state profile of substrate-bound enzymes is

$$D \underbrace{\frac{d^2 \rho_{\text{ES}}}{dx^2}}_{\text{diffusion}} - \underbrace{k_{\text{off}}^{\text{S}} \rho_{\text{ES}}(x)}_{\text{unbinding}} + \underbrace{k_{\text{on}} \rho_{\text{S}}(0) e^{-x/\lambda_{\text{S}}}}_{\text{binding}} \rho_{\text{E}}(x) = 0. \quad (\text{S4.1})$$

Here $\rho_{\text{S}}(0)$ is the substrate density at the leftmost boundary, whose value can be calculated from the condition that the total number of free substrates is S_{total} , namely

$$\begin{aligned} S_{\text{total}} &= \int_{x=0}^L \rho_{\text{S}}(0) e^{-x/\lambda_{\text{S}}} dx \\ &= \rho_{\text{S}}(0) \lambda_{\text{S}} \left(1 - e^{-L/\lambda_{\text{S}}} \right) \Rightarrow \end{aligned} \quad (\text{S4.2})$$

$$\rho_{\text{S}}(0) = \frac{S_{\text{total}}}{\lambda_{\text{S}} \left(1 - e^{-L/\lambda_{\text{S}}} \right)}. \quad (\text{S4.3})$$

In the limit of low substrate amounts where the approximation $\rho_{\text{E}}(x) \approx \text{constant}$ is valid, Eq. S4.1 represents a linear nonhomogeneous ODE. Hence, its solution can be written as

$$\rho_{\text{ES}}(x) = \rho_{\text{ES}}^{(\text{h})}(x) + \rho_{\text{ES}}^{(\text{p})}(x), \quad (\text{S4.4})$$

where $\rho_{\text{ES}}^{(\text{h})}(x)$ is the general solution to the corresponding homogeneous equation, while $\rho_{\text{ES}}^{(\text{p})}(x)$ is a particular solution.

Looking for solutions of the form $Ce^{-x/\lambda}$ for the homogeneous part, we find

$$C \left(\frac{D}{\lambda^2} - k_{\text{off}}^{\text{S}} \right) e^{-x/\lambda} = 0. \quad (\text{S4.5})$$

The two possible roots for λ are $\pm\sqrt{D/k_{\text{off}}^{\text{S}}}$. Calling the positive root λ_{ES} , which represents the mean distance traveled by the substrate–bound enzyme before releasing the substrate, we can write the general solution to the homogeneous part of Eq. S4.1 as

$$\rho_{\text{ES}}^{(\text{h})}(x) = C_1 e^{-x/\lambda_{\text{ES}}} + C_2 e^{x/\lambda_{\text{ES}}}, \quad (\text{S4.6})$$

where C_1 and C_2 are constants which will be determined from the boundary conditions.

Since the nonhomogeneous part of Eq. S4.1 is a scaled exponential, we look for a particular solution of the same functional form, namely $\rho_{\text{ES}}^{(\text{p})}(x) = C_{\text{p}} e^{-x/\lambda_{\text{S}}}$. Substituting this form into the ODE, we obtain

$$C_{\text{p}} \left(\frac{D}{\lambda_{\text{S}}^2} - k_{\text{off}}^{\text{S}} \right) e^{-x/\lambda_{\text{S}}} = -k_{\text{on}} \rho_{\text{S}}(0) e^{-x/\lambda_{\text{S}}} \rho_{\text{E}}. \quad (\text{S4.7})$$

The constant coefficient C_{p} can then be found as

$$\begin{aligned} C_{\text{p}} &= \frac{k_{\text{on}} \rho_{\text{S}}(0) \rho_{\text{E}}}{k_{\text{off}}^{\text{S}} - \frac{D}{\lambda_{\text{S}}^2}} = \frac{k_{\text{on}} \rho_{\text{S}}(0) \rho_{\text{E}}}{k_{\text{off}}^{\text{S}} \left(1 - \frac{D/k_{\text{off}}^{\text{S}}}{\lambda_{\text{S}}^2} \right)} \\ &= \frac{k_{\text{on}} \rho_{\text{S}}(0) \rho_{\text{E}}}{k_{\text{off}}^{\text{S}} \left(1 - \frac{\lambda_{\text{ES}}^2}{\lambda_{\text{S}}^2} \right)}, \end{aligned} \quad (\text{S4.8})$$

where we have used the equality $\lambda_{\text{ES}} = \sqrt{D/k_{\text{off}}^{\text{S}}}$.

Now, to find the unknown coefficients C_1 and C_2 , we impose the no-flux boundary conditions for the density $\rho_{\text{ES}}(x)$ at the left and right boundaries of the compartment, namely

$$\left. \frac{d\rho_{\text{ES}}}{dx} \right|_{x=0} = -\frac{C_1}{\lambda_{\text{ES}}} + \frac{C_2}{\lambda_{\text{ES}}} - \frac{C_{\text{p}}}{\lambda_{\text{S}}} = 0, \quad (\text{S4.9})$$

$$\left. \frac{d\rho_{\text{ES}}}{dx} \right|_{x=L} = -\frac{C_1}{\lambda_{\text{ES}}} e^{-L/\lambda_{\text{ES}}} + \frac{C_2}{\lambda_{\text{ES}}} e^{L/\lambda_{\text{ES}}} - \frac{C_p}{\lambda_s} e^{-L/\lambda_s} = 0. \quad (\text{S4.10})$$

Note that we did not take into account the product formation flux at the rightmost boundary when writing Eq. S4.10 in order to simplify our calculations. This is justified in the limit of slow catalysis – an assumption that we make in our treatment. The above system of two equations can then be solved for C_1 and C_2 , yielding

$$C_1 = -\frac{\lambda_{\text{ES}}}{2\lambda_s} \frac{e^{L/\lambda_{\text{ES}}} - e^{-L/\lambda_s}}{\sinh(L/\lambda_{\text{ES}})} C_p, \quad (\text{S4.11})$$

$$C_2 = \frac{\lambda_{\text{ES}}}{2\lambda_s} \frac{e^{-L/\lambda_s} - e^{-L/\lambda_{\text{ES}}}}{\sinh(L/\lambda_{\text{ES}})} C_p. \quad (\text{S4.12})$$

With the constant coefficients known, we obtain the general solution for the complex profile as

$$\begin{aligned} \rho_{\text{ES}}(x) &= C_1 e^{-x/\lambda_{\text{ES}}} + C_2 e^{x/\lambda_{\text{ES}}} + C_p e^{-x/\lambda_s} \\ &= C_p \left(\frac{\lambda_{\text{ES}}}{\lambda_s \sinh(L/\lambda_{\text{ES}})} \left[-\frac{e^{(L-x)/\lambda_{\text{ES}}} + e^{(x-L)/\lambda_{\text{ES}}}}{2} + \frac{e^{-x/\lambda_{\text{ES}}} + e^{x/\lambda_{\text{ES}}}}{2} e^{-L/\lambda_s} \right] + e^{-x/\lambda_s} \right) \\ &= \frac{k_{\text{on}} \rho_s(0) \rho_E}{k_{\text{off}}^S (1 - \lambda_{\text{ES}}^2 / \lambda_s^2)} \left(\frac{\lambda_{\text{ES}}}{\lambda_s \sinh(L/\lambda_{\text{ES}})} \left[-\cosh\left(\frac{L-x}{\lambda_{\text{ES}}}\right) + \cosh\left(\frac{x}{\lambda_{\text{ES}}}\right) e^{-L/\lambda_s} \right] + e^{-x/\lambda_s} \right) \\ &= \frac{k_{\text{on}} \rho_s(0) \rho_E}{k_{\text{off}}^S (1 - \lambda_{\text{ES}}^2 / \lambda_s^2)} \left(\frac{\lambda_{\text{ES}}}{\lambda_s \sinh(L/\lambda_{\text{ES}})} \left[-\cosh\left(\frac{L-x}{\lambda_{\text{ES}}}\right) + \cosh\left(\frac{x}{\lambda_{\text{ES}}}\right) e^{-L/\lambda_s} \right] + e^{-x/\lambda_s} \right). \end{aligned} \quad (\text{S4.13})$$

S4.1.2 Density profile in low and high substrate localization regimes

If substrate localization is very poor ($\lambda_s \gg L$), the substrate distribution will be uniform ($\rho_s(x) = \bar{\rho}_s = S_{\text{total}}/L$), resulting in a similarly flat profile of enzyme–substrate complexes with their density ρ_{ES}^∞ given by

$$\begin{aligned} \rho_{\text{ES}}^\infty &= \frac{k_{\text{on}} \rho_s(0) \rho_E}{k_{\text{off}}^S} \\ &= \frac{k_{\text{on}} \bar{\rho}_s \rho_E}{k_{\text{off}}^S}. \end{aligned} \quad (\text{S4.14})$$

This is the expected equilibrium result where the complex concentration is inversely proportional to the dissociation constant ($k_{\text{off}}^S/k_{\text{on}}$).

In the opposite limit where the substrates are highly localized ($\lambda_s \ll \lambda_{\text{ES}}, L$ and $\rho_s(0) \approx S_{\text{total}}/\lambda_s$ from Eq. S4.3), the complex density profile simplifies into

$$\rho_{\text{ES}}(x) \approx \frac{k_{\text{on}} S_{\text{total}} \rho_E}{k_{\text{off}}^S \lambda_s (-\lambda_{\text{ES}}^2 / \lambda_s^2)} \left(-\frac{\lambda_{\text{ES}}}{\lambda_s \sinh(L/\lambda_{\text{ES}})} \cosh\left(\frac{L-x}{\lambda_{\text{ES}}}\right) \right)$$

$$\begin{aligned}
&= \frac{k_{\text{on}} S_{\text{total}} \rho_E}{k_{\text{off}}^S L} \frac{L/\lambda_{\text{ES}}}{\sinh(L/\lambda_{\text{ES}})} \cosh\left(\frac{L-x}{\lambda_{\text{ES}}}\right) \\
&= \rho_{\text{ES}}^\infty \times \frac{L/\lambda_{\text{ES}}}{\sinh(L/\lambda_{\text{ES}})} \cosh\left(\frac{L-x}{\lambda_{\text{ES}}}\right). \tag{S4.15}
\end{aligned}$$

The x -dependence through the $\cosh(\cdot)$ function suggests that the complex density is the highest at the leftmost boundary and lowest at the rightmost boundary, with the degree of complex localization dictated by the length scale parameter λ_{ES} . Notably, this localization of complexes does not alter their total number, since the average complex density is conserved, that is,

$$\begin{aligned}
\langle \rho_{\text{ES}} \rangle &= \int_0^L \rho_{\text{ES}}(x) dx \\
&= \rho_{\text{ES}}^\infty \times \frac{L/\lambda_{\text{ES}}}{\sinh(L/\lambda_{\text{ES}})} \times \frac{1}{L} \int_0^L \cosh\left(\frac{L-x}{\lambda_{\text{ES}}}\right) dx \\
&= \rho_{\text{ES}}^\infty \times \frac{L/\lambda_{\text{ES}}}{\sinh(L/\lambda_{\text{ES}})} \times \frac{\lambda_{\text{ES}}}{L} \sinh(L/\lambda_{\text{ES}}) \\
&= \rho_{\text{ES}}^\infty. \tag{S4.16}
\end{aligned}$$

Eq. S4.15 for the complex profile can be alternatively written in terms of the diffusion time scale $\tau_D = L^2/D$ and the substrate off-rate k_{off}^S . Noting that $L/\lambda_{\text{ES}} = \sqrt{L^2 k_{\text{off}}^S / D} = \sqrt{\tau_D k_{\text{off}}^S}$ and introducing a dimensionless coordinate $\tilde{x} = x/L$, we find

$$\rho_{\text{ES}}(x) = \rho_{\text{ES}}^\infty \times \frac{\sqrt{\tau_D k_{\text{off}}^S}}{\sinh\left(\sqrt{\tau_D k_{\text{off}}^S}\right)} \cosh\left(\sqrt{\tau_D k_{\text{off}}^S}(1-\tilde{x})\right). \tag{S4.17}$$

The above equation is what was used for generating the plots in Fig. 4.3B of the main text for different choices of the diffusion time scale.

S4.1.3 Fidelity in low and high substrate localization regimes

Let us now evaluate the fidelity of the model in the two limiting regimes discussed earlier. In the poor substrate localization case, which corresponds to an equilibrium setting, the fidelity can be found from Eq. S4.14 as

$$\eta_{\text{eq}} = \frac{r \rho_{\text{ER}}^\infty}{r \rho_{\text{EW}}^\infty} = \frac{k_{\text{off}}^W}{k_{\text{off}}^R}, \tag{S4.18}$$

where we have employed the assumption about the right and wrong substrates having identical density profiles. This is the expected result for equilibrium discrimination where no advantage is taken of the system's spatial structure.

In the regime with high substrate localization, the enzyme–substrate complexes have a nonuniform distribution. What matters for product formation is the complex density at the rightmost boundary ($\tilde{x} = 1$), which we obtain from Eq. S4.17 as

$$\rho_{\text{ES}}(L) = \rho_{\text{ES}}^{\infty} \times \frac{\sqrt{\tau_D k_{\text{off}}^{\text{S}}}}{\sinh\left(\sqrt{\tau_D k_{\text{off}}^{\text{S}}}\right)}. \quad (\text{S4.19})$$

Substituting the above expression written for right and wrong complexes into the definition of fidelity, we find

$$\begin{aligned} \eta &= \frac{r\rho_{\text{ER}}(L)}{r\rho_{\text{EW}}(L)} \\ &= \eta_{\text{eq}} \times \sqrt{\frac{k_{\text{off}}^{\text{R}} \sinh\left(\sqrt{\tau_D k_{\text{off}}^{\text{W}}}\right)}{k_{\text{off}}^{\text{W}} \sinh\left(\sqrt{\tau_D k_{\text{off}}^{\text{R}}}\right)}} \\ &= \sqrt{\eta_{\text{eq}}} \frac{\sinh\left(\sqrt{\tau_D k_{\text{off}}^{\text{W}}}\right)}{\sinh\left(\sqrt{\tau_D k_{\text{off}}^{\text{R}}}\right)}. \end{aligned} \quad (\text{S4.20})$$

This is the result reported in Eq. 5 of the main text. To gain more intuition about it and draw parallels with traditional kinetic proofreading, let us consider the limit of long diffusion time scales where proofreading is the most effective. In this limit, the hyperbolic sine functions above can be approximated as $\sinh(\sqrt{\tau_D k_{\text{off}}^{\text{S}}}) \approx 0.5 e^{\sqrt{\tau_D k_{\text{off}}^{\text{S}}}}$, simplifying the fidelity expression into

$$\begin{aligned} \eta &= \sqrt{\eta_{\text{eq}}} \frac{e^{\sqrt{\tau_D k_{\text{off}}^{\text{W}}}}}{e^{\sqrt{\tau_D k_{\text{off}}^{\text{R}}}}} \\ &= \sqrt{\eta_{\text{eq}}} e^{\sqrt{\tau_D k_{\text{off}}^{\text{W}}} - \sqrt{\tau_D k_{\text{off}}^{\text{R}}}} \\ &= \sqrt{\eta_{\text{eq}}} e^{\sqrt{\tau_D k_{\text{off}}^{\text{R}}}(\sqrt{\eta_{\text{eq}}} - 1)}, \end{aligned} \quad (\text{S4.21})$$

where we have used the definition of equilibrium fidelity (Eq. S4.18). In traditional proofreading, a scheme with n proofreading realizations can yield a maximum fidelity of $\eta/\eta_{\text{eq}} = \eta_{\text{eq}}^n$. The value of n for the original Hopfield model, for instance, is 1. It would be informative to also know the effective parameter n for the spatial proofreading model. Dividing Eq. S4.21 by η_{eq} , we find

$$\frac{\eta}{\eta_{\text{eq}}} = \frac{1}{\sqrt{\eta_{\text{eq}}}} e^{\sqrt{\tau_D k_{\text{off}}^{\text{R}}}(\sqrt{\eta_{\text{eq}}} - 1)} = \eta_{\text{eq}}^n,$$

$$\begin{aligned}
e^{\sqrt{\tau_D k_{\text{off}}^R}(\sqrt{\eta_{\text{eq}}}-1)} &= \eta_{\text{eq}}^{n+\frac{1}{2}}, \\
\sqrt{\tau_D k_{\text{off}}^R}(\sqrt{\eta_{\text{eq}}}-1) &= \left(n + \frac{1}{2}\right) \ln \eta_{\text{eq}} \Rightarrow \\
n + \frac{1}{2} &= \frac{\sqrt{\eta_{\text{eq}}}-1}{\ln \eta_{\text{eq}}} \sqrt{\tau_D k_{\text{off}}^R}. \tag{S4.22}
\end{aligned}$$

This exact result can be simplified into an approximate form when diffusion is slow and $\eta_{\text{eq}} \gg 1$, yielding the expression reported in Eq. 7 of the main text, namely,

$$n \approx \frac{\sqrt{\eta_{\text{eq}}}\sqrt{\tau_D k_{\text{off}}^R}}{\ln \eta_{\text{eq}}} = \frac{\sqrt{\tau_D k_{\text{off}}^W}}{\ln \eta_{\text{eq}}}. \tag{S4.23}$$

S4.1.4 Fidelity in an intermediate substrate localization regime

The generic expression for complex density at the rightmost boundary ($x = L$) can be written using Eq. S4.13 as

$$\rho_{\text{ES}}(L) = \frac{k_{\text{on}}\rho_S(0)\rho_E}{k_{\text{off}}^S(1 - \lambda_{\text{ES}}^2/\lambda_S^2)} \left(\frac{\lambda_{\text{ES}}}{\lambda_S \sinh(L/\lambda_{\text{ES}})} \left[\cosh\left(\frac{L}{\lambda_{\text{ES}}}\right) e^{-L/\lambda_S} - 1 \right] + e^{-L/\lambda_S} \right). \tag{S4.24}$$

For the system to proofread, substrates need to be sufficiently localized ($\lambda_S < L$) and diffusion needs to be sufficiently slow ($\tau_D k_{\text{off}}^S > 1$ or, $\lambda_{\text{ES}} < L$). Under these conditions, the substrate profile can be approximated using Eq. S4.3 as $\rho_S(x) \approx \lambda_S^{-1} S_{\text{total}} e^{-x/\lambda_S}$, while the hyperbolic sine and cosine functions used above can be approximated as $\sinh(L/\lambda_{\text{ES}}) \approx \cosh(L/\lambda_{\text{ES}}) \approx 0.5 e^{L/\lambda_{\text{ES}}}$. With these approximations, the complex density expression simplifies into

$$\begin{aligned}
\rho_{\text{ES}}(L) &= \frac{k_{\text{on}} S_{\text{total}} \rho_E}{k_{\text{off}}^S \lambda_S (1 - \lambda_{\text{ES}}^2/\lambda_S^2)} \left(\frac{\lambda_{\text{ES}}}{\lambda_S} \left[e^{-L/\lambda_S} - 2e^{-L/\lambda_{\text{ES}}} \right] + e^{-L/\lambda_S} \right) \\
&= \frac{k_{\text{on}} S_{\text{total}} \rho_E}{k_{\text{off}}^S (\lambda_S^2 - \lambda_{\text{ES}}^2)} \left((\lambda_S + \lambda_{\text{ES}}) e^{-L/\lambda_S} - 2\lambda_{\text{ES}} e^{-L/\lambda_{\text{ES}}} \right). \tag{S4.25}
\end{aligned}$$

Now, depending on how λ_S compares with λ_{ES} , there can be two qualitatively different regimes for the complex density, namely

$$\rho_{\text{ES}}(L) = \rho_{\text{ES}}^{\infty} \times \begin{cases} \frac{2L}{\lambda_{\text{ES}}} e^{-L/\lambda_{\text{ES}}}, & \text{if } \lambda_S \ll \lambda_{\text{ES}} \left(L/\lambda_S \gg \sqrt{\tau_D k_{\text{off}}^S} \right) \\ \frac{L}{\lambda_S} e^{-L/\lambda_S}, & \text{if } \lambda_{\text{ES}} \ll \lambda_S \left(\sqrt{\tau_D k_{\text{off}}^S} \gg L/\lambda_S \right) \end{cases} \tag{S4.26}$$

where we used the equilibrium complex density $\rho_{\text{ES}}^{\infty}$ defined in Eq. S4.14.

Notably, the first regime effectively corresponds to the case of ideal substrate localization where complex density is independent of the precise value of λ_s . The dimensionless number $\sqrt{\tau_D k_{\text{off}}^S}$ sets the scale for the minimum L/λ_s value beyond which ideal localization can be assumed. Conversely, the second regime corresponds to the case where the distance traveled by a complex before dissociating is so short that the complex profile is dictated by the substrate profile itself. Because of that, the complex density reduction from its equilibrium limit is independent of the precise values of τ_D and k_{off}^S , as long as the condition $\lambda_{\text{ES}} \ll \lambda_s$ is met.

	$\lambda_s \ll \lambda_{\text{ER}}$	$\lambda_s \gg \lambda_{\text{ER}}$
$\lambda_s \ll \lambda_{\text{EW}}$	$\frac{\lambda_{\text{EW}}}{\lambda_{\text{ER}}} e^{L(\lambda_{\text{EW}}^{-1} - \lambda_{\text{ER}}^{-1})}$	-
$\lambda_s \gg \lambda_{\text{EW}}$	$\frac{2\lambda_s}{\lambda_{\text{ER}}} e^{L(\lambda_s^{-1} - \lambda_{\text{ER}}^{-1})}$	η_{eq}

Table S4.1: Fidelity of the scheme in different regimes of right and wrong complex densities. The upper-right cell is empty because the two conditions on λ_s cannot be simultaneously met, since $\lambda_{\text{ER}} > \lambda_{\text{EW}}$ by construction (follows from $k_{\text{off}}^{\text{R}} < k_{\text{off}}^{\text{W}}$).

The scheme yields its highest fidelity when both right and wrong complex densities are in the first regime (ideal localization). When both densities are in the second regime, fidelity is reduced down to its equilibrium value η_{eq} (Table S4.1). The transition between these two extremes happens when the density profiles of right and wrong complexes fall under different regimes. Fidelity can be navigated in the transition zone by tuning the substrate gradient length scale λ_s . This is demonstrated in Fig. S4.1 for three different choices of η_{eq} . In all three cases, the dimensionless numbers $\sqrt{\tau_D k_{\text{off}}^{\text{R}}}$ and $\sqrt{\tau_D k_{\text{off}}^{\text{W}}}$ set the approximate range in which the bulk of fidelity enhancement occurs, as stated in the main text.

S4.1.5 Optimal diffusion time scale for maximum fidelity

Fig. 4.3C of the main text illustrated the non-monotonic dependence of fidelity on the diffusion time scale τ_D for different fixed values of λ_s . Here, we further explore this feature by asking what sets the optimal τ_D .

To gain analytical insights, we focus on the case where the system can proofread, which, as we argued in the previous section, happens when $\lambda_s, \lambda_{\text{ES}} < L$. Under this condition, we identified two qualitatively different regimes of complex density

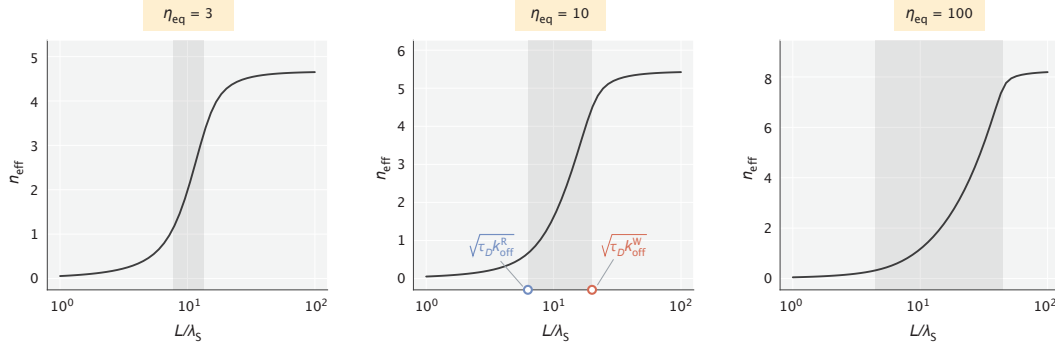


Figure S4.1: The effective number of proofreading realizations (n_{eff}) as a function of L/λ_s . The shaded region represents the range of L/λ_s values set by the key dimensionless numbers $\sqrt{\tau_D k_{\text{off}}^R}$ and $\sqrt{\tau_D k_{\text{off}}^W}$. τ_D values chosen for the demonstration were 60, 40, and 20 (in $1/k_{\text{off}}^R$ units) for the three different choices of η_{eq} , respectively.

reduction (Eq. S4.26). Namely, we found that for sufficiently fast diffusion the system acted as if the substrates were localized ideally, whereas for sufficiently slow diffusion the complex density reduction was dictated solely by λ_s and did not discriminate between the two substrate kinds. These two limiting behaviors are indeed reflected in Fig. 4.3C where in the low τ_D limit (fast diffusion), the family of curves matches the dotted ideal localization curve, while in the high τ_D limit (slow diffusion), all curves decay to 1, corresponding to the loss of error correction.

An intuitive approach for identifying the optimal τ_D is to slow down diffusion up to the point where the density of wrong complexes at $x = L$ approaches a plateau and effectively stops decreasing. Going past this threshold would only reduce the density of right complexes at $x = L$, and thereby, reduce the fidelity. We know from Eq. S4.26 that plateauing for wrong complexes happens when $\lambda_{\text{EW}} \ll \lambda_s$ (equivalently, $\sqrt{\tau_D k_{\text{off}}^W} \gg L/\lambda_s$). Hence, our first guess for the optimal diffusion time scale τ_D^* is

$$\tau_D^* k_{\text{off}}^W \sim \left(\frac{L}{\lambda_s}\right)^2 \Rightarrow \quad (\text{S4.27})$$

$$\tau_D^* k_{\text{off}}^R \sim \frac{k_{\text{off}}^R}{k_{\text{off}}^W} \left(\frac{L}{\lambda_s}\right)^2 \Rightarrow \quad (\text{S4.28})$$

$$\tau_D^*/\tau_{\text{off}}^R \sim \frac{1}{\eta_{\text{eq}}} \left(\frac{L}{\lambda_s}\right)^2. \quad (\text{S4.29})$$

To test the soundness of this expression, we compared its predictions to the optimal τ_D values in Fig. 4.3 that were identified numerically for different choices of λ_S . The results of the comparison are shown in Fig. S4.2. As can be seen, for sufficiently high degrees of substrate localization (L/λ_S), the prediction of Eq. S4.29 provides a good approximation of the true optimum. However, it is apparent that the prediction consistently underestimates the true τ_D^* , which was expected since plateauing of $\rho_{\text{EW}}(L)$ happens not under equality but a strict inequality condition (i.e., $\sqrt{\tau_D^* k_{\text{off}}^{\text{W}}} \gg L/\lambda_S$). Because an exact analytical expression for τ_D^* is not available, we performed different approximations to the fidelity formula and found an empirical correction term for our earlier estimate given by $2(L/\lambda_S)/\sqrt{\eta_{\text{eq}}}$. The prediction for τ_D^* with the correction term is now accurate starting a much lower value of L/λ_S , corresponding to a regime where the system proofreads once ($n_{\text{eff}} \approx 1$). Overall, these analytical results provide good initial guesses for τ_D^* which should be refined using a numerical approach for a higher accuracy.

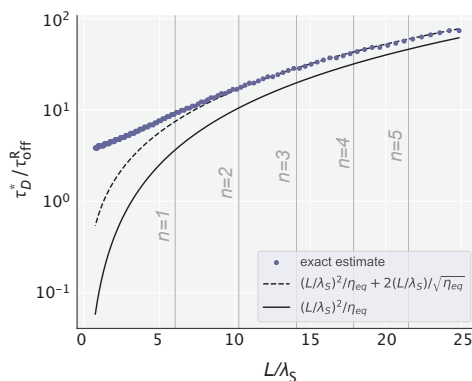


Figure S4.2: Optimal diffusion time scale for different choices of λ_S . Blue dots represent the exact values obtained numerically for the data in Fig. 4.3C. Dashed and solid lines represent the analytical estimates with and without the correction term. Vertical lines correspond to those values of L/λ_S that yield an integer number of effective proofreading realizations.

S4.2 Energetics of the scheme

We start this section by deriving an analytical expression for the minimum dissipated power, which was used in making Fig. 4.4 of the main text. Then, we calculate the upper limit on fidelity enhancement available to our model for a finite substrate gradient length scale and compare this limit with the fundamental thermodynamic bound. We end the section by providing an estimate for the baseline cost of setting up gradients and compare this cost with the maintenance cost reported in the main

text. Similar to our treatment of Appendix S4.1, here too our calculations are based on the $\rho_E \approx \text{constant}$ assumption to allow for intuitive analytical results.

S4.2.1 Derivation of the minimum dissipated power

As stated in the main text, we calculate the minimum rate of energy dissipation necessary for maintaining the substrate profiles as

$$P = \sum_{S=R,W} \int_0^L j_S(x) \mu(x) dx, \quad (\text{S4.30})$$

where $j_S(x) = k_{\text{on}} \rho_S(x) \rho_E - k_{\text{off}}^S \rho_{ES}(x)$ is the net local substrate binding flux and $\mu(x) = \mu(0) + k_B T \ln \rho_S(x) / \rho_S(0) = \mu(0) - k_B T \cdot x / \lambda_S$ is the local chemical potential.

Our choice for the expression of power at steady state is motivated by that fact that the enzyme transport is passive and therefore, energy needs to be spent only on counteracting the local binding/unbinding events that tend to homogenize the substrate profile. To demonstrate the validity of our proposed expression more formally, we invoke the standard approaches for calculating power [1, 2]. In particular, for a system that is described through discrete states with transition rates $k_{i \rightarrow j}$ between them, the rate of energy dissipation at steady state is given by

$$P = k_B T \sum_{i>j} (J_{i \rightarrow j} - J_{j \rightarrow i}) \ln \frac{k_{i \rightarrow j}}{k_{j \rightarrow i}}, \quad (\text{S4.31})$$

where $J_{i \rightarrow j}$ is the flux from state i into state j . We note here that a similar expression for the rate of total entropy production involves a $\ln(J_{i \rightarrow j} / J_{j \rightarrow i})$ term (statistical forces) instead of the $\ln(k_{i \rightarrow j} / k_{j \rightarrow i})$ term (deterministic driving forces). At steady state, however, these two expressions are mathematically equivalent [2]. Our choice for Eq. S4.31 stems from the better physical intuition that it provides in our context.

So far, the description of our system has been in terms of continuous density functions. To apply Eq. S4.31 for calculating power, we consider the discrete-state representation of enzyme dynamics shown in Fig. S4.3. There, space is discretized into intervals of size δx and diffusion is represented through jumps between neighboring sites with a rate $D / \delta x^2$. What keeps the system out of equilibrium is the spatially varying substrate profile $\rho_S(x)$.

Because forward and backward diffusive transitions have identical rates, according to Eq. S4.31 they will not contribute to energy dissipation (since $\ln(1) = 0$). The

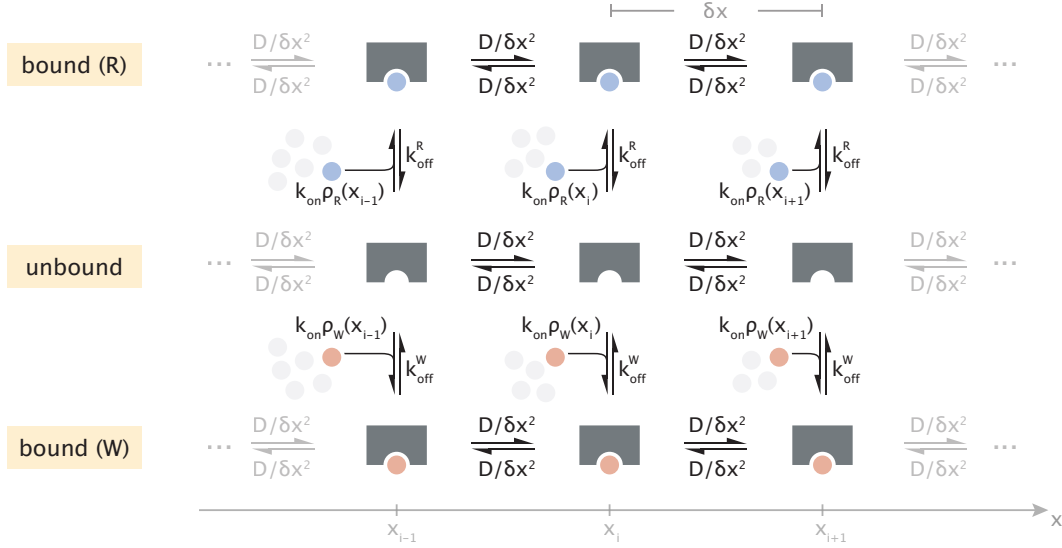


Figure S4.3: Discrete-state representation of diffusive transport and substrate binding/unbinding events. Transparent clusters of different numbers of substrates illustrate the spatial variation of substrate concentration.

contribution from the remaining substrate binding/unbinding events can then be written as

$$P = k_B T \sum_{S=R,W} \sum_i \left(k_{on} \rho_S(x_i) \times \delta n_i^E - k_{off}^S \times \delta n_i^{ES} \right) \ln \frac{k_{on} \rho_S(x_i)}{k_{off}^S}, \quad (\text{S4.32})$$

where $\delta n_i^E = \rho_E \delta x$ and $\delta n_i^{ES} = \rho_{ES}(x_i) \delta x$ are the numbers of free and substrate-bound enzymes, respectively, in the $[x_i, x_i + \delta x]$ interval. In the limit of a large number of discrete spatial intervals, the sum over i in Eq. S4.32 can be rewritten as an integral over the coordinate x , namely

$$P = k_B T \sum_{S=R,W} \int_{x=0}^{\infty} \underbrace{\left(k_{on} \rho_S(x) \rho_E - k_{off}^S \rho_{ES}(x) \right)}_{j_S(x)} \ln \frac{k_{on} \rho_S(x)}{k_{off}^S} dx. \quad (\text{S4.33})$$

Comparing the form of Eq. S4.33 to that of Eq. S4.30 (with $\mu(x)$ substituted), one can notice a difference in the terms that multiply $j_S(x)$. Specifically, in Eq. S4.30 we have $\mu(x) = \mu(0) - k_B T \ln \rho_S(0) + k_B T \ln \rho_S(x)$ while the corresponding term in Eq. S4.33 is $k_B T \ln(k_{on}/k_{off}^S) + k_B T \ln \rho_S(x)$. The difference between them, however, is in the parts that do not depend on x , while the spatially varying parts (namely, the $k_B T \ln \rho_S(x)$ contributions) are identical. Now, since the number of bound complexes is constant at steady state, we have $\int_0^{\infty} j_S(x) dx = 0$. This means that the x -independent parts discussed earlier all integrate to zero, making the power

estimates by Eq. S4.30 and Eq. S4.33 identical, thereby justifying our proposed expression.

To estimate power, we substitute the analytical expression for $\rho_{\text{ES}}(x)$ found earlier (Eq. S4.13) into $j_s(x)$ and, performing a somewhat cumbersome integral, obtain

$$\beta P = J_{\text{bind}} \sum_{\text{S=R,W}} \frac{1}{1 - \lambda_{\text{S}}^2/\lambda_{\text{ES}}^2} \left(\frac{\lambda_{\text{ES}}}{\lambda_{\text{S}}} \frac{\tanh(L/2\lambda_{\text{ES}})}{\tanh(L/2\lambda_{\text{S}})} - 1 \right), \quad (\text{S4.34})$$

where $\beta^{-1} = k_{\text{B}}T$, and $J_{\text{bind}} = k_{\text{on}}S_{\text{total}}\rho_{\text{E}}$ is the net binding rate of each substrate. Fig. 4.4 in the main text was made using this expression for power.

To get additional insights about this result, let us consider the case where substrates are highly localized ($\lambda_{\text{S}} \ll L$) and diffusion is slow ($\lambda_{\text{ES}} \ll L$) – conditions needed for effective proofreading. Under these conditions, the hyperbolic tangent terms become 1 and the expression for the power expenditure simplifies into

$$\beta P = J_{\text{bind}} \sum_{\text{S=R,W}} \frac{\lambda_{\text{ES}}^2}{\lambda_{\text{S}}(\lambda_{\text{ES}} + \lambda_{\text{S}})}. \quad (\text{S4.35})$$

The monotonic increase of power with λ_{ES} suggests that energy is primarily spent on maintaining the concentration gradient of right substrates. This is not surprising, since typically right complexes travel a much greater distance into the low concentration region of the compartment before releasing the bound substrate (i.e., $\lambda_{\text{ER}} \gg \lambda_{\text{EW}}$). Therefore, neglecting the contribution from wrong substrates and considering the range of λ_{S} values where the bulk of power–fidelity trade-off takes place ($\lambda_{\text{ER}} > \lambda_{\text{S}} > \lambda_{\text{EW}}$), we further simplify the power expression into

$$\beta P \approx \frac{J_{\text{bind}}\lambda_{\text{ER}}}{\lambda_{\text{S}}} = \frac{J_{\text{bind}} \cdot \beta\Delta\mu}{\sqrt{\tau_{\text{D}}k_{\text{off}}^{\text{R}}}}, \quad (\text{S4.36})$$

where we used the identities $\beta\Delta\mu = L/\lambda_{\text{S}}$ and $\lambda_{\text{ER}} = L/\sqrt{\tau_{\text{D}}k_{\text{off}}^{\text{R}}}$. This simple linear relation suggests that in order to maintain the exponential substrate profile, the minimum energy spent per substrate binding event should be at least $P/J_{\text{bind}} \approx k_{\text{B}}T \cdot \lambda_{\text{ER}}/\lambda_{\text{S}} > 1 k_{\text{B}}T$ (since $\lambda_{\text{ER}} > \lambda_{\text{S}}$).

We can also use Eq. S4.36 to estimate the minimum dissipation per substrate binding event at $\lambda_{\text{S}} \approx \lambda_{\text{EW}}$ where the logarithmic power–fidelity scaling regime ends (see Fig. 4.4 of the main text). Substituting the value of λ_{S} , we obtain $\beta P/J_{\text{bind}} \approx (\lambda_{\text{ER}}/\lambda_{\text{EW}}) = \sqrt{\eta_{\text{eq}}}$, which is the result illustrated in Fig. 4.4.

S4.2.2 Limits on fidelity enhancement

The error reduction capacity of the spatial proofreading scheme improves with a greater difference in substrate off-rates, as was demonstrated in Fig. 4.2 of the main text. At the same time, Fig. 4.3C showed that the finite length scale of substrate localization (or finite driving force) sets an upper limit on fidelity enhancement for substrates with fixed off-rates. It is therefore of interest to consider these two features together to find the absolute limit on fidelity enhancement available to our model, and then compare it with the fundamental bound set by thermodynamics.

Intuitively, fidelity will be enhanced the most if the density of right complexes does not decay across the compartment, while that of wrong complexes decays maximally. The first condition can be met if diffusion is fast or if the unbinding rate of right substrates is low, in which case we have

$$\rho_{\text{ER}}(L) \approx \rho_{\text{ER}}^{\infty}, \quad (\text{S4.37})$$

where $\rho_{\text{ER}}^{\infty}$ is the equilibrium density of right complexes. Conversely, when the unbinding rate of wrong substrates is very large, the density of wrong complexes is maximally reduced at the rightmost boundary and can be obtained from Eq. S4.24 by taking the $\lambda_{\text{ES}} \rightarrow 0$ limit, namely

$$\begin{aligned} \rho_{\text{EW}}(L) &\approx \frac{k_{\text{on}}\rho_{\text{E}}\rho_{\text{S}}(0)e^{-L/\lambda_{\text{S}}}}{k_{\text{off}}^{\text{W}}} = \frac{k_{\text{on}}\rho_{\text{E}}S_{\text{total}}e^{-L/\lambda_{\text{S}}}}{\lambda_{\text{S}}(1 - e^{-L/\lambda_{\text{S}}})k_{\text{off}}^{\text{W}}} \\ &= \frac{k_{\text{on}}\rho_{\text{E}}S_{\text{total}}}{k_{\text{off}}^{\text{W}}L} \times \frac{Le^{-L/\lambda_{\text{S}}}}{\lambda_{\text{S}}(1 - e^{-L/\lambda_{\text{S}}})} \\ &= \rho_{\text{EW}}^{\infty} \times \frac{\beta\Delta\mu e^{-\beta\Delta\mu}}{1 - e^{-\beta\Delta\mu}}. \end{aligned} \quad (\text{S4.38})$$

Here $\rho_{\text{EW}}^{\infty}$ is the equilibrium density of wrong complexes, and $\beta\Delta\mu = L/\lambda_{\text{S}}$ is the effective driving force of the scheme. Taking the ratio of Eqs. S4.37 and S4.38, we obtain the largest fidelity enhancement of the scheme for the given driving force, namely

$$\eta^{\text{max}} = \frac{\rho_{\text{ER}}(L)}{\rho_{\text{EW}}(L)} = \frac{\rho_{\text{ER}}^{\infty}}{\underbrace{\rho_{\text{EW}}^{\infty}}_{\eta_{\text{eq}}}} \times \frac{e^{\beta\Delta\mu} - 1}{\beta\Delta\mu} \Rightarrow \quad (\text{S4.39})$$

$$(\eta/\eta_{\text{eq}})^{\text{max}} = (e^{\beta\Delta\mu} - 1)/\beta\Delta\mu. \quad (\text{S4.40})$$

When $\beta\Delta\mu \gtrsim 1$ (or, $\lambda_{\text{S}} \lesssim L$), the limit above gets further simplified into

$$(\eta/\eta_{\text{eq}})^{\text{max}} \approx e^{\beta\Delta\mu}/\beta\Delta\mu. \quad (\text{S4.41})$$

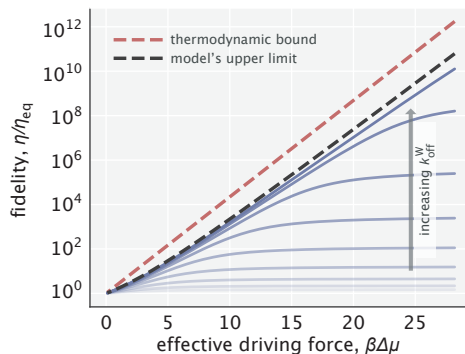


Figure S4.4: Fidelity enhancement as a function of the effective driving force for varying choices of k_{off}^W . The red dashed line indicates the thermodynamic bound given by $e^{\beta\Delta\mu}$. The black dashed line corresponds to the model's upper limit on fidelity enhancement given by Eq. S4.40.

Now, thermodynamics imposes an upper bound on fidelity enhancement by any proofreading scheme operating with a finite chemical potential $\Delta\mu$. This bound is equal to $e^{\beta\Delta\mu}$ and is reached when the entire chemical potential is used to increase the free energy difference between right and wrong substrates [3]. Comparing it with the result in Eq. S4.41, we can see that fidelity enhancement in the spatial proofreading model has the same exponential scaling term, but with an additional linear factor. Since the dominant contribution comes from the exponential term (as captured also in Fig. S4.4), we can claim that our proposed model can operate very close to the fundamental thermodynamic limit.

S4.2.3 Energetic cost to set up a concentration gradient

Earlier in the section, we calculated the rate at which energy needs to be dissipated to counteract the homogenizing effect that enzyme activity has on the substrate gradient. In addition to this cost, however, there is also a baseline cost for setting up a gradient in the absence of any enzyme. Here, we calculate this cost in the case where the gradient formation mechanism needs to work against diffusion that tends to flatten the substrate profile.

As before, we consider an exponentially decaying substrate gradient with a decay length scale λ_s and a total number of substrates S_{total} . We write the minimum power P_D required for counteracting the diffusion of substrates as

$$P_D = - \int_0^L J_D(x) \mu'(x) dx, \quad (\text{S4.42})$$

where $J_D = -D_s \nabla \rho_s(x)$ is the diffusive flux, with D_s being the substrate diffusion constant. The rationale for writing this form is that diffusion moves substrates from a higher chemical potential region into a neighboring lower chemical potential region. The gradient maintaining mechanism would need to spend at least this chemical potential difference ($\delta\mu = -\mu'(x)\delta x$) per each substrate diffusing a distance δx down the chemical potential gradient. Adding up the contribution from all local neighborhoods with a local diffusive flux $J_D(x)$ results in Eq. S4.42.

Now, substituting $\rho_s(x) \sim e^{-x/\lambda_s}$ for the substrate profile and $\mu(x) = \mu(0) + k_B T \ln(\rho_s(x)/\rho_s(0))$ for the chemical potential, we obtain

$$\begin{aligned} \beta P_D &= \int_0^L D_s \rho_s'(x) (\ln \rho_s(x))' dx \\ &= D_s \int_0^L \frac{(\rho_s'(x))^2}{\rho_s(x)} dx \\ &= D_s \int_0^L \frac{\rho_s(x)}{\lambda_s^2} dx \\ &= \frac{D_s S_{\text{total}}}{\lambda_s^2}, \end{aligned} \tag{S4.43}$$

where in the third step, we used the relation $\rho_s'(x) = -\rho_s(x)/\lambda_s$. This suggests that the minimum dissipated power required for setting up an exponential gradient increases quadratically with decreasing localization length scale λ_s .

It is informative to also make a comparison between this result and the earlier calculated minimum dissipation needed to counteract the enzyme's homogenizing activity. Recall that when substrates were sufficiently localized and when diffusion was sufficiently slow, proofreading power could be approximated as (Eq. S4.35)

$$\beta P \approx J_{\text{bind}} \frac{\lambda_{\text{ES}}^2}{\lambda_s (\lambda_{\text{ES}} + \lambda_s)}, \tag{S4.44}$$

where $J_{\text{bind}} = k_{\text{on}} S_{\text{total}} \rho_E$ is the total substrate binding flux. Using the identities $\lambda_{\text{ES}} = \sqrt{D/k_{\text{off}}^S}$ and $K_d^S = k_{\text{off}}^S/k_{\text{on}}$, we can calculate the ratio of the proofreading power to baseline power as

$$\begin{aligned} \frac{P}{P_D} &= \frac{k_{\text{on}} S_{\text{total}} \rho_E \lambda_{\text{ES}}^2}{D_s S_{\text{total}}} \times \frac{\lambda_s^2}{\lambda_s (\lambda_{\text{ES}} + \lambda_s)} \\ &= \frac{D}{D_s} \times \frac{\rho_E}{K_d^S} \times \frac{\lambda_s/\lambda_{\text{ES}}}{1 + \lambda_s/\lambda_{\text{ES}}}. \end{aligned} \tag{S4.45}$$

Presuming for simplicity that the enzyme and substrate diffusion constants are the same, we see that two factors determine the power ratio: 1) the amount of free enzyme in the system (ρ_E/K_d^S) and 2) the substrate localization length scale relative to the characteristic length scale of complex diffusion (λ_s/λ_{ES}). Now, recall that the proofreading cost is spent largely on counteracting the homogenizing activity of the enzyme on right substrates (Appendix S4.2.1) and that the bulk of fidelity enhancement takes place when $\lambda_s \lesssim \lambda_{ER}$ (Appendix S4.1.4). Therefore, when tuning λ_s down, initially the power ratio would only depend on the amount of free enzyme in the system (ρ_E/K_d^S), and then, with tighter substrate localization, the relative contribution of the proofreading power would start to decrease.

In the end, we would like to note that spatial gradients can also be set up using an external potential without a continuous dissipation of energy. In an *in vivo* setting, gravity can give rise to spatial structures in oocytes [4], while in an *in vitro* setting, electric fields can create gradients and power the transport of the complex [5]. We leave the investigations of such alternative strategies to future work.

S4.3 Studies on the effect of catalysis on the model performance

In Appendix S4.1, we considered the rate of catalysis at the right boundary to be very small for the analytical simplicity of our derivations. This resulted in expressions for fidelity that were independent of the rate of catalysis r and allowed us to use the complex density at the right boundary as a proxy for speed. In this section, we relax this assumption and explore the consequences of having non-negligible catalysis rates on the model's fidelity and on the speed–fidelity trade-off.

S4.3.1 Derivation of the complex density profile $\rho_{ES}(x)$

Accounting for catalysis in our model should be done through a boundary condition for the complex density equation (Eq. S4.1). Earlier, we imposed a no-flux boundary condition at $x = L$ under the slow catalysis assumption. With non-negligible catalysis, this assumption is no longer valid, and the boundary condition is modified into

$$-D \frac{d\rho_{ES}}{dx} \Big|_{x=L} = \underbrace{r\rho_{ES}(L)}_{\text{catalysis flux}} . \quad (\text{S4.46})$$

Recall from Eqs. S4.4, S4.6 and S4.8 that the general solution for the complex profile had the form

$$\rho_{ES}(x) = C_1 e^{-x/\lambda_{ES}} + C_2 e^{x/\lambda_{ES}} + C_p e^{-x/\lambda_s}, \quad \text{where} \quad (\text{S4.47})$$

$$C_p = \frac{k_{\text{on}}\rho_s(0)\rho_E}{k_{\text{off}}^S \left(1 - \frac{\lambda_{\text{ES}}^2}{\lambda_s^2}\right)}. \quad (\text{S4.48})$$

Imposing the no-flux boundary condition at $x = 0$ allows us to eliminate one of the integration constants, namely,

$$-D \frac{d\rho_{\text{ES}}}{dx} \Big|_{x=0} = -D \left(-\frac{C_1}{\lambda_{\text{ES}}} + \frac{C_2}{\lambda_{\text{ES}}} - \frac{C_p}{\lambda_s} \right) = 0 \Rightarrow \quad (\text{S4.49})$$

$$C_2 = C_1 + \frac{\lambda_{\text{ES}}}{\lambda_s} C_p \Rightarrow \quad (\text{S4.50})$$

$$\begin{aligned} \rho_{\text{ES}}(x) &= C_1 \left(e^{-x/\lambda_{\text{ES}}} + e^{x/\lambda_{\text{ES}}} \right) + \frac{C_p}{\lambda_s} \left(\lambda_{\text{ES}} e^{x/\lambda_{\text{ES}}} + \lambda_s e^{-x/\lambda_s} \right) \\ &= 2C_1 \cosh(x/\lambda_{\text{ES}}) + \frac{C_p}{\lambda_s} \left(\lambda_{\text{ES}} e^{x/\lambda_{\text{ES}}} + \lambda_s e^{-x/\lambda_s} \right). \end{aligned} \quad (\text{S4.51})$$

Next, we impose the new boundary condition at $x = L$ (Eq. S4.46), which yields

$$\begin{aligned} -D \left(\frac{2C_1}{\lambda_{\text{ES}}} \sinh(L/\lambda_{\text{ES}}) + \frac{C_p}{\lambda_s} \left(e^{L/\lambda_{\text{ES}}} - e^{-L/\lambda_s} \right) \right) &= r \left(2C_1 \cosh(L/\lambda_{\text{ES}}) + \frac{C_p}{\lambda_s} \left(\lambda_{\text{ES}} e^{L/\lambda_{\text{ES}}} + \lambda_s e^{-L/\lambda_s} \right) \right) \Rightarrow \\ 2C_1 \sinh(L/\lambda_{\text{ES}}) + \frac{C_p}{\lambda_s} \lambda_{\text{ES}} \left(e^{L/\lambda_{\text{ES}}} - e^{-L/\lambda_s} \right) &= - \underbrace{\frac{\lambda_{\text{ES}} r}{D}}_{\varepsilon} \left(2C_1 \cosh(L/\lambda_{\text{ES}}) + \frac{C_p}{\lambda_s} \left(\lambda_{\text{ES}} e^{L/\lambda_{\text{ES}}} + \lambda_s e^{-L/\lambda_s} \right) \right). \end{aligned} \quad (\text{S4.52})$$

Note that we have introduced the dimensionless variable ε , which, as we will see later, will define the extent to which the presence of catalysis affects the fidelity. For convenience, here we write different equivalent forms for ε as

$$\varepsilon = \frac{\lambda_{\text{ES}} r}{D} = \frac{r}{\sqrt{Dk_{\text{off}}^S}} = \frac{r}{Lk_{\text{off}}^S} \sqrt{\tau_D k_{\text{off}}^S}. \quad (\text{S4.53})$$

Solving for the remaining unknown coefficient C_1 in Eq. S4.52, we find

$$C_1 = -\frac{C_p}{2\lambda_s} \frac{\lambda_{\text{ES}} \left(e^{L/\lambda_{\text{ES}}} - e^{-L/\lambda_s} \right) + \varepsilon \left(\lambda_{\text{ES}} e^{L/\lambda_{\text{ES}}} + \lambda_s e^{-L/\lambda_s} \right)}{\sinh(L/\lambda_{\text{ES}}) + \varepsilon \cosh(L/\lambda_{\text{ES}})}. \quad (\text{S4.54})$$

Lastly, we substitute this result for C_1 into Eq. S4.51 and obtain a general expression for the complex density profile as

$$\rho_{\text{ES}}(x) = -\frac{C_p}{\lambda_s} \frac{\lambda_{\text{ES}} \left(e^{L/\lambda_{\text{ES}}} - e^{-L/\lambda_s} \right) + \varepsilon \left(\lambda_{\text{ES}} e^{L/\lambda_{\text{ES}}} + \lambda_s e^{-L/\lambda_s} \right)}{\sinh(L/\lambda_{\text{ES}}) + \varepsilon \cosh(L/\lambda_{\text{ES}})} \cosh(x/\lambda_{\text{ES}}) + \frac{C_p}{\lambda_s} \left(\lambda_{\text{ES}} e^{x/\lambda_{\text{ES}}} + \lambda_s e^{-x/\lambda_s} \right). \quad (\text{S4.55})$$

One can show in a straightforward way that this result reduces to Eq. S4.13 in the $\varepsilon \rightarrow 0$ limit.

S4.3.2 Effects on fidelity in low and high substrate localization regimes

Accounting for the catalysis flux has made the general expression for the complex density profile even more incomprehensible. In order to gain insights about the qualitative as well as quantitative changes introduced by catalysis, we will focus on two characteristic limits of substrate localization – uniform substrate profile ($\lambda_s \rightarrow \infty$) and ideal substrate localization ($\lambda_s \rightarrow 0$).

S4.3.2.1 Uniform substrate profile

In this case, no mechanism for localizing substrates is in play. Let us start off by evaluating the coefficient C_p (Eq. S4.48) in the $\lambda_s \rightarrow \infty$ limit. Recalling from Eq. S4.3 that $\rho_s(0) = S_{\text{total}}/(\lambda_s(1 - e^{-L/\lambda_s}))$, we find

$$\rho_s(0) \approx \frac{S_{\text{total}}}{L} \Rightarrow \quad (\text{S4.56})$$

$$\begin{aligned} C_p &\approx \frac{k_{\text{on}}\rho_s(0)\rho_E}{k_{\text{off}}^S} \\ &\approx \frac{k_{\text{on}}S_{\text{total}}\rho_E}{Lk_{\text{off}}^S} \\ &= \frac{J_{\text{bind}}}{Lk_{\text{off}}^S}, \end{aligned} \quad (\text{S4.57})$$

where $J_{\text{bind}} = k_{\text{on}}S_{\text{total}}\rho_E$ is the total substrate binding flux.

Substituting the expression for C_p into Eq. S4.55 and eliminating all the terms that vanish upon taking the $\lambda_s \rightarrow \infty$ limit, we obtain

$$\begin{aligned} \rho_{\text{ES}}(x) &\approx C_p \left(1 - \frac{\varepsilon \cosh(x/\lambda_{\text{ES}})}{\sinh(L/\lambda_{\text{ES}}) + \varepsilon \cosh(L/\lambda_{\text{ES}})} \right) \\ &= \frac{J_{\text{bind}}}{Lk_{\text{off}}^S} \times \frac{\sinh(L/\lambda_{\text{ES}}) + \varepsilon (\cosh(L/\lambda_{\text{ES}}) - \cosh(x/\lambda_{\text{ES}}))}{\sinh(L/\lambda_{\text{ES}}) + \varepsilon \cosh(L/\lambda_{\text{ES}})}. \end{aligned} \quad (\text{S4.58})$$

Ultimately, we are interested in knowing the rate of product formation defined via $v_S = r\rho_{\text{ES}}(L)$. We therefore evaluate the complex density at $x = L$ and multiply it by r , which yields

$$\begin{aligned} v_S = r\rho_{\text{ES}}(L) &= J_{\text{bind}} \times \left(\frac{r}{Lk_{\text{off}}^S} \right) \times \frac{\sinh(L/\lambda_{\text{ES}})}{\sinh(L/\lambda_{\text{ES}}) + \varepsilon \cosh(L/\lambda_{\text{ES}})} \\ &= J_{\text{bind}} \times \left(\frac{r}{Lk_{\text{off}}^S} \right) \times \frac{\tanh(L/\lambda_{\text{ES}})}{\tanh(L/\lambda_{\text{ES}}) + \varepsilon} \end{aligned}$$

$$\equiv J_{\text{bind}} \times \left(\frac{r}{Lk_{\text{off}}^S} \right) \times \frac{\tanh\left(\sqrt{\tau_D k_{\text{off}}^S}\right)}{\tanh\left(\sqrt{\tau_D k_{\text{off}}^S}\right) + \varepsilon}, \quad (\text{S4.59})$$

where in the last step, we wrote an equivalent expression using the $L/\lambda_{\text{ES}} = \sqrt{\tau_D k_{\text{off}}^S}$ identity. To analyze this result further, we will consider two limiting cases.

Case 1: Fast diffusion ($\sqrt{\tau_D k_{\text{off}}^S} \ll 1$). If diffusion is fast, we can approximate the hyperbolic tangent functions as the arguments themselves (i.e., $\tanh(z) \approx z$ for $z \ll 1$). Then, using the last form of ε in Eq. S4.53, we simplify the expression for speed as

$$\begin{aligned} v_S &\approx J_{\text{bind}} \times \left(\frac{r}{Lk_{\text{off}}^S} \right) \times \frac{\sqrt{\tau_D k_{\text{off}}^S}}{\sqrt{\tau_D k_{\text{off}}^S} + \frac{r}{Lk_{\text{off}}^S} \sqrt{\tau_D k_{\text{off}}^S}} \\ &= J_{\text{bind}} \times \left(\frac{r}{Lk_{\text{off}}^S} \right) \times \frac{1}{1 + \frac{r}{Lk_{\text{off}}^S}} \Rightarrow \end{aligned} \quad (\text{S4.60})$$

$$v_S = J_{\text{bind}} \times \frac{\tilde{r}}{k_{\text{off}}^S + \tilde{r}}, \quad \text{where} \quad (\text{S4.61})$$

$$\tilde{r} = r/L. \quad (\text{S4.62})$$

This is an intuitive result, suggesting that an enzyme that diffuses fast acts like a standard Michaelis–Menten enzyme with an effective catalysis rate \tilde{r} . For such an enzyme, the probability of catalysis for a bound substrate is $\tilde{r}/(k_{\text{off}}^S + \tilde{r})$. Multiplying this probability by the net substrate binding flux yields the expression for speed in Eq. S4.61.

Fidelity of the model in this fast diffusion setting can be written as

$$\eta = \frac{v_R}{v_W} = \frac{k_{\text{off}}^W + \tilde{r}}{k_{\text{off}}^R + \tilde{r}}. \quad (\text{S4.63})$$

In the limit where catalysis is very slow ($\tilde{r} \ll k_{\text{off}}^R$), the equilibrium fidelity given by the ratio of off-rates is recovered, and in the opposite limit of very fast catalysis ($\tilde{r} \gg k_{\text{off}}^W$), the discriminatory capacity of the enzyme disappears altogether (Fig. S4.5A).

Case 2: Slow diffusion ($\sqrt{\tau_D k_{\text{off}}^S} \gtrsim 1$). A more interesting case is when diffusion is slow. Now, the hyperbolic tangent functions in Eq. S4.59 are approximately 1,

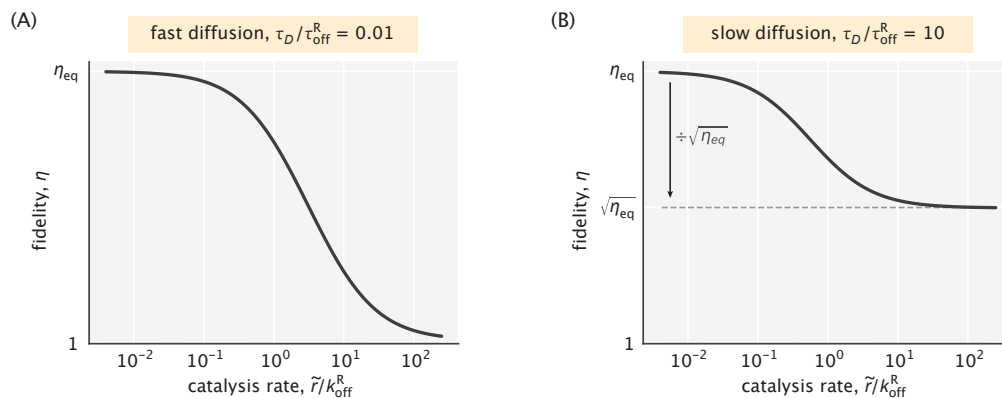


Figure S4.5: Dependence of fidelity on the catalysis rate in the case where the substrate profile is uniform. (A) Fast diffusion setting ($\sqrt{\tau_D k_{\text{off}}^R} \ll 1$). The highest fidelity reduction is a factor of η_{eq} . (B) Slow diffusion setting ($\sqrt{\tau_D k_{\text{off}}^R} \gtrsim 1$). The highest fidelity reduction is a factor of $\sqrt{\eta_{\text{eq}}}$. In both cases, $\eta_{\text{eq}} = 10$ was used.

allowing us to simplify the expression for speed into

$$\begin{aligned}
 v_S &= J_{\text{bind}} \times \left(\frac{r}{L k_{\text{off}}^S} \right) \times \frac{1}{1 + \frac{r}{L k_{\text{off}}^S} \sqrt{\tau_D k_{\text{off}}^S}} \\
 &= J_{\text{bind}} \times \frac{\tilde{r}}{k_{\text{off}}^S + \tilde{r} \sqrt{\tau_D k_{\text{off}}^S}}.
 \end{aligned} \tag{S4.64}$$

Drawing an analogy between the above result and Eq. S4.61, one can notice the presence of an extra $\sqrt{\tau_D k_{\text{off}}^S}$ factor for \tilde{r} in the denominator.

Evaluating the speeds of right and wrong product formation, we can write fidelity in this slow diffusion setting as

$$\eta = \frac{v_R}{v_W} = \frac{k_{\text{off}}^W + \tilde{r} \sqrt{\tau_D k_{\text{off}}^W}}{k_{\text{off}}^R + \tilde{r} \sqrt{\tau_D k_{\text{off}}^R}}. \tag{S4.65}$$

Like the fast diffusion case, when catalysis is very slow ($\tilde{r} \ll \sqrt{k_{\text{off}}^R / \tau_D}$ or, equivalently, $r \ll \sqrt{D k_{\text{off}}^R}$), the equilibrium fidelity is recovered. Unlike the fast diffusion case, however, if catalysis is very fast ($r \gg \sqrt{D k_{\text{off}}^W}$), the enzyme partly preserves its discriminatory capacity (Fig. S4.5B). In this limit, a fidelity equal to the square root of the equilibrium fidelity is still attainable, namely

$$\eta \approx \frac{\sqrt{k_{\text{off}}^{\text{W}}}}{\sqrt{k_{\text{off}}^{\text{R}}}} = \sqrt{\eta_{\text{eq}}}. \quad (\text{S4.66})$$

This unexpected result suggests a potential advantage of localizing fast catalytic reactions instead of having them occur in a well-mixed solution.

S4.3.2.2 Ideal substrate localization

We next consider the effect of catalysis on model fidelity in the ideal substrate localization limit ($\lambda_s \rightarrow 0$). We begin by evaluating the C_p/λ_s ratio that appears in the density profile expression (Eq. S4.55). Using Eqs. S4.48 and S4.3, we find

$$\begin{aligned} \rho_s(0) &\approx \frac{S_{\text{total}}}{\lambda_s} & (\text{S4.67}) \\ \frac{C_p}{\lambda_s} &= \frac{k_{\text{on}}\rho_s(0)\rho_E}{\lambda_s k_{\text{off}}^{\text{S}}(1 - \lambda_{\text{ES}}^2/\lambda_s^2)} \\ &\approx -\frac{k_{\text{on}}S_{\text{total}}\rho_E}{-k_{\text{off}}^{\text{S}}\lambda_{\text{ES}}^2} \\ &= -\frac{J_{\text{bind}}}{D}, & (\text{S4.68}) \end{aligned}$$

where in the last step, we invoked the identities $\lambda_{\text{ES}}^2 = D/k_{\text{off}}^{\text{S}}$ and $J_{\text{bind}} = k_{\text{on}}S_{\text{total}}\rho_E$. We then substitute our result for C_p/λ_s into Eq. S4.55 and simplify the complex density expression into

$$\begin{aligned} \rho_{\text{ES}}(x) &= \frac{J_{\text{bind}}}{D} \times \lambda_{\text{ES}} \left(\frac{e^{L/\lambda_{\text{ES}}} + \varepsilon e^{L/\lambda_{\text{ES}}}}{\sinh(L/\lambda_{\text{ES}}} + \varepsilon \cosh(L/\lambda_{\text{ES}})} \cosh(x/\lambda_{\text{ES}}) - e^{x/\lambda_{\text{ES}}} \right) \\ &= J_{\text{bind}} \times \frac{\lambda_{\text{ES}}}{D} \frac{\cosh((L-x)/\lambda_{\text{ES}}} + \varepsilon \sinh((L-x)/\lambda_{\text{ES}})}{\sinh(L/\lambda_{\text{ES}}} + \varepsilon \cosh(L/\lambda_{\text{ES}})}. & (\text{S4.69}) \end{aligned}$$

To obtain the speed, we evaluate $\rho_{\text{ES}}(x)$ at the right boundary ($x = L$) and multiply it by r , namely

$$\begin{aligned} v_{\text{S}} = r\rho_{\text{ES}}(L) &= J_{\text{bind}} \underbrace{\frac{\lambda_{\text{ES}} r}{D}}_{\varepsilon} \frac{1}{\sinh(L/\lambda_{\text{ES}}} + \varepsilon \cosh(L/\lambda_{\text{ES}})} \\ &= J_{\text{bind}} \times \frac{\varepsilon}{\sinh\left(\sqrt{\tau_D k_{\text{off}}^{\text{S}}}\right) + \varepsilon \cosh\left(\sqrt{\tau_D k_{\text{off}}^{\text{S}}}\right)}. & (\text{S4.70}) \end{aligned}$$

To evaluate the effect of catalysis further, we again consider two special limits – those of fast and slow diffusion.

Case 1: Fast diffusion ($\sqrt{\tau_D k_{\text{off}}^S} \ll 1$). In this limit, the hyperbolic sine function can be approximated by its argument (i.e., $\sinh(z) \approx z$ for $z \ll 1$), while the hyperbolic cosine function is approximately 1. Making these approximations and substituting the expression for ε , we obtain

$$\begin{aligned}
 v_S &\approx J_{\text{bind}} \times \frac{\frac{r}{Lk_{\text{off}}^S} \sqrt{\tau_D k_{\text{off}}^S}}{\sqrt{\tau_D k_{\text{off}}^S} + \frac{r}{Lk_{\text{off}}^S} \sqrt{\tau_D k_{\text{off}}^S}} \\
 &= J_{\text{bind}} \times \frac{\frac{r}{Lk_{\text{off}}^S}}{1 + \frac{r}{Lk_{\text{off}}^S}} \\
 &= J_{\text{bind}} \times \frac{\tilde{r}}{k_{\text{off}}^S + \tilde{r}}.
 \end{aligned} \tag{S4.71}$$

This result is identical to what we found in the fast diffusion limit for the $\lambda_s \rightarrow \infty$ setting (Eq. S4.61), which is reasonable, since the location of substrate binding is irrelevant if diffusion is very fast (Fig. S4.6A).

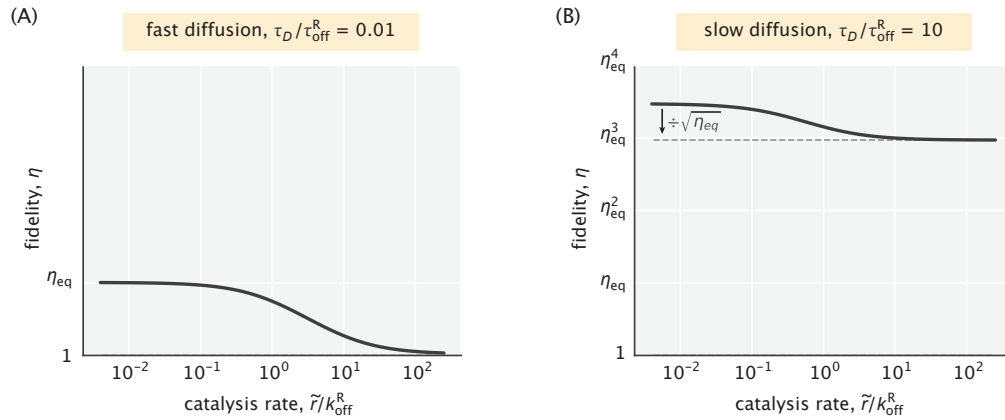


Figure S4.6: Fidelity as a function of the catalysis rate in an ideal substrate localization setting. (A) Fast diffusion case, where the behavior of the system is identical to that in Fig. S4.5A. (B) Slow diffusion case where efficient proofreading is achieved. Catalysis can reduce the fidelity by up to a factor of $\sqrt{\eta_{\text{eq}}}$. In both cases, $\eta_{\text{eq}} = 10$ was used.

Case 2: Slow diffusion ($\sqrt{\tau_D k_{\text{off}}^S} \gg 1$). In this limit, the hyperbolic sine and cosine functions can be approximated as exponentials with a 1/2 prefactor, simplifying the expression of speed into

$$v_S \approx J_{\text{bind}} \times \frac{2\varepsilon}{1 + \varepsilon} e^{-\sqrt{\tau_D k_{\text{off}}^S}}. \quad (\text{S4.72})$$

Recalling the identity $\varepsilon = r/\sqrt{Dk_{\text{off}}^S}$ (note that ε depends on the substrate kind), we evaluate the speed for right and wrong product formation and, dividing them, obtain the fidelity as

$$\begin{aligned} \eta = \frac{v_R}{v_W} &= \frac{1 + r/\sqrt{Dk_{\text{off}}^W}}{1 + r/\sqrt{Dk_{\text{off}}^R}} \times \frac{\sqrt{k_{\text{off}}^W}}{\sqrt{k_{\text{off}}^R}} e^{\sqrt{\tau_D k_{\text{off}}^W} - \sqrt{\tau_D k_{\text{off}}^R}} \\ &= \frac{1 + r/\sqrt{Dk_{\text{off}}^W}}{1 + r/\sqrt{Dk_{\text{off}}^R}} \times \sqrt{\eta_{\text{eq}}} e^{\sqrt{\tau_D k_{\text{off}}^R}(\sqrt{\eta_{\text{eq}}}-1)}. \end{aligned} \quad (\text{S4.73})$$

In the case where catalysis is slow ($r \ll \sqrt{Dk_{\text{off}}^R}$), the first term in the fidelity expression becomes approximately 1, and our earlier result obtained with no account of catalysis is recovered (Eq. S4.21). In the opposite limit of fast catalysis ($r \gg \sqrt{Dk_{\text{off}}^W}$), the first term is no longer 1, and we find

$$\begin{aligned} \eta &\approx \underbrace{\sqrt{\frac{k_{\text{off}}^R}{k_{\text{off}}^W}} \sqrt{\eta_{\text{eq}}}}_1 e^{\sqrt{\tau_D k_{\text{off}}^R}(\sqrt{\eta_{\text{eq}}}-1)} \\ &= e^{\sqrt{\tau_D k_{\text{off}}^R}(\sqrt{\eta_{\text{eq}}}-1)}. \end{aligned} \quad (\text{S4.74})$$

As we can see, fast catalysis in the slow diffusion regime reduces the fidelity by $\sqrt{\eta_{\text{eq}}}$ or, equivalently, reduces the effective number of proofreading realizations by one half, without affecting the exponential amplification term (Fig. S4.6B).

To conclude, our study demonstrated the expected reduction of fidelity with increasing catalysis rate. In the case of fast diffusion, up to a factor of η_{eq} reduction is possible, as is the case for the original Hopfield model [6, 7]. In the case of slow diffusion, however, the cap on the amount of reduction is decreased to $\sqrt{\eta_{\text{eq}}}$. The advantage of this feature is most notable in the limit of a non-localized (i.e., uniform) substrate profile and fast catalysis where a diffusing enzyme is still capable of discriminating between substrates. This behavior would not be possible for a Michaelis–Menten enzyme in a well-mixed solution.

S4.3.3 Effects on the speed–fidelity trade-off

In Fig. 4.3A of the main text, we explored the speed–fidelity trade-off in the slow catalysis limit. This trade-off arose in response to tuning the substrate localization length scale (λ_s) and the diffusion time scale (τ_D). Here, we explore the changes to this trade-off behavior in the case where the effects of catalysis are not negligible. For concreteness, we focus on alterations to the Pareto front of the trade-off achieved in the $\lambda_s \rightarrow 0$ limit.

Fig. S4.7A compares the Pareto fronts in the cases of slow and fast catalysis limits. In each case, speed is normalized by the corresponding effective Michaelis–Menten speed that is reached in the fast diffusion limit and is given by $v_{\text{MM}} = J_{\text{bind}} \times \tilde{r} / (k_{\text{off}}^{\text{R}} + \tilde{r})$, where $\tilde{r} = r/L$. One can notice a shift of the fast catalysis front toward the low fidelity region, which was expected since earlier, we observed the complete loss of substrate discrimination when diffusion and catalysis were both fast (Fig. S4.6A).

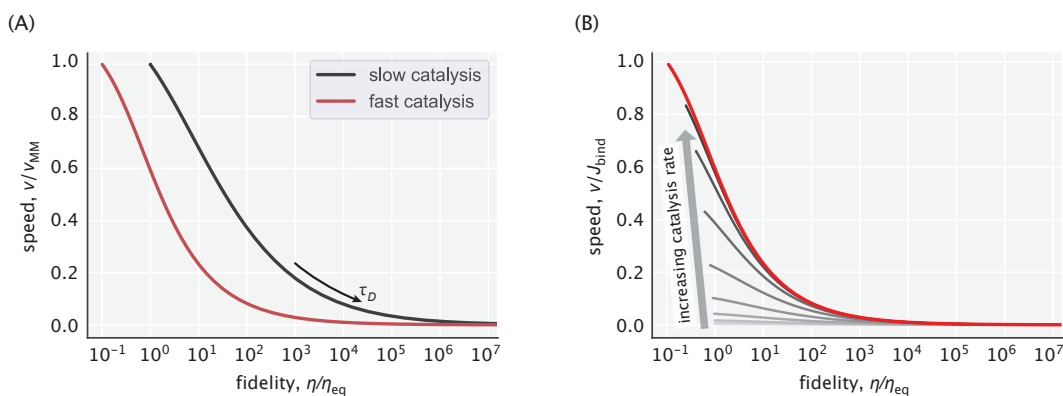


Figure S4.7: Pareto front of the speed–fidelity trade-off at different levels of catalytic activity. (A) Cases of slow and fast catalysis limits, with the y-axis for speed normalized to the $[0,1]$ interval. (B) Family of Pareto fronts for different choices of the catalysis rate. Speed on the y-axis is reported relative to the substrate binding flux J_{bind} .

Fig. S4.7A may leave an impression that faster catalysis leads to a less favorable speed–fidelity trade-off. Note, however, that the speed $v_{\text{MM}}(\tilde{r})$ used to normalize the y-axis is itself a function of the catalysis rate and penalizes the fast catalysis case more than its slow counterpart. To eliminate this ambiguity, we plotted a family of Pareto fronts for increasing values of the catalysis rate but this time normalizing the y-axis by the r -independent quantity J_{bind} (Fig. S4.7B). As can be seen, faster catalysis in fact improves the speed–fidelity trade-off, meaning that in order to maximize fidelity at a given speed level, the best strategy would be to increase the catalysis rate and correspondingly slow down the diffusion. A trade-off between

is an increasing function of λ_{ES} , and hence, a decreasing function of k_{off}^S , implying that $\Delta b > 0$.

With this condition in mind, we can see from Eq. S4.78 that speed and fidelity are anticorrelated with a linear slope when tuning the catalysis rate, unlike the more sophisticated trade-off relations when tuning the other model parameters. The peak fidelity η_0 is attained in the limit of vanishing speed. And conversely, speed is the highest when fidelity is the lowest for the given fixed values of λ_s and τ_D (Fig. S4.8).

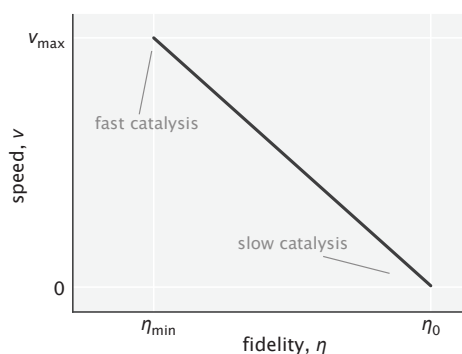


Figure S4.8: Linear trade-off between speed and fidelity when tuning the rate of catalysis. η_{min} is the fidelity in the fast catalysis limit and is up to η_{eq} lower than η_0 (based on the results of the previous section). Linear scale is used for both axes.

Overall, our result illustrates the simple speed–fidelity trade-off that can be navigated by tuning the catalysis rate. This, for instance, can be achieved by changing the concentration of effectors that activate the enzyme for catalysis.

S4.4 Proofreading for substrates with different localization conditions

Following the original treatment by Hopfield [6], we have performed the studies of our model under the assumption that discrimination between right and wrong substrates is solely based on their off–rates ($k_{off}^W > k_{off}^R$). Though this is often the signature difference between substrates, in a cellular setting, substrate discrimination may occur through other factors also. For example, substrates may be present at different amounts or they may have non-identical on–rates. These differences, however, have a multiplicative effect on the fidelity (i.e., $\eta \sim k_{on}^R/k_{on}^W \times [R]/[W]$) and do not highlight the proofreading capacity of a particular model.

Unlike these two features, differences in the degree to which right and wrong substrates are localized can have a non-trivial effect on the proofreading performance.

In this Appendix, we generalize our study of the model fidelity to cases where right and wrong substrates have unequal localization length scales λ_R and λ_W , respectively.

S4.4.1 Limiting cases

We start off by exploring the limiting cases first. From the earlier derived Eq. S4.14 and Eq. S4.15, we know that the complex density at $x = L$ in very low ($\lambda_s \gg L$) and very high ($\lambda_s \ll L$) substrate localization regimes is given by

$$\rho_{ES}^\infty = \frac{k_{\text{on}} \bar{\rho}_s \rho_E}{k_{\text{off}}^S} \quad \text{and} \quad (\text{S4.79})$$

$$\rho_{ES}^{\text{ideal}}(L) = \rho_{ES}^\infty \times \frac{L/\lambda_{ES}}{\sinh(L/\lambda_{ES})}, \quad (\text{S4.80})$$

respectively. Note that the complex density in the ideal localization case is necessarily lower than that in the case of a uniform profile, since the inequality $\sinh(L/\lambda_{ES}) > L/\lambda_{ES}$ holds for all choices of λ_{ES} . If λ_R and λ_W are not constrained to be equal, then the highest fidelity for a given τ_D will be attained when the right substrates are distributed uniformly while the wrong substrates are highly localized ($\lambda_R \gg L$ and $\lambda_W \ll L$, respectively). We obtain the fidelity in this case as

$$\begin{aligned} \eta^{\text{max}} &= \frac{\rho_{ER}^\infty}{\rho_{EW}^{\text{ideal}}(L)} \\ &= \frac{\rho_{ER}^\infty}{\rho_{EW}^\infty} \times \frac{\sinh(L/\lambda_{EW})}{L/\lambda_{EW}} \\ &= \eta_{\text{eq}} \times \frac{\sinh(L/\lambda_{EW})}{L/\lambda_{EW}} \Rightarrow \end{aligned} \quad (\text{S4.81})$$

$$\frac{\eta^{\text{max}}}{\eta_{\text{eq}}} = \frac{\sinh(L/\lambda_{EW})}{L/\lambda_{EW}} \equiv \frac{\sinh\left(\sqrt{\tau_D k_{\text{off}}^W}\right)}{\sqrt{\tau_D k_{\text{off}}^W}}. \quad (\text{S4.82})$$

Notably, this result for maximum fidelity enhancement is independent of k_{off}^R . Furthermore, it exceeds the ideal localization fidelity reported in the main text (Eq. 5, derived in the $\lambda_R, \lambda_W \rightarrow 0$ limit), which was expected since now the right complexes on average travel a shorter distance to reach the activation site than the wrong complexes.

In the opposite scenario where the wrong substrates are uniformly distributed and the right ones are highly localized ($\lambda_R \ll L$ and $\lambda_W \gg L$, respectively), the system attains its lowest fidelity for a given τ_D , namely,

$$\eta^{\text{min}} = \frac{\rho_{ER}^{\text{ideal}}(L)}{\rho_{EW}^\infty}$$

$$\begin{aligned}
&= \frac{\rho_{\text{ER}}^{\infty}}{\rho_{\text{EW}}^{\infty}} \times \frac{L/\lambda_{\text{ER}}}{\sinh(L/\lambda_{\text{ER}})} \\
&= \eta_{\text{eq}} \times \frac{L/\lambda_{\text{ER}}}{\sinh(L/\lambda_{\text{ER}})} \Rightarrow
\end{aligned} \tag{S4.83}$$

$$\frac{\eta^{\text{min}}}{\eta_{\text{eq}}} = \frac{L/\lambda_{\text{ER}}}{\sinh(L/\lambda_{\text{ER}})} = \frac{\sqrt{\tau_D k_{\text{off}}^{\text{R}}}}{\sinh\left(\sqrt{\tau_D k_{\text{off}}^{\text{R}}}\right)}. \tag{S4.84}$$

Since $L/\lambda_{\text{ER}} < \sinh(L/\lambda_{\text{ER}})$, the lowest fidelity is less than the equilibrium fidelity itself ($\eta^{\text{min}} < \eta_{\text{eq}}$), suggesting that the enzyme may in fact do *anti-proofreading* [8] if the wrong substrates are generally closer to the catalytic site.

S4.4.2 Intermediate levels of substrate localization

In Fig. 4.3 inset as well as in Appendix S4.1.4, we explored the dependence of fidelity on the substrate localization length scale λ_s when it was the same for the two substrate kinds. Here, we expand this study to the case where this constraint is relaxed.

In particular, using Eq. S4.24, we calculate complex densities and corresponding fidelity values as a function of λ_r for different fixed choices of the length scale ratio λ_r/λ_w . The results of the study are captured in Fig. S4.9. In the special case where the two length scales are equal ($\lambda_r = \lambda_w$, solid black line), fidelity exhibits a monotonic dependence on L/λ_r , and in the limit of ideal localization (very large L/λ_r) the result in Eq. 5 of the main text is recovered.

When $\lambda_r \neq \lambda_w$, the dependence of fidelity on L/λ_r is no longer monotonic. If right substrates are more localized than the wrong ones (red curves), then the fidelity curves have a minimum where the enzyme does anti-proofreading (i.e., $\eta < \eta_{\text{eq}}$). The proofreading portion of the curves (when $\eta > \eta_{\text{eq}}$) is shifted to the right, suggesting that much higher substrate localization is needed for the enzyme to proofread.

The opposite case is when the right substrates have a shallower gradient than the wrong ones (blue curves). The fidelity curves are now shifted to the left and have a peak that is greater than the large L/λ_r limit of fidelity. This means that there is an optimal degree of substrate localization, going beyond which makes the model performance worse in terms of both error correction and energy consumption.

Over the course of its diffusive transport, a bound enzyme is more likely to deposit a right substrate in a substrate-depleted region than a wrong one, because right

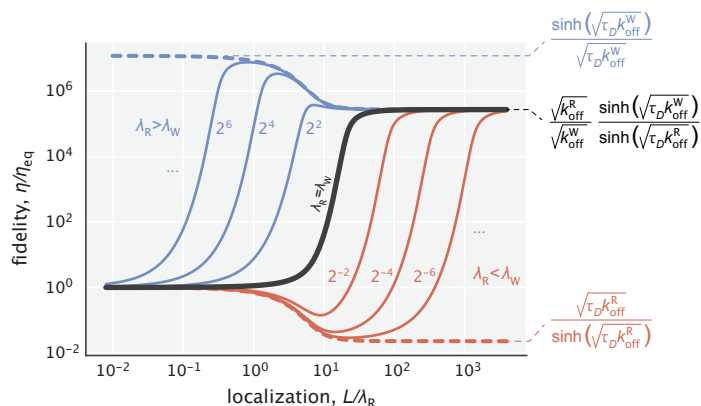


Figure S4.9: Fidelity as a function of L/λ_R for different choices of the ratio λ_R/λ_W . The solid black line corresponds to the earlier studied regime where substrates had identical localization length scales. The blue curves represent the cases where $\lambda_R > \lambda_W$, while the red curves represent the cases where $\lambda_R < \lambda_W$. Numbers next to the curves correspond to the λ_R/λ_W ratios used for generating them. Expressions for the highest and lowest fidelity values, as well as the fidelity expression in the limit where both substrates are highly localized are shown on the right side of the figure. $\tau_D = 40 \tau_{\text{off}}^R$ and $\eta_{\text{eq}} = 10$ were used for demonstration.

substrates stay attached to the enzyme for a longer time. Therefore, if the gradient-maintaining mechanism does not discriminate between substrates (which we assume is the case for the kinase/phosphatase-based one), then it will be easier for it to maintain the wrong ones localized since they tend to get deposited closer to the localization site (see Fig. S4.14C as an example). This means that in a realistic setting, the spatial organization of substrates is more likely to be in the advantageous blue region of Fig. S4.9 where $\lambda_R > \lambda_W$, facilitating the realization of spatial proofreading.

S4.5 Studies on the validity of the uniform free enzyme profile assumption

In our treatment of the model so far, we have assumed for mathematical convenience that free enzymes are in excess, which suggested the approximation $\rho_E(x) \approx \text{constant}$. Example enzyme density profiles shown in Fig. S4.10, however, demonstrate that this assumption does not hold in general. Specifically, there is a depletion of free enzymes near the substrate localization site and abundance near the catalysis site. Because of this depletion at the leftmost edge, we expect a reduction in speed in comparison with our earlier treatment where a flat profile was assumed. In addition, if substrates have a weak gradient, we expect the fidelity to also be reduced, since more enzymes will bind substrates at intermediate positions, reducing the average

travel distance to the catalytic site. In what follows, we discuss in greater detail the consequences of having a nonuniform free enzyme distribution on the model performance.

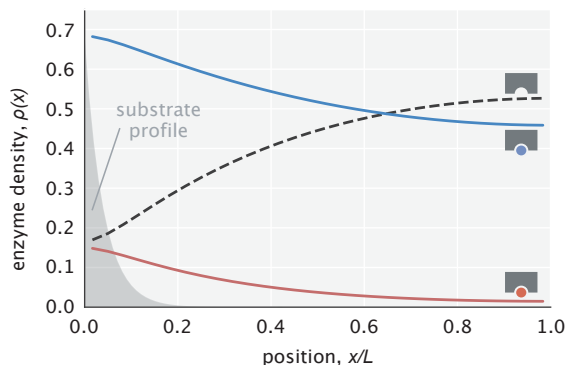


Figure S4.10: Example profiles of free and substrate-bound enzymes. Enzyme profiles are normalized so that the sum of areas under the curves is 1. The substrate profile (rescaled on the y-axis) is shown in transparent gray.

S4.5.1 Effects that relaxing the $\rho_E(x) \approx \text{constant}$ assumption has on the Pareto front

We begin by studying the effects of relaxing the uniform free enzyme profile assumption on the Pareto front of the speed–fidelity trade-off (Fig. 4.3A of the main text). This front is reached in the ideal substrate localization limit ($\lambda_s \rightarrow 0$). Though in general enzyme profiles need to be obtained using numerical methods due to the nonlinearity of reaction–diffusion equations, in this particular limit ($\lambda_s \rightarrow 0$), an analytical solution is available. To obtain it, we write the reaction–diffusion equations in the bulk region of space as

$$\frac{\partial \rho_{ER}}{\partial t} = D \frac{\partial^2 \rho_{ER}}{\partial x^2} - k_{\text{off}}^R \rho_{ER} \quad (\text{S4.85})$$

$$\frac{\partial \rho_{EW}}{\partial t} = D \frac{\partial^2 \rho_{EW}}{\partial x^2} - k_{\text{off}}^W \rho_{EW} \quad (\text{S4.86})$$

$$\frac{\partial \rho_E}{\partial t} = D \frac{\partial^2 \rho_E}{\partial x^2} + \sum_{S=R,W} k_{\text{off}}^S \rho_{ES}. \quad (\text{S4.87})$$

Substrate binding reactions did not enter the above equations, as they occur at the leftmost boundary only. They are instead accounted for via boundary conditions, which read

$$-D \frac{\partial \rho_{ER}}{\partial x} \Big|_{x=0} = k_{\text{on}} S_{\text{total}} \rho_E(0), \quad (\text{S4.88})$$

$$-D \left. \frac{\partial \rho_{EW}}{\partial x} \right|_{x=0} = k_{on} S_{total} \rho_E(0), \quad (S4.89)$$

$$-D \left. \frac{\partial \rho_E}{\partial x} \right|_{x=0} = -2k_{on} S_{total} \rho_E(0), \quad (S4.90)$$

where S_{total} is the total amount of free substrate of each kind concentrated at $x = 0$.

Relating local enzyme concentrations. Considering the system at steady state, we add Eqs. S4.85-S4.87 and obtain

$$0 = D \frac{d^2 \rho_{ER}}{dx^2} + D \frac{d^2 \rho_{EW}}{dx^2} + D \frac{d^2 \rho_E}{dx^2}, \quad (S4.91)$$

where we replaced the partial derivatives with the total derivative since the profiles are time-independent. Dividing Eq. S4.91 by D and integrating once, we find

$$\frac{d\rho_{ER}}{dx} + \frac{d\rho_{EW}}{dx} + \frac{d\rho_E}{dx} = C_1. \quad (S4.92)$$

The above relation must hold for arbitrary position x . Choosing $x = 0$ and noting that from Eqs. S4.88-S4.90, the sum of fluxes should be zero, we can claim that $C_1 = 0$. Integrating for the second time, we obtain

$$\rho_{ER}(x) + \rho_{EW}(x) + \rho_E(x) = C_2, \quad (S4.93)$$

where C_2 is now a different constant. To find it, we perform an integral for the last time across the entire compartment, namely

$$\int_0^L (\rho_{ER}(x) + \rho_{EW}(x) + \rho_E(x)) dx = E_{total} = C_2 L. \quad (S4.94)$$

Here we introduced the parameter E_{total} as the total number of enzymes in the system (in free or bound forms). The constant C_2 , which we will rename into ρ_0 , is then the average enzyme density, i.e.,

$$\rho_0 = E_{total}/L. \quad (S4.95)$$

Substituting this result into Eq. S4.93, we find an insightful relation between free and bound enzyme densities at an arbitrary position, namely

$$\rho_E(x) = \rho_0 - \rho_{ER}(x) - \rho_{EW}(x). \quad (S4.96)$$

This relation suggests that whenever the local concentration of bound enzymes is high, the local concentration of free enzymes should be correspondingly low, as we see reflected in the profiles of Fig. S4.10.

Deriving the fidelity expression. Next, we consider Eqs. S4.85 and S4.86 separately at steady state, written in the form

$$D \frac{d^2 \rho_{\text{ES}}}{dx^2} - k_{\text{off}}^{\text{S}} \rho_{\text{ES}} = 0. \quad (\text{S4.97})$$

The general solution to this ODE reads

$$\rho_{\text{ES}}(x) = C_1^{\text{S}} e^{-x/\lambda_{\text{ES}}} + C_2^{\text{S}} e^{x/\lambda_{\text{ES}}}, \quad (\text{S4.98})$$

where $\lambda_{\text{ES}} = \sqrt{D/k_{\text{off}}^{\text{S}}}$, and C_1^{S} and C_2^{S} ($\text{S} = \text{R}, \text{W}$) are constants which are different for right and wrong complexes. The no-flux boundary condition at $x = L$ can be used to relate these constants and simplify the complex profile expression, namely

$$-D \left. \frac{d\rho_{\text{ES}}(x)}{dx} \right|_{x=L} = -\frac{D}{\lambda_{\text{ES}}} \left(-C_1^{\text{S}} e^{-L/\lambda_{\text{ES}}} + C_2^{\text{S}} e^{L/\lambda_{\text{ES}}} \right) = 0 \Rightarrow \quad (\text{S4.99})$$

$$C_2^{\text{S}} = e^{-2L/\lambda_{\text{ES}}} C_1^{\text{S}} \Rightarrow \quad (\text{S4.100})$$

$$\begin{aligned} \rho_{\text{ES}}(x) &= C_1^{\text{S}} e^{-x/\lambda_{\text{ES}}} + C_1^{\text{S}} e^{-2L/\lambda_{\text{ES}}} e^{x/\lambda_{\text{ES}}} \\ &= 2C_1^{\text{S}} e^{-L/\lambda_{\text{ES}}} \cosh\left(\frac{L-x}{\lambda_{\text{ES}}}\right) \\ &= \tilde{C}_1^{\text{S}} \cosh\left(\frac{L-x}{\lambda_{\text{ES}}}\right), \end{aligned} \quad (\text{S4.101})$$

where $\tilde{C}_1^{\text{S}} = 2C_1^{\text{S}} e^{-L/\lambda_{\text{ES}}}$ is a new constant coefficient introduced for convenience.

Now, the fidelity of the scheme is the ratio of right and wrong complex densities at $x = L$. Using the result above, the fidelity can be written as

$$\eta = \frac{\rho_{\text{ER}}(L)}{\rho_{\text{EW}}(L)} = \frac{\tilde{C}_1^{\text{R}}}{\tilde{C}_1^{\text{W}}}. \quad (\text{S4.102})$$

The ratio of these constant coefficients can be obtained by noting that the diffusive fluxes of right and wrong complexes at $x = 0$ are identical (from Eqs. S4.88 and S4.89), that is,

$$-D \left. \frac{\partial \rho_{\text{ER}}}{\partial x} \right|_{x=0} = -D \left. \frac{\partial \rho_{\text{EW}}}{\partial x} \right|_{x=0} \Rightarrow \quad (\text{S4.103})$$

$$\tilde{C}_1^{\text{R}} \times \frac{\sinh(L/\lambda_{\text{ER}})}{\lambda_{\text{ER}}} = \tilde{C}_1^{\text{W}} \times \frac{\sinh(L/\lambda_{\text{EW}})}{\lambda_{\text{EW}}} \Rightarrow \quad (\text{S4.104})$$

$$\frac{\tilde{C}_1^{\text{R}}}{\tilde{C}_1^{\text{W}}} = \frac{\lambda_{\text{ER}} \sinh(L/\lambda_{\text{EW}})}{\lambda_{\text{EW}} \sinh(L/\lambda_{\text{ER}})}. \quad (\text{S4.105})$$

Substituting this result into Eq. S4.102, and recalling the equality $L/\lambda_{\text{ES}} = \sqrt{\tau_D k_{\text{off}}^{\text{S}}}$, we obtain

$$\eta = \frac{\sqrt{\tau_D k_{\text{off}}^{\text{W}}} \sinh\left(\sqrt{\tau_D k_{\text{off}}^{\text{W}}}\right)}{\sqrt{\tau_D k_{\text{off}}^{\text{R}}} \sinh\left(\sqrt{\tau_D k_{\text{off}}^{\text{R}}}\right)} = \sqrt{\eta_{\text{eq}}} \frac{\sinh\left(\sqrt{\tau_D k_{\text{off}}^{\text{W}}}\right)}{\sinh\left(\sqrt{\tau_D k_{\text{off}}^{\text{R}}}\right)}. \quad (\text{S4.106})$$

This expression is identical to that in Eq. S4.20 which was derived under the $\rho_{\text{E}}(x) \approx \text{constant}$ assumption, suggesting that when substrates are highly localized, the shape of the free enzyme profile does not dictate the fidelity.

Deriving the speed expression. To keep the expression of speed compact while still illustrating the key consequences of relaxing the $\rho(x) \approx \text{constant}$ assumption, we will assume moving forward that the density of wrong complexes is much lower than that of the right complexes, i.e., $\rho_{\text{EW}}(x) \ll \rho_{\text{ER}}(x)$. This assumption holds as long as the right and wrong complexes have sufficiently different off-rates. To see why it is the case, note that the ratio $\rho_{\text{EW}}(x)/\rho_{\text{ER}}(x)$ is the highest at $x = 0$. We therefore calculate an upper bound for the ratio using Eq. S4.101 and Eq. S4.105 as

$$\frac{\rho_{\text{EW}}(x)}{\rho_{\text{ER}}(x)} < \frac{\rho_{\text{EW}}(0)}{\rho_{\text{ER}}(0)} = \frac{\lambda_{\text{EW}} \tanh(L/\lambda_{\text{ER}})}{\lambda_{\text{ER}} \tanh(L/\lambda_{\text{EW}})} < \frac{\lambda_{\text{EW}}}{\lambda_{\text{ER}}} = \sqrt{\frac{k_{\text{off}}^{\text{R}}}{k_{\text{off}}^{\text{W}}}} = \frac{1}{\sqrt{\eta_{\text{eq}}}}. \quad (\text{S4.107})$$

As long as $\eta_{\text{eq}} \gtrsim 10$, it is fair to assume that the right complexes greatly outnumber the wrong ones, which allows us to approximate the free enzyme density from Eq. S4.96 as $\rho_{\text{E}}(x) \approx \rho_0 - \rho_{\text{ER}}(x)$.

The specification of the right complex density profile requires the knowledge of the unknown coefficient \tilde{C}_1^{R} . To find this coefficient, we use the boundary condition in Eq. S4.88 and the approximation $\rho_{\text{E}}(x) \approx \rho_0 - \rho_{\text{ER}}(x)$ to write

$$D \frac{\tilde{C}_1^{\text{R}}}{\lambda_{\text{ER}}} \sinh(L/\lambda_{\text{ER}}) = k_{\text{on}} S_{\text{total}} \left(\rho_0 - \tilde{C}_1^{\text{R}} \cosh(L/\lambda_{\text{ER}}) \right) \Rightarrow \quad (\text{S4.108})$$

$$\begin{aligned} \tilde{C}_1^{\text{R}} &= \frac{k_{\text{on}} S_{\text{total}} \rho_0}{\frac{D}{\lambda_{\text{ER}}} \sinh(L/\lambda_{\text{ER}}) + k_{\text{on}} S_{\text{total}} \cosh(L/\lambda_{\text{ER}})} \\ &= \frac{k_{\text{on}} S_{\text{total}} \rho_0}{\lambda_{\text{ER}} k_{\text{off}}^{\text{R}} \sinh(L/\lambda_{\text{ER}}) + k_{\text{on}} S_{\text{total}} \cosh(L/\lambda_{\text{ER}})} \\ &= \rho_0 \times \frac{\frac{k_{\text{on}} S_{\text{total}}}{k_{\text{off}}^{\text{R}} L}}{1 + \frac{L \cosh(L/\lambda_{\text{ER}}) k_{\text{on}} S_{\text{total}}}{\lambda_{\text{ER}} \sinh(L/\lambda_{\text{ER}}) k_{\text{off}}^{\text{R}} L}} \times \frac{L/\lambda_{\text{ER}}}{\sinh(L/\lambda_{\text{ER}})}. \end{aligned} \quad (\text{S4.109})$$

With the constant coefficient known, the right complex density then becomes

$$\rho_{\text{ER}}(x) = \rho_0 \times \frac{\frac{\bar{\rho}_s}{K_d^{\text{R}}}}{1 + \frac{L \cosh(L/\lambda_{\text{ER}}) \bar{\rho}_s}{\lambda_{\text{ER}} \sinh(L/\lambda_{\text{ER}}) K_d^{\text{R}}}} \times \frac{L/\lambda_{\text{ER}}}{\sinh(L/\lambda_{\text{ER}})} \cosh\left(\frac{L-x}{\lambda_{\text{ER}}}\right), \quad (\text{S4.110})$$

where we used the definitions of the mean substrate density $\bar{\rho}_s = S_{\text{total}}/L$ and the dissociation constant $K_d^{\text{R}} = k_{\text{off}}^{\text{R}}/k_{\text{on}}^{\text{R}}$.

To enable a direct parallel between this general treatment and the earlier one with the $\rho_{\text{E}}(x) \approx \text{constant}$ approximation, let us introduce $\rho_{\text{ER}}^{\infty}$ as the uniform right complex density when diffusion is very fast ($\lambda_{\text{ER}} \gg L$) and calculate it from Eq. S4.110 as

$$\rho_{\text{ER}}^{\infty} = \rho_0 \times \frac{\frac{\bar{\rho}_s}{K_d^{\text{R}}}}{1 + \frac{\bar{\rho}_s}{K_d^{\text{R}}}}. \quad (\text{S4.111})$$

Now, using the $\rho_{\text{ER}}^{\infty}$ expression, we rewrite Eq. S4.110 as

$$\begin{aligned} \rho_{\text{ER}}(x) &= \frac{1 + \frac{\bar{\rho}_s}{K_d^{\text{R}}}}{1 + \frac{L \cosh(L/\lambda_{\text{ER}}) \bar{\rho}_s}{\lambda_{\text{ER}} \sinh(L/\lambda_{\text{ER}}) K_d^{\text{R}}}} \times \rho_{\text{ER}}^{\infty} \times \frac{L/\lambda_{\text{ER}}}{\sinh(L/\lambda_{\text{ER}})} \cosh\left(\frac{L-x}{\lambda_{\text{ER}}}\right) \\ &= \frac{1 + \frac{\bar{\rho}_s}{K_d^{\text{R}}}}{1 + \underbrace{\frac{L \cosh(L/\lambda_{\text{ER}}) \bar{\rho}_s}{\lambda_{\text{ER}} \sinh(L/\lambda_{\text{ER}}) K_d^{\text{R}}}}_{\gamma}} \times \rho_{\text{ER}}^{\text{const}}(x), \end{aligned} \quad (\text{S4.112})$$

where $\rho_{\text{ER}}^{\text{const}}(x)$ is the complex density obtained under the $\rho_{\text{E}}(x) \approx \text{constant}$ assumption (Eq. S4.15). The extra factor that appears on front does not exceed 1 since $\gamma \geq 1$, indicating a reduction in speed, as we anticipated in our more qualitative discussion at the beginning of the section. The presence of the extra factor suggests two possibilities for the approximation to hold true; first, $\gamma \approx 1$ which happens when $\lambda_{\text{ER}} \gtrsim L$ or when the right complex does not decay noticeably across the compartment, and second, when $\gamma > 1$ and $\bar{\rho}_s \ll \gamma^{-1} K_d^{\text{R}}$, which is when right complexes do decay, but their fraction is low compared with free enzymes because of low substrate concentration.

Let us demonstrate the last statement more explicitly. Specifically, let us show that the validity of the approximation $\rho_{\text{E}}(x) \approx \text{constant}$ is indeed linked directly to the

fraction of bound enzymes. To that end, we evaluate $\rho_E(0)/\rho_E(L)$ as a metric that quantifies the degree to which $\rho_E(x) \approx \text{constant}$ holds. If there is a large depletion of free enzymes near the substrate binding site, then the metric will be significantly less than 1; conversely, if the free enzyme profile is practically flat, then the metric will be close to 1. Invoking the relation $\rho_E(x) \approx \rho_0 - \rho_{ER}(x)$ and using our result for the complex density (Eq. S4.110) as well as the definition of γ in Eq. S4.112, we evaluate this metric as

$$\begin{aligned}
 \frac{\rho_E(0)}{\rho_E(L)} &\approx \frac{\rho_0 - \rho_{ER}(0)}{\rho_0 - \rho_{ER}(L)} \\
 &= \frac{1 - \frac{\gamma \bar{\rho}_s / K_d^R}{1 + \gamma \bar{\rho}_s / K_d^R}}{1 - \frac{\gamma \bar{\rho}_s / K_d^R}{\cosh(L/\lambda_{ER})(1 + \gamma \bar{\rho}_s / K_d^R)}} \\
 &= \frac{1}{1 + \left(1 - \frac{1}{\cosh(L/\lambda_{ER})}\right) \gamma \bar{\rho}_s / K_d^R}. \tag{S4.113}
 \end{aligned}$$

Next, we calculate the fraction of bound enzymes p_{bound} from Eq. S4.110 as

$$\begin{aligned}
 p_{\text{bound}} &\approx E_{\text{total}}^{-1} \int_0^L \rho_{ER}(x) dx \\
 &= \frac{\rho_0 L}{E_{\text{total}}} \frac{\bar{\rho}_s / K_d^R}{1 + \gamma \bar{\rho}_s / K_d^R} \\
 &= \frac{\bar{\rho}_s / K_d^R}{1 + \gamma \bar{\rho}_s / K_d^R}. \tag{S4.114}
 \end{aligned}$$

Note that γ^{-1} emerges as the highest fraction of bound enzymes ($p_{\text{bound}}^{\text{max}}$) reached in the large substrate concentration limit.

To link the metric $\rho_E(0)/\rho_E(L)$ to the fraction of bound enzymes, we express $\bar{\rho}_s / K_d^R$ in terms of p_{bound} and substitute it into Eq. S4.113, namely

$$\begin{aligned}
 \bar{\rho}_s / K_d^R &= \frac{p_{\text{bound}}}{1 - \gamma p_{\text{bound}}} \Rightarrow \tag{S4.115} \\
 \frac{\rho_E(0)}{\rho_E(L)} &= \frac{1}{1 + \left(1 - \frac{1}{\cosh(L/\lambda_{ER})}\right) \frac{\gamma p_{\text{bound}}}{1 - \gamma p_{\text{bound}}}} \\
 &= \frac{1 - \gamma p_{\text{bound}}}{(1 - \gamma p_{\text{bound}}) + \left(1 - \frac{1}{\cosh(L/\lambda_{ER})}\right) \gamma p_{\text{bound}}}
 \end{aligned}$$

$$\begin{aligned}
&= \frac{1 - \gamma p_{\text{bound}}}{1 - \gamma p_{\text{bound}} / \cosh(L/\lambda_{\text{ER}})} \\
&= \frac{p_{\text{bound}}^{\text{max}} - p_{\text{bound}}}{p_{\text{bound}}^{\text{max}} - p_{\text{bound}} / \cosh(L/\lambda_{\text{ER}})}. \tag{S4.116}
\end{aligned}$$

Now, when the complexes do not decay appreciably across the compartment ($\lambda_{\text{ER}} \gtrsim L$ and thus, $\cosh(L/\lambda_{\text{ER}}) \approx 1$), the metric becomes roughly equal to 1, suggesting that the free enzyme profile is practically flat. A more interesting case is when the complexes do decay ($\lambda_{\text{ER}} < L$), as in Fig. S4.10. In this case, applying the condition $\cosh(L/\lambda_{\text{ER}}) \gg 1$, we find

$$\frac{\rho_{\text{E}}(0)}{\rho_{\text{E}}(L)} \approx 1 - \frac{p_{\text{bound}}}{p_{\text{bound}}^{\text{max}}}. \tag{S4.117}$$

The anti-correlation between the $\rho_{\text{E}}(0)/\rho_{\text{E}}(L)$ and p_{bound} in the above result demonstrates that the degree to which the approximation $\rho_{\text{E}}(x) \approx \text{constant}$ is violated is indeed dictated by the fraction of bound enzymes.

Pareto front shift. The previous calculations showed that in the ideal substrate localization limit, relaxing the $\rho(x) \approx \text{constant}$ assumption keeps the fidelity the same while the speed gets reduced, and this reduction is greater for higher substrate concentrations. We therefore expect a shift in the Pareto front when going to the high substrate concentration limit, as is illustrated in Fig. S4.11A. To get more intuition about the effect of this shift caused by tuning the amount of substrates, we consider the effective number of proofreading realizations at half-maximum speed (n_{50}) and study how this number changes as a function of the fraction of enzymes bound (p_{bound}), which increases monotonically with S_{total} as suggested by Eq. S4.114. Fig. S4.11B shows this dependence. As can be seen, n_{50} reduces roughly linearly with p_{bound} ; e.g., if 10% of the enzymes are bound, then a 10% reduction in n_{50} is expected. This suggests that as long as the fraction of bound enzymes is low, our findings related to the Pareto front made under the $\rho_{\text{E}} \approx \text{constant}$ assumption will generally hold true.

S4.5.2 Effects that relaxing the $\rho_{\text{E}}(x) \approx \text{constant}$ assumption has on fidelity in a weak substrate gradient setting

In this section, we study how accounting for the spatial distribution of free enzymes affects our results on the model's fidelity in the setting where substrates have a finite localization length scale λ_{s} . In this setting, Eqs. (1)-(3) (in the main text) describing

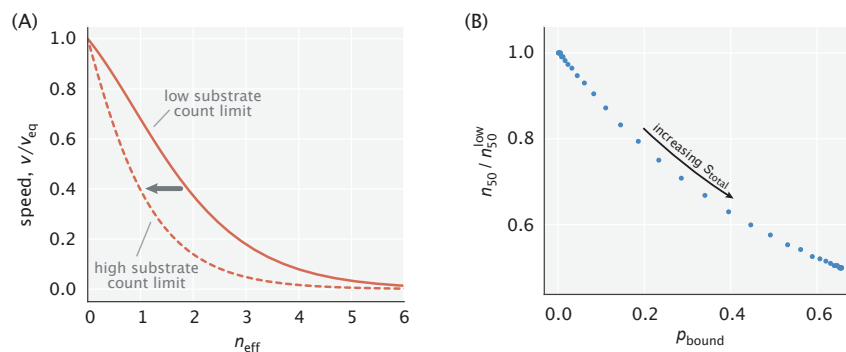


Figure S4.11: Consequences of relaxing the $\rho_E(x) \approx \text{constant}$ assumption on the Pareto front. (A) Pareto fronts in the low and high substrate concentration limits. (B) Reduction in the effective number of proofreading realizations at half-maximum speed as a function of the fraction of enzymes bound. $\eta_{eq} = 10$ was used in making the plots.

the system's dynamics become a system of nonlinear equations, which we solve at steady state using numerical methods.

An example curve of how fidelity changes with tuning diffusion time scale in a finite λ_s setting is shown in Fig. S4.12. As expected, the nonuniform free enzyme profile leads to a reduction in fidelity. This reduction is not significant when diffusion is relatively fast as, in that case, the free enzyme profile manages to flatten out rapidly. The reduction is not significant also in the very slow diffusion limit where binding events that lead to production primarily take place in the proximity of the activation region, and hence, the nonuniform profile of free enzymes across the compartment has little impact on fidelity. The greatest reduction happens at intermediate diffusion time scales; in particular, when the system achieves its peak fidelity.

To quantify the extent of this highest reduction, we calculated the peak value of the effective number of proofreading realizations (n_{max}) for different free substrate amounts which regulate the fraction of bound enzymes (p_{bound}). The results obtained for different choices of λ_s are summarized in Fig. S4.13. As can be seen, for the high substrate localization case ($\lambda_s/L = 0.04$), there is a roughly linear dependence between n_{max} and p_{bound} . The initial decrease in n_{max} with growing p_{bound} is even slower when substrates are less tightly localized ($\lambda_s/L = 0.10, 0.30$).

Taken together, these results suggest that if the substrate concentration is low enough to leave most of the enzymes unbound, then our proposed scheme will proofread efficiently. This requirement on substrate amount will be further relaxed if diffusion is fast, or if substrates are not very tightly localized.

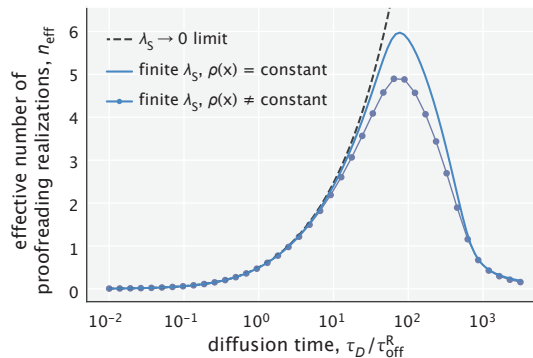


Figure S4.12: Fidelity as a function of diffusion time scale calculated with and without making the $\rho_E(x) \approx \text{constant}$ approximation. The total number of free substrates is chosen so that $\bar{\rho}_S / K_d^R = 3$. The substrate localization length scale used for generating the solid curves is $\lambda_S / L = 0.04$.

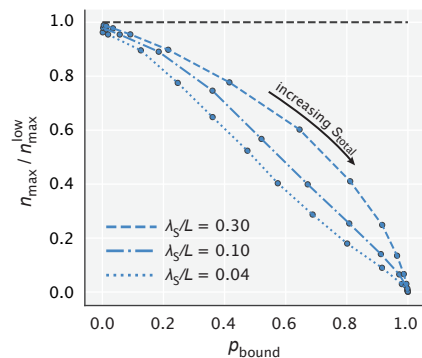


Figure S4.13: Reduction in the peak effective number of proofreading realizations as a function of p_{bound} . $n_{\text{max}}^{\text{low}}$ represents the peak value of n_{eff} in the limit of low substrate concentration (the maximum of the solid blue curve in Fig. S4.12).

S4.6 Proofreading on a kinase/phosphatase-induced gradient

In this section, we introduce the mathematical modeling setup for the kinase/phosphatase-based gradient formation scheme and describe how its fidelity is calculated numerically. In the end, we discuss the energetics of setting up the substrate concentration gradient and link our calculations to the lower bounds on energy cost obtained earlier in Appendix S4.2.

S4.6.1 Setup and estimation of fidelity

In the analysis thus far, we have imposed a gradient of free substrates and analyzed the proofreading capability of an enzyme acting on this gradient. In a living cell, gradients themselves are maintained by active cellular processes. However, the action of the enzyme – that is, binding a substrate in one spatial location, diffusing

away, and releasing the substrate elsewhere – can destroy the gradient, and thereby lead to a loss of proofreading. Here, we analyze the consequences of free substrate depletion and gradient flattening caused by the enzyme.

We model the formation of a substrate gradient by a combination of localized activation and delocalized deactivation. We suppose that substrates can exist in phosphorylated or dephosphorylated forms, and that only the phosphorylated form is capable of binding to the enzyme. The substrates are phosphorylated by a kinase with rate $k_{\text{kin}} = 0.2 \text{ s}^{-1}$, and dephosphorylated by a phosphatase with rate $k_{\text{p}} = 5 \text{ s}^{-1}$. Crucially, we assume that phosphatases are found everywhere in the domain of size $L \sim 10 \mu\text{m}$ (a typical length scale in a eukaryotic cell), while kinases are localized to one end of the domain (at $x = 0$), as may occur naturally if kinases are bound to one of the membranes enclosing the domain.

The minimal dynamics of phosphorylated substrates and enzyme–substrate complexes is then given by

$$\begin{aligned}\frac{\partial \rho_{\text{S}}}{\partial t} &= D \nabla^2 \rho_{\text{S}} - k_{\text{b}} \rho_{\text{S}} + k_{\text{off}}^{\text{S}} \rho_{\text{ES}} - k_{\text{p}} \rho_{\text{S}}, \\ \frac{\partial \rho_{\text{ES}}}{\partial t} &= D \nabla^2 \rho_{\text{ES}} + k_{\text{b}} \rho_{\text{S}} - k_{\text{off}}^{\text{S}} \rho_{\text{ES}},\end{aligned}\tag{S4.118}$$

augmented by the boundary conditions

$$\begin{aligned}\text{Substrate phosphorylation: } & -D \nabla \rho_{\text{S}}|_{x=0} = k_{\text{kin}}, \\ \text{No-flux: } & -D \nabla \rho_{\text{S}}|_{x=L} = -D \nabla \rho_{\text{ES}}|_{x=L} = -D \nabla \rho_{\text{ES}}|_{x=0} = 0.\end{aligned}\tag{S4.119}$$

Here, we have supposed that the densities of free enzymes, dephosphorylated substrates, and phosphatases are fixed and uniform, and have absorbed them into the relevant rate constants ($k_{\text{b}} = k_{\text{on}} \rho_{\text{E}}$, k_{kin} , and k_{p} , respectively). For simplicity, we have also assumed that the free substrates and enzyme–substrate complexes have the same diffusion coefficient $D = 1 \mu\text{m}^2/\text{s}$. We note that accounting for distinct diffusivities of phosphorylated and unphosphorylated substrate forms [9] would affect the speed, while accounting for the slower diffusion of the enzyme–substrate complex would alter the estimates of both speed and fidelity of the model. One or several of these effects can be considered when studying a specific biological system where these microscopic details are known.

We numerically solve Eqs. S4.118 and S4.119 at steady state to obtain the concentration profiles. First, the equations of dynamics are made dimensionless

by setting units of length and time by L ($\bar{x} = x/L$) and $\tau_D \equiv L^2/D$ ($\bar{t} = t/\tau_D$), respectively. At steady state, the dimensionless equations read

$$\begin{aligned}\bar{\nabla}^2 \bar{\rho}_s &= (\bar{k}_b + \bar{k}_p) \bar{\rho}_s - \bar{k}_{\text{off}}^S \bar{\rho}_{\text{ES}}, \\ \bar{\nabla}^2 \bar{\rho}_{\text{ES}} &= -\bar{k}_b \bar{\rho}_s + \bar{k}_{\text{off}}^S \bar{\rho}_{\text{ES}},\end{aligned}\quad (\text{S4.120})$$

with boundary conditions

$$\begin{aligned}\bar{\nabla} \bar{\rho}_s|_{\bar{x}=0} &= -\bar{k}_{\text{kin}}, \\ \bar{\nabla} \bar{\rho}_s|_{\bar{x}=1} &= \bar{\nabla} \bar{\rho}_{\text{ES}}|_{\bar{x}=1} = \bar{\nabla} \bar{\rho}_{\text{ES}}|_{\bar{x}=0} = 0,\end{aligned}\quad (\text{S4.121})$$

where concentrations have been rescaled as $\bar{\rho} = \rho L$, and kinetic rates as $\bar{k} = k \tau_D$.

We discretize the steady state equations on a grid with spacing $\Delta\bar{x} = 0.01$, approximating the second derivative as

$$\bar{\nabla}^2 \bar{\rho} \approx \frac{1}{\Delta\bar{x}^2} (\bar{\rho}(\bar{x} + \Delta\bar{x}) + \bar{\rho}(\bar{x} - \Delta\bar{x}) - 2\bar{\rho}(\bar{x})). \quad (\text{S4.122})$$

This is ill-defined at the boundaries $\bar{x} = 0$ and $\bar{x} = 1$, which is addressed by incorporating the boundary conditions. For illustration, consider the left boundary, $\bar{x} = 0$, and suppose that our domain included also a point at $\bar{x} = -\Delta\bar{x}$. Then, we could approximate the boundary condition $\bar{\nabla} \bar{\rho}_s|_{\bar{x}=0} = -\bar{k}_{\text{kin}}$ by a centered difference scheme, and solve out for the fictional point at $\bar{x} = -\Delta\bar{x}$, namely

$$\begin{aligned}\bar{\nabla} \bar{\rho}_s|_{\bar{x}=0} &= -\bar{k}_{\text{kin}} \\ \Rightarrow \frac{1}{2\Delta\bar{x}} (\bar{\rho}_s(\Delta\bar{x}) - \bar{\rho}_s(-\Delta\bar{x})) &= -\bar{k}_{\text{kin}} \\ \Rightarrow \bar{\rho}_s(-\Delta\bar{x}) &= \bar{\rho}_s(\Delta\bar{x}) + 2\Delta\bar{x} \bar{k}_{\text{kin}},\end{aligned}$$

which, when inserted into Eq. S4.122, specifies $\bar{\nabla}^2 \bar{\rho}_s$ at $\bar{x} = 0$, i.e.,

$$\bar{\nabla}^2 \bar{\rho}_s|_{\bar{x}=0} = \frac{1}{\Delta\bar{x}^2} (2\bar{\rho}_s(\Delta\bar{x}) - 2\bar{\rho}_s(0)) + \frac{2}{\Delta\bar{x}} \bar{k}_{\text{kin}}. \quad (\text{S4.123})$$

For the boundary at the right ($\bar{x} = 1$) as well as for the boundary conditions for $\bar{\rho}_{\text{ES}}$, we similarly implement no-flux boundary conditions. After discretizing, Eq. S4.120 can then be written in a matrix form as

$$\overbrace{\left(\frac{1}{\Delta\bar{x}^2} \begin{pmatrix} -2 & 2 & 0 & \cdots & 0 \\ 1 & -2 & 1 & \cdots & 0 \\ \vdots & \vdots & \vdots & \ddots & \vdots \\ 0 & \cdots & & 1 & -2 & 1 \\ 0 & 0 & \cdots & & 1 & -1 \end{pmatrix} - (\bar{k}_b + \bar{k}_p) \mathbf{I} \right)}^{\mathbf{M}_S} \vec{\rho}_S = -\bar{k}_{\text{off}}^S \vec{\rho}_{\text{ES}} + \overbrace{\begin{pmatrix} -\frac{2}{\Delta\bar{x}} \bar{k}_{\text{kin}} \\ 0 \\ \vdots \\ 0 \\ 0 \end{pmatrix}}^{\vec{b}},$$

$$\underbrace{\begin{pmatrix} \frac{1}{\Delta\bar{x}^2} \begin{pmatrix} -1 & 1 & 0 & \cdots & 0 \\ 1 & -2 & 1 & \cdots & 0 \\ \vdots & \vdots & \vdots & \ddots & \vdots \\ 0 & \cdots & & 1 & -2 & 1 \\ 0 & 0 & \cdots & & 1 & -1 \end{pmatrix} - \bar{k}_{\text{off}}^S \mathbf{I} \end{pmatrix}}_{\mathbf{M}_{\text{ES}}} \vec{\rho}_{\text{ES}} = -\bar{k}_{\text{b}} \vec{\rho}_{\text{S}}, \quad (\text{S4.124})$$

where $\vec{\rho}_{\text{S}}, \vec{\rho}_{\text{ES}}$ are column vectors of the nondimensionalized concentration profiles evaluated at the spatial grid points, i.e., $[\bar{\rho}(0), \bar{\rho}(\Delta\bar{x}), \dots]^T$. Solving these matrix equations yields

$$\begin{aligned} \vec{\rho}_{\text{S}} &= \left(\mathbf{M}_{\text{S}} - \bar{k}_{\text{off}}^S \bar{k}_{\text{b}} \mathbf{M}_{\text{ES}}^{-1} \right)^{-1} \vec{b}, \\ \vec{\rho}_{\text{ES}} &= -\bar{k}_{\text{b}} \left(\mathbf{M}_{\text{S}} \mathbf{M}_{\text{ES}} - \bar{k}_{\text{off}}^S \bar{k}_{\text{b}} \mathbf{I} \right)^{-1} \vec{b}. \end{aligned} \quad (\text{S4.125})$$

We compute Eqs. S4.125 numerically for two substrates: a cognate ('R') and a non-cognate ('W'), which differ in their off-rates ($k_{\text{off}}^{\text{R}} = 0.1 \text{ s}^{-1}$ and $k_{\text{off}}^{\text{W}} = 1 \text{ s}^{-1}$, respectively). Having the density profiles, the fidelity of the model becomes $\eta \approx \bar{\rho}_{\text{ER}}(\bar{x} = 1) / \bar{\rho}_{\text{EW}}(\bar{x} = 1)$. We calculate the fidelity for different choices of the first-order rate of enzyme-substrate binding ($k_{\text{b}} = k_{\text{on}} \rho_{\text{E}}$); this may be thought of as varying the concentration of free enzymes in the cell. The results are shown in Fig. 4.5 of the main text.

S4.6.2 Energy dissipation

In Appendices S4.2.1 and S4.2.3, we estimated lower bounds on the minimum power that needs to be dissipated in order to counter the homogenizing effect that enzyme activity and substrate diffusion, respectively, have on localized substrate profiles. Here, we calculate the energy dissipation required to run the kinase/phosphatase-based mechanism and compare it with these lower bounds estimated earlier.

Let us assume that phosphorylation and dephosphorylation reactions by kinases and phosphatases are nearly irreversible with associated free energy costs of $\Delta\epsilon_{\text{kin}}$ and $\Delta\epsilon_{\text{phosph}}$ per reaction, respectively. The net rate at which active substrates get dephosphorylated is $k_{\text{p}} S_{\text{phosphorylated}}$, and it needs to be identical to the net phosphorylation rate of inactive substrates in order for $S_{\text{phosphorylated}}$ to remain constant. With the costs of each reaction known, we can write the rate of energy dissipation $P_{\text{k/p}}$ as

$$P_{\text{k/p}} = k_{\text{p}} S_{\text{phosphorylated}} (\Delta\epsilon_{\text{kin}} + \Delta\epsilon_{\text{phosph}}). \quad (\text{S4.126})$$

To gain analytical intuition, we first consider the case where the enzyme activity is very low, so that the kinase/phosphatase–based mechanism maintains an exponential profile of active substrates with a decay length scale $\lambda_s = \sqrt{D_s/k_p}$. Expressing the rate of phosphorylation in terms of λ_s and D_s (i.e., $k_p = D_s/\lambda_s^2$), and substituting it into Eq. S4.126, we obtain

$$P_{k/p} = \frac{D_s S_{\text{phosphorylated}}}{\lambda_s^2} (\Delta\varepsilon_{\text{kin}} + \Delta\varepsilon_{\text{phosph}}). \quad (\text{S4.127})$$

Comparing this result with the lower dissipation bound found earlier (Eq. S4.43), we can note the presence of an extra factor $\beta(\Delta\varepsilon_{\text{kin}} + \Delta\varepsilon_{\text{phosph}})$. Since the free energy consumption during ATP hydrolysis is $\sim 10 k_B T$, we can say that the power dissipated by the kinase/phosphatase system for setting up an exponential gradient surpasses the lower limit necessary for counteracting diffusion roughly by an order of magnitude.

Next, we explore the energetics of the kinase/phosphatase–based mechanism in the context of the power–fidelity trade-off. Our study of the trade-off in Fig. 4.4 of the main text was performed under the assumption that substrate profiles were exponentially decaying in the entire spatial domain. In Fig. S4.14A, we show the trade-off curves obtained under this assumption and compare them with the trade-off curve for the kinase/phosphatase–based mechanism that arises in response to changing the substrate localization by tuning k_p . As can be seen, the predicted lower bound (sum of the minimum powers needed to counteract the enzyme action and substrate diffusion) is roughly an order of magnitude lower than the total dissipation of the mechanism, and this difference increases with higher fidelity.

Note, however, that the assumption about an exponential substrate localization is not generally valid for the kinase/phosphatase–based mechanism because substrates can be deposited in low–concentration regions and not get immediately dephosphorylated (Fig. S4.14C). We therefore refine our lower bounds on the dissipated power by estimating them numerically using their generic definitions, namely, Eq. S4.30 for counteracting the enzymatic action, and Eq. S4.42 for counteracting substrate diffusion. These refined estimates suggest a factor of ~ 10 difference between the total cost and its lower bound consistently across a wide region of the trade-off curve. This means that substrate gradient maintenance through practically irreversible phosphorylation and dephosphorylation reactions has low energetic efficiency for doing spatial proofreading, which, however, may be sustainable depending on the energy budget of the cell.

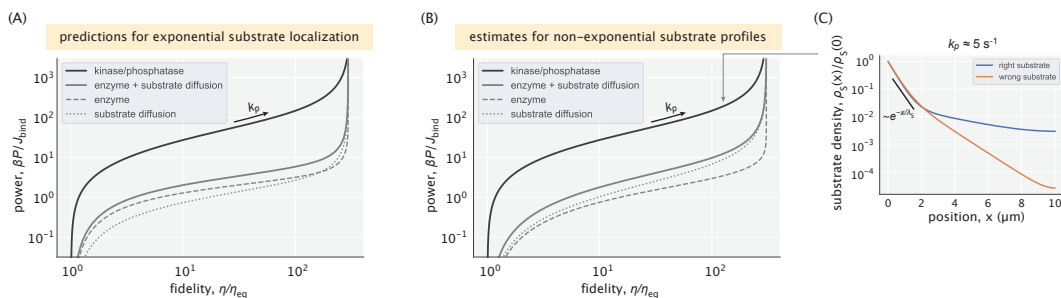
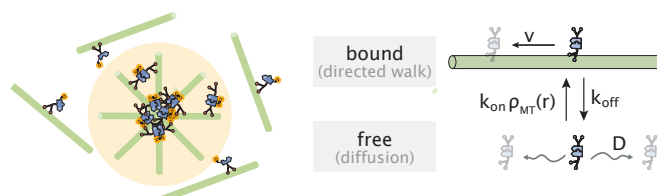


Figure S4.14: Energetic performance of the kinase/phosphatase-based mechanism. (A) Total dissipation and calculated lower bounds under the assumption of exponential substrate localization. (B) Total dissipation and lower bounds estimated without assuming exponential substrate profiles. In both (A) and (B), $k_b = 1 \text{ s}^{-1}$ and $\Delta\varepsilon_{\text{kin}} = \Delta\varepsilon_{\text{phosph}} = 10 k_B T$ were used. (C) Example profiles of right and wrong substrates for the physiologically relevant dephosphorylation rate $k_p = 5 \text{ s}^{-1}$. Exponential decay of the substrate profile with the predicted length scale $\lambda_s = \sqrt{D_s/k_p}$ holds in the first $\sim 2 \mu\text{m}$ of the compartment.

References

1. Hill, T. L. *Free Energy Transduction in Biology* (Academic Press, 1977).
2. Zhang, X. J., Qian, H. & Qian, M. Stochastic theory of nonequilibrium steady states and its applications. Part I. *Phys. Rep.* **510**, 1–86 (2012).
3. Qian, H. Reducing intrinsic biochemical noise in cells and its thermodynamic limit. *J. Mol. Biol.* **362**, 387–392 (2006).
4. Feric, M. & Brangwynne, C. P. A nuclear F-actin scaffold stabilizes ribonucleoprotein droplets against gravity in large cells. *Nat. Cell Biol.* **15**, 1253–1259 (2013).
5. Hansen, C. H., Yang, D., Koussa, M. A. & Wong, W. P. Nanoswitch-linked immunosorbent assay (NLISA) for fast, sensitive, and specific protein detection. *Proc. Natl. Acad. Sci. U.S.A.* **114**, 10367–10372 (2017).
6. Hopfield, J. J. Kinetic proofreading: A new mechanism for reducing errors in biosynthetic processes requiring high specificity. *Proc. Natl. Acad. Sci. U.S.A.* **71**, 4135–4139 (1974).
7. Wong, F., Amir, A. & Gunawardena, J. Energy-speed-accuracy relation in complex networks for biological discrimination. *Phys. Rev. E* **98**, 012420 (2018).
8. Murugan, A., Huse, D. A. & Leibler, S. Discriminatory proofreading regimes in nonequilibrium systems. *Phys. Rev. X* **4**, 021016 (2014).
9. Kholodenko, B. N. Spatially distributed cell signalling. *FEBS Lett.* **583**, 4006–4012 (2009).

Chapter 5

SPATIAL ORGANIZATION OF MOTORS IN MICROTUBULE
ASTERS

This chapter is based on the theory and modeling components of a manuscript in preparation: Banks, R. A., Galstyan, V., Lee, H. J., Hirokawa, S., Ross, T., Ierokomos, A., Bryant, Z., Thomson, M. & Phillips, R. Kinesin motor properties determine size and formation speed of motor-microtubule assemblies.

5.1 Introduction

The cytoskeleton, comprised of a mixture of filaments, motors, and passive crosslinkers, is an integral component of the cell responsible for many of its vital functions. One of the key cytoskeletal structures is the spindle – a football-shaped bipolar organization of motors, microtubules, and microtubule-associated proteins, that is responsible for chromosome segregation during cell division.

While many of the spindle components are known, our understanding of the principles of its self-organization and maintenance is still incomplete. To understand these principles with a bottom-up approach, *in vitro* experiments with mixtures of minimal components (tubulin, motors, and energy source) have been conducted, managing to recapitulate various ordered structures present in the spindle such as dynamic asters of microtubules or microtubule bundles. Since the earliest reconstitution work [1], experimental techniques and the complexity of studies have advanced [2, 3], with one of the most recent developments being the optogenetic control of microtubule organization through a light-activatable dimerization of the crosslinking motors [4].

Applying this novel optogenetic tool, we formed asters using motors of different kinds (kinesin-1 (K401), kinesin-5 (Kif11), and kinesin-14 (Ncd)) and studied the link between the microscopic properties of motors (Table 5.1) and their corresponding

Motor	Speed	Processivity	Direction
K401	600 nm/s	100 steps [5]	plus [6]
Ncd236	115 nm/s	≈ 1 step [7]	minus [8]
Kif11(513)	70 nm/s	10 steps [9]	plus [9]

Table 5.1: Motor proteins used and their properties.

structures. Here, we present our theoretical efforts to capture the spatial distribution of the various motors in the formed aster structures. Developing a minimal model, we identified key effective microscopic parameters that define the motor distribution. Our model manages to capture the measured profiles with high accuracy, yielding motor-specific effective parameters that can be linked to their microscopic properties, such as their speed or processivity. Further, we explore the shapes of the motor and tubulin distributions and find that the latter is necessarily broader. We use our minimal model to provide insights on this observation and end by commenting on its physiological relevance. Overall, the modeling work presented here is a rigorous characterization of the self-organization principles of microtubule-motor assemblies.

5.2 A minimal model accurately captures the observed motor profiles

The nonuniform distribution of filaments and motors in an aster is a key feature of its organization and has been the subject of previous studies. In these studies, continuum models were developed for motor-filament mixtures which predicted the radial profile of motors in confined two-dimensional systems [10–13]. A notable example is the power-law decay prediction by Nedelec *et al.*, who obtained it for a prescribed organization of microtubules obeying a $1/r$ decay law [10]. Measuring the motor profiles in asters formed in a quasi-two-dimensional geometry (with the z dimension of the sample being only a few microns deep) and fitting them to a power-law decay, the authors found a reasonable yet noisy match between the predicted and measured trends in the decay exponent.

In our work, we also develop and test a minimal model that predicts the motor profile from the microtubule distribution and the microscopic properties of the motor. In contrast to the earlier study [10], asters formed in our experiments are three-dimensional due to the much larger depth of the flow cells (roughly 100 μm). While the largest asters are likely partially compressed in the z -direction, we assume that this effect does not significantly alter the protein distributions in the central z -slice and hence, for modeling purposes we consider our asters to be

radially symmetric, as depicted schematically in Fig. 5.1A. Our modeling applies to locations outside the central disordered region (called aster ‘core’), beyond which microtubules have a predominantly polar organization.

Similar to the treatment in earlier works [10, 12, 13], we introduce two states of the motor - an unbound state where the motor can freely diffuse with a diffusion constant D and a bound state where the motor walks towards the aster center with a speed v (Fig. 5.1B). In the steady-state of the system, which we assume our asters have reached at the end of the experiment, microtubules on average have no radial movement and hence, do not contribute to motor speed. We denote the rates of motor binding and unbinding by k_{on} and k_{off} , respectively. When defining the first-order rate of motor binding, namely, $k_{\text{on}}\rho_{\text{MT}}(r)$, we explicitly account for the local microtubule concentration $\rho_{\text{MT}}(r)$ extracted from fluorescence images. This is unlike the previous models which imposed specific functional forms on the microtubule distribution (e.g., a constant value [11, 12], or a power-law decay [10]), making them unable to capture the specific features often seen in our measured microtubule profiles, such as the presence of an inflection point.

The governing equations for the bound (m_b) and free (m_f) motor concentrations are shown in Fig. 5.1C. They involve binding and unbinding terms, as well as a separate flux divergence term for each population. Solving them at steady-state, we arrive at an equation for the total local concentration of motors defined as $m_{\text{tot}}(r) = m_b(r) + m_f(r)$. The derivation of this result can be found in Appendix S5.1. As seen in the equation for $m_{\text{tot}}(r)$ (Fig. 5.1C), knowing the microtubule distribution $\rho_{\text{MT}}(r)$ along with two effective microscopic parameters, namely the dissociation constant $K_d = k_{\text{off}}/k_{\text{on}}$ and the length scale $\lambda_0 = D/v$, one can obtain the motor distribution up to a multiplicative constant (C in the equation). Note that in the special case where the motors do not move ($v \rightarrow 0$ or $\lambda_0 \rightarrow \infty$), the exponential term becomes 1 and an equilibrium relation between the motor and microtubule distributions dependent only on K_d is recovered.

To test this model, we extract the average radial distributions of microtubule and motor concentrations for each aster. Then, using the microtubule profile as an input, we fit our model to the motor data and infer the effective parameters K_d and λ_0 (see Appendices S5.2 and S5.3 for details). A demonstration of this procedure on an example Kif aster is shown in Fig. 5.1D where a good fit to the average motor data can be observed. As a validation of our inference method, we additionally extract the radial concentration profiles inside separate wedges of the aster and show

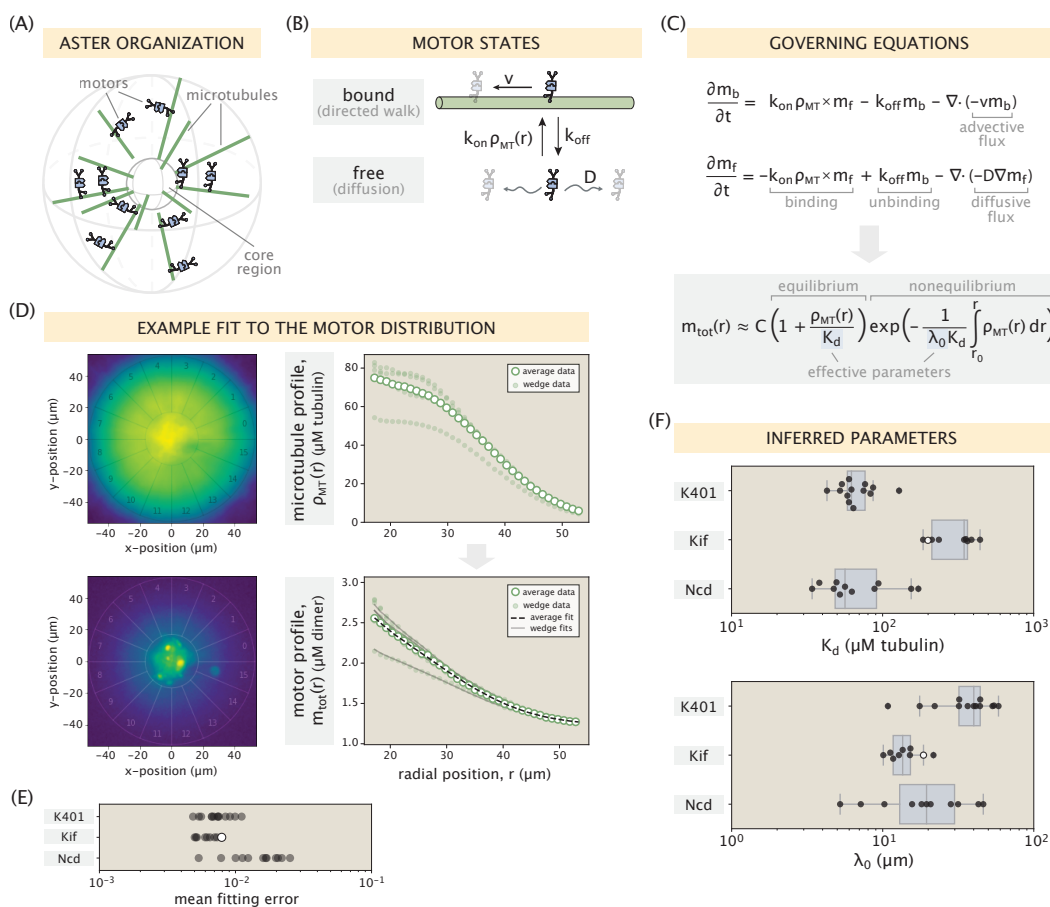


Figure 5.1: Modeling the motor distribution. (A) Schematic of the radial microtubule organization in an aster. Modeling applies to locations outside the disordered core region at the aster center. (B) Motor states and transitions between them. (C) Governing equations for the bound and free motor populations, along with our solution for the total motor distribution at steady state (see Appendix S5.1 for details). (D) Demonstration of the model fitting procedure on an example Kif aster. Fits to the average motor profile as well as to 5 out of 16 wedge profiles are shown. The outlier case with a lower concentration corresponds to wedge 13 in the fluorescence images. (E) Mean fitting errors for all asters calculated from the fits to the wedge profiles. The error is defined as the ratio of the mean residual to the concentration value at the inner boundary. (F) Inferred parameters K_d and λ_0 grouped by the kind of motor. Box plots indicate the quartiles of the inferred parameter. The white dots in panels E and F represent the corresponding values for the Kif aster in panel D.

that they can be accurately captured by only choosing an appropriate multiplicative constant C for each wedge, while keeping the pair (K_d, λ_0) inferred from average profile fixed (fits to 5 out of 16 different wedge profiles are shown in Fig. 5.1D for clarity). The fitting error for other asters is similarly low (Fig. 5.1E, see Fig. S5.3 for the collection of fitted profiles).

Plotting the inferred parameters K_d and λ_0 from all fits (Fig. 5.1F), we find that they are clustered around single values for each motor type and vary between the motors. Based on the single-molecule motor properties, our expectation was that the highly processive K401 motors would have the lowest K_d , while the opposite would be true for Ncd motors. However, the inferred K_d for Ncd looks comparable to that of K401. One possible resolution of this discrepancy comes from the finding of an *in vitro* study that suggested a substantial increase in the processivity of Ncd motors that act collectively [14]. Specifically, a pair of Ncd motors coupled through a DNA scaffold was shown to have a processivity reaching $1\ \mu\text{m}$ (or, ≈ 100 steps) – a value similar to that reported for K401 motors. This collective effect, likely realized for Ncd motors in highly concentrated aster structures, is therefore a possible cause for the low inferred values of their effective K_d .

Next, looking at the inference results for the λ_0 parameter (Fig. 5.1F), we can see that Kif and Ncd motors have an average λ_0 value of $\approx 10 - 20\ \mu\text{m}$, while the average value for K401 motors is $\approx 40\ \mu\text{m}$. From the measured diffusion coefficient of $D \approx 1\ \mu\text{m}^2/\text{s}$ for tagged kinesin motors [15] and the single-molecule motor speeds reported in Table 5.1, our guess for the λ_0 parameter for Kif and Ncd motors was $\approx 10 - 15\ \mu\text{m}$, and $\approx 2\ \mu\text{m}$ for K401. While the inferred values for the two slower motors are well within the order-of-magnitude of our guess, the inferred λ_0 for K401 is much higher than what we anticipated. This suggests a significant reduction in the effective speed. One contributor to this reduction is the stalling of motors upon reaching the microtubule ends. Recall that in our model formulation (Fig. 5.1B), we assumed an unobstructed walk for bound motors. Since the mean length of microtubules ($\approx 2\ \mu\text{m}$) is comparable to the processivity of K401 motors ($\approx 1\ \mu\text{m}$), stalling events at microtubule ends will be common, leading to a reduction of their effective speed by a factor of ≈ 1.5 (see Appendix S5.4 for details). This correction alone, however, is not sufficient to capture the factor of ≈ 25 discrepancy between our inference and the estimate of λ_0 . We hypothesize that an additional contribution may come from the jamming of K401 motors in dense aster regions. This is motivated by the experiments which showed that K401 motors would pause when encountering obstructions during their walk [16, 17]. Overall, our study shows that the minimal model of motor distributions proposed in Fig. 5.1 is able to capture the distinctions in aster structure through motor-specific effective parameters.

5.3 Microtubules in an aster have a broader distribution than motors

In addition to being able to tell the motor distribution from the microtubule distribution, it is also of interest to study how the shapes of these two distributions compare to each other. Such a question was studied theoretically for actomyosin asters, where the formation of a broader ‘cloud’ of myosin motors over a narrower actin profile was predicted, and this particular arrangement was shown to be important for aster integrity and dynamics [18].

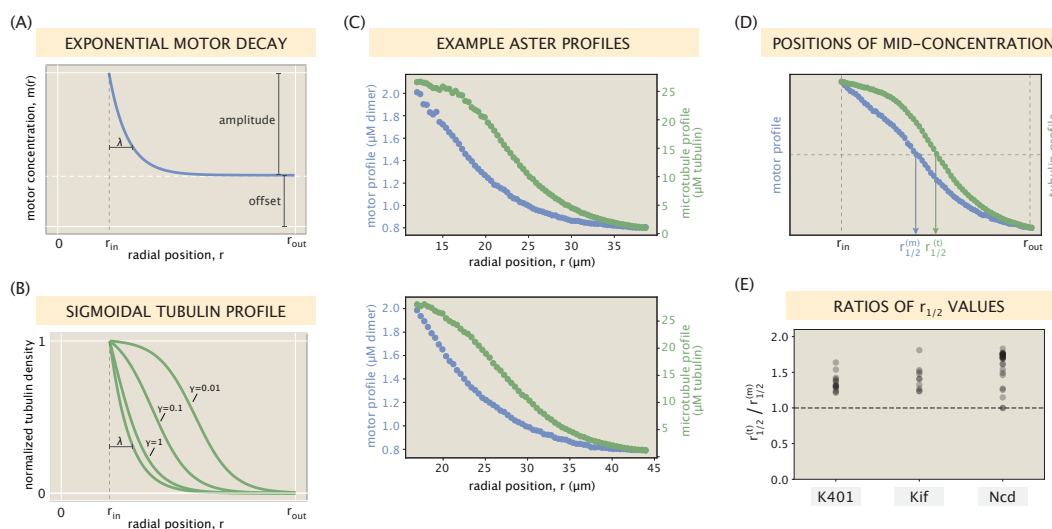


Figure 5.2: Relationship between motor and microtubule distributions. (A) An idealized exponentially decaying motor profile with a constant offset. (B) Set of sigmoidal tubulin profiles corresponding to the exponentially decaying motor profile. The precise curve depends on the shape parameters of the motor profile and the motor type via an effective constant γ (see Appendix S5.5 for details). (C) Two example profiles from Ncd asters that resemble the setting in panels A and B. Blue and green dots represent measured concentrations of motors and microtubules, respectively. (D) Radial positions in the $[r_{in}, r_{out}]$ interval where the motor and tubulin concentrations take their middle values. (E) The ratio $r_{1/2}^{(t)}/r_{1/2}^{(m)}$ calculated for all of the aster profiles.

To gain analytical insights about this question for our system, we first consider an idealized scenario where the motor profile can be represented as an exponential decay with a constant offset for the free motor population (Fig. 5.2A). Such a scenario is approximately met for many of our measured motor profiles. Using the modeling framework in Fig. 5.1A-C, we find that the microtubule distribution corresponding to such a motor profile has the shape of a truncated sigmoid (Fig. 5.2B, see Appendix S5.5 for the derivation). Indeed, microtubule distributions resembling

a sigmoidal shape are observed often in our asters (Fig. S5.3), two examples of which are shown in Fig. 5.2C.

One notable implication of this analytical connection between the two profiles is that, unlike the analogous actomyosin case [18], microtubules necessarily have a broader distribution than motors, once the offset levels at the aster edge are subtracted off. To find whether this is a ubiquitous feature of our asters, we introduce radial distances $r_{1/2}^{(m)}$ and $r_{1/2}^{(t)}$ standing for the positions where the motor and tubulin distributions, respectively, are at their mid-concentrations (Fig. 5.2D). The ratio $r_{1/2}^{(t)}/r_{1/2}^{(m)}$, if greater than 1, would then be an indicator of a wider tubulin profile. Calculating this ratio for all of our asters, we find that it is always greater than or very close to 1 for all motor types (Fig. 5.2E), suggesting the generality of the feature. This feature may be an important factor in the spatial organization of end-directed motors (e.g., dynein) in the spindle where their localization to the spindle pole is of physiological importance.

References

1. Nédélec, F. J., Surrey, T., Maggs, A. C. & Leibler, S. Self-organization of microtubules and motors. *Nature* **389**, 305 (1997).
2. Sanchez, T., Chen, D. T. N., DeCamp, S. J., Heymann, M. & Dogic, Z. Spontaneous motion in hierarchically assembled active matter. *Nature* **491**, 431.
3. DeCamp, S. J., Redner, G. S., Baskaran, A., Hagan, M. F. & Dogic, Z. Orientational order of motile defects in active nematics. *Nat. Mater.* **14**, 1110 (2015).
4. Ross, T. D., Lee, H. J., Qu, Z., Banks, R. A., Phillips, R. & Thomson, M. Controlling organization and forces in active matter through optically defined boundaries. *Nature* **572**, 224–229 (2019).
5. Block, S. M., Goldstein, L. S. B. & Schnapp, B. J. Bead movement by single kinesin molecules studied with optical tweezers. *Nature* **348**, 348–352 (1990).
6. Hirokawa, N., Sato-Yoshitake, R., Kobayashi, N., Pfister, K. K., Bloom, G. S. & Brady, S. T. Kinesin associates with anterogradely transported membranous organelles in vivo. *J. Cell Biol.* **114**, 295–302 (1991).
7. deCastro, M. J., Fondecave, R. M., Clarke, L. A., Schmidt, C. F. & Stewart, R. J. Working strokes by single molecules of the kinesin-related microtubule motor ncd. *Nat. Cell Biol.* **2**, 724–729 (2000).
8. Walker, R. A., Salmon, E. D. & Endow, S. A. The *Drosophila* claret segregation protein is a minus-end directed motor molecule. *Nature* **347**, 780–782 (1990).

9. Valentine, M. T., Fordyce, P. M., Krzysiak, T. C., Gilbert, S. P. & Block, S. M. Individual dimers of the mitotic kinesin motor Eg5 step processively and support substantial loads *in vitro*. *Nat. Cell Biol.* **8**, 470–476 (2006).
10. Nédélec, F., Surrey, T. & Maggs, A. C. Dynamic concentration of motors in microtubule arrays. *Phys. Rev. Lett.* **86**, 3192–3195 (2001).
11. Lee, H. Y. & Kardar, M. Macroscopic equations for pattern formation in mixtures of microtubules and molecular motors. *Phys. Rev. E* **64**, 056113 (2001).
12. Sankararaman, S., Menon, G. I. & Kumar, P. S. Self-organized pattern formation in motor–microtubule mixtures. *Phys. Rev. E* **70**, 031905 (2004).
13. Aranson, I. S. & Tsimring, L. S. Theory of self-assembly of microtubules and motors. *Phys. Rev. E* **74**, 031915 (2006).
14. Furuta, K. Y., Furuta, A., Toyoshima, Y. Y., Amino, M., Oiwa, K. & Kojima, H. Measuring collective transport by defined numbers of processive and nonprocessive kinesin motors. *Proc. Natl. Acad. Sci. U.S.A.* **110**, 501–506 (2013).
15. Grover, R., Fischer, J., Schwarz, F. W., Walter, W. J., Schwille, P. & Diez, S. Transport efficiency of membrane-anchored kinesin-1 motors depends on motor density and diffusivity. *Proc. Natl. Acad. Sci. U.S.A.* **113**, E7185–E7193 (2016).
16. Ferro, L. S., Can, S., Turner, M. A., ElShenawy, M. M. & Yildiz, A. Kinesin and dynein use distinct mechanisms to bypass obstacles. *Elife* **8**, e48629 (2019).
17. Schneider, R., Korten, T., Walter, W. J. & Diez, S. Kinesin-1 motors can circumvent permanent roadblocks by side-shifting to neighboring protofilaments. *Biophys. J.* **108**, 2249–2257 (2015).
18. Husain, K. & Rao, M. Emergent structures in an active polar fluid: Dynamics of shape, scattering, and merger. *Phys. Rev. Lett.* **118**, 078104 (2017).

SUPPORTING INFORMATION FOR CHAPTER 5 |
SPATIAL ORGANIZATION OF MOTORS IN MICROTUBULE
ASTERS

S5.1 Model formulation

To predict the spatial distribution of motors in aster structures, we model the dynamic steady state of free ('f') and bound ('b') motor concentrations via

$$\frac{\partial m_b}{\partial t} = k_{\text{on}}\rho_{\text{MT}}(\mathbf{r})m_f(\mathbf{r}) - k_{\text{off}}m_b(\mathbf{r}) - \nabla \cdot \mathbf{J}_v = 0, \quad (\text{S5.1})$$

$$\frac{\partial m_f}{\partial t} = -k_{\text{on}}\rho_{\text{MT}}(\mathbf{r})m_f(\mathbf{r}) + k_{\text{off}}m_b(\mathbf{r}) - \nabla \cdot \mathbf{J}_D = 0. \quad (\text{S5.2})$$

Here, k_{on} and k_{off} are the motor binding and unbinding rates, respectively, $\rho_{\text{MT}}(\mathbf{r})$ is the spatially varying steady state microtubule concentration (measured as μM tubulin), \mathbf{J}_v is the advective flux of bound motors, and \mathbf{J}_D is the diffusive flux of free motors. Our modeling approach is similar to that used by Nédélec *et al.* [1] with the main difference being in the handling of $\rho_{\text{MT}}(\mathbf{r})$. Namely, they imposed a particular functional form on this distribution ($\rho_{\text{MT}}(\mathbf{r}) = 1/|\mathbf{r}|^{d-1}$ with d as the spatial dimension) based on an idealized representation of microtubule organization in an aster, whereas in our treatment, $\rho_{\text{MT}}(\mathbf{r})$ stands for the experimentally measured microtubule profiles which cannot be captured through an analogous idealization.

If the free motors have a diffusion coefficient D , then, in the radially symmetric setting considered in our modeling, the diffusive flux will be given by

$$\mathbf{J}_D(r) = -D\nabla m_f(\mathbf{r}) = -Dm'_f(r)\hat{\mathbf{r}}, \quad (\text{S5.3})$$

where $\hat{\mathbf{r}}$ is an outward-pointing unit radial vector. And if v is the advection speed of bound motors, then the advective motor flux on radially organized microtubules will be

$$\mathbf{J}_v(r) = -vm_b(r)\hat{\mathbf{r}}. \quad (\text{S5.4})$$

Here, we are implicitly assuming that motors constantly walk when bound, ignoring the fact that they can stall upon reaching a microtubule end. We discuss the impact of this effect later in Appendix S5.4.

At steady state, the net flux of motors at any radial distance r should be zero ($\mathbf{J}_D(r) + \mathbf{J}_v(r) = 0$), which implies a general relation between the profiles of free and bound motors, namely

$$0 = -Dm'_f(r)\hat{\mathbf{r}} - vm_b(r)\hat{\mathbf{r}} \Rightarrow$$

$$m_b(r) = - \underbrace{\left(\frac{D}{v}\right)}_{\lambda_0} m'_f(r). \quad (\text{S5.5})$$

Above we introduced λ_0 as a length scale parameter that can be interpreted as the distance which is traveled by free and bound motors at similar time scales, i.e., diffusion time scale (λ_0^2/D) = advection time scale (λ_0/v). Note also that the ‘-’ sign at the right-hand side indicates that the free motor population should necessarily have a decaying radial profile ($m'_f(r) < 0$) which is intuitive since at steady state the outward diffusion needs to counteract the inward advection.

To make further analytical progress, we will assume that motor binding and unbinding events are locally equilibrated [2]. This assumption is valid if motor transport is sufficiently slow compared with binding/unbinding reactions. We will justify this quasi-equilibrium condition for the motors used in our study at the end of the section. It follows from this condition that

$$k_{\text{off}}m_b(r) \approx k_{\text{on}}\rho_{\text{MT}}(r)m_f(r) \Rightarrow$$

$$m_b(r) \approx \frac{\rho_{\text{MT}}(r)}{K_d} m_f(r), \quad (\text{S5.6})$$

where $K_d = k_{\text{off}}/k_{\text{on}}$ is the dissociation constant. Since the experimental readout reflects the *total* motor concentration ($m_{\text{tot}} = m_f + m_b$), we use our results (Eq. S5.5 and Eq. S5.6) to link $m_{\text{tot}}(r)$ with the microtubule profile $\rho_{\text{MT}}(r)$. Specifically, using Eq. S5.6, we find

$$m_{\text{tot}}(r) = m_b(r) + m_f(r)$$

$$= \left(1 + \frac{\rho_{\text{MT}}(r)}{K_d}\right) m_f(r) \Rightarrow \quad (\text{S5.7})$$

$$m_f(r) = \frac{K_d}{K_d + \rho_{\text{MT}}(r)} m_{\text{tot}}(r), \quad (\text{S5.8})$$

$$m_b(r) = \frac{\rho_{\text{MT}}(r)}{K_d + \rho_{\text{MT}}(r)} m_{\text{tot}}(r). \quad (\text{S5.9})$$

Next, substituting the above expressions for m_f and m_b into Eq. S5.5 and simplifying, we relate the motor and microtubule profiles, namely

$$\begin{aligned} \frac{\rho_{\text{MT}}(r)}{K_d + \rho_{\text{MT}}(r)} m_{\text{tot}}(r) &= -\lambda_0 \underbrace{\left(\frac{K_d}{K_d + \rho_{\text{MT}}(r)} m'_{\text{tot}}(r) - \frac{K_d \rho'_{\text{MT}}(r)}{(K_d + \rho_{\text{MT}}(r))^2} m_{\text{tot}}(r) \right)}_{m'_f(r)} \Rightarrow \\ \frac{m'_{\text{tot}}(r)}{m_{\text{tot}}(r)} &= -\frac{\rho_{\text{MT}}(r)}{K_d \lambda_0} + \frac{\rho'_{\text{MT}}(r)}{K_d + \rho_{\text{MT}}(r)} \Rightarrow \\ (\ln m_{\text{tot}}(r))' &= -\frac{\rho_{\text{MT}}(r)}{K_d \lambda_0} + (\ln(K_d + \rho_{\text{MT}}(r)))' \Rightarrow \\ \ln m_{\text{tot}}(r) &= -\frac{R_{\text{MT}}(r)}{K_d \lambda_0} + \ln(K_d + \rho_{\text{MT}}(r)) + C_1 \Rightarrow \\ m_{\text{tot}}(r) &= C \left(1 + \frac{\rho_{\text{MT}}(r)}{K_d} \right) \exp\left(-\frac{R_{\text{MT}}(r)}{K_d \lambda_0}\right), \end{aligned} \quad (\text{S5.10})$$

where $R_{\text{MT}}(r) = \int \rho_{\text{MT}}(r) dr$ is the integrated microtubule concentration, and $C = K_d e^{C_1}$ is a positive constant. The presence of the multiplicative constant C is a consequence of the fact that the two equations used for deriving our result (Eq. S5.5 and Eq. S5.6) specify the *ratios* of motor populations. Therefore, the result in Eq. S5.10 predicts the relative level of the total motor concentration, given the two effective model parameters (K_d and λ_0), which we infer in our fitting procedure.

Note that the two variable factors on the right-hand side of Eq. S5.10 have qualitatively different structures. The first one is local and depends only on the dissociation constant (an equilibrium parameter), while the second term involves an integrated (hence, non-local) microtubule density term and $\lambda_0 = D/v$ which depends on the advection speed v (a non-equilibrium parameter). As anticipated, in the limit of vanishingly slow advection ($v \rightarrow 0$ or, $\lambda_0 \rightarrow \infty$) the second factor becomes 1 and an equilibrium result is recovered.

Connections to related works

Before proceeding further into our analysis, we briefly compare the expression for the motor distribution (Eq. S5.10) with analogous results in the literature. Specifically, Nédélec *et al.* [1] studied quasi-two-dimensional asters and in their modeling treated microtubules as very long filaments, all converging at the aster center. This setting implied $\sim 1/r$ scaling of the microtubule concentration. With this scaling, the integrated microtubule concentration in our framework becomes $R_{\text{MT}}(r) = \int \frac{\alpha}{r} dr = \alpha \ln r$ where α is a constant. Substituting this form into the exponential term in Eq. S5.10, we find $\exp\{-(K_d \lambda_0)^{-1} R_{\text{MT}}(r)\} = \exp\{-\alpha (K_d \lambda_0)^{-1} \ln r\} \sim 1/r^\beta$, where

$\beta = \alpha(K_d\lambda_0)^{-1}$. It then follows from Eq. S5.10 and the scaling $\rho_{\text{MT}}(r) \sim 1/r$ that the motor concentration is a sum of two decaying power laws (namely $\sim 1/r^\beta$ and $\sim 1/r^{\beta+1}$) – the result obtained by Nédélec *et al.* [1]. A more detailed calculation can be done to demonstrate that the exponent β matches exactly with the result derived in the earlier work, but for the purposes of our study we do not elaborate further on this comparison. We note that the experimentally measured microtubule profiles in asters (e.g., Fig. 2b or Fig. 3d) often have an inflection point and cannot be fitted to decaying power law functions (e.g., $1/r^2$ for 3D asters), which is why the idealized setting considered by Nédélec *et al.* [1] cannot be applied to our system.

Another set of works [3, 4] also studied motor distributions in asters, but this time under the assumption of a uniform microtubule concentration ($\rho_{\text{MT}}(r) \sim \text{constant}$). In such a setting, our framework predicts an exponentially decaying motor profile, because $R_{\text{MT}}(r) = \int \rho_{\text{MT}}(r) dr \sim \rho_{\text{MT}}r$ and thus, $m_{\text{tot}}(r) \sim e^{-\rho_{\text{MT}}r/K_d\lambda_0}$. An exponential decay was also the prediction of Lee and Kardar [3], although in their treatment, all motors were assumed to be in the bound state. The two distinct motor states were considered in the work by Sankararaman *et al.* [4] who predicted an exponential decay of motor concentration modulated by a power-law tail. One can show, however, that when the decay length scale of motor concentration greatly exceeds the motor processivity (as in the case of asters which we generated), the prediction of Sankararaman *et al.* [4] also reduces into a pure exponential decay, matching the prediction of our model. But since the assumption of a uniform microtubule profile is clearly violated in our system, these predictions are not applicable for us.

Validity of the quasi-equilibrium assumption

Earlier in the section, we assumed that motor binding and unbinding reactions were locally equilibrated, from which Eq. S5.6 followed. Looking at the governing equation of bound motor dynamics (Eq. S5.1), we can see that this assumption will hold true if $k_{\text{off}}m_b(r) \gg |\nabla \cdot \mathbf{J}_v|$. Substituting the expression of advective flux (Eq. S5.4) and recalling that in three dimensions, the divergence of a radial vector $\mathbf{A} = A\hat{\mathbf{r}}$ takes the form $r^{-2}\partial_r(r^2A)$, we rewrite the quasi-equilibrium condition as

$$k_{\text{off}}m_b(r) \gg |\nabla \cdot (-vm_b(r)\hat{\mathbf{r}})| \Rightarrow \quad (\text{S5.11})$$

$$\frac{k_{\text{off}}}{v}m_b(r) \gg \left| m'_b(r) + \frac{2}{r}m_b(r) \right|. \quad (\text{S5.12})$$

Now, many of the motor profiles can be approximated reasonably well by an exponentially decaying function (see Fig. S5.3 for a collection of experimental

motor	processivity (steps)	processivity, λ_v (μm)	decay length scale, λ (μm)	λ/λ_v
K401	≈ 100	1	10–40	10–40
Ncd236	≈ 1	10^{-2}	5–20	500–2000
Kif11(513)	≈ 10	10^{-1}	10–20	100–200

Table S5.1: Processivities of motors, decay length scales of motor profiles, and corresponding ratios of these two length scales. Step size of ≈ 10 nm corresponding to the length of a tubulin dimer was used for estimating the motor processivities in μm units. Estimates for the decay length scales λ were made based on the motor profiles in Fig. S5.3.

profiles). This suggests an empirical functional form $m_b(r) \sim e^{-r/\lambda}$ for the concentration of bound motors, where λ is the decay length scale (note that the constant saturation level contributes to the *free* motor population). This functional form implies that $m'_b(r) \approx -m_b(r)/\lambda$, which, upon substituting into Eq. S5.12, leads to

$$\underbrace{\frac{k_{\text{off}}}{v}}_{\lambda_v^{-1}} m_b(r) \gg \left| -\frac{1}{\lambda} m_b(r) + \frac{2}{r} m_b(r) \right| \Rightarrow \quad (\text{S5.13})$$

$$\frac{\lambda}{\lambda_v} \gg \left| \frac{2\lambda}{r} - 1 \right|, \quad (\text{S5.14})$$

where $\lambda_v = v/k_{\text{off}}$ is introduced as the motor processivity (distance traveled before unbinding). The processivities (λ_v) of the three different kinesins used in our study, together with the observed ranges of decay length scales (λ) of corresponding motor profiles are listed in Table S5.1. As can be seen, in all cases the ratio λ/λ_v is much greater than one, verifying the intuitive expectation that the length scales of aster structures are much greater than the single run lengths of motors.

It is obvious from the presence of the r^{-1} term on the right-hand side of Eq. S5.14 that the condition can only be satisfied past a certain radius, since r^{-1} becomes very large when r approaches zero. This threshold radius (r^*) is set by $r^* \sim 2\lambda_v$, where the two sides of Eq. S5.14 become comparable. The threshold radial distance that we choose to isolate the core is at least 5 – 10 μm for the asters of our study (see the lower x -limits in the profiles of Fig. S5.3) which exceed r^* at least a few times. This suggests that Eq. S5.14 is valid, justifying our use of the quasi-equilibrium assumption for modeling the motor distribution.

S5.2 Extraction of concentration profiles from raw images

In this section, we describe our approach for extracting the radial profiles of motor and microtubule concentrations from raw fluorescence images.

Fluorescence normalization and calibration

When taking images with a microscope, several sources contribute to the detected pixel intensities: the camera offset, autofluorescence from the energy mix, and fluorescence coming from the tagged proteins (tubulin or motors). In addition, due to the uneven illumination of the field of view, the same protein concentration may correspond to different intensities in the raw image.

We begin the processing of raw images by first correcting for the uneven illumination. For microtubule images, we use the first movie frames as references with a uniform tubulin concentration in order to obtain an intensity normalization matrix. Each pixel intensity of the final image frame is then rescaled by the corresponding normalization factor.

Although the motor concentration is also initially uniform, the light activation region in the first frame appears photobleached, making it unsuitable for the construction of a normalization matrix. Instead, we obtain this matrix from the final frame, after masking out the neighboring region of the aster, outside of which the nonuniformity of the fluorescence serves as a proxy for uneven illumination. Intensity normalization factors inside the masked out circular region are obtained through a biquadratic interpolation scheme. The steps leading to a normalized motor image are depicted in Fig. S5.1A.

After fluorescence normalization, we convert intensities into units of protein concentration using calibration factors estimated from images of samples with known protein contents. For K401 and Kif motors, we use the conversion 1000 intensity units \rightarrow 815 nM motor dimer. For Ncd dimers, which have fluorescent tags on both iLid and Micro units, we use the 1000 intensity units \rightarrow 407 nM conversion. In all three cases, 200 ms exposure time is used in the imaging. For tubulin, we make a rough estimate that after spinning the energy mix with tubulin, around 1 μ M of tubulin remain, all of which polymerize into GMP-CPP stabilized microtubules. This leads to the calibration of 360 intensity units \rightarrow 1 μ M tubulin (100 ms exposure time).

Aster center identification

In the next step of the profile extraction pipeline, we crop out the aster region from the normalized image and identify the aster center in an automated fashion. In particular, we divide the aster into 16 equal wedges, calculate the radial profile of motors within each wedge, and define the aster center as the position that yields the minimum variability between the motor profiles extracted from the different

wedges. Having identified the center, a mean radial profile for the aster is defined as the average of the 16 wedge profiles (Fig. S5.1B).

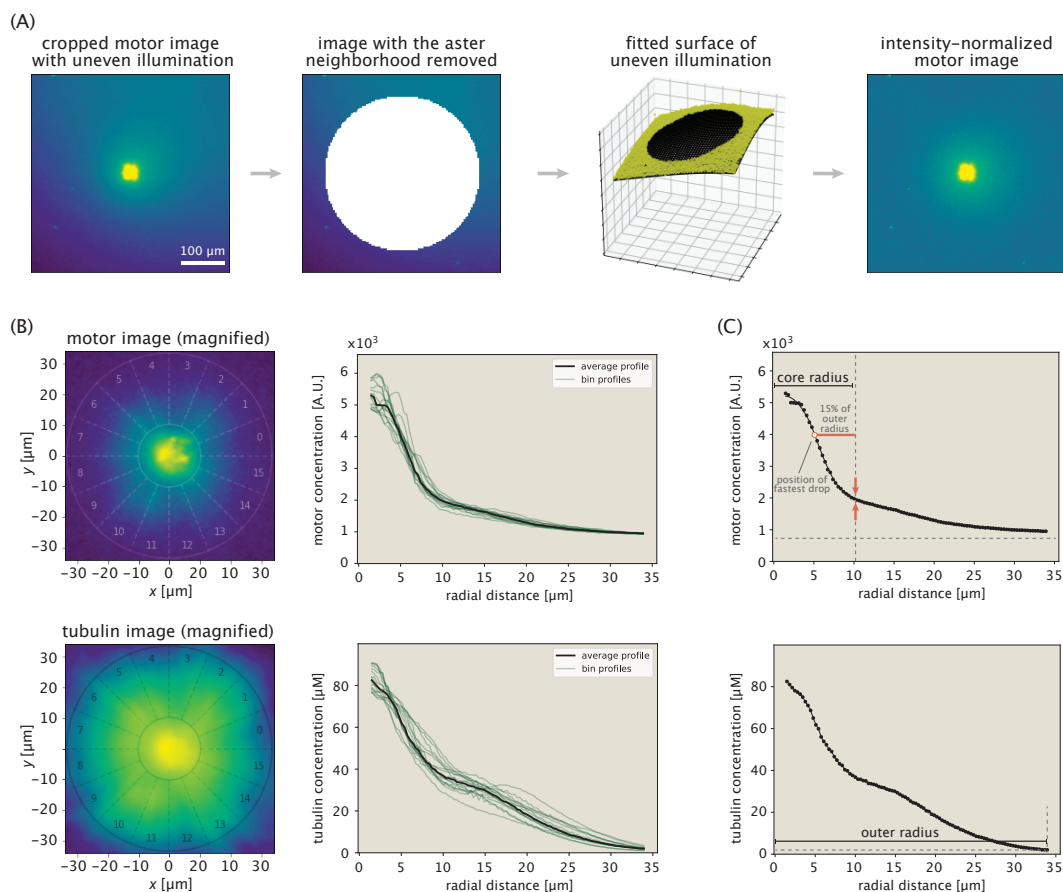


Figure S5.1: Procedure for extracting protein concentration profiles demonstrated on an example aster. (A) Steps taken in normalizing the fluorescence of motor images. The immediate aster region is shown with a saturated color to make it possible to see the nonuniform background fluorescence. (B) Aster center identification and extraction of radial concentration profiles. The numbers indicate the wedges at different angular positions. The two circles in the images indicate the inner and outer bounds. (C) Determination of inner and outer bounds based on the motor and tubulin profiles, respectively.

Inner and outer boundary determination

Since our modeling framework applies to regions of the aster where the microtubules are ordered, we consider the concentration profiles in a limited radial range for the model fitting procedure. As we do not have a PolScope image for every aster to precisely identify the disordered core region, we prescribe a lower threshold on the radial range by identifying the position of the fastest intensity drop and adding to it a buffer interval (equal to 15% of the outer radius) to ensure that the region of

transitioning from the disordered core into the ordered aster ‘arms’ is not included (Fig. S5.1C, top panel). As for the outer boundary, we set it as the radial position where the tubulin concentration exceeds its background value by a factor of two (Fig. S5.1C, bottom panel).

S5.3 Model fitting

Here we provide the details of fitting the expression we derived for the motor distribution (Eq. S5.10) to the profiles extracted from aster images. Since smaller asters are typically irregular and hence, do not meet the polar organization and radial symmetry assumptions of the model, we constrain the fitting procedure to larger asters formed in experiments with a minimum light illumination disk diameter of $200\ \mu\text{m}$.

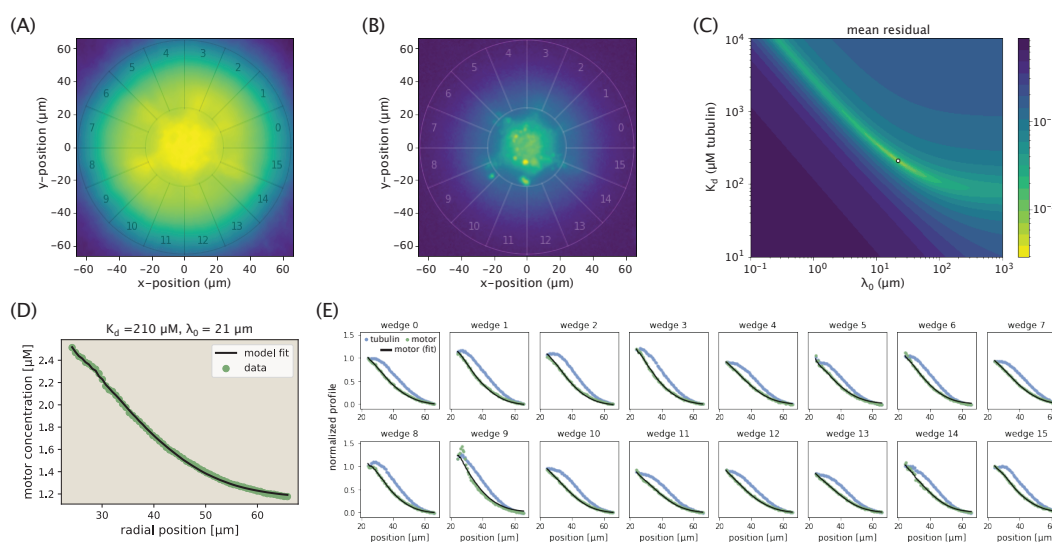


Figure S5.2: Demonstration of the model fitting procedure for average as well as separate wedge profiles. (A,B) Fluorescence images of an example Kif aster. 16 different wedges are separated and numbered. (C) Landscape of fit residuals when varying the two effective parameters K_d and λ_0 . For each pair, an optimal scaling coefficient C is inferred before calculating the residual. The dot at the brightest spot stands for the optimal pair (or, the arrow indicates the location of the optimal pair in the landscape). (D) Average motor profile and the model fit, along with the inferred parameters. (E) Collection of fits to separate wedge profiles using the optimal (K_d , λ_0) pair inferred from the average profile.

The different aspects of the fitting procedure are demonstrated in Fig. S5.2. Extracting the average tubulin and motor profiles, we fit our model to the motor profile and obtain the optimal values of the effective parameters K_d and λ_0 . With the exception of a few cases, the optimal pair (K_d , λ_0) corresponds to a distinct peak in the residual

landscape (Fig. S5.2C, note the logarithmic scale of the colorbar), suggesting that the parameters are well-defined. The fit to the motor data for the example aster is shown in Fig. S5.2D.

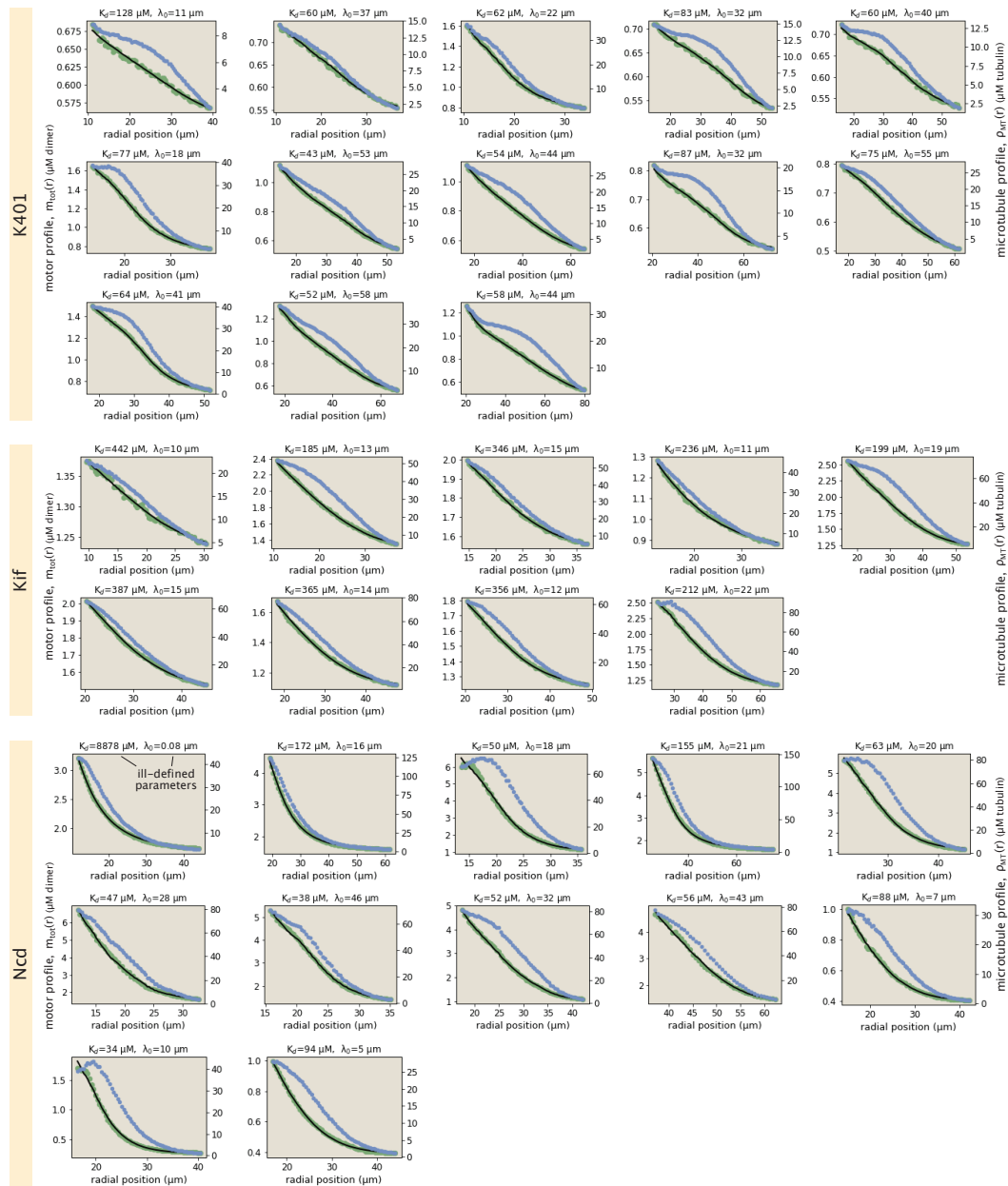


Figure S5.3: Collection of all fits to motor profiles. The green and blue dots represent the radially averaged motor and tubulin concentrations. The solid black lines represent the model fits.

As stated in the main text, we then use the data from the separate aster wedges to assess the quality of fit for each aster. Specifically, keeping the (K_d, λ_0) pair inferred from the average profile fixed, we fit the 16 separate wedge profiles by optimizing

over the scaling coefficient C for each of the wedges, and use the model residuals to assess the fit quality. In the set shown in Fig. S5.2E, with the exception of wedge 9 which contains an aggregate near the core radius, fits to all other wedge profiles are of good quality, translating into a low fitting error reported in Fig. 5.1E of the main text.

Repeating this procedure for all other asters, we obtain the best fits to their motor profiles and the corresponding values of the optimal (K_d, λ_0) pairs. The collection of all average profiles, along with the best model fits and inferred parameters are shown in Fig. S5.3.

S5.4 Accounting for finite MT lengths

Analysis of purified microtubule images shows that the microtubule length distribution is roughly exponential with a mean of $\ell_{\text{MT}} \approx 2 \mu\text{m}$ (Fig. S5.4). Taking the size of a tubulin dimer to be 8 nm, this mean length translates into the distance traveled in ≈ 250 motor steps, which is comparable to the processivity of K401 motors reported in Table 1 of the main text. Since motors stall when reaching microtubule ends, their effective advection speed will get reduced. Here, we account for this reduction and estimate its magnitude for the different motors used in our study.

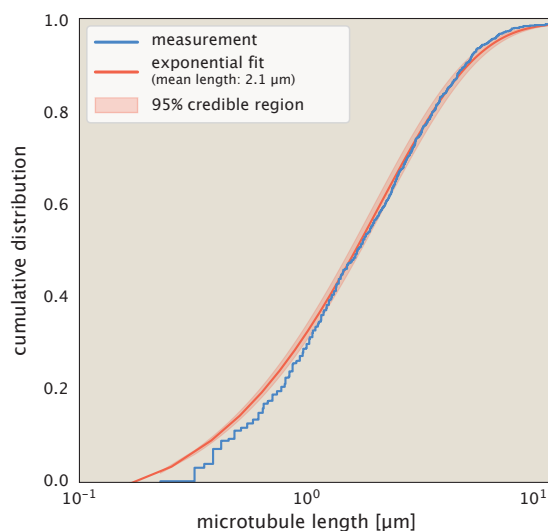


Figure S5.4: Measured cumulative distribution of microtubule lengths. See the supporting Jupyter notebook for details on how the distribution was extracted.

Consider the schematic in Fig. S5.5 where a motor is shown advecting on a microtubule with length L . If the distance x between the motor and microtubule end at the moment of binding is less than the motor processivity λ_v , then the motor will

reach the end and stall for a time period $\tau = 1/k_{\text{off}}^{\text{end}}$ before unbinding. On the other hand, if x is greater than λ_v , the motor will not stall while bound to the microtubule and hence, its effective speed will not be reduced.

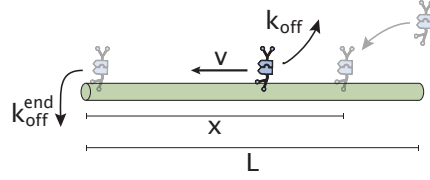


Figure S5.5: Schematic representation of initial motor binding, advection, and stalling at the microtubule end.

Assuming that the location of initial binding is uniformly distributed in the $[0, L]$ interval (hence, the chances of binding between x and $x + dx$ is dx/L), we can calculate the effective speeds in the above two cases as

$$\begin{aligned} v_{\text{eff}}(L < \lambda_v) &= L^{-1} \int_0^L \frac{x}{x/v + \tau} dx, \\ &= v \left(1 - \frac{v\tau}{L} \ln \left(1 + \frac{L}{v\tau} \right) \right), \end{aligned} \quad (\text{S5.15})$$

$$\begin{aligned} v_{\text{eff}}(L > \lambda_v) &= \underbrace{L^{-1} \int_0^{\lambda_v} \frac{x}{x/v + \tau} dx}_{\text{initial position} < \lambda_v} + \underbrace{L^{-1} \int_{\lambda_v}^L v dx}_{\text{initial position} > \lambda_v} \\ &= v \left(\frac{\lambda_v}{L} - \frac{v\tau}{L} \ln \left(1 + \frac{\lambda_v}{v\tau} \right) \right) + v \left(1 - \frac{\lambda_v}{L} \right) \\ &= v \left(1 - \frac{v\tau}{L} \ln \left(1 + \frac{\lambda_v}{v\tau} \right) \right). \end{aligned} \quad (\text{S5.16})$$

As can be seen, in both cases the effective speed is lower than the walking speed v . Now, if $p(L) = \ell_{\text{MT}}^{-1} e^{-L/\ell_{\text{MT}}}$ is the exponential distribution of microtubule lengths, then the mean effective motor speed evaluated over the whole microtubule population becomes

$$\langle v_{\text{eff}} \rangle = \int_0^{\infty} v_{\text{eff}}(L) p(L) dL. \quad (\text{S5.17})$$

An exact analytical expression is not available for the integral, and therefore, we evaluate it numerically for each motor.

The end-residence time τ was measured for rat kinesin-1 motors to be ≈ 0.5 s [5]. We take this estimate for our K401 motors (*D. melanogaster* kinesin-1) and since,

to our knowledge, there is no available data on end-residence times for Ncd and Kif motors, we use the same estimate for them.

Using this τ estimate, the value for the mean microtubule length ($\ell_{\text{MT}} \approx 2 \mu\text{m}$), and the motor speed (v) and processivity (λ_v) values from Table 5.1, we numerically evaluate the relative decrease in the effective speeds of the motors as

$$\text{K401: } \langle v_{\text{eff}} \rangle / v \approx 0.65, \quad (\text{S5.18})$$

$$\text{Kif: } \langle v_{\text{eff}} \rangle / v \approx 0.87, \quad (\text{S5.19})$$

$$\text{Ncd: } \langle v_{\text{eff}} \rangle / v \approx 0.98 \text{ (0.65)}. \quad (\text{S5.20})$$

Here we made two estimates for Ncd, first using its single-molecule processivity (≈ 1 step) reported in Table 5.1, and then the 100-fold increased processivity that is potentially reached due to collective effects mentioned in the main text. As a consequence of this effective speed reduction, we expect factors of ≈ 1.5 , ≈ 1.15 , and ≈ 1.02 (1.5) increase in the inferred λ_0 values of K401, Kif, and Ncd motors, respectively.

S5.5 Broader spread of the tubulin profile

In this section, we first derive the analytical form for the tubulin distribution in the idealized scenario where the motor profile can be approximated as an exponential decay. We then demonstrate that, when normalized, this distribution is always broader than the motor distribution.

We start off by writing the motor distribution as

$$m_{\text{tot}}(r) \approx m_{\infty} + \Delta m e^{-(r-r_{\text{in}})/\lambda}, \quad (\text{S5.21})$$

where λ is the decay length scale, m_{∞} is the background motor concentration corresponding to the free motor population, and Δm is the amplitude of the exponential decay. Next, using Eq. S5.5 as well as the definition $m_{\text{tot}}(r) = m_{\text{b}}(r) + m_{\text{f}}(r)$, we set out to obtain the distributions of bound and free motor populations. From Eq. S5.5, we have

$$\begin{aligned} m_{\text{b}}(r) &= -\lambda_0 m'_{\text{f}}(r) \\ &= -\lambda_0 (m'_{\text{tot}}(r) - m'_{\text{b}}(r)) \Rightarrow \end{aligned} \quad (\text{S5.22})$$

$$m'_{\text{b}}(r) - \frac{m_{\text{b}}(r)}{\lambda_0} = m'_{\text{tot}}(r) = -\frac{\Delta m}{\lambda} e^{-(r-r_{\text{in}})/\lambda}. \quad (\text{S5.23})$$

Solving for $m_{\text{b}}(r)$, we find

$$m_{\text{b}}(r) = C_{\text{b}} e^{(r-r_{\text{in}})/\lambda_0} + \Delta m \frac{\lambda_0}{\lambda + \lambda_0} e^{-(r-r_{\text{in}})/\lambda}, \quad (\text{S5.24})$$

where C_b is an integration constant. Because the approximation Eq. S5.21 applies to a finite radial interval $r \in [r_{\text{in}}, r_{\text{out}}]$, the constant C_b is generally nonzero. It specifies the relative contributions of free and bound motor populations to the total motor distribution $m_{\text{tot}}(r)$.

The free motor population is found by simply subtracting Eq. S5.24 from Eq. S5.21, that is,

$$\begin{aligned} m_f(r) &= m_{\text{tot}}(r) - m_b(r) \\ &= m_\infty + \Delta m \frac{\lambda}{\lambda + \lambda_0} e^{-(r-r_{\text{in}})/\lambda} - C_b e^{(r-r_{\text{in}})/\lambda_0}. \end{aligned} \quad (\text{S5.25})$$

Having obtained expressions for the two motor populations (bound and free), we now recall Eq. S5.6 that relates these two populations through the local tubulin density. Using Eq. S5.6, we find the tubulin density as

$$\begin{aligned} \rho_{\text{MT}}(r) &= K_d \frac{m_b(r)}{m_f(r)} \\ &= K_d \frac{\Delta m \frac{\lambda_0}{\lambda + \lambda_0} e^{-(r-r_{\text{in}})/\lambda}}{m_\infty + \Delta m \frac{\lambda}{\lambda + \lambda_0} e^{-(r-r_{\text{in}})/\lambda}} \\ &= K_d \frac{\lambda_0}{\lambda} \frac{e^{-(r-r_{\text{in}})/\lambda}}{\frac{m_\infty}{\Delta m} (1 + \lambda_0/\lambda) + e^{-(r-r_{\text{in}})/\lambda}} \\ &= K_d \frac{\lambda_0}{\lambda} \frac{e^{-(r-r_{\text{in}})/\lambda}}{\gamma + e^{-(r-r_{\text{in}})/\lambda}}, \end{aligned} \quad (\text{S5.26})$$

where we introduced the effective parameter $\gamma \equiv (m_\infty/\Delta m)(1 + \lambda_0/\lambda)$. Eq. S5.26 represents a partial sigmoid, the precise shape of which in the $r > r_{\text{in}}$ region is defined through the parameter γ (Fig. 5.2B).

To formally demonstrate that the tubulin profiles predicted in Eq. S5.26 are necessarily broader than the motor profile, we first normalized them after subtracting off the concentration values at the outer boundary, namely

$$\begin{aligned} \hat{m}_{\text{tot}}(r) &= \frac{m_{\text{tot}}(r) - m_{\text{tot}}(r_{\text{out}})}{m_{\text{tot}}(r_{\text{in}}) - m_{\text{tot}}(r_{\text{out}})} \\ &= \frac{\Delta m e^{-(r-r_{\text{in}})/\lambda} - \Delta m e^{-(r_{\text{out}}-r_{\text{in}})/\lambda}}{\Delta m - \Delta m e^{-(r_{\text{out}}-r_{\text{in}})/\lambda}} \\ &= \frac{e^{-(r-r_{\text{in}})/\lambda} - e^{-(r_{\text{out}}-r_{\text{in}})/\lambda}}{1 - e^{-(r_{\text{out}}-r_{\text{in}})/\lambda}}, \end{aligned} \quad (\text{S5.27})$$

$$\hat{\rho}_{\text{MT}}(r) = \frac{\rho_{\text{MT}}(r) - \rho_{\text{MT}}(r_{\text{out}})}{\rho_{\text{MT}}(r_{\text{in}}) - \rho_{\text{MT}}(r_{\text{out}})}$$

$$\begin{aligned}
&= \frac{\frac{e^{-(r-r_{\text{in}})/\lambda}}{\gamma+e^{-(r-r_{\text{in}})/\lambda}} - \frac{e^{-(r_{\text{out}}-r_{\text{in}})/\lambda}}{\gamma+e^{-(r_{\text{out}}-r_{\text{in}})/\lambda}}}{\frac{1}{\gamma+1} - \frac{e^{-(r_{\text{out}}-r_{\text{in}})/\lambda}}{\gamma+e^{-(r_{\text{out}}-r_{\text{in}})/\lambda}}} \\
&= \frac{(\gamma+1)(\gamma+e^{-(r_{\text{out}}-r_{\text{in}})/\lambda})}{(\gamma+e^{-(r-r_{\text{in}})/\lambda})(\gamma+e^{-(r_{\text{out}}-r_{\text{in}})/\lambda})} \times \frac{\gamma e^{-(r-r_{\text{in}})/\lambda} - \gamma e^{-(r_{\text{out}}-r_{\text{in}})/\lambda}}{\gamma - \gamma e^{-(r_{\text{out}}-r_{\text{in}})/\lambda}} \\
&= \frac{\gamma+1}{\gamma+e^{-(r-r_{\text{in}})/\lambda}} \times \underbrace{\frac{e^{-(r-r_{\text{in}})/\lambda} - e^{-(r_{\text{out}}-r_{\text{in}})/\lambda}}{1 - e^{-(r_{\text{out}}-r_{\text{in}})/\lambda}}}_{\hat{m}_{\text{tot}}(r)} \\
&= \frac{\gamma+1}{\gamma+e^{-(r-r_{\text{in}})/\lambda}} \times \hat{m}_{\text{tot}}(r). \tag{S5.28}
\end{aligned}$$

The local ratio of normalized tubulin and motor densities then becomes

$$\frac{\hat{\rho}_{\text{MT}}(r)}{\hat{m}_{\text{tot}}(r)} = \frac{\gamma+1}{\gamma+e^{-(r-r_{\text{in}})/\lambda}} > 1, \tag{S5.29}$$

which is always greater than 1 in the $r > r_{\text{in}}$ region. This is indicative of the ‘shoulder’ that the normalized tubulin profile often forms over normalized motor profile and demonstrates the broader spread of the tubulin distribution in this idealized setting.

References

1. Nédélec, F., Surrey, T. & Maggs, A. C. Dynamic concentration of motors in microtubule arrays. *Phys. Rev. Lett.* **86**, 3192–3195 (2001).
2. Aranson, I. S. & Tsimring, L. S. Theory of self-assembly of microtubules and motors. *Phys. Rev. E* **74**, 031915 (2006).
3. Lee, H. Y. & Kardar, M. Macroscopic equations for pattern formation in mixtures of microtubules and molecular motors. *Phys. Rev. E* **64**, 056113 (2001).
4. Sankararaman, S., Menon, G. I. & Kumar, P. S. Self-organized pattern formation in motor–microtubule mixtures. *Phys. Rev. E* **70**, 031905 (2004).
5. Belsham, H. R. & Friel, C. T. Identification of key residues that regulate the interaction of kinesins with microtubule ends. *Cytoskeleton* **76**, 440–446 (2019).